MODELLING AND SIMULATION OF SOOT GENERATION AND TRANSPORT

XIAOQIN HU

A thesis submitted in partial fulfilment of the
requirement of the University of Greenwich
for the Degree of Doctor of Philosophy

March 2016

The University of Greenwich
Faculty of Architecture, Computing and Humanities
30 Park Row, Greenwich, SE10 9LS

DECLARATION

I certify that this work has not been accepted in substance for any degree, and is not concurrently being submitted for any degree other than that of Doctor of Philosophy (PhD) being studied at the University of Greenwich. I also declare that this work is the result of my own investigations except where otherwise identified by references and that I have not plagiarised the work of others.

_____

Xiaoqin Hu

_____

Dr. Fuchen Jia (first supervisor)

_____

Prof. Edwin Galea (second supervisor)

ACKNOWLEDGEMENTS

I would like to give my special thanks to Dr Fuchen Jia, Prof Ed Galea, Dr Zhaozhi Wang for their advice and assistance during my studies at University of Greenwich. They opened a gate and led me into a new world of fire modelling. Without their support, I would not finish the dissertation.

I would like to thank Arun Mahalingam for sharing his experiments data. I would like to thank John Ewer, Angus Grandison and David Cooney, for technical support. I would like to thank Hui Xie, Lynn Hulse, Steven Deere, Maria Pretorius, Kristen Salzer-Frost, Sidra Athar, Yang Hai in no particular order, for their help to modify my dissertation. I would give my thanks to all staff in FSEG group for their kind and invaluable help during this PhD study.

Finally, I would like to express my love and gratitude to my family, for their understanding and endless love, through the duration of my study.

ABSTRACT

Soot released from fires not only causes danger to lives and property damage, but also effects fire spread by altering the radiation characteristics of fire effluents. In many situations, it is the soot concentration that controls the fire development. Therefore, soot modelling is of great importance in fire safety science. This necessitates the development of a global and general soot model within fire field models that can simulate the amount of soot generated and transported in large-scale fires in order to obtain an accurate soot concentration distribution within the building.

A soot transport model, called Multi-Particle-Size (MPS) model, has been developed in this study to improve the prediction of soot particle behaviour during transportation by considering the uneven soot mass size distributions and gravitational settling force on soot particles. The efficiency of the MPS model was investigated by simulating soot movements in three real experiments. The first two validation experiments were cable fires in a large-scale enclosed corridor and the third experiment analysed the soot produced from a soot generator in a warehouse with a high ceiling. The soot layers predicted by the MPS model matched the measurements/observation better than that from the Conventional Model in which the soot generation is modelled with a constant soot yield (CY) value and soot particles are treated as a gaseous combustion product.

A global soot generation model, called Beta soot generation (BSG) model has also been developed for non-premixed laminar flames. By making use of the characteristics of the beta function, the model has been extended to turbulent flames in the pre-scribed probability density function (PDF) approach with low cost in terms of computational resources. The model was validated by two turbulent methane and ethylene pool fires. The simulation results demonstrated that the soot volume fractions produced by the BSG model were in good agreement with the experimental data.

Further, the two new models have been integrated into a single soot model called BSG+MPS model. The performance of the model was examined by predicting the soot generation and transport in a large-scale enclosed corridor. The BSG+MPS model improved the prediction of soot concentration distribution in the corridor compared with the CY +MPS model.

Finally, the entire work is summarised and future work is suggested.

PUBLICATIONS

1. Hu X., Wang Z., Jia F. and Galea, E.R., (2010). Simulating a train car fire using a flame spread model, In *Proceedings of the 12th International Fire Science & Engineering Conference*, Interflam 2010, University of Nottingham, UK, (Vol. 2, pp. 1725-1730).
2. Hu X., Wang Z., Jia F. and Galea, E.R.,, (2012).Numerically Investigating the Effects of Interior Materials on Train Compartment Fires, *Journal of Fire Protection Engineering* 22(4), 245-270.
3. Hu X., Wang Z., Jia F. and Galea, E.R., Mayur. K. P. (2011). Simulating Smoke Transport in Large Scale Enclosure Fires Using a Multi-Particle-Size Model. *Fire Safety Science*, (10), 445-458.
4. Wang, Z., Hu **X.**, Jia, F., Galea, E.R., (2013). A two-step method for predicting time to flashover in room corner test fires using cone calorimeter data, *Fire and Materials*, 37(6), 457-473. DOI: 10.1002/fam.2139.

In preparation

5. Hu X., Jia F., Wang Z., and Galea, E.R., Grouping strategies for Multi-Particle-Size Soot Transport Model and Its Application to Simulate Soot Movement in a Building with High Ceiling.
6. Hu X., Jia F., Wang Z., and Galea, E.R., Predicting Soot layer in Large-scale Enclosure Fires Using Multi-Particle-Size model.
7. Hu X., Jia F., Wang Z., and Galea, E.R., Beta soot generation model and its validation with two turbulent pool fires.
8. Hu X., Jia F., Wang Z., and Galea, E.R., Simulating soot generation and transport in a large-scale enclosure fires.

CONTENTS

LIST OF FIGURES

LIST OF TABLES

NOMENCLATURE

a_f : Acceleration rates of fluid

a_p : Acceleration rates of particles

A_s : The soot particulate surface area

B: Brightness or luminance of the object

c_p : Specific heat capacity

C_D : Drag coefficient

$C_{V:}$ A contrast threshold at which an black object can be discerned

C_s: The concentration of soot

d_p : Soot size/diameter

d_{gn} Geometric mean size

D: The optical density per meter

D_a The Damkohler number

D_B : Brownian diffusion coefficient

D_f : Soot particle fractal dimension

D_m: Mass optical density

E_I Internal (thermal) energy

E_a :Activation energy

f_v : Soot volume fraction

F_B Buoyancy force

F_D : Drag force

F_G : Gravitational force

F_L : Shear-induced lift force

F_p : Pressure gradient force

F_T : Thermophoretic force

h The specific enthalpy

h_0 Specific total enthalpy

I_λ: Light intensity,

I: Radiation intensity

I_b denotes the black-body intensity

J : The diffusive flux

k_f : Thermal conductivities of the fluid

k_p : Thermal conductivities of the particle

K: Soot extinction coefficient

K_m: The specific extinction coefficient per unit mass

K_a : Karlowitz number

K_B: the Boltzmann's constant

Kn : Knudsen number

l_I : Integral length scale

l_L : The large-eddy turbulent length scale

l_K : Kolmogorov length

L_{sp} :laminar smoke point

Δm : mass loss

m_{fu} : Mass fraction of fuel

m_{ox} : Mass fraction of oxygen

M_α : Molecular weight of species α

N: Particle number density

p: Pressure

r_f : Forward reaction rate

r_b Backward reaction rate

R_g is the radius of gyration

R_u : The universal gas constant

Re: Reynolds number

Re_P : Particle Reynolds number

s : The stoichiometric oxygen/fuel ratio

S: The visibility distance

S_x : Soot obscuration

S_ϕ The source term for the variable ϕ

T_a :Activation temperature

t_L : The large-eddy turbulent time scale

t_I : Integral time scales

t_K : Kolmogorov time

t_α : Chemical time scale for species α

u_f : Velocity of the fluid

u_P : Velocity of the particle

v: Kinematic viscosity

$\vec{v}_s$: Particle settling velocity

V_c : Volume of the chamber

X_i : The mole fraction of component i,

Y_s : Soot mass fraction

Y_α the mass fractions of species α

Greek

μ : Dynamic viscosity

μ_t : Eddy viscosity

ν_t : Kinematic eddy viscosity

ρ : Density

σ_t Turbulence Prandlt/Schmidt number

σ_l Laminar Prandtl number

σ_{gn} : Geometric standard deviation

σ_s : Scattering coefficient

κ Absorption coefficient

κ_s : Absorption coefficient due to soot

κ_g Absorption coefficients of gas

ξ : Mixture fraction

ξ_{st} : Stoichiomentric mixture fraction

ε : Eddy diffusivity rate

ε_s : Surface emissivity

δ_{ij} : Kronecker delta

ω : Turbulence frequency

$\dot{\omega}_\alpha$ is the volumetric rate of generation of a species α

ω_c :Scattering albedo

ω''_{so} : Surface soot oxidation rate

ω'''_{sf} : Volumetric soot formation rate

τ_{rs} : Resident time

τ_{ij} Stress component acts in the j -direction on a surface normal to the i -direction

χ_C : Effective equivalence ratio

Γ : Diffusion coefficient

Γ_t : Eddy or turbulent diffusivity

Γ_c : Coagulation coefficient

ϑ : Turbulence velocity scale

Abbreviation

A-CSE : Alternative conditional source-term estimation

BSG: Beta soot generation model

CFD: Computational fluid dynamics

CMC: Conditional Moment Closure

CY+MPS: Constant soot yield + Multi-Particle-Size soot transport model

DNS: Direct Numerical Simulation

DOM: Discrete ordinates method

DTM: Discrete transfer method

EBU: Eddy break-up model

EDC: Eddy dissipation concept model

EDM: Eddy dissipation model

HACA hydrogen abstraction with acetylene addition

HRR: Heat release rate

HRRPUA: Heat release rate per unit area

LES: Large Eddy Simulation

MC: Monte Carlo method

MPS: Multi-Particle-Size

PDF: Probability density function

PE: Polyethylene

PHAs Polycyclic aromatic hydrocarbons

RANS: Reynolds-Averaged-Navier-Stokes

RTE : Radiation transport equation

SCRS: The simple chemical reacting system

SIMPLE: Semi-Implicit Method for Pressure Linked Equations

TSI: a threshold soot index

Chapter 1
Introduction

This chapter provides a description of the research background together with the motivation for conducting this study and sets out the research. Finally, the structure of the dissertation is outlined.

1.1 General background and research motivation

The combustion process releases energy and this has been central to the technical development of our society. However, combustion in the form of uncontrolled fires is an undesirable phenomenon that may result in the tragic loss of life, injuries to people or damage to property. It is reported that fire claims the lives of around 10 people per million population each year in the developed world [Anon, 2007]. In the lifetime of a person, about 1 in 784 people in the US and 1 in 135 in Russia died in fire accidents [Quintiere, 2006; Quintiere, 1998]. In the UK, fires cause more than 400 fatal casualties each year [Chowdhury *et al*., 2013]. Some dramatic disastrous fires that happened in the last decade are listed in Table 1.1. In addition to the human consequences, the economic cost, including direct property losses, emergency services, fire department costs, fire insurance administration and consequential losses to commerce, is estimated at around 1% of GDP (Gross Domestic Product) for most developed countries [Wilmot, 1986; Hall, 2014; Ashe *et al*., 2009].

1.1.1 Fire Safety Science

Fire is arguably one of the most complex phenomena considered in combustion science. It embraces intimate interplay between chemical reactions, aerodynamics, heat transfer, kinetics and multi-phase flow effects. This complexity delayed the development of fire research as a science until approximately the 1950s.

Table 1.1 fire disasters in the 21st century

Year	Event	Casualties
2001	Mesa Redonda shopping centre fire, Lima, Peru [Gonzales, 2002]	291
2003	The Station nightclub fire, Rhode Island, United States [Grosshandler, *et al*., 2005]	100
2004	San Pedro Sula prison fire, Honduras [Zhang & Huang, 2014]	103
2004	Ycuá Bolaños supermarket fire, Asunción, Paraguay [Benson, 2004]	283
2004	República Cromagnon nightclub fire, Buenos Aires [Strick, 2014]	194
2006	KTS Composite Textile factory fire, Chittagong, Bangladesh [Skeers, 2006]	54
2007	Nursing home fire at Kamyshevatskaya, Krasnodar, southern Russia [Venyavsky, 2007]	63
2009	Perm Lame Horse Night club fire in Perm, Russia [Strick, 2014]	153
2010	A fire in a prison in Santiago [Zhang & Huang, 2014]	81
2011	AMRI hospital Kolkata, West Bengal [Pal & Ghosh, 2014]	90
2012	A prison fire in Comayagua, Honduras [Zhang & Huang, 2014]	360
2012	A fire in a Karachi garment factory [Imtiaz, 2012]	312
2013	A fire in the Kiss nightclub in Santa Maria, Rio Grande do Sul, Brazil [Strick, 2014]	233
2013	The Jilin Baoyuanfeng Poultry Plant fire, Jilin Province, China [APTEC, 2013]	119
2014	A fire at a hospital in Jangseong County in South Korea [Kwon & Mullen, 2014]	21

Fire safety science comprises a range of disciplines including engineering, chemistry, computer science, psychology, mathematics and so on. It has grown significantly over the last three decades. However, mathematical modelling of fire is still a relatively young subject and it is an extreme challenge to describe the fire phenomenon from the mathematical point of view. The underlying combustion, fluid dynamics and turbulence have not yet been fully understood even with the help of modern experimental techniques and powerful computers. The first generation of computer fire models, called zone models, were developed from semi-empirical and analytical models in the 1960s. The development of computational fluid dynamics (CFD) led to a new fire modelling approach, which made it possible to describe fire phenomena via solutions of the basic conservation theorems. The CFD models, also called field models, have shown great fire simulation potential through numerous validations and have been successfully applied to various fire safety problems and is now an established approach in fire safety engineering. The CFD approach has become an established and important area in fire research and is considered to be fundamental to the future development of fire models.

Realisation of absolute safety is a practical impossibility, so fire safety science is not expected to eliminate all possible risks but should help manage and reduce risk to a level deemed

acceptable by society. Generally, the development of fire safety science should obey two basic rules [Yao, 2010]:

- The fire loss, including life and property loss, should be controlled to satisfy the minimum requirement of social safety;
- The total fire cost (fire investment +fire loss) should be minimized.

To reach the minimum requirement of social safety with a minimum total fire cost, a great effort is required to improve the current state of fire technology (see Figure 1.1).

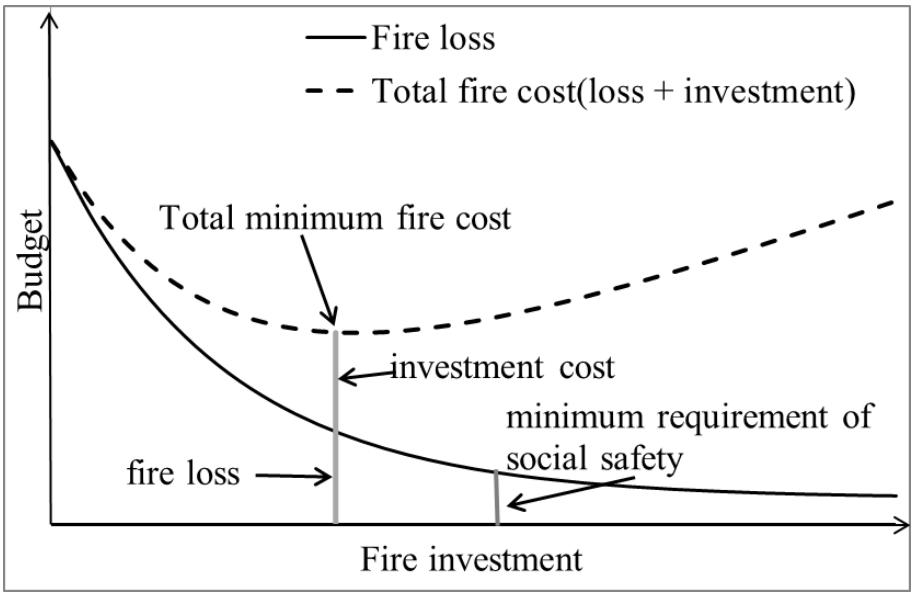

Figure 1.1 Relationship between fire loss and total fire cost (reproduced from[Yao, 2010])

Studies show that the existing fire research represents excellent value for money. For example, the National Institute of Standards and Technology (NIST) announced that their fire research programs, costing less than $9 million per year to run, contributed to total annual savings of $5-9 billion in fire cost [Shaenman, 1991]. Fire statistics indicated great reductions in the average fire death rates for most developed countries for the period 1979 to 1992. The reduction in fire deaths for the United Kingdom was 38%, or 9.0 fire deaths per million population. The United States had a reduction of 46%, or 16.8 fire deaths per million population [Anon, 1997]. A wide usage of smoke detectors brought about a 50% reduction in the fire death rate [Quintiere, 2006]. Even greater rewards can be expected from a greater investment in research ensuring fire safety engineering remains a scientifically robust profession.

1.1.2 Hazards of smoke

One noticeable phenomenon in fire is heavy smoke released from the fire flame, which indicates incomplete combustion (see Figure 1.2 (a)). Fire statistics suggests that the most commonly identified cause of death during fire incidents is being overcome by fire effluent, in particular smoke containing toxic gases. Together with other toxic gases, smoke contributed approximately two thirds of the fatalities according to a Fire and Rescue Services report (see Figure1.2 (b)) [Chowdhury *et.al.*, 2013].

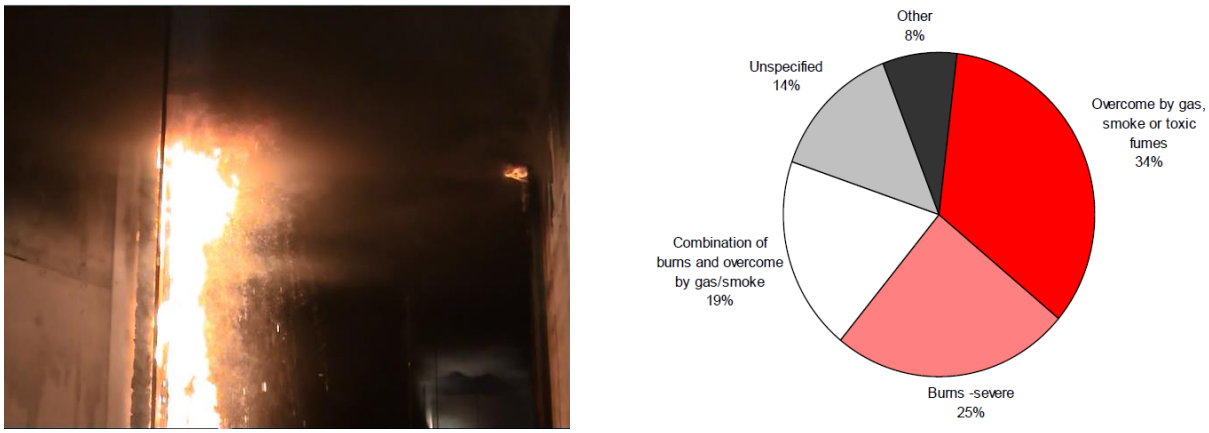

(a) (b)

Figure 1.2 (a) Smoke rising from a cable fire in a corridor [Persson, 2006], (b)Fatalities by cause, Great Britain, 2011/12 [Chowdhury *et.al.*, 2013].

The hazards presented by fire smoke to life safety and property loss can be classified into the following groups. Firstly, by reducing visibility smoke can delay the escape of the occupants and cause them to be exposed to the products of combustion for an unacceptably long period of time. Secondly, the large number of particles within the fire smoke may absorb toxic species which may pose a threat to exposed occupants. Full-scale fire tests have demonstrated that the mass fraction of HCl in smoke particles in a fire involving PVC carpet can be as high as 10% [Hertzberg, *et al.*, 2003]. Inhalation of particle-laden smoke makes breathing difficult and may damage the lungs of those exposed. It has been shown that smoke particles with a diameter smaller than 4 μm could penetrate deep into the respiratory system. Thirdly, smoke directly affects radiation exchange via absorption and scattering processes, which contributes to fast fire spread and growth. Finally, smoke deposited on the walls and inside devices may damage the building and equipment making them inoperable. Therefore, it is important to accurately predict smoke generation and transport within compartment fires for fire safety assessment.

1.1.3 The problems in soot modelling

”Smoke” is defined as the aerosol or condensed phase component of the products of combustion [Mulholland, 2002]. The impure carbon product in smoke is called soot. The above discussion shows that soot not only causes severe injury death and property damage, but also affects fire spread by altering the radiation characteristics. In many situations, it is the soot concentration which controls the fire development. Flashover is often associated with soot layer temperature at 800 to 900 K in compartment fires [Quintiere, 1998]. Therefore, soot modelling is of great importance in fire simulations.

Soot generation

The mechanisms of soot generation are very complex and there are still gaps in understanding nowadays. A lot of effort has been made to reveal the underlying mechanisms and a large number of models have been developed to describe the soot generation in various combustion situations [Kennedy, 1997]. These models range from a simple chemical approach to detailed chemical kinetics models. Soot models developed via an empirical approach are based totally on experimental data, which limits the general application in various fuel and combustion conditions. More detailed models such as detailed chemical kinetics models, model the full panoply of soot phenomena, from the initial pyrolysis of fuel, nucleation of soot particles, surface growth and coagulation, to final oxidation. However, these models are not appropriate for fire simulations because they come with a very high computational expense and detailed gas-phase chemistry is usually unknown. Semi-empirical soot models describe a limited number of phenomena which are usually considered to be important for soot generation. Those models may provide a good compromise between detailed chemical kinetics models and empirical models in terms of generality and computational cost. One shortcoming of this kind of model is that they are usually designed for a specific fuel and extension of this type of model beyond the operating conditions for which it was developed may lead to unreliable predictions.

Recently, two global semi-empirical models were proposed to calculate soot generation rate based on global species information, such as temperature and mixture fraction [Lautenberger *et al*., 2005; Yao *et al*., 2011a]. Estimating soot generation rate from global information may simplify the models and avoid solving intermediate incipient species, which are usually not fully unknown. These models have been used to simulate several laboratory experiments and acceptable predictions have been achieved. However, the above models are usually validated

in small laminar flames with grid size less than 1mm which would be impracticable in real fire simulations.

Therefore, efforts are still needed to develop a soot generation model for practical applications in fire simulations. The urgent problems calling for a solution in the field of soot generation modelling include:

- The soot generation rate varies with fuels and combustion configurations, which limits the application of soot models to just a number of fuels in real fires. Until now, the existing soot models have not yet been universally accepted for use in diffusion flames.

- The chemical reactions that produce soot are very sensitive to some scalars (temperature, species concentration etc.). In highly turbulent reacting flow, the fluctuations of these scalars usually deviate greatly from the mean scalar values, which can cause large errors when estimating the soot generation rate from mean scalar values. Although some combustion modelling methods closing chemical reaction source term such as CMC (Conditional Moment Closure) eliminates the effect of fluctuating scalars, they can come with an enormous computational cost. Tens of hours might be required to simulate a fire with a burner size less than 10 cm [Yao, 2010].

- In the applications of the existing soot models, the simulation regions often have to be discretised with a very fine mesh (cell size in the order of millimetres) to obtain accurate information to estimate soot generation rates, which makes the soot models impracticable in real fire simulations.

Soot transport

There can be great variation in the size of soot particles that generated by flames. While their diameters may vary in the magnitude of micrometres, most of them are smaller than 1 μm. In most of the existing models, soot is often simply treated as being in a gaseous state, thereby assuming soot move in the same manner as the other gaseous combustion products. This assumption is valid only for ultrafine particles. However, these models usually under-predict soot concentrations, especially in the lower layer. Some other models also ignore soot

movement by using other variables such as temperature or oxygen depletion to predict soot concentrations. This simplification is sometimes invalid as soot is a particle phenomenon which differs from gas behaviour or temperature distribution. Existing soot models have been developed with the assumption of constant particle size, which is not appropriate to simulate the soot motion behaviour because the size of soot particles often varies widely.

The characteristics of soot particles make soot motion behaviour in transportation different from the behaviour of gaseous species. Moreover, the possible large variation in soot particle size makes the assumption of constant particle size inappropriate to estimate the forces exerted on soot particles and hence soot movement. To predict soot movement with reasonable accuracy, the following issues have to be taken into account:

- Soot is a particle phenomenon and the mechanisms behind soot movement are different from those behind gaseous species. Soot particles behave in a different way from gaseous species as they move down to the cold lower layer.

- Some of the forces (gravitational force, drag force, *etc*.) that influence soot particle motion are heavily dependent on particle size. However, the soot particle size varies within a large range.

- For the applications in simulations of large-scale fires, any new approach of modelling soot transport should not cause a significant increase in the computational cost.

1.1.4 Research objectives

Given the importance of accurately modelling soot generation and transport in large fire simulations, the objectives of this work are:

Objective 1: To develop a soot transport model, which:

(a) addresses the influence of soot particle characteristics on the movement of soot particles;

(b) is computationally efficient. The model must not cause a significant increase in the simulation overheads compared with typical CFD runtime requirements;

(c) is validated using appropriate experimental data.

Objective 2: To develop a soot generation model, which:

(a) is able to generally model the yield of soot in non-premixed fires;
(b) requires as few as possible pieces of input data that are measurable or available from the literature for a variety of fuels;
(c) is computationally efficient. The model must be able to be applied to large-scale fires without a significant increase in computational cost;
(d) is validated using appropriate experimental data.

Objective 3: To integrate the soot generation and transport model to form a single soot model, which:

(a) is implemented within the framework of the CFD fire modelling tool SMARTFIRE;
(b) is validated using appropriate experimental data.

1.2 Structure of dissertation

The remainder of the dissertation is laid out as follows:

Chapter 2, the theoretical background to CFD based fire field models is presented at the beginning, followed by a review of CFD fire models and their sub-models, including turbulence, combustion and radiation models. Also a brief summary of boundary conditions and numerical solution procedure for CFD fire models are presented. Finally, the performance of field models is investigated by comparing CFD fire simulations with the measured data and observation in a rail car compartment fire.

Chapter 3 begins by introducing basic soot properties. Then the state-of-the-art knowledge concerning soot generation mechanisms is presented, followed by a review of existing soot models, including empirical, semi-empirical, and detailed chemistry soot models. The mechanisms of soot particle movement are outlined together with the methodology for modelling soot transport.

Chapter 4 presents the first original contribution in the dissertation and addresses Objectives 1(a) and 1(b). A soot transport model, called Multi-Particle-Size model, is developed to improve the prediction of the transport of soot particles in fire by considering uneven soot mass size distributions and gravitational forces on soot particles. To make the model practical

for fire simulations, a group division strategy is proposed for a variety of building materials by taking into account computational efficiency and performance accuracy.

Chapter 5 and 6 address Objectives 1(b) and 1(c) by validating the Multi-Particle-Size model by simulating soot movement in three experiments. One experiment examines soot movement within a warehouse with a high ceiling and the other two examine fires in a large-scale corridor. The predictions of soot behaviour are compared with the measured data and video recordings at various positions.

Chapter 7 presents the second original contribution to the dissertation and addresses Objectives 2(a) to 2(c). It develops a new global approach to modelling soot generation in non-premixed hydrocarbon flames. The new model, called the Beta soot generation model, is mixture fraction-based and relates the peak soot formation rate to the fuels' laminar smoke point height. By making use of the characteristics of the beta function, the model is extended to turbulent combustion with modest additional computational cost.

Chapter 8 addresses Objectives 2(c) and 2(d). The Beta soot generation model developed in Chapter 7 is applied to the simulations of turbulent ethylene and methane pool fires. The predicted soot volume fractions at different heights are compared with the experimental measurements and predictions from other models.

Chapter 9 addresses Objectives 3(a) and 3(b). It focuses on the performance derived from integrating the soot transport model and the soot generation model. The large-scale corridor fire simulated in Chapter 5 is simulated again by the integrated model.

Finally, the entire study is summarised and future work is suggested.

It is hoped that this dissertation will provide an invaluable contribution to soot modelling research, improving the accuracy and efficiency of predicting soot generation and transport in fires.

Chapter 2

Theoretical background and field models

Mathematical modelling of fires has over the last few decades undergone a transition from zone to field modelling. Field modelling is based on the theory of computational fluid dynamics (CFD). In this chapter, the fundamental theories of CFD are presented first. Then the most widely used sub-models of CFD fire modelling are summarized, including turbulence, combustion, radiation and other various sub-models for specific physical process. Numerical techniques of the CFD equations are introduced briefly. The final part discusses the performance of a CFD fire model by comparing the prediction and measured data in a rail car apartment fire, which has been published [Hu, *et al*., 2010; Hu, *et al*., 2011].

2.1 Fire modelling

Mathematical modelling of fire started in 1950s and has grown dramatically, especially over the last three decades [Markatos, *et al.,* 1982; Walton, 1985; Ierotheou & Galea, 1992; Ewer, *et al.,* 1999]. Fire modelling may be classified into two major strategies: zone modelling developed from semi-empirical and analytical methods and field modelling based on CFD.

2.1.1 Zone models

Zone models, which rely heavily on empiricism and analytical approaches in searching a solution of a model, form the first generation of computer fire models. These models attempt to divide the burning enclosure into several distinct regions of consistent fire behaviour. Most zone models adopt the two layer approximation, involving upper hot gas layer and lower cold air layer. Within zones, experimentally based empirical expressions are used to describe the averaged physical quantities (e.g. temperature, mass, energy, etc.) over zones while interaction between zones is determined by conservation laws. A comprehensive discussion of the zone modelling technique may be found in [Cox, 1995].

The main strengths –conceptual simplicity and modest use of computer resources –make this approach relatively easy and inexpensive to use. Zone models have been applied in fire safety design with considerable success for a long period of time. However, this approach suffers from a number of major problems which limit the models to give more useful and reliable information about fire development. First, Zone models are in nature one-dimensional models which are incapable of spatial resolution and supply limited information about the fire environment. Second, the zone models rely on the prior understanding of how a fire behaves, thus these models can never be decoupled from supporting experimental studies. Third, the assumptions which make zone models relatively simple are not strictly correct. For example, it is not true that the layers connect each other only by the thermal plume and the gradients of physical quantities do not develop within layers.

2.1.2 Field models

Fire field models employ CFD techniques to represent the fundamental laws of fluid behaviour via a set of conservation equations [Versteeg & Malalasekera, 2007; Novozhilov, 2001]. The generalised governing equation for all conserved variables (e.g. energy, mass, momentum, etc.) is expressed in the form of the following partial differential equation

$$\frac{\partial \rho\phi}{\partial t} + div(\rho\vec{U}\phi) = div(\Gamma_\phi \nabla\phi) + S_\Phi \qquad (2.1)$$

Accumulation rate Convection Diffusion source

where ϕ represents a conserved fluid variable; ρ and $\vec{U}$ are the local density and velocity vector; Γ_ϕ is the effective exchange coefficient of ϕ; S_Φ represents the source term for the corresponding variable ϕ and time t is an independent variable.

The CFD approach makes it possible to model fire phenomena from basic principles via solution of the basic conservation equations and has been considered to be the fundamental to the future development of fire models. Following the development of computer resources, field modelling has become practical and has been applied successfully in various fire safety problems [Wang, *et al.*, 2012; Jia, *et al.*, 2006a; Jia, *et al.*, 2006b; Wang, *et al.*, 2001; Jia, *et al.*,1999; Galea, *et al.*, 1992; Wang, *et al.*, 2011; *Wang, et al.*, 2007; Wen, *et al.*, 2011]. However, CFD based fire modelling is still a relatively young discipline and the complexity of fire phenomena makes it extremely challenging to model every aspect of the fire processes.

2.2 Basic conservation equations

2.2.1 Governing equations of fluid flow

The governing equations of fluid flow represent mathematical statements of the conservation laws of physics: conservation of mass, momentum and energy. These lead to a general governing equation of fluid flow.

Continuity equation

The mass balance for a fluid can be expressed in the equation below:

$$\frac{\partial \rho}{\partial t} + div(\rho \vec{U}) = 0 \tag{2.2}$$

where $div(\rho\vec{U}) = \frac{\partial(\rho u_i)}{\partial x_i} + \frac{\partial(\rho u_j)}{\partial x_j} + \frac{\partial(\rho u_k)}{\partial x_k}$.

The first term in Equation (2.2) is the rate of the density change in time (mass per unit volume). The second term, called the convective term, describes the net flow of mass out of the fluid across boundaries.

Momentum equations

The momentum equations are derived from Newton's second law, which states the rate of change of momentum of fluid is equal to the sum of the forces on the fluid. Equations describing the conservation of momentum are presented below:

$$\frac{\partial}{\partial t}(\rho u_s) + div(\rho u_s \vec{U}) = -\frac{\partial p}{\partial x_s} + \frac{\partial \tau_{is}}{\partial x_i} + \frac{\partial \tau_{js}}{\partial x_j} + \frac{\partial \tau_{ks}}{\partial x_k} + S_{Mx_s}' \tag{2.3}$$

There are three directions, $x_s, s = i, j, k$ and u_s means the corresponding velocity. The suffix i and s in viscous stresses τ_{is} indicate that the stress component acts in the s-direction on a surface normal to the i-direction. The source term S_{Mx_s} includes contributions due to body force only.

Energy equation

Here the specific energy E of a fluid is defined as the sum of internal (thermal) energy E_I and kinetic energy $\frac{1}{2}(u_i^2 + u_j^2 + u_k^2)$, thus it may be written as $E = E_I + \frac{1}{2}(u_i^2 + u_j^2 + u_k^2)$. The

first law of thermodynamics states that the change rate of energy of a fluid element equals the rate of heat addition to the fluid plus the rate of work done on the fluid. The equation describing the conservation of energy is presented as follows:

$$\frac{\partial}{\partial t}(\rho E) + div(\rho E\vec{U}) = -div(p\vec{U}) + div(k_f\ gradT) + \Phi + S_E \tag{2.4}$$

where the dissipation function Φ is:

$$\Phi = \frac{\partial u_i \tau_{ii}}{\partial x_i} + \frac{\partial u_i \tau_{ji}}{\partial x_j} + \frac{\partial u_i \tau_{ki}}{\partial x_k} + \frac{\partial u_j \tau_{ij}}{\partial x_i} + \frac{\partial u_j \tau_{jj}}{\partial x_j} + \frac{\partial u_j \tau_{kj}}{\partial x_k} + \frac{\partial u_k \tau_{ik}}{\partial x_i} + \frac{\partial u_k \tau_{jk}}{\partial x_j} + \frac{\partial u_k \tau_{kk}}{\partial x_k} \tag{2.5}$$

In compressible flows, enthalpy is used to replace the energy. The specific enthalpy h and specific total enthalpy h_0 of a fluid are defined as:

$$h = E_I + p/\rho \tag{2.6}$$

$$h_0 = h + \frac{1}{2}(u_i^{\ 2} + u_j^{\ 2} + u_k^{\ 2}) = E + p/\rho \tag{2.7}$$

Substitution of Equation (2.7) into Equation (2.4) and some rearrangement yields the enthalpy equation:

$$\frac{\partial}{\partial t}(\rho h_0) + div(\rho h_0\vec{U}) = \frac{\partial p}{\partial t} + div(k_f\ gradT) + \Phi + S_h \tag{2.8}$$

where k_f is the thermal conductivity of the fluid flow.

Equations of state

Relationships between the unknown four thermodynamic variables ρ, p, T, E_I can be obtained through the assumption of thermodynamic equilibrium.

$$p = p(\rho, T) \text{ and } E_I = E_I(\rho, T) \tag{2.9}$$

For a perfect gas the following equations of state are used:

$$p = \rho R_u T \text{ and } E_I = C_v T \tag{2.10}$$

where C_v is the specific heat at a constant volume and R_u is the universal gas constant with the value of $8.3142\,(J/mol\,K)$. Thus the state of a substance in thermodynamic equilibrium can be described by means of just two state variables.

2.2.2 Navier-Stokes equations

The governing equations contain further unknowns, the viscous stress components τ_{ij}, $i, j = 1,2,3$, which can be expressed as functions of local deformation rate or strain rate in many fluid flows. The local deformation rate is composed of the linear deformation rate and the volumetric deformation rate.

The rate of the linear deformation of a fluid has nine components s_{ij}, $i, j = 1,2,3$. Three of them are linear elongating deformation components:

$$s_{ii} = \frac{\partial u_i}{\partial x_i}, \ i = 1,2,3 \tag{2.11}$$

The other six are shearing linear deformation components:

$$s_{ij} = s_{ji} = \frac{1}{2}\left(\frac{\partial u_i}{\partial x_j} + \frac{\partial u_j}{\partial x_i}\right), \ i, j = 1,2,3, \ i \neq j \tag{2.12}$$

The volumetric deformation is given by:

$$div\vec{U} = \frac{\partial u_i}{\partial x_i} + \frac{\partial u_j}{\partial x_j} + \frac{\partial u_k}{\partial x_k} \tag{2.13}$$

The useful forms of the momentum conservation equations are obtained by introducing a suitable model for the viscous stresses τ_{ij}. In a Newtonian fluid the viscous stresses τ_{ij} are proportional to the rates of deformation:

$$\tau_{ii} = 2\mu\frac{\partial u_i}{\partial x_i} + \lambda div\vec{U}, \qquad i = 1,2,3 \tag{2.14}$$

$$\tau_{ij} = \tau_{ji} = \mu\left(\frac{\partial u_i}{\partial x_j} + \frac{\partial u_j}{\partial x_i}\right), \qquad i, j = 1,2,3, \ i \neq j \tag{2.15}$$

where the first (dynamic) viscosity, μ, relates stresses to linear deformations, and the second viscosity, λ, relates stresses to the volumetric deformation. For gases a good approximation can be obtained by taking the value $\lambda = -\frac{2}{3}\mu$.

Substitution of the above Equations (2.14)-(2.15) into Equation (2.3) yields the Navier-Stokes equations:

$$\frac{\partial}{\partial t}(\rho u_i) + div(\rho u_i \vec{U}) = -\frac{\partial p}{\partial x_i} + div(\mu \, gradu_i) + S_{Mx_i} \tag{2.16}$$

Using the Equation (2.14)-(2.15) in the energy conservation Equation (2.4) and rearranging it, we obtain:

$$\frac{\partial}{\partial t}(\rho E_I) + div(\rho E_I \vec{U}) = -div(p\vec{U}) + div(k_f \, grad T) + \Phi + S_{E_I} \tag{2.17}$$

Here the dissipation function Φ can be shown to be:

$$\Phi = \mu\left\{2\sum_i\left(\frac{\partial u_i}{\partial x_i}\right)^2 + \sum_{i,j}\left(\frac{\partial u_i}{\partial x_j} + \frac{\partial u_i}{\partial x_j}\right)^2\right\} + \lambda(div\vec{U})^2 \tag{2.18}$$

2.2.3 Transport equation (general equation)

As there are significant commonalities between the conservation equations, the conservative form of all fluid flow equations can usefully be written in the following form:

$$\frac{\partial(\rho\phi)}{\partial t} + div(\rho\phi\vec{U}) = div(\Gamma grad\phi) + S_\phi \tag{2.19}$$

Where ϕ represents the dependent variable to be solved, S_ϕ is the additional source term of variable ϕ. The first term in Equation (2.19) is the transient term, which represents the accumulation per unit volume. The second term is the convection term, which denotes the accumulation of ϕ per unit volume due to the divergence in its convective flux field. The third term is the diffusion term (Γ is the diffusion coefficient), which represents the accumulation of ϕ per unit volume due to the divergence in its diffusive flux field. The last term is the source term, which includes all the additional sources of ϕ. For example, the change of heat via radiation is a source term of the energy conservation equation and the reaction rate per unit volume of the fuel is a source term of the fuel mass fraction equation.

2.3 Turbulence modelling

2.3.1 Nature of turbulence

In 1975, Hinze gave a formal definition of turbulence [Hinze, 1975]:

> *"Turbulent fluid motion is an irregular condition of flow in which the various quantities show a random variation with time and space coordinates."*

The transition between laminar and turbulent flow is characterised in a dimensionless quantity called Reynolds number (Re), which is defined as the ratio of inertial forces to viscous forces, expressed as:

$$\mathrm{Re} = \frac{\text{Velocity} \cdot \text{Length scale}}{\text{Kinematic viscosity}} = \rho u L / \mu \tag{2.20}$$

Usually the flow with a Reynolds number greater than 4000 is turbulent [Holman, 2002].

In a turbulent flow the instantaneous value of a general flow variable ϕ is decomposed into a mean component $\overline{\phi}$ and a time varying fluctuating component $\phi'(t)$ with zero mean value, hence $\phi(t) = \overline{\phi} + \phi'(t)$. There are usually two type of averaging for $\overline{\phi}$.

2.3.1.1 Reynolds averaging (time averaging)

$$\overline{\phi} = \frac{1}{\Delta t}\int_0^{\Delta t} \phi(t)\mathrm{d}t \tag{2.21}$$

Here Δt is required to be much greater than the characteristic time scales of the turbulent fluctuations, but smaller than characteristic time-scales of the mean flow.

Since the fluctuating components of the flow oscillate randomly with positive and negative values, the time average of the fluctuations, $\overline{\phi'(t)}$, is zero:

$$\overline{\phi'} = \frac{1}{\Delta t}\int_0^{\Delta t} \phi'(t)dt \equiv 0 \tag{2.22}$$

The instantaneous value is then written as $\phi = \overline{\phi} + \phi'$.

2.3.1.2 Favre average (density-weighted time averaging)

In compressible turbulent flows, the density fluctuations appear to affect the flow significantly sometimes. The density-weighted mean is defined as:

$$\tilde{\phi} = \frac{\overline{\rho\phi}}{\overline{\rho}} \tag{2.23}$$

The instantaneous value of ϕ is then expressed in the form of:

$$\phi = \tilde{\phi} + \phi'' \tag{2.24}$$

In contrast to the Reynolds decomposition, the quantity ϕ'' also include the effect of density fluctuations. The average of the Favre fluctuation is non-zero: $\overline{\phi''} \neq 0$ but $\overline{\rho\phi''} = 0$.

2.3.1.3 Turbulent scales

In turbulent flow the kinetic energy is transferred from the largest scales of turbulent motion to smaller scales and dissipated by viscous action at smallest scales finally. To describe the characteristics of turbulence, time scales and length scales are introduced here.

The large-eddy turbulent time scale and length scale are defined respectively as function of kinetic energy k and dissipation rate ε:

$$t_L = \frac{k}{\varepsilon} \tag{2.25}$$

$$l_L = \frac{k^{3/2}}{\varepsilon} \tag{2.26}$$

The mean size of the anisotropic large eddies in the energy spectrum is represented by integral length scale:

$$l_I = \int_0^\infty \frac{\overline{u_i'(x)u_i'(x+r)}}{\overline{u_i'^2}} dr \tag{2.27}$$

The integral time scales is approximated by:

$$t_I \approx \left(\frac{l_I}{u'}\right)^{1/2} \tag{2.28}$$

Here u' is the integral velocity calculated as:

$$u' = \sqrt{\frac{1}{2}\widetilde{u}_i''^2} \tag{2.29}$$

Another important length scale is the smallest turbulent length scale, called Kolmogorov length, which is related to the energy dissipation:

$$l_K \approx \left(\frac{\nu^3}{\varepsilon}\right)^{1/4} \tag{2.30}$$

The Kolmogorov time is defined as a function of the molecular kinematic viscosity and the dissipation rate:

$$t_K = \left(\frac{\nu}{\varepsilon}\right)^{1/2} \tag{2.31}$$

In non-premixed combustion flames, the chemical time scale for species α is defined as:

$$t_c = \frac{\rho Y_\alpha}{\omega_\alpha} \tag{2.32}$$

where ω_α is the reaction rate for species α.

The Damkohler number D_a is used to indicate whether chemistry is fast, (D_a >>1), or slow, (D_a <<1)), relative to the turbulence time scales. D_a is defined as the ratio between integral time scale and the chemical reaction time scale:

$$D_a = \frac{t_I}{t_c} \tag{2.33}$$

Another measure of turbulence is the Karlowitz number K_a, which describes the ratio of the integral time scale and smallest Kolmogorov time scale:

$$K_a = \frac{t_I}{t_K} \tag{2.34}$$

When Karlowitz number is close to unity, the smallest eddies penetrate the laminar flamelet preheated zones.

2.3.2 Reynolds-Averaged Navier-Stokes (RANS) equations

The turbulence velocity fluctuations cause extra momentum exchange between eddies and produced extra turbulent shear stresses. The additional stresses known as the Reynolds stresses cannot be negligible as they are usually very large compared with the viscous stresses in a turbulent flow. The Reynolds stress terms can be written as:

$$\tau''_{ii} = -\rho\overline{u_i''^2}, \qquad i = 1,2,3 \tag{2.35}$$

$$\tau''_{ij} = \tau''_{ji} = -\rho\overline{u_i'' \, u_j''}, \qquad i, j = 1,2,3, \; i \neq j \tag{2.36}$$

Considering the Reynolds stresses and the density fluctuation effect, the turbulent flow equations [Pletcher, *et al*., 2012] for compressible flows are expressed below:

Continuity equation:

$$\frac{\partial \overline{\rho}}{\partial t} + div(\overline{\rho}\tilde{\vec{U}}) = 0 \tag{2.37}$$

Momentum equations:

$$\begin{aligned}\frac{\partial}{\partial t}(\overline{\rho}\tilde{u}_s) + div(\overline{\rho}\tilde{u}_s\tilde{\vec{U}}) &= -\frac{\partial \overline{p}}{\partial x_s} + div(\mu\ grad\ \tilde{u}_s) \\ &+ \left[-\frac{\partial(\overline{\rho u_s'' u_i''})}{\partial x_i} - \frac{\partial(\overline{\rho u_s'' u_j''})}{\partial x_j} - \frac{\partial(\overline{\rho u_s'' u_k''})}{\partial x_k} \right] + S_{Ms},\ s = i, j, k\end{aligned} \tag{2.38}$$

Enthalpy equation:

$$\begin{aligned}\frac{\partial(\overline{\rho}\tilde{h}_0)}{\partial t} + div(\overline{\rho}\tilde{h}_0\tilde{\vec{U}}) &= div(\Gamma_{h_0} grad\tilde{h}_0) \\ &+ \left[-\frac{\partial(\overline{\rho u_i'' h_0''})}{\partial x} - \frac{\partial(\overline{\rho u_j'' h_0''})}{\partial y} - \frac{\partial(\overline{\rho u_k'' h_0''})}{\partial z} \right] + S_{h_0}\end{aligned} \tag{2.39}$$

Scalar transport equation

$$\begin{aligned}\frac{\partial(\overline{\rho}\tilde{\phi})}{\partial t} + div(\overline{\rho}\tilde{\phi}\tilde{\vec{U}}) &= div(\Gamma_{\varphi} grad\tilde{\phi}) \\ &+ \left[-\frac{\partial(\overline{\rho u_i'' \phi''})}{\partial x} - \frac{\partial(\overline{\rho u_j'' \phi''})}{\partial y} - \frac{\partial(\overline{\rho u_k'' \phi''})}{\partial z} \right] + S_{\phi}\end{aligned} \tag{2.40}$$

where the over-bar indicates a time-averaged variable and the tilde indicates a Favre-averaged variable.

2.3.3 Calculation of turbulence models

As the turbulent fluctuation causes eddies with a wide range of length and time scales that interact in a dynamically complex way, turbulent models are, therefore, naturally classified based on the methods by which the turbulence phenomenon is treated. The methods can be grouped into three major categories: Direct Numerical Simulation (DNS), Large Eddy Simulation (LES) and Reynolds-Averaged Navier-Stokes (RANS). The sections that now follow will discuss each of the method in brief. A more comprehensive discussion of the DNS and LES simulation may be found in [Jiang & Lai, 2009].

Direct Numerical Simulation (DNS)

This simulation directly resolves the whole spectrum of turbulent scales without modelling required to solve the unsteady Navier-Stokes equations [Moin & Mahesh, 1998]. The spatial grids required in DNS are sufficiently fine to deal with the entire range of length scales at

which energy dissipation takes place. In practice, the number of grids is no less than $Re^{9/4}$, where Re is the turbulent Reynolds number. The time steps should be sufficiently small to resolve the period of the fastest fluctuations. The typical values of turbulent Re might be in the order of 10^5, which indicates that the calculations are highly costly in terms of computing resources and the method is not practical in industrial flow computations.

Large Eddy Simulation (LES)

This method makes use of the fact that large scale eddies are generally more energetic than small ones, and they dominate the transport of conserved properties. Therefore, it is feasible to resolve the large scale motion more accurately than the small scale motion. In LES simulation, a filtering function is selected to remove eddies with a length scale less than a certain cut-off width prior to computing the unsteady Navier-Stokes equations. Then the filtering operation is performed on the time-dependent flow equations. Thus the information relating to the smaller, filtered-out turbulent eddies is destroyed. The interaction effects between the larger, resolved eddies and the smaller unresolved ones, give rise to SGS stresses, which can be described by means of a so-called sub-grid scale model. The demands of LES on computing resources in terms of storage and volume of calculations are large, and this technique needs further research and development to deal with CFD problems with complex geometry. Until now, several commercial CFD codes use the LES technique and a more widespread industrial application is likely to happen [Moin, 2002; Ferraris & Wen, 2008].

Reynolds-Averaged Navier-Stokes (RANS)

As engineers are almost always interested in the prediction of the mean properties of the flow, RANS models are focused on the mean flow and the effects of turbulence on mean flow properties. Prior to resolving the Navier-Stoke equations, the extra Reynolds stresses and fluxes caused by interactions between various turbulent fluctuations are modelled with RANS models. Some classical RANS turbulence models, such as $k-\varepsilon$ model and $k-\omega$ model, have been successful in expressing the main features of turbulent flow. The computing resources required for reasonably accurate flow computations are modest, so this approach has been the mainstay of engineering flow calculations over the last three decades.

2.3.4 Classification of RANS turbulence models

A description of the effects of turbulence on the mean flow gives rise to additional unknowns in the RANS equations: Reynolds stresses and Reynolds fluxes, $\overline{u_i\varphi''}$. It is necessary to develop turbulence models to determine the unknown turbulence transport terms before computing the RANS equations. Therefore, the common RANS turbulence models are classified on the basis of the number of additional transport equations that need to be solved for Reynolds stresses and fluxes.

Table 2.1: classification of turbulence RANS models

No. of extra transport equations	Classical models
Zero-equation	Prandtl's mix-length
One-equation	Prandtl's K-L model
Two-equation	$k-\varepsilon$ model $k-\omega$ model

In the following sections, the concepts of eddy viscosity and eddy diffusivity are introduced first. Then the RANS turbulence models are represented in detail according to the classification of models.

2.3.4.1 Eddy viscosity and eddy diffusivity

Most turbulence models propose that the Reynolds stresses might be proportional to mean rates of deformation,

$$\tau_{ij}'' = -\rho\overline{u_i''\ u_j''} = \mu_t\left(\frac{\partial\tilde{u}_i}{\partial x_j}+\frac{\partial\tilde{u}_j}{\partial x_i}\right)-\frac{2}{3}\rho\delta_{ij}k \tag{2.41}$$

where $k=\frac{1}{2}(\overline{u_i''^2}+\overline{u_j''^2}+\overline{u_k''^2})$ is the turbulent kinetic energy per unit mass and δ_{ij} is the Kronecker delta (δ_{ij}=1 if $i=j$ and $\delta_{ij}=0$ if $i\neq j$).

μ_t is a local eddy or turbulent viscosity which depends on the state of turbulence and must be determined by the turbulence model. By applying dimensional analysis, μ_t is proportional to a turbulence velocity scale ϑ and a length scale l which characterize the large-scale turbulent motion.

$$\mu_t = C\rho\vartheta l \tag{2.42}$$

where C is an empirical constant. The kinematic turbulent or eddy viscosity v_t is denoted by:

$$v_t = \mu_t / \rho \tag{2.43}$$

Similar to the calculation of the Reynolds stresses, Reynolds fluxes of a scalar (turbulent transport of heat, mass etc.) are linearly related to the mean scalar gradient:

$$-\rho\overline{u_i'' \phi} = -\Gamma_t \frac{\partial \tilde{\phi}}{\partial x_i} \tag{2.44}$$

where Γ_t is the eddy or turbulent diffusivity for scalar ϕ and is expect to be close to that of the turbulent viscosity μ_t. Turbulent Prandlt/Schmidt number σ_t is used to indicate the ratio of eddy viscosity and eddy diffusivity:

$$\sigma_t = \frac{\mu_t}{\Gamma_t} \tag{2.45}$$

The value of Prandlt number is expected close to 1 since the turbulent transport of momentum, energy or mass is due to the same mechanism--eddy mixing.

2.3.4.2 Zero-equation models

In zero-equation models, the turbulence velocity scale ϑ and length scale l are calculated directly from local mean flow quantities. This kind of model is simple and computationally economical, but is only suitable for simple shear-layer-dominated or pressure-driven flows.

Prandtl's mixing-length model

The model calculates the turbulence velocity scale ϑ as a product of a turbulent velocity gradient with a particular length scale of the turbulent motion:

$$\vartheta = C_m l \left| \frac{\partial \vec{U}}{\partial y} \right| \tag{2.46}$$

Thus the dynamic turbulent viscosity μ_t is obtained by:

$$\mu_t = C\rho\vartheta l = \rho l_m^2 \left| \frac{\partial \vec{U}}{\partial y} \right| \tag{2.47}$$

where y is the distance from a wall, and the mixing length l_m varies with the turbulent structure [Rodi, 1993]. For example, a simple algebraic formula is used to describe l_m: near

wall $l_m = k_a y$ (where $k_a = 0.4$, the von Karman constant); in a free flow $l_m = c\varsigma$ (where ς is the radius of the turbulence. c is 0.07 for plane mixing layer, 0.09 for plane turbulent jet and 0.16 for plane wake); in a boundary layer, a ramp-distribution of l_m is often suitable.

2.3.4.3 One-equation models

These models usually calculate the turbulence velocity scale ϑ from a suitable transport equation, usually the turbulent kinetic energy ($k = \frac{1}{2}(u_i''^2 + u_j''^2 + u_k''^2)$) and the length scale, l, is prescribed empirically. The main shortcoming of one-equation models is unsuitable for complex flows because it is very difficult to estimate the distribution of the mixing length and cannot account for the transport effects of turbulence.

Prandtl's one-equation model

The model [Wilcox, 2004] may solve an additional equation for turbulent kinetic energy:

$$\frac{\partial k}{\partial t} + div(k\vec{U}) = div\left[v_t grad k\right] + P + B - C_D \frac{k^{3/2}}{l} \tag{2.48}$$

where the turbulent eddy viscosity $v_t = k^{1/2} l$, $P = v_t \frac{\partial u_i}{\partial x_i}\left(\frac{\partial u_i}{\partial x_j} + \frac{\partial u_j}{\partial x_i}\right)$, $B = -\frac{\varepsilon g_i}{\rho}\frac{\partial \rho}{\partial x_i}$. The g_i is the i^{th} component of the gravity vector, i = 1, 2 and 3, the empirical constant $C_D = 0.08$, and l has to be prescribed.

The dynamic turbulent viscosity μ_t is calculated as:

$$\mu_t = C_\mu \rho k^{1/2} l \tag{2.49}$$

where $C_\mu = 0.09$ and l is the same as in Prandtl's mixing-length model.

2.3.4.4 Two-equation models

In two-equation models, the turbulence velocity scale ϑ is calculated from a solution of a transport equation for turbulent kinetic energy k, and the dependent variable of the second equation is not usually a length scale l, but varies with models.

Two equation models are by far the most widely used in industry for they form a good compromise between generality and economy for many CFD problems. But the two-equation models presented so far are valid only at high Reynolds numbers, and therefore they are not valid in the near-wall viscosity-affected regions.

$k-\varepsilon$ Turbulence Model

The standard $k-\varepsilon$ model [Launder & Spalding, 1974] uses two transport equations for turbulent kinetic energy k and dissipation rate of turbulent kinetic energy per unit mass ε ($\varepsilon = 2\nu\overline{s_{ij}'\cdot s_{ij}'}$). The rate of change of k or ε equals the rate of production and destruction of k or ε plus the transport by convection and diffusion, which are expressed in equations:

$$\frac{\partial}{\partial t}(\bar{\rho}k) + div(\bar{\rho}k\vec{U}) = div\left[\frac{\mu_t}{\sigma_k} gradk\right] + 2\mu_t \bar{s}_{ij}\cdot\bar{s}_{ij} - \bar{\rho}\varepsilon \tag{2.50}$$

$$\frac{\partial}{\partial t}(\bar{\rho}\varepsilon) + div(\bar{\rho}\varepsilon\vec{U}) = div\left[\frac{\mu_t}{\sigma_\varepsilon} grad\varepsilon\right] + C_{1\varepsilon}\frac{\varepsilon}{k}2\mu_t\bar{s}_{ij}\cdot\bar{s}_{ij} - C_{2\varepsilon}\frac{\varepsilon^2}{k}\bar{\rho} \tag{2.51}$$

where the five constants C_μ, $C_{1\varepsilon}$, $C_{2\varepsilon}$ σ_ε and σ_k, have been adjusted to certain values that are arrived at by a comprehensive data fitting for a wide range of turbulent flows.

Table 2.2: Constants used in $k-\varepsilon$ turbulence model

C_μ	σ_k	σ_ε	$C_{1\varepsilon}$	$C_{2\varepsilon}$
0.09	1.0	1.3	1.44	1.92

The velocity scale ϑ and length scale l can be represented by k and ε as follows:

$$\vartheta = k^{1/2} \tag{2.52}$$

$$l = k^{3/2}/\varepsilon \tag{2.53}$$

Thus the turbulent viscosity μ_t is calculated by:

$$\mu_t = C\rho\vartheta l = C_\mu\rho\frac{k^2}{\varepsilon} \tag{2.54}$$

The standard $k-\varepsilon$ model has been proved to be the most popular in industrial internal flow computations, mainly because of its robustness, and it succeeds in calculating a wide variety of thin shear layer and recirculating flows without the need for case-by-case adjustment of the

model constants and does not require a near-wall correction term. But it performs poorly in a variety of cases such as curved boundary layers, swirling flows and fully developed flows in non-circular ducts.

RNG $k-\varepsilon$ Turbulence Model

The RNG $k-\varepsilon$ model [Yakhot, *et al*., 1992] is derived by representing the effects of the small scales of turbulent motions by means of a random forcing function in Navier-Stokes equation. The transport equations are similar to those of the standard $k-\varepsilon$ model but with different constants and additional terms and functions:

$$\frac{\partial}{\partial t}(\bar{\rho}k)+div(\bar{\rho}k\vec{U})=div\left[\alpha_k\mu_{eff}\ grad\ k\right]+\tau_{ij}\cdot\bar{s}_{ij}-\bar{\rho}\varepsilon \tag{2.55}$$

$$\frac{\partial}{\partial t}(\bar{\rho}\varepsilon)+div(\bar{\rho}\varepsilon\vec{U})=div\left[\alpha_\varepsilon\mu_{eff}\,grad\ \varepsilon\right]+C_{1\varepsilon}^{*}\frac{\varepsilon}{k}\tau_{ij}\cdot\bar{s}_{ij}-C_{2\varepsilon}\frac{\varepsilon^2}{k}\bar{\rho} \tag{2.56}$$

with

$$\mu_{eff}=\mu+\mu_t+\qquad+\mu_t=C_\mu\rho\frac{k^2}{\varepsilon} \tag{2.57}$$

$$C_{1\varepsilon}^{*}=C_{1\varepsilon}-\frac{\eta(1-\eta_0/\eta)}{1+\beta\eta^3} \tag{2.58}$$

$$\eta=\frac{k}{\varepsilon}\sqrt{\bar{s}_{ij}\cdot\bar{s}_{ij}} \tag{2.59}$$

and

Table 2.3: Constants used in RNG $k-\varepsilon$ turbulence model

C_μ	σ_k	σ_ε	$C_{1\varepsilon}^{*}$	$C_{2\varepsilon}$	η_0	β
0.0845	1.39	1.39	1.42	1.68	4.377	0.012

The ε-equation in the standard $k-\varepsilon$ has been suspected as one of the main sources of accuracy limitations and a RNG model uses a strain-dependent correction term in the constant $C_{1\varepsilon}$. The model was reported to perform better than the standard model for expanding duct flows, but worse for a contraction with the same area ratio.

Wilcox $k-\omega$ Turbulence Model

Instead of using ε as the second variable, the $k-\omega$ model [Wilcox, 1988; Wilcox, 1994] changes the variable to the turbulence frequency $\omega=\varepsilon/k$. The length scale $l=k^{1/2}/\omega$ and the eddy viscosity is given by:

$$\mu_t = \rho \frac{k}{\omega} \tag{2.60}$$

The transport equations for k and ω are as follows:

$$\frac{\partial}{\partial t}(\bar{\rho}k) + div(\bar{\rho}k\vec{U}) = div\left[(\mu + \frac{\mu_t}{\sigma_k})grad\ k\right] + P_k - \beta^* \bar{\rho}k\omega \tag{2.61}$$

$$\begin{aligned}\frac{\partial}{\partial t}(\bar{\rho}\omega) + div(\bar{\rho}\omega\vec{U}) = div\left[(\mu + \frac{\mu_t}{\sigma_\omega})grad\ \omega\right] \\ + \gamma_1(2\bar{\rho}\bar{s}_{ij}\cdot\bar{s}_{ij} - \frac{2}{3}\bar{\rho}\omega\frac{\partial u_i}{\partial x_j}\delta_{ij}) - \beta_1\bar{\rho}\omega^2\end{aligned} \tag{2.62}$$

where

$$P_k = (2\mu_t \bar{s}_{ij}\cdot\bar{s}_{ij} - \frac{2}{3}\bar{\rho}k\frac{\partial u_i}{\partial x_j}\delta_{ij}) \tag{2.63}$$

and

Table 2.4: Constants used in Wilcox $k-\omega$ turbulence model

σ_k	σ_ω	γ_1	β_1	β^*
2.0	2.0	0.553	0.075	0.09

The $k-\omega$ model was initially developed on the hypothesis that the integration to the wall does not require wall-damping functions in low Reynolds number flows. At inlet and outlet boundaries the value of k and ω must be specified. Unfortunately, practical experience with the model has shown that the model tends to be dependent on the assumed free stream value of ω at boundary conditions.

2.4 Combustion modelling

Combustion is an exothermic chemical reaction between fuels and an oxidant accompanied by the production of heat and conversion of chemical species. There are many types of combustion and only gaseous non-premixed combustion is considered in this section due to most unwanted fires at which the models developed in this study are aimed involve this type of combustion.

Generally the combustion models are essentially classified into two categories: models based on a conserved scalar approach and volumetric reaction model. As the majority of the models

belong to the fist category, the conserved scalar models will be introduced in more detail. Before that, some important combustion theory is outlined.

2.4.1 Concepts of combustion

Enthalpy of formation

The enthalpy of a species α related to temperature is defined as:

$$h_\alpha = h_{\alpha,chem} + \int_{T_0}^{T_1} c_{p,\alpha} dT \tag{2.64}$$

where $h_{\alpha,chem}$ is the standard enthalpy (J/kg) of species α at a reference pressure and temperature T_0, and the second term on the right hand-sides is the additional enthalpy at temperature T_1. $c_{p,\alpha}$ is the specific heat capacity for species α at constant volume and pressure.

Consider a mixture of gases each with mass fraction Y_α, the total enthalpy may be calculated from the following expression:

$$h_{mix} = \sum_{\alpha}^{all\ species} Y_\alpha h_\alpha \tag{2.65}$$

Mixture fraction and stoichiometric mixture fraction

For a one-step infinitely fast combustion, chemical reaction can be assumed to take place where the oxidant reacts with the fuel in stoichiometric proportions to form products:

$$1kg\ \ Fuel + skg\ \ Oxidant \rightarrow (1+s)kg\ \ \mathrm{Pr}oducts \tag{2.66}$$

where s is the stoichiometric oxidant/fuel ratio. The rate of consumption of the fuel is 1/s times the rate of consumption of the oxidant during stoichiometric combustion:

$$\dot{\omega}_{fu} = \frac{1}{s}\dot{\omega}_{ox} \tag{2.67}$$

A conserved scalar called mixture fraction is defined as:

$$\xi = \frac{\phi - \phi_0}{\phi_1 - \phi_0} \tag{2.68}$$

where $\phi = sY_{fu} - Y_{ox}$, Y_{fu}, Y_{ox} are the mass fractions of the fuel and the oxidant respectively and subscripts 0 denotes the oxidant stream and 1 denotes the fuel stream. If the mixture contains

no oxidant in the fuel stream and no fuel in the oxidant stream, mixture fraction may be simplified as follows:

$$\xi = \frac{sY_{fu,} - Y_{ox} + Y_{ox,0}}{sY_{fu,1} + Y_{ox,0}} \tag{2.69}$$

In a stoichiometric mixture neither fuel nor oxygen is present in the products, and the stoichiometric mixture fraction ξ_{st} is defined as:

$$\xi_{st} = \frac{Y_{ox,0}}{sY_{fu,1} + Y_{ox,0}} \tag{2.70}$$

Properties of gaseous mixture

The mass fraction of species α in a mixture is defined as:

$$Y_\alpha = \frac{m_\alpha}{m_{total}} \tag{2.71}$$

where m_α, m_{total} are the mass of species α and the total mass of the mixture respectively.

The mole fraction of a species α in a mixture is:

$$X_\alpha = \frac{n_\alpha}{n_{total}} \tag{2.72}$$

where n_α, n_{total} are the number of moles of specie α and the total number of moles of the mixture respectively.

The mole fraction and mass fraction are related by:

$$Y_\alpha = X_\alpha \frac{M_\alpha}{M_{mix}} \tag{2.73}$$

$$X_\alpha = Y_\alpha \frac{M_{mix}}{M_\alpha} \tag{2.74}$$

where M_α is the molecular weight of species α and the molecular weight of the mixture is calculated by:

$$M_{mix} = \sum_{\alpha}^{all\ species} X_\alpha M_\alpha \tag{2.75}$$

The density of the mixture is:

$$\rho_{mix} = \sum_{\alpha}^{all\ species} \frac{pX_\alpha}{(R_u / M_\alpha)T} = \frac{p}{R_u T} M_{mix} \tag{2.76}$$

The concentration of a species α (kmol/m^3) is:

$$C_\alpha = Y_\alpha \frac{\rho_{mix}}{M_\alpha} = X_\alpha \frac{p}{R_u T} \tag{2.77}$$

Chemical reaction rate

Combustion of a fuel does not occur in a single reaction, but involves a number of different steps where some of reactions may be reversible. For the illustration purpose, a scheme of multi-reactions is considered:

$$\sum_{\alpha=1}^{N} v_{\alpha j}^{'} M_\alpha = \sum_{\alpha=1}^{N} v_{\alpha j}^{''} M_\alpha \qquad \text{for } j = 1,2,\cdots,n \tag{2.78}$$

where $v_{\alpha j}^{'}$ are stoichiometric coefficients of reactant species α and $v_{\alpha j}^{''}$ are stoichiometric coefficients of product species α in the reaction j.

The reaction progress rate $\dot{q}_{\alpha j}$ ($kmol/m^3 \cdot s$) for species α by reaction j is given by the forward reaction rate minus the backward reaction rate:

$$\dot{q}_{\alpha j} = \frac{dC_\alpha}{dt}|_j = (v_{\alpha j}^{''} - v_{\alpha j}^{'})(r_f \prod_{\gamma=1}^{N} (C_\gamma)^{v_{\gamma j}^{'}} - r_b \prod_{\gamma=1}^{N} (C_\gamma)^{v_{\gamma j}^{''}}) \tag{2.79}$$

where C_α is the mole concentration of species α. In the expression the forward reaction rate r_f is independent of the concentration of any species involved in the combustion and is usually calculated using the Arrhenius law:

$$r_f = AT^\beta \exp(-\frac{E_a}{R_u T}) \tag{2.80}$$

and the backward reaction rate r_b is expressed as:

$$r_b = r_f / K_j \tag{2.81}$$

where A is the pre-exponential constant, parameter β is a temperature exponent (dimensionless) and E_a is activation energy for the reaction ($J/mol\,Kg$). K_j is the chemical equilibrium constant for the j^{th} reaction.

In complex chemical schemes involving n reactions, the total of production rate of species α is the sum of individual rates of each step:

$$\dot{q}_\alpha = \sum_{j=1}^{n} \dot{q}_{\alpha j} \tag{2.82}$$

Note here the unit of a reaction rate is $kmol/m^3 \cdot s$ while the unit of the source term used in the species transport equation is $kg/m^3 \cdot s$. The mass reaction rate of species α may be written as:

$$\omega_\alpha = M_\alpha \dot{q}_\alpha \tag{2.83}$$

2.4.2 Governing equations for combusting flows

In the non-premixed combustion simulation, additional transport equations for gaseous species are needed.

Transport equations for species

The rate of change of mass of species α is equal to the mass change due to convection and diffusion plus the generation of species α due to chemical reactions:

$$\frac{\partial}{\partial t}(\rho Y_\alpha) + \frac{\partial}{\partial x_i}(\rho u_i Y_\alpha) = \frac{\partial}{\partial x_i}\left[\rho D_\alpha \frac{\partial Y_\alpha}{\partial x_i}\right] + \dot{\omega}_\alpha \tag{2.84}$$

where D_α is the diffusion coefficient of species α which is usually assumed to be a single diffusion coefficient for all species in practice. $\dot{\omega}_\alpha$ is the volumetric rate of the generation of a species α due to chemical reactions.

2.4.3 Modelling strategies

The following section begins with a brief introduction of the basic combustion concepts. Then modelling approaches of combustion, especially for modelling the combustion source term in Equation (2.84), are represented.

2.4.3.1 The simple chemical reacting system (SCRS)

Concerning with the global nature of the combustion process and with final major species concentrations only, a global one-step, infinitely fast ($D_a >> 1$) chemical reaction assumes that the reaction time is negligibly short compared with the fluid mixing time and the

intermediate reactions are ignored. The transport equations of the fuel and oxygen mass fraction are:

$$\frac{\partial}{\partial t}(\rho Y_{fu}) + div(\rho Y_{fu}\vec{U}) = div\left(\Gamma_{fu}\ gradY_{fu}\right) + \dot{\omega}_{fu} \tag{2.85}$$

$$\frac{\partial}{\partial t}(\rho Y_{ox}) + div(\rho Y_{ox}\vec{U}) = div\left(\Gamma_{ox} gradY_{ox}\right) + \dot{\omega}_{ox} \tag{2.86}$$

Using $s\cdot\dot{\omega}_{fu} - \dot{\omega}_{ox} = 0$ and the assumption ($\rho D_{fu} = \rho D_{ox} = \Gamma_{\phi}$), the combination of $s\times$ Equation (2.85)-Equation (2.86) results in a transport equation of $\phi = sY_{fu} - Y_{ox}$

$$\frac{\partial}{\partial t}(\rho\phi) + div(\rho\phi\vec{U}) = div\left(\Gamma_{\phi} grad\phi\right) \tag{2.87}$$

Replacing ϕ by mixture fraction ξ in Equation (2.87), a transport equation for mixture fraction is obtained:

$$\frac{\partial}{\partial t}(\rho\xi) + \frac{\partial}{\partial x_j}(\rho\xi\vec{U}) = div\left(\Gamma_{\xi}\ \text{grad}\ \xi\right) \tag{2.88}$$

The above equation shows that mixture fraction ξ is a passive scalar.

Fast chemistry implies that, there will be no oxidant present in the region where the mixture is fuel rich ($\xi > \xi_{st}$), and no fuel present in the weak mixture region ($\xi < \xi_{st}$). Hence $Y_{fu} = 0$ if $Y_{ox} > 0$, so:

$$\text{If } \xi < \xi_{st},\ \xi = \frac{-Y_{ox} + Y_{ox,0}}{sY_{fu,1} + Y_{ox,0}} \tag{2.89}$$

and $Y_{ox} = 0$ if $Y_{fu} > 0$, so:

$$\text{if } \xi > \xi_{st},\ \xi = \frac{sY_{fu} + Y_{ox,0}}{sY_{fu,1} + Y_{ox,0}} \tag{2.90}$$

We can rearrange Equations (2.70) and (2.89)-(2.90) to give values of oxygen and fuel mass fractions after combustion:

$$\text{if } \xi_{st} < \xi < 1 \quad Y_{ox} = 0,\ Y_f = \frac{(\xi - \xi_{st})}{1-\xi_{st}} Y_{fu,1} \tag{2.91}$$

$$\text{if } 0 < \xi < \xi_{st} \quad Y_{fu} = 0,\ Y_{ox} = \frac{(\xi_{st} - \xi)}{\xi_{st}} Y_{ox,0} \tag{2.92}$$

The above formulae show that the mass fraction Y_{fu} of the fuel in the fuel rich region is linearly related to mixture fraction ξ and oxygen Y_{ox} is linearly related to mixture fraction ξ in the oxidant rich region.

The total mass fraction of the inert species Y_{in} after combustion at any value of ξ is:

$$Y_{in} = Y_{in,0}(1-\xi) + Y_{in,1}\xi \tag{2.93}$$

The mass fraction of products may be obtained from

$$Y_{pr} = 1-(Y_{fu} + Y_{ox} + Y_{in}) \tag{2.94}$$

The above Equations (2.88) and (2.91)-(2.94) represent the SCRS model [Spalding, 1979].

2.4.3.2 Eddy break-up model (EBU)

The simple and very efficient approach called eddy break-up model was originally developed by Spalding [Spalding, 1971]. This model assumes that the chemical time scale is far smaller than the turbulent mixing time scale and the chemical reaction rate is completely determined by the mixing-controlled rate, which in turn is related to the rate of dissipation of turbulent eddies ($D_\alpha >> 1$). The turbulent mean reaction rate of products is expressed as:

$$\tilde{\dot{w}}_{pr} = \bar{\rho} C_{EBU} \frac{\varepsilon}{k} (\tilde{Y''^2_{pr}})^{1/2} \tag{2.95}$$

$\tilde{Y''^2_{pr}}$ is the variance of the product mass fraction and C_{EBU} is the model constants. A typical value used in the literature is $C_{EBU} = 1$.

The eddy break-up model is widely used in fire simulations because it makes reasonably good predictions and is fairly straightforward to implement in CFD codes. However, due to the dependence of the fuel dissipation rate on the turbulence time scale k/ε, the quality of the predictions depends on the performance of the turbulence model.

2.4.3.3 Eddy dissipation model (EDM)

The Eddy dissipation model [Magnussen & Hjertager, 1977; Gao & Chow, 2005] is a modified version of the EBU model. The model assumes that the combustion is a single step reaction and combustion chemical kinetics is faster than the overall fine structure mixing. Then the consumption rate of the fuel, oxygen and products may be expressed as a function of

the turbulence time scale ε / k and the actual reaction rate of the fuel is assumed to be equal to the slowest of these dissipation rates:

$$\overline{\dot{w}_{fu}} = A\overline{\rho}\frac{\varepsilon}{k}\min\left[\tilde{Y}_{fu,}\ \frac{\tilde{Y}_{ox}}{s}, B\frac{\tilde{Y}_{pr}}{(1+s)}\right] \tag{2.96}$$

The typical values for the model constants are A=4.0 and B=0.5. s is the stoichiometric oxygen to fuel mass ratio, which is defined in Equation (2.66).

2.4.3.4 Eddy dissipation concept model (EDC)

The Eddy dissipation concept model is an extension of the EDM model [Magnussen & Hjertager, 1981; Magnussen, 2005]. In the model, most of the reactions occur in the smallest scales of the turbulence, the fine structure. It is assumed that the mass fraction occupied by the fine structure regions is:

$$\gamma^* = 4.6(\frac{\nu\varepsilon}{k^2})^{1/2} \tag{2.97}$$

The reacting fraction of the fine structure is:

$$\chi = \frac{\tilde{Y}_{pr}/(1+s)}{\tilde{Y}_{\min} + \tilde{Y}_{pr}/(1+s)} \tag{2.98}$$

where $\tilde{Y}_{pr}$ is the same as in EBU model and $\tilde{Y}_{\min} = \min(\tilde{Y}_{fu}, \tilde{Y}_{ox}/s)$. Then the reaction rate of fuel is:

$$\tilde{\dot{w}}_{fu} = -\overline{\rho}\frac{\varepsilon}{\kappa}C_{EDC}\min\left[\tilde{Y}_{fu,}\frac{\tilde{Y}_{ox}}{s}\right]\left[\frac{\chi}{1-\gamma^*\chi}\right] \tag{2.99}$$

where C_{EDC} is a model constant with a recommended value of 11.2.

2.4.3.5 Laminar flamelet model

The infinitely fast chemistry assumption is not always valid and a method based on laminar flamelet considerations was developed to incorporate finite rate chemistry. Steady flamelet model assumes that the chemical time scales are shorter than the characteristic turbulence time scale and reaction zone thickness is smaller than the Kolmogorov length scale ($D_a > 1 \& K_a < 1$). The model views the flame as an ensemble of thin, laminar, locally one-dimensional flamelet structures embedded within the turbulent flow field.

The following set of flamelet equations can be used to describe the embedded reactive-diffusive flamelet structure:

$$\rho\frac{\partial Y_\alpha}{\partial t} = \frac{\chi}{2}\rho\frac{\partial^2 Y_\alpha}{\partial \xi^2} + \dot{\omega}_\alpha \tag{2.100}$$

for species concentration Y_α, $\alpha = 1,2,\cdots,N$ and temperature. Here χ is the scalar dissipation rate:

$$\chi = 2D\left|\nabla \xi\right|^2 \tag{2.101}$$

And D is a mean molecular diffusivity.

As the response time of the flamelet to changes in local mixing environment is usually much smaller than the mixing time scale, the left hand side of Equation (2.100) is assumed to be zero. Hence, the equation can be simplified as:

$$\rho\chi\frac{\partial^2 Y_\alpha}{\partial \xi^2} + 2\dot{\omega}_\alpha = 0 \tag{2.102}$$

The properties ϕ of laminar flamelets, e.g. temperature, density and species mass fractions as a function of the mixture fraction $\phi(\xi)$, are evaluated once and for all outside the flow field calculation to yield a so-called laminar flamelet library. A key advantage of the laminar flamelet methodology is that detailed chemistry can be incorporated relatively economically within the calculations, because the library contains information relating to major species, minor species, density and temperature. But the validity of the approach must be checked carefully to make sure that the reaction zone is thinner than the Kolmogorov length scale. More details of laminar flamelet models can be found in [Williams, 2000; Veynante & Vervisch, 2002].

2.4.4 Probability density function (PDF) method

Given the difficulties associated with modelling the Favre-averaged quantities, especially the source terms, it is useful to use a statistical approach to calculate mean quantities using probability density function (PDF) in turbulent combustion calculations.

In the combustion calculations the density-weighted PDF $\widetilde{P}(\xi)$ for the mixture fraction ξ at every location is related to un-weighted PDF $P(\xi)$:

$$\widetilde{P}(\xi) = \frac{\rho(\xi)}{\bar{\rho}}P(\xi) \tag{2.103}$$

So the density-weighted average of scalar quantity ϕ, which is itself a function of ξ, may now be obtained by integrating over the mixture fraction space to include the effect of turbulent fluctuations:

$$\phi = \int_0^1 \phi(\xi)\widetilde{P}(\xi)d\xi \tag{2.104}$$

Using an appropriate density-weighted PDF $\widetilde{P}(\xi)$ is crucial and different analytical PDFs have been chosen to approximate the mixture fraction distribution in fires. Currently the clipped Gaussian and beta distributions have been proved to be most successful [Bilger, 1976; Pope, 1985]. The beta PDF for $\widetilde{P}(\xi)$ is usually more accurate than the clipped Gaussian and is more commonly used in combustion modelling [Warnatz, *et al.*, 2006; Liu, *et al*., 2002]. More details of the beta PDF approach are given below.

Beta PDF

The beta PDF is defined as:

$$\widetilde{P}(\xi) = \frac{\xi^{\alpha-1}(1-\xi)^{\beta-1}\Gamma(\alpha+\beta)}{\Gamma(\alpha)\Gamma(\beta)} \tag{2.105}$$

with

$$\alpha = \widetilde{\xi}\left(\frac{\widetilde{\xi}(1-\widetilde{\xi})}{\widetilde{\xi''^2}} - 1\right) \tag{2.106}$$

$$\beta = \alpha\frac{(1-\widetilde{\xi})}{\widetilde{\xi}} \tag{2.107}$$

where $\Gamma(\alpha)$ denotes the gamma function. $\widetilde{\xi}$ is the Favre mean of mixture fraction ξ and $\widetilde{\xi''^2}$ is the Favre-average variance of ξ. $0<\widetilde{\xi''^2}<\widetilde{\xi}(1-\widetilde{\xi})$ should be checked before the PDF is used. Figure 2.1 illustrates the beta PDF with some different values of the parameters.

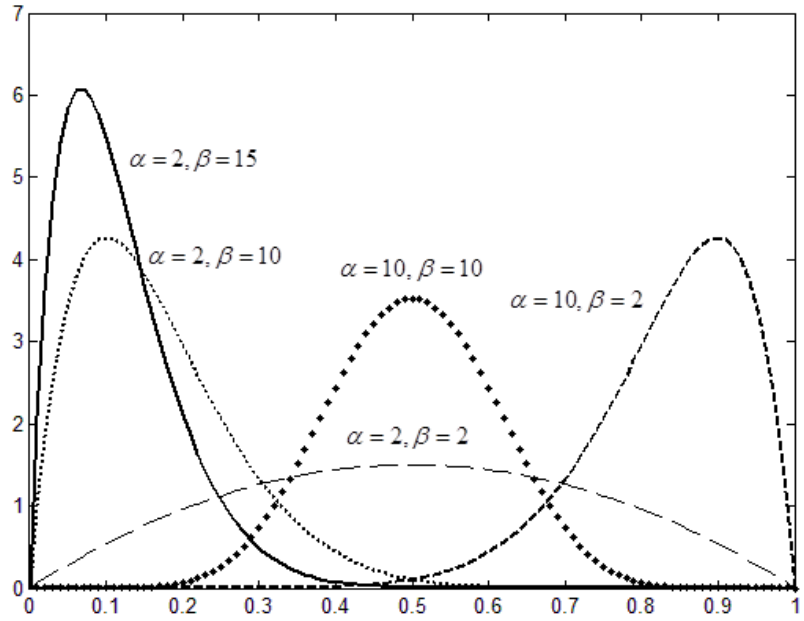

Figure 2.1: beta function for different values of α and β.

To generate the beta PDF it is necessary to solve an additional transport equation for mixture fraction variance $\widetilde{\xi}''^2$:

$$\frac{\partial}{\partial t}(\overline{\rho}\widetilde{\xi}''^2)+\frac{\partial}{\partial x_i}(\overline{\rho}\widetilde{u}_i\widetilde{\xi}''^2)=\frac{\partial}{\partial x_i}\left(\Gamma_\xi\frac{\partial\widetilde{\xi}''^2}{\partial x_i}\right)+C_{g1}\mu_t\left(\frac{\partial\widetilde{\xi}''^2}{\partial x_i}\right)^2-C_{g2}\overline{\rho}\frac{\widetilde{\varepsilon}}{\widetilde{k}}\widetilde{\xi}''^2 \qquad (2.108)$$

Note that the model takes the diffusion coefficient for mixture fraction variance to be the same as that for mixture fraction. C_{g1} and C_{g2} are dimensionless constants with recommended values of 2.0 and 2.8 respectively.

2.4.5 Flame spread model

Flame spread rate is the moving velocity of the pyrolysis front on a solid surface. This velocity for thermally thick solids is a function of the external heat flux to the solid surface, the ignition temperature and the thermal inertia of the solid [Babrauskas, 2003; Hasemi, 2008].

The current flame spread model in the software FDS uses the HRRPUA (heat release rate per unit area) approach [McGrattan, *et al*., 2004]. In the model, a simple one-dimensional heat conduction is solved along the thickness of the material modelled. The heat flux at the top surface, the face exposed to the fire, is the sum of convective and radiative heat fluxes. The bottom surface can be assumed to experience no heat loss or alternatively to be at ambient temperature. Once the ignition temperature of the burnable material is obtained at the top

surface, the fuel gases are generated from the surface. No charring effects are considered. The materials burn at a rate proportional to the energy fed back from the fire.

In theory, the criterion of surface ignition temperature alone is sufficient for the simulation of fire spread along combustible solid surfaces. In practice, however, within CFD fire simulations, ignition of a solid surface can be strongly mesh dependent because no flame spread might be achieved if the distance from one mesh cell to another is too large and heat flux from the gas phase is "smeared out". In the case of the wind opposed flame spread, extremely fine meshes in areas of flame fronts are required to accurately predict fire spread. It is very likely that with coarse meshes, no fire spread is predicted at all. But as a practical fire simulation is normally concerned with a large-scale phenomenon, it can be prohibitively expensive and impractical to use extremely fine meshes in fire simulations. In addition to this dilemma, it is impossible to know in advance at the mesh generation stage what fire conditions (wind assisted or opposed) are likely to occur at any given point. Therefore, as a practical engineering method, the flame spread rate, which is measurable from fire tests, is introduced alongside surface ignition temperature in an enhanced flame spread model implemented in SMARTFIRE [Jia, *et al*., 2006a; Jia, *et al*., 2006b; Wang *et al*., 2007; Galea, *et al*., 2008]. The ignition of the interior materials is determined by one of the following ignition criteria:

(a) The material surface temperature reaches its ignition temperature;
(b) The pyrolysis front advances from an adjacent burning cell face to the cell face in question;

In SMARTFIRE, all combustible surfaces are assigned a face patch which identifies them as a burnable material. Each face patch is labelled with a unique patch number which defines their location and material properties. If one of these two ignition criteria is reached, a cell face begins to burn. Once a cell face is ignited, it starts to release a certain amount of fuel according to the time dependent burning rate (kg/m^2s) or heat release rate (HRR) for this material. The model inputs for the burnable materials are: density, thickness, conductivity, specific heat, ignition temperature, heat release rate from cone calorimeter experiments with flame spread rate being the only additional parameter. Of the two ignition criteria used in the enhanced flame spread model, criterion (a) is the dominant one once the fire is sufficiently large to sustain the fire development. The effect of criterion (b) is significant only in the very early stage of fire development when the fire is weak and the dominant heat transfer for flame

spread is convective heat transfer from the flame to the solid surface and heat conduction within the solid.

2.5 Radiation modelling

Radiation is caused by energy emission in the form of electromagnetic waves and is one of three mechanisms of heat transfer in fire. It is recognized that radiation is the dominant mode of heat transfer in fires in many situations, especially in very large scale fires.

2.5.1 Radiation transfer equation

Radiation intensity I (unit $W/m^2.sr$): is the fundamental quantity of radiation transfer defined as the rate of heat passing per unit area perpendicular to the rays and per unit solid angle (steradians = sr).

Governing equation

The change in radiation intensity per unit path length at a point $\boldsymbol{r}$ along a radiation ray $\boldsymbol{s}$ is due to emission, absorption and scattering in a fluid medium,

$$W_I = W_{emission} - W_{absoption} - W_{out\_scattering} + W_{in\_scattering} \tag{2.109}$$

Thus the governing equation, which represents the radiative heat transfer along a ray path indicated by the direction vector $\boldsymbol{s}$, is expressed in the equation as follows:

$$\frac{d}{ds} I(\boldsymbol{r},\boldsymbol{s}) = \kappa I_b(\boldsymbol{r}) - \kappa I(\boldsymbol{r},\boldsymbol{s}) - \sigma_s I(\boldsymbol{r},\boldsymbol{s}) + \frac{\sigma_s}{4\pi}\int_{\Omega'=4\pi} I_{-}(\boldsymbol{s}_i)\Phi(\boldsymbol{s}_i,\boldsymbol{s})d\Omega_i \tag{2.110}$$

where I_b denotes the black-body intensity, which is calculated by $I_b = \sigma T_4/\pi$, where σ is a constant with a value of 5.67×10^{-8}. κ is the absorption coefficient of the medium and σ_s is the scattering coefficient (both unit m^{-1}). $\Phi(\boldsymbol{s}_i,\boldsymbol{s})$ is the phase function representing the probability of light with propagation direction $\boldsymbol{s}$ being scattered into solid angle $d\Omega_i$ around $\boldsymbol{s}_i$. I_{-} is the incident intensity. The last term on the right hand side of the equation accounts for the increase in the spectral intensity by radiation at the point $\boldsymbol{r}$ scattered into the ray along the direction $\boldsymbol{s}$.

The sum of absorption coefficient κ and scattering coefficient σ_s defines the extinction coefficient, $K_r = \kappa + \sigma_s$. Thus Equation (2.110) may be written as:

$$\frac{d}{ds} I(\boldsymbol{r},\boldsymbol{s}) = \kappa I_b(\boldsymbol{r}) - K_r I(\boldsymbol{r},\boldsymbol{s}) + \frac{\sigma_s}{4\pi} \int_{\Omega'=4\pi} I_-(\boldsymbol{s}_i) \Phi(\boldsymbol{s}_i,\boldsymbol{s}) d\Omega_i \tag{2.111}$$

Equation (2.111) is called radiative transfer equation (RTE). It is a first-order ordinary differential equation if the last term is somehow known. The absorption, scattering and extinction coefficients are related to the single scattering albedo:

$$\omega_c = \frac{\sigma_s}{\kappa + \sigma_s} \tag{2.112}$$

Boundary condition

The most widely used boundary condition of radiation for a point on a diffusely emitting and reflecting opaque surface located at position vector r_w is

$$I(\boldsymbol{r}_w, s) = \varepsilon_s I_b(\boldsymbol{r}_w) + \frac{(1-\varepsilon_s)}{2\pi} \int_{2\pi} I_-(\boldsymbol{r}_w,\boldsymbol{s}_i) \boldsymbol{n}.\boldsymbol{s}_i d\Omega_i \tag{2.113}$$

where vector $\boldsymbol{n}$ is the normal direction of the surface and ε_s is the surface emissivity.

2.5.2 Radiation calculation techniques

The radiation transport equation (RTE) is an integral-differential equation which is clearly different in nature from other transport equations. The exact analytical general solution of Equation (2.111) is not available as the incident intensity integrals are unknown. Many methods have been developed to calculate the integrals as a function of position in the computational domain, angular direction, and radiation wavelength.

2.5.2.1 Monte Carlo method (MC)

In the MC ray tracing method, a statistically large number of energy bundles are released randomly at emission points and the energy of each bundle may gain or lose through the computational domain. By keeping track of the energy gained or lost in the transport process, the net energy source or sink in the medium due to radiation is tallied.

The calculation process starts by producing a series of independent random variables $(x_1, x_2, \cdots, x_N)$ between 0 and 1, which are used to determine the emission location and direction of energy bundles as well as the fractions of emission, absorption and scattering

during interactions with the medium and boundary surfaces. For each bundle with initial energy E, the remaining energy after travelling through a grey medium with a constant absorption coefficient κ is calculated by

$$E_{bundle} = Ee^{-\kappa s} \tag{2.114}$$

The energy gained by medium is

$$E_{absorbed} = E(1 - e^{-\kappa s}) \tag{2.115}$$

where the path length travelled is calculated by $s = -\ln(R_l)/\kappa$,. R_l is a random number [Siegel & Howell, 1992].

When an energy bundle reaches a surface with absorptivity α, the bundle is absorbed in probability. A random number R_α is compared with the absorptivity value α to determine if the bundle is absorbed ($R_\alpha < \alpha$) or reflected ($R_\alpha > \alpha$).

The radiation source term for the enthalpy equation may be estimated by

$$S_{h_j,rad} = \frac{1}{V_j}\left(\sum^{absorbed\,\text{bundles}} \mathrm{E}_{\text{absorbed}} - \sum^{reflceted\,\text{bundles}} E_{reflected} \right) \tag{2.116}$$

The accuracy of the MC method is proportional to the square root of the total number of the bundles. The method gains accuracy at the expense of large amounts of computing resource and is, therefore, unsuitable for general purpose CFD calculations.

2.5.2.2 Discrete transfer method (DTM)

The discrete transfer method [Lockwood & Shah, 1981; Malalasekera, *et al.*, 2002] is based on tracing a number of rays leaving from the bounding surfaces through a computational domain. Usually it assumes that the rays are emitted from the centre of each boundary surface element and the number and directions of rays from each point are chosen a prior to provide a desired level of accuracy.

If the temperature, absorption and scattering are uniform in a computational domain, the intensity distribution along the path of a ray is solved with the recurrence relation:

$$I_{n+1} = I_n e^{-K_r \delta s} + S(1 - \exp^{-K_r \delta s}) \tag{2.117}$$

where $n+1$ and n are successive boundary locations, separated by a distance δs of a control volume. The source function S is:

$$S = (1-\omega_c)I_b + \frac{\omega_c}{4\pi}\int_{4\pi} I_-(\boldsymbol{s}_i)\Phi(\boldsymbol{s}_i,\boldsymbol{s})d\Omega_i$$
$$= (1-\omega_c)I_b + \frac{\omega_c}{4\pi}\sum_{i=1}^{N} I_{-,ave}(\boldsymbol{s}_i)\Phi(\boldsymbol{s}_i,\boldsymbol{s})\delta\Omega_i \quad (2.118)$$

For the ray with direction $\boldsymbol{s}_i$ passing through the finite solid angles, $\delta\Omega$, $I_-,ave(\boldsymbol{s}_i)$ is taken the arithmetic mean of the entering and leaving radiant intensity. The single scattering albedo ω_c is calculated by Equation (2.112).

The net gain or loss of radiant energy in each control volume is the sum of the gain or loss of energy of all rays crossing the volume. The initial intensity of each ray is calculated at the originating surface element with iterative method. The detail of this method can be found in [Lockwood, & Shah, 1981].

The DTM method is computationally efficient and also applicable to any geometrical configuration. It has been well established in applications to fire modelling problems. However, the method is not suitable for anisotropic scattering applications and sensitive to the levels of soot volume fraction. Several extensions and modifications of the method have been discussed in [Cumber, 1995; Coelho & Carvalho, 1997].

2.5.2.3 Discrete ordinates method (DOM)

The discrete ordinates method solves the radiation transfer equation for a finite different directions in the total 4π solid angle, and the integrals over directions are approximately replaced by numerical quadrature. The equation may be written as:

$$\frac{d}{ds}I(\boldsymbol{r},\boldsymbol{s}_i) = \kappa I_b(\boldsymbol{r}) - K_r I(\boldsymbol{r},\boldsymbol{s}_i) + \frac{\sigma_s}{4\pi}\sum_{j=1}^{n} w_j I_-(\boldsymbol{s}_i)\Phi(\boldsymbol{s}_i,\boldsymbol{s}_j) \quad \mathbf{i = 1,2,\cdots,n} \quad (2.119)$$

where w_j is the quadrature weight associated with the direction $\boldsymbol{s}_j = \zeta\boldsymbol{i} + \eta\boldsymbol{j} + \mu\boldsymbol{k}$ [Modest, 2013].

The total number of directions (n) may be calculated as $n = N(N+2)$, where N is the number of different cosines used to determine principal directions. The angular approximation transforms Equation (2.119) into a set of coupled differential equations:

$$\zeta_i\frac{dI_i}{dx} + \eta_i\frac{dI_i}{dy} + \mu_i\frac{dI_i}{dz} + K_r I_i = K_r S_i, \quad \mathrm{i} = 1,2,\cdots,\mathrm{n} \quad (2.120)$$

where

$$S_i = (1-\omega_c)I_b + \frac{\omega_c}{4\pi}\sum_{j=1}^{n} w_j I_j \Phi_{ij}, \quad i = 1,2,\cdots,n \tag{2.121}$$

Solving the set of Equation (2.120)-(2.121) by discretisation using the finite volume method and the source term for the enthalpy equation may be calculated from:

$$S_{h,rad} = 4\pi\kappa I_b - \kappa\sum_{i=1}^{n} w_i I_i(\boldsymbol{r},\boldsymbol{s}) \tag{2.122}$$

The DOM provides a good compromise between computational economy and accuracy in applications for unstructured meshes and complex geometries. One of its drawbacks is that it is non-conservative and can suffer from what are known as 'gray effects'. Further details of the method can be found in [Modest, 2013; Fiveland, 1991].

2.5.3 Calculation of radiation properties

Generally, the absorption of radiation in a mixture of gases is mainly determined by the combustion products such as soot, CO_2 and H_2O. Thus the absorption coefficient of the mixture may be split into two parts:

$$\kappa = \kappa_g + \kappa_s \tag{2.123}$$

where κ_g and κ_s are absorption coefficients of gases and soot respectively.

Fletcher *et al*. [1994] proposed an approximation to the absorption coefficient of gas κ_g as follows:

$$\kappa_g = C_g \exp(-T/C_T) \tag{2.124}$$

where the constants C_g and C_T are 0.28 and 1135 respectively.

According to Mie theory, the soot absorption and emission is proportional to the soot volume fraction if the soot particle diameter is less than the radiation wavelength. κ_s may be obtained from:

$$\kappa_s = C f_v T \tag{2.125}$$

The constant C in Equation (2.124) has been discussed by Denenno with a value 1264.0 [DiNenno *et al*., 1988] and Lautenberger with a value 1225.0 [Lautenberger, *et al*., 2005] respectively.

In FLUENT [Manual, 2005], the absorption coefficient due to soot κ_s is calculated by:

$$\kappa_s = b_1 \rho_s f_v [1 + b_T (T - 2000)] \tag{2.126}$$

with $b_1 = 1.2324 \times 10^3 m^2 / kg$ and $b_T \approx 4.8 \times 10^{-4} K^{-1}$.

The soot volume fraction f_v is calculated from soot mass fraction Y_s:

$$f_v = \rho_{mix} Y_s / \rho_s \tag{2.127}$$

where soot particulate density $\rho_s = 1.8 \times 10^3 kg / m^3$ and ρ_{mix} is the density of the mixture.

2.6 Numerical solution procedure

In the 1988 edition of the SFPE handbook, the only mention of CFD fire modelling was limited to a single sentence [DiNenno, *et al*, 1988]:

> *"Currently the computational demands of most field models exceed the computer resources of the typical user.''*

Fortunately, especial in the last two decades, the development of numerical methods and the availability of large digital computer with remarkable speed make these models cable of dealing with almost any practice. The above sections show that fire phenomena can be modelled by a set of partial differential equations, which can be expressed in terms of a general equation (Equation (2.19)). In this section, the common methods for solving of the governing RANS equations will be discussed briefly.

The numerical method based on volume integration called finite volume FV (or control volume) method is the most widely used technique in CFD calculation. In the method, the entire computational domain is divided into discrete volumes and each of the governing partial differential equations is transformed into a set of discrete algebraic equations using approximations in both space and time [Patankar, 1980]. The discrete equation for a variable over a control volume is expressed in the form of a linear algebraic equation, which connects all neighbour nodes around nodal point P in the volume:

$$a_p \phi_p = \sum_{i=1}^{n=\text{all neighbours}} (a_i \ \phi_i) + a_t \phi_{p,old} + \int_{vol-p} S_\phi \tag{2.128}$$

As the pressure field cannot be extracted from the equation of state, a specific procedure has to be designed to derive the pressure correction. Therefore, a pressure correction scheme,

which allows calculating the hydrodynamic pressure and velocity fields, should be performed first. One procedure called SIMPLE algorithm (Semi-Implicit Method for Pressure Linked Equations) is commonly used in many CFD codes. Assume that a control volume contains grid P and *w*, *e*, *s*, *n*, *b*, and *t* represent the west, east, south, north, bottom and top faces of the volume respectively. The *x*-momentum equation at face *e* is discretised as:

$$a_e u_e = \sum_{nb}^{\text{all neighbours}} a_{nb} u_{nb} + A_e (p_P - p_E) + b_e \tag{2.129}$$

The momentum equations for *y*-direction and *z*-direction are handled in a similar manner.

Then the procedure of the SIMPLE algorithm is summarized as follows:

1. Guess an initial pressure field *p**
2. Use momentum Equation (2.130) and the discretised momentum equations for the other two directions to create velocity fields u^*, v^*, w^* from this pressure field.

$$a_e u_e^* = \sum_{nb}^{\text{all neighbours}} a_{nb} u_{nb}^* + A_e (p_P^* - p_E^*) + b_e \tag{2.130}$$

The velocity-correction is defined as $u' = u - u^*$. Subtracting Equation (2.130) from Equation (2.129):

$$a_e u_e' = \sum_{nb}^{\text{all neighbours}} a_{nb} u_{nb}' + A_e (p_P' - p_E') \tag{2.131}$$

The term $\sum a_{nb} u_{nb}'$ is dropped from the above equation to obtain an approximation of the velocity-correction term:

$$u_e = u_e^* + (p_P' - p_E') A_e / a_e \tag{2.132}$$

3. Turn the continuity equation into a discretised equation and substitute all the velocity components by the velocity-correction (Equation (2.132)):

$$a_P p_P' = \sum_{nb}^{\text{all neighbours}} a_{nb} p_{nb}' + b' \tag{2.133}$$

where

$$\begin{aligned} b' = {} & [(\rho u^* A)_w - (\rho u^* A)_e] + [(\rho u^* A)_s - (\rho u^* A)_n] \\ & + [(\rho u^* A)_b - (\rho u^* A)_t] + (\rho_P - \rho_p^0) \Delta V / \Delta t \end{aligned} \tag{2.134}$$

The velocities and densities are all at time $t + \Delta t$ while ρ_p^0 is the old density at time t.

4. Then correct the pressure by $p = p^* + p'$.
5. Correct the velocities by Equation (2.132).

6. Repeat steps 2-5, until the mass residual drops below a predetermined limit.

Other variants of SIMPLE are SIMPLER, SIMPLEC and SIMPLEST that can be found in [Versteeg & Malalasekera, 2007].

There are a number of solution procedures to tackle the linear algebraic Equation (2.128), including point-by point, line-by-line, plane-by-plane and whole field. Lots of research activities have been devoted into the development of faster techniques [Wesseling, 1995; Briggs & McCormick,, 2000; Vetterling, *et al.*, 1989].

2.7 Boundary conditions

The initial values of all the flow variables and boundary conditions both need to be specified in the flow domain before solving the discretised equations in a transient problem. The most common boundary conditions are: Inlet, outlet, wall, symmetry and prescribed pressure.

The boundary conditions are incorporated by suppressing of the link to the boundary side and modification of the source terms. For a note *p* with a boundary note B, the link coefficient in Equation (2.128) is set to zero:

$$a_B = 0 \tag{2.135}$$

The boundary side flux –exact or linearly approximated—is introduced through a source term s_ϕ. If there is a fixed flux, the source term is set to the fixed flux:

$$s_\phi = q_B \tag{2.136}$$

If ϕ_p is fixed with a boundary value ϕ_B, the source term is set to:

$$s_\phi = C\phi_B - C\phi_p \tag{2.137}$$

where the number C is an arbitrary large number compared with all coefficients in the discretised equation, for example, C=10^{30}. The source term is added into Equation (2.128) we have

$$(a_p + 10^{30})\phi_p = \sum a_{nb}\phi_{nb} + 10^{30}\phi_B \tag{2.138}$$

Thus the above equation states that $\phi_p = \phi_B$.

The wall is the most common boundary encountered in the confined fluid flow problems. Details of the wall boundary conditions will further be explained as follows.

Wall boundary conditions

A multi-layered structure of the near wall assumes that an extremely thin viscous sub-layer followed by a buffer layer and the turbulent core in the immediate adjacent to the wall. The normalized distance from the wall surface is defined as:

$$y^+ = \frac{y}{\nu}\sqrt{\frac{\tau_w}{\rho}} \tag{2.139}$$

where the local wall sheer stress $\tau_w = \rho C_\mu^{1/2} k$. And the scaled velocity component parallel to the wall is:

$$u^+ = u / u_\tau \tag{2.140}$$

where $u_\tau = \sqrt{\frac{\tau_w}{\rho}}$.

1) The flow is deemed to be laminar when $y^+ \le 11.36$

   The velocity varies linearly with distance from the wall;

2) The flow is deemed to be turbulent and the wall function below is used when $y^+ > 11.36$

$$u^+ = \frac{1}{\kappa_a}\ln(Ey^+) \tag{2.141}$$

where Karman's constant κ_a =0.41 and E =9.8 for smooth walls [Schlichting, 2000].

The wall function for temperature distribution valid at high Reynolds number [Launder &Spalding, 1974]:

$$T^+ = \sigma_{T,t}\left(u^+ + P\left[\frac{\sigma_{T,l}}{\sigma_{T,t}}\right]\right) \tag{2.142}$$

where $\sigma_{T,t}$ is the turbulent Prandtl number and $\sigma_{T,l}$ is the laminar Prandtl number. P is the pee-function, a correction dependent on the ratio of laminar to turbulent Prandtl number.

2.8 Performance of field modelling on a rail car compartment fire

Although full-scale tests can provide reliable fire assessments, the high costs of conducting such tests limit their use in fire investigation. By contrast, numerical simulations can be set up with relative ease and lower costs. In addition, they can run for different fire scenarios with changes of the environmental conditions to provide more detailed information. This section

demonstrates the advantages of CFD fire simulation through simulating a fire experiment investigating the fire development in a rail car compartment.

The experiment

A rail car compartment (see Figure 2.2) fire test was conducted by The SP Technical Research Institute of Sweden in 2009 [Hjohlman, *et al.*, 2009]. A burner with a HRR of 7 kW was applied to the seat in one of the rear corners for 76 seconds. The properties of burnable materials and other additional information were estimated from separate tests and can be found in [Hjohlman, *et al.*, 2009]. The heat fluxes received by the seats and walls in the test fires were around 35kW/m^2 and 50kW/m^2 respectively. Therefore, the cone calorimeter HRR data for these materials under corresponding heat fluxes was used in the simulations presented in this section (see Figure 2.2(c)).

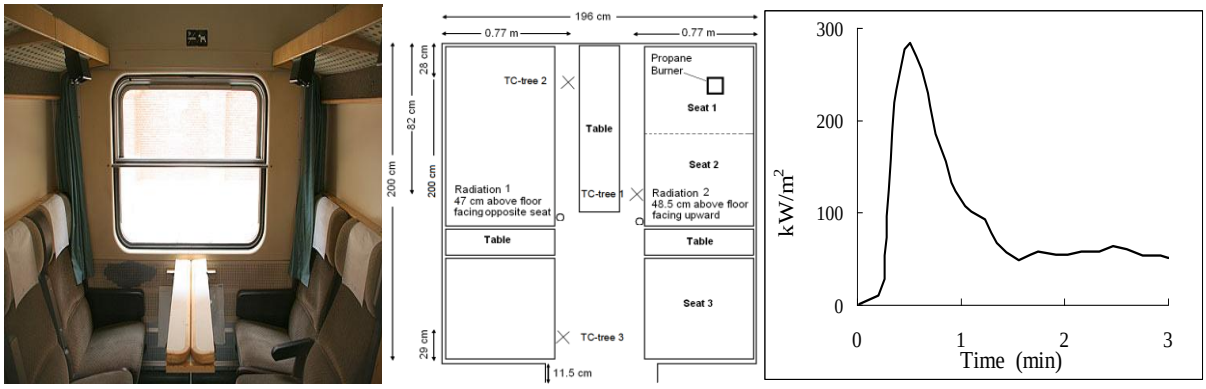

(a) (b) (c)

Figure 2.2 (a) Interior and (b) top view of the compartment; (c) Cone calorimeter HRR data for seats [Hjohlman, 2009].

Base case simulation and results

The field fire simulation tool SMARTFIRE [Ewer, *et al.*, 2008] was used to simulate the fire test. The eddy dissipation combustion model (EDM) was used to simulate the burning of the combustible gases released from the ignited materials, with an effective heat of combustion of 17.5 MJ/kg for polyurethane foam. The multi-ray radiation model with 48 rays was used to represent thermal radiation. The enhanced flame spread model was used to simulate the advance of flame front on the burnable materials such as seats and wall panels. Wall emissivity is assumed to be 0.8 for all surface materials.

Flame spread rates of the seat surface were not provided in the experimental report [Hjohlman, *et al.,* 2009]. However, the fire behavior of the double seat was experimentally investigated twice, free-burning in the furniture calorimeter and burning inside the ISO 9705 room respectively. The two tests shown that it took approximately 125 s for the flame to spread from the seat base to the top of the seat backrest (approximately 0.7 m) in the free burning tests. From this information, it was estimated that an average upward flame spread rate was no less than 0.005 m/s for the seat. The lateral flame spread rate was estimated to be 0.0025 m/s and the downward flame spread rate was assumed to be 0.001 m/s in the test inside the ISO 9705 room. No burning tests similar to the seat test were conducted for other interior materials. Considering the fact that the fire was well established after the seats were in flame, the ignition of other materials was expected to be predominantly caused by ignition criterion (a) in section 2.4.5, i.e. the surface ignition temperature. Therefore, the lack of flame spread rates for other materials does not significantly affect the simulations. However, as a model parameter, a very low value of 0.001 m/s was assigned for the interior materials other than the seat.

An unstructured mesh with mesh size of around 0.06 m was applied to represent the complex rail car geometry based on a mesh sensitivity study as seen in Figure 2.3(a), in which the solid squares represented the actual measured heat release rate before 190 seconds while the empty squares were estimations after this time.

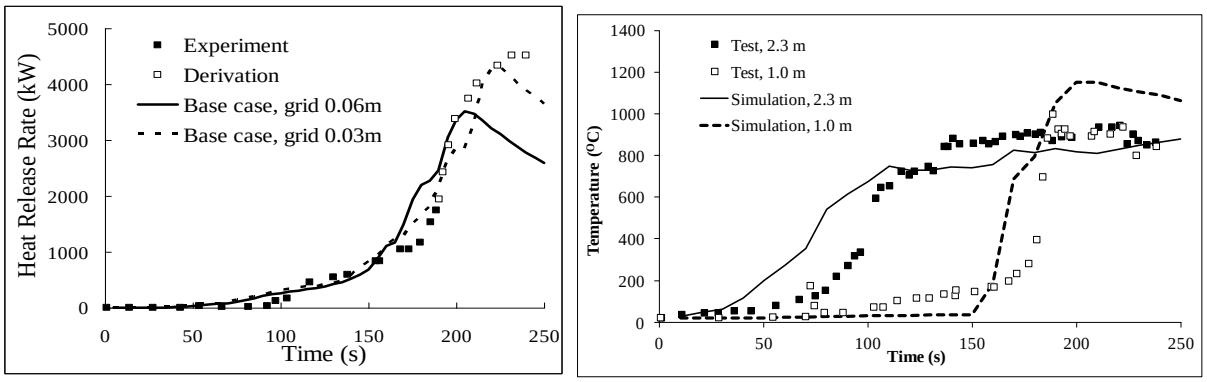

(a) (b)

Figure 2.3 Measured and predicted (a) HRRs and (b) temperatures of tree 1.

The seats, walls, floor and wood tables were set in the model as combustible. The flammability properties of these combustible materials, including the thickness, density, heat release rate, ignition temperature, thermal conductivity, specific heat and heat of combustion,

were taken from the experimental report [Hjohlman, *et al*., 2009; Hu, *et al*., 2012; Hu, *et.al*. 2010]. This setup with these material properties is called Base Case.

The simulation results from the Base Case are compared with the experimental observations, such as, the measured HRR and temperatures:

- The predicted HRR essentially follows the measured trends and is in good agreement with the measured HRR during the pre-flashover fire development stage, 90-150s (Figure 2.3(a));
- The measured and predicted temperatures at 2.3 m and 1.0 m above the floor at three thermocouple trees are in good agreement (Figure 2.3(b));
- The predicted ignited surface has a similar shape and size when compared with the experimental observation (Figure 2.4).

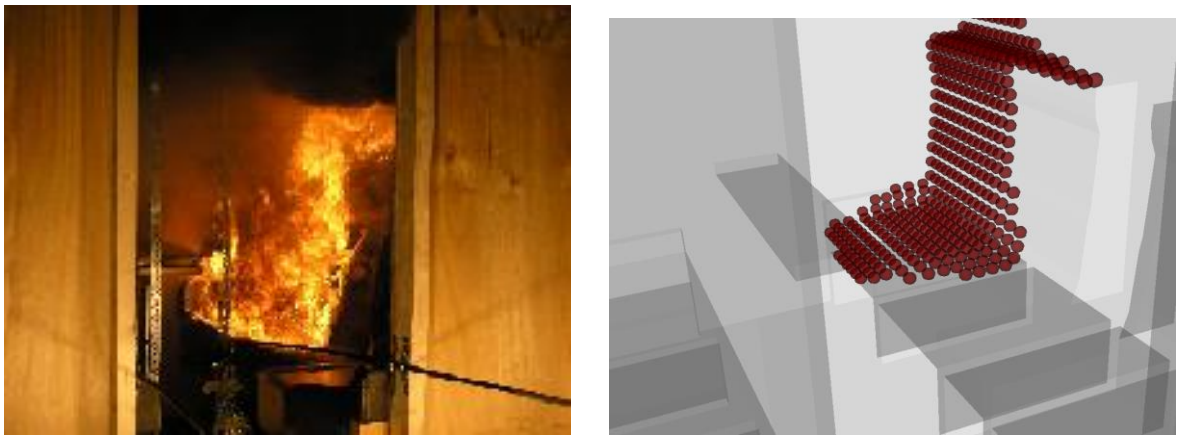

(a) (b)

Figure 2.4 (a) Observed fire plume at 132 s and (b) Predicted burning location at 132 s

Investigation of sensitivities of material properties for flashover

Flashover is a critical factor affecting passengers' survivability in rail cars. The ability to accurately predict the onset of flashover is therefore one of the key requirements for fire models. The definition of flashover for enclosure fires is generally accepted as occurring when the upper layer gas temperature exceeds 600^{O}C. For the purpose of convenient comparisons among all scenarios, the measured HRR value of 1.17 MW at the reported time of flashover (180 seconds) is regarded as a criterion for flashover in this study.

Table 2.5 Sensitivities of predicted times to flashover to uncertainties in material properties.

Material	Uncertainty	Predicted time to flashover (s)	Relative changes (%) compared with Base Case
PUR seat	+15% for HRR	106	-36
	-15% for HRR	247	+50
	+15% for ignition temperature	244	+48
	-15% for ignition temperature	100	-39
	+15% for flame spread of seat	145	-12
	-15% for flame spread of seat	195	+18
Metal laminate wall panel	+30% for HRR	165	0
	-30% for HRR	165	0
	+30% for ignition temperature	165	0
	-30% for ignition temperature	155	-6
Metal HPL laminate wall panel	+30% for HRR	127	-23
	-30% for HRR	242	+47
	+30% for ignition temperature	248	+50
	-30% for ignition temperature	142	-14
Wood tables and racks	+15% for HRR	138	-16
	-15% for HRR	242	+47
	+15% for ignition temperature	241	+46
	-15% for ignition temperature	126	-24

The variations of the predicted time to flashover caused by the uncertainty of the measured material properties are investigated in this section. A total of 18 fire scenarios [Hu, *et al*., 2012] were examined in which the uncertainties in the measured material properties were systematically examined (see Table 2.5).

From the results of these simulations it is found that:

- With the exception of the metal laminate, under-estimating the HRR or over-estimating the ignition temperature by 15% to 30% can increase the time to flashover by 46% to 50%.
- With the exception of the metal laminate, over-estimating the HRR or under-estimating the ignition temperature by 15% to 30% can increase the time to flashover by 14% to 39%.
- The time to flashover is most strongly dependent on variations in seat material properties and least dependent on variations in the material properties of the metal laminate.

The outcome of these simulations has been published in [Hu, *et al*., 2012; Hu, *et.al*. 2010].

2.9 Conclusion and future research

Without a doubt, field fire models have certain advantages over zone models for they are more advanced and flexible in predictive capability for fire safety design purpose. There have been a great deal of validations performed on field models over the last few decades which have proved the capability of producing much more detailed and more comprehensive results than zone modelling.

However, field models in their present form still have some shortcomings. The central problem facing the fire models mainly associate with accurate prediction of turbulent flow field and its coupling with chemical kinetics. In the case of RANS models, the simplified treatment of turbulence via the time averaging procedure is likely to introduce significant errors into predictions of the turbulent transport by largest eddies in the flow. Apart from the limits of spatial and physical resolution in turbulence modelling, improvements are also required in the prediction of formation rates of toxic life-threatening products and soot. The soot transport sometimes has been ignored without considering the characteristics of soot particles. This study will focus on the modelling of soot transport and generation.

Chapter 3

Soot Theory and Models

Soot plays a significant role in energy exchange in large scale fires via absorption and scattering of radiation. The basic properties of soot are first presented in brief in this chapter. Then the mechanisms of soot generation and transport are introduced, followed by the methodology of modelling soot generation and transport.

3.1 Introduction

Soot particles are impure carbon particles generated from incomplete combustion of hydrocarbons. Soot released into the environment represents a significant health risk, primarily associated with ailments in the respiratory system. From a thermodynamic perspective, the particle phenomena of soot alter the radiation character of flames and influence the overall energetics of a combustion system.

The effects of soot on human health and combustion process depend on the amount of soot produced and the properties of the soot. The following sections present the current state of knowledge about soot and its generation, including the physical and chemical characteristics. Generally, the soot characteristics are dynamic due to thermophoresis, sedimentation, diffusion and agglomerate growth, etc.. Here we focus on the soot released from flames where soot characteristics tend toward stability.

3.1.1 Structure of soot

Soot represents a very broad assortment of carbon or carbonaceous matter which ranges from small, individual particles to large, often aggregated chains containing thousands of primary particles. In this section, the structure of soot is introduced and discussed.

3.1.1.1 Appearance and size

The most common characteristic used to describe soot particles is average size, d_p (m). If the particles are assumed to be spherical, the volume fraction are related to number density and mean diameter as:

$$f_v = N\frac{1}{6}\pi d_p^3 \tag{3.1}$$

The soot size distributions are strongly positively skewed, with the majority of particles much smaller than the average size. Log-normal distribution function is thus a better fit to the data than Gaussian distribution. The geometric mean d_{gn} is defined as:

$$\log d_{gn} = \sum_i^n \frac{N_i \log d_{p,i}}{N} \tag{3.2}$$

And the geometric standard deviation σ_{gn} is:

$$\log \sigma_{gn} = \left[\sum_{i=1}^{n} \frac{(\log d_{p,i} - \log d_{gn})^2 N_i}{N-1} \right]^{1/2} \tag{3.3}$$

where N is the total number density and N_i is the number density with diameter $d_{p,i}$, i = 1, 2, …, n. This distribution shows that 68.3% of the total particles are in the size range $d_{gn} \pm \sigma_g$. The soot particle distributions for some commercial materials are available from work conducted by Mulholland and Butler [Mulholland, 2002; Butler & Mulholland, 2004].

The primary particles are roughly spherical, but the structures are far from spherical after the particles have aggregated. Another characteristic has been used to describe the nature of the irregularity, known as the fractal dimension (D_f). A fractal dimension is an index for characterizing fractal patterns by quantifying their complexity as a ratio of the change in detail to the change in scale. The soot fractal dimension is often obtained by image analysis of transmission electron microscopy and light scattering and has been measured to be in the range of 1.6 to 2.6 for a number of different fuels and combustion configurations [Hamins, 1993; Samson, *et al.*, 1987; Butler & Mulholland, 2004]. The number of primacy particles N inside an agglomerate sphere is approximately calculated as:

$$N \approx k_0 (R_g / r_p)^{D_f} \tag{3.4}$$

where R_g is the radius of gyration, r_p is the radius of the primary spheres, and k_0 is the pre-factor of the scaling relationship.

3.1.1.2 Morphology and chemical structure

Soot particles are generated from the pyrolysis of a fuel molecule typically containing a few hydrogen atoms and many carbon atoms within tens of milliseconds. The primary particles that contain millions of carbon atoms are nearly spherical (3 to 12 *nm*). During the soot development process, particles take on a chain-like appearance and the chain is typically composed of hundreds or thousands of primary particles each 2 to 35 *nm* in diameter [Hamins, 1993].

As the soot leaves the flame cools, smaller molecules, including water, benzene, other hydrocarbons, and acid gases may be adsorbed on its surface. The main constituent of soot is carbon and small amounts of hydrogen and oxygen. The proportion of these elements varies for different fuels and changes as the soot particle grows and matures. For example, the representative diesel soot contains the atoms of approximately 70 % C, 20% O, 3% S, 1.5% H, <1% N and <1% other trace elements [Fredrik & Ingemar, 1989]. There is a high level of volatile hydrocarbons in fresh soot compared to that of aged soot.

3.1.2 Soot properties

In this section, soot properties of primary interest to the fire community, light extinction coefficient of soot, soot obscuration and visibility in a medium containing soot, are introduced. One of the most widely measured soot properties is the light extinction coefficient. Soot obscuration or the reduction in visibility is one of the major hazards that impede the safe evacuationof occupants in a fire event.

3.1.2.1 Light extinction

Light extinction is the ratio of the light intensity, I_λ, passing through a distance of L to the initial light intensity, I_λ^0, which is a function of the soot extinction coefficient K [Mulholland, 2002] and expressed as follows:

$$\frac{I_\lambda}{I_\lambda^0} = e^{-KL} \tag{3.5}$$

The soot extinction coefficient K (1/m) can be expressed as the product of the specific extinction coefficient per unit mass K_m with soot mass concentration:

$$K = K_m C_s \tag{3.6}$$

where C_s is the concentration of soot in kg/m^3. The value of K_m is 7600 m^2/kg for soot produced during flaming combustion of wood and plastic and 4400 m^2/kg for soot produced during pyrolysis of these materials [Seader & Einhorn, 1977].

Equation (3.5) expressed in term of base 10 is a function of the optical density per meter (D)

$$\frac{I_\lambda}{I_\lambda^0} = 10^{-DL} \tag{3.7}$$

The coefficient D is calculated by $D=K/2.3$.

One quantity related to D, called mass optical density D_m, is widely used for convenient measurement. The mass optical density D_m (m^2/kg) is calculated by Equation (3.8) if the mass loss of the sample Δm is measured:

$$D_m = \frac{DV_c}{\Delta m} \tag{3.8}$$

where V_c is the volume of the chamber. The values of mass optical density D_m were measured for a variety of materials based on small-scale experiments [Gross, *et al*., 1967; Chien, *et al*., 1975; Breden & Meisters, 1976]. Investigations indicate that there is a qualitative correlation between D_m measured in small-scale and in large-scale tests but the correlation breaks down as fires become more complex [Peacock & Babrauskas, 1991].

3.1.2.2 Soot obscuration

Soot obscuration is widely used in engineering [He, *et al*., 2004]. The definition of the soot obscuration S_x (%) is given as follows:

$$S_x = 100(1-\frac{I_\lambda}{I_\lambda^0}) \tag{3.9}$$

where I_λ and I_λ^0 have the same definition as that in Section 3.1.2.1. The obscuration per meter (%/m) can be obtain from the equation:

$$S_x / L = 100(1-\frac{I_\lambda}{I_\lambda^0}) / L \tag{3.10}$$

3.1.2.3 Visibility

The visibility of an object requires a certain level of contrast between the object and its background. The contrast C_V can be defined as:

$$C_V = \frac{B}{B_0} - 1 \tag{3.11}$$

where B and B_0 are the brightness or luminance of the object and its background respectively. A value of C_V=*-0.02* is often used as a contrast threshold at which a black object can be discerned against a white background under daylight conditions.

The visibility distance is the minimum distance above which the object is no longer visible, but it is often determined as the distance at which the contrast is reduced to -0.02. Visibility depends on many factors such as soot concentrations, background lighting and so on [Rubini, *et al*., 2007]. Jin [1978] has obtained a fair correlation between visibility of test subjects and the extinction coefficient of the soot. The visibility of subjects is calculated with the empirical formula:

$$S = C_{SK} / K \tag{3.12}$$

where S is the visibility distance and constant C_{SK} takes the values of 8 and 3 for light emitting signs and light reflecting signs respectively. The constant 8 for C_{SK} is derived from the condition of illumination under 3cd/m^2, which is the illumination of the exit sign.

3.2 Soot generation mechanisms

The amount and character of soot generated by a fuel are strongly affected by the combustion conditions under which soot is produced–flaming, pyrolysis, and smouldering. Small scale studies have shown that the value range of the soot yield was between 0.001 to 0.17 for flaming combustions, and this range is greater than that for pyrolysis and smouldering, with values in the range 0.01 to 0.17 [Bankston, *et al*., 1981]. The flaming combustions are usually further classified into two kinds of flames: premixed and non-premixed flames. In premixed flames, gas-phase reaction rates are relatively rapid due to the large concentrations of free radicals. Thus, the available soot surface area controls the formation and destruction of soot. In contrast, the soot generation in non-premixed flames is usually controlled by gas-phase processes on the fuel-rich side, and by soot surface area in the narrow heat-release reaction zone where the concentration of free radicals are high. In this chapter, only the soot generation in non-premixed flames is discussed.

Figure 3.1 shows an idealized process of soot formation and oxidation schematic. After the formation of cyclic benzene or acetylene in the gas phase, the cyclic molecules grow further into primary soot particles through inception and condensation. The particles keep growing by

surface growth and coagulation, ending their experiences with oxidation. These processes, however, are not entirely organized as implied by the mechanistic description. It is not absolutely clear where one process starts and another ends in a flame. Some processes may occur simultaneously on the same particle, some causing mass growth and others maybe decreasing the particle mass. The description of soot formation and oxidation processes serves as a basis for comparison with experimental measurements.

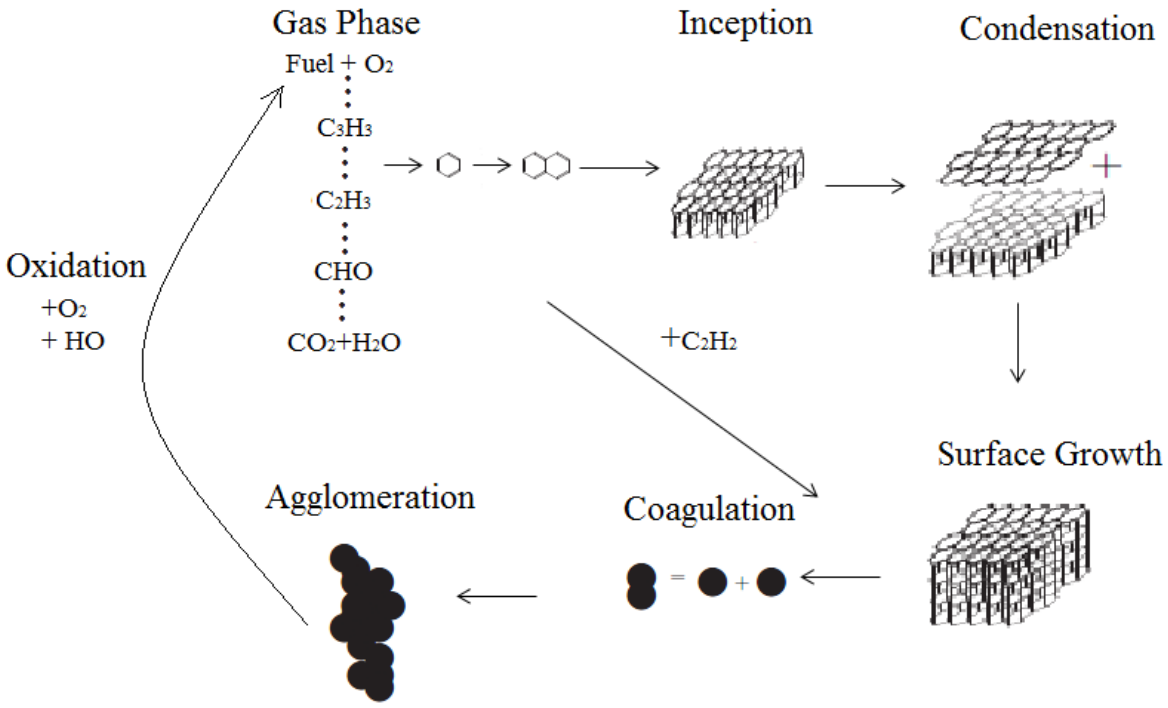

Figure 3.1 A schematic of soot generation (reproduced from the work of Dederiches[2004])

3.2.1 Soot formation

The chemistry issues involved in soot formation are very complex and still far from resolution. Research has shown that there exist at least two main chemical mechanisms, including polycyclic aromatic hydrocarbons (PAHs) and hydrogen abstraction with acetylene (i.e., carbon) addition (HACA). HACA increases the mass of existing soot particles by impacting H• atoms on the soot surface to activate acetylene. Thereby it is likely to occur in the main flame reaction zone where H• atoms concentrations generally exceed equilibrium values. PAHs are the key ingredient leading to soot formation where negligible H• atoms are present. Thus PAHs is likely to occur in hydrocarbon-rich regions (away from the main reaction zone). The above mentioned process shows the PAH mechanism is controlled by homogeneous gas-phase reaction while HACA mechanism is controlled by heterogeneous surface reaction.

Generally, the formation and growth of soot can be mechanistically divided into several processes: formation of particle nucleation/inception, surface growth, coagulation /agglomeration. The essential features of each phase are outlined in the sections that now follow.

Nucleation/inception

In high temperature flame environments, fuel molecules are pyrolysed into smaller fuel fragments. These fragments react to form stable molecules such as benzene, acetylene and radical species including H•, OH•, and small hydrocarbon radicals. The radical-stable species interactions are generally important in the molecular growth process as they are much more competitive compared with the radical-radical interactions and chemical reactions between two stable species. Carrying with nonbonding or free electrons, free radicals are highly reactive which leads one-ring benzene to undergo a number of reactions to form multi-ring species termed PHAs. The two-dimensional PHAs continue to grow to form three-dimensional particles, which are on the order of a few nanometres [Kennedy, 1997].

Surface growth

Subsequent particle growth takes place by gas species reacting on the soot surface. The surface growth is through surface polymerization with gas phase species, where a HACA mechanism is proposed. Kennedy [1997] proposed that it was surface growth not particle inception which controlled soot production. However, Harris and Weiner [1983] found the initial surface area (the product of particle number density and average surface area) controlled the soot fraction distribution by measuring surface growth rates in premixed flames.

Coagulation

Coagulation is the process of particle-particle collisions, followed by coalescence into a single particle. The coagulation process takes place simultaneously during the surface growth phase. Surface growth forms a rigid layered structure of the outer shell, which smooth the appearance of particles and cause two coagulated particles to merge into one spherical particle. The size of particles at this step increases to the order of 0.02 μm to 0.05 μm.

Agglomeration

Growth continues through agglomeration which lines up these primary particles end-to-end to form large clusters of particles. The agglomeration process occurs in the flame where the primary particles are partially fused. The particle number density is reduced and the particle size increases after the process, however, the change of specific surface area of soot is not noticeable.

3.2.2 Soot oxidation

As soot particles transport towards the high temperature combustion zone with oxidants present, soot oxidation reaction becomes more competitive compared with soot growth processes. During the soot oxidation phase, the soot particles reduce mass and size through reactions with radicals OH•, O_2, and other oxygenated species such as O atoms, H_2O (water vapour), CO_2 and NO_2.

The oxidation rate in non-premixed flames is highly dependent on the temperature field and concentration distribution of oxidizing species in the zone of active soot oxidation [Neoh, *et al.*, 1981]. Reaction rates associated with oxidation are lowered when flame temperature decreases. If the temperatures in oxidation region drop below 1300K, soot particles break out from the diffusion flame. Usually the reactions associated with oxidation are relatively fast at temperature above 1400K, and not strongly temperature sensitive for temperature in the range of 1800K-1900K [Gomez, *et al*., 1984; Gomez, *et al*., 1987]. When temperature is sufficiently high for oxygen to react with H• to form OH• radicals, the soot oxidation is controlled by the diffusion of oxygen into the soot oxidation zone rather than being controlled by the reaction of OH• radicals impinging on the available soot surface area. Most notable species linked to soot oxidation in diffusion flame are OH• O_2. And O•. Puri *et al*. [1994; 1995] measured the oxidizing species concentrations in the oxidation zone and showed that OH• reacts more readily with CO than with soot and O_2 concentration remains very small in the presence of oxidizing soot particles. However, Neoh *et al*. [1981] demonstrated that OH• was the principal oxidant, particularly on the fuel side of stoichiometry. The molecular oxygen becomes important only for O_2 concentrations above 5% [Xu, *et al*., 2003].

As the flame temperature, the concentration of oxidizing species and the soot volume fraction all play a role in oxidation process, it is too complicated to give a complete description of the soot oxidation phenomena. Empirically, the increase of soot concentration causes increasing

radiative losses, which decreases flame temperature and lowers the oxidation rate in turn. Decreased temperature promotes soot breakout from the diffusion flame, which represents an enthalpy loss from the combustion system, further decreasing flame temperature.

3.2.3 Factors affecting on soot emission

The amount of soot emission from a fire's flame is strongly dependent on the type of fuels [Tewarson, 2002; Mulholland, 2002, Butler & Mulholland, 2004]. However, soot yield for one certain fuel also varies with the combustion conditions. Experiments have been carried out to investigate the effects of pressure, temperature etc. on the soot field, and some trends have emerged from these experiments [Joo & Gülder, 2009; Shahad & Mohammed, 2000; Axelbaum & Law, 1991; Du & Axelbaum, 1995; Bento, *et al*., 2006]. The factors that have been identified in the literature as important aspects in soot emission are described in more detail in the sections that now follow.

3.2.3.1 Pressure

As pressure increases, the cross-section area of a flame becomes more narrow and soot formation region moves closer to the burner [Bento, *et al*., 2006; Balthasar, 2002]. The cross-section area of flames depends on pressure by an inverse law: $A_{cs} \sim P^{-1}$ [Bento, *et al.,* 2006]. The increase of pressure causes an increase in flow density, species concentrations as well as soot residence time, which leads to an increase in soot concentration. On the other hand, diffusion flames were observed to become expansive as pressure decreased from 1 atm to 0.1 atm (1 atm = 0.1013 MPa). The visible flame height increased slightly while the flow density reduced with decreased pressures in the range of [0.1atm, 1 atm].

Roditcheva and Bai [2001] pointed out that the relationship between soot volume fraction f_v and pressure p can be expressed as $f_v \sim \exp(\Gamma_s p \tau_{rs})$, where Γ_s is only weakly dependent on pressure and τ_{rs} is the resident time. More details of the dependence of soot production on pressure have been studied. Experiments on laminar non-premixed methane-air flames at the pressure from 0.5 to 4 MPa shown the maximum soot volume fraction $f_{v,\max} \sim P^2$ for a pressure range of 0.5 to 2.0 MPa, and $f_{v,\max} \sim P^{1.2}$ for a pressure range of 2.0~4.0MPa [Thomson, *et al*., 2005]. Bento *et.al*. [2006] pointed out that $f_{v,\max} \sim P^{1.8}$ held true for a

pressure between 0.2 MPa and 0.37 MPa. Zhu and Gore [2005] observed that the peak soot mass fraction $Y_{s,max}$ increased approximately linearly with pressure at a pressure below 4 MPa.

3.2.3.2 Temperature

Experiments indicate temperature exerts a strong influence on soot concentration field, but results in different outcomes in non-premixed and premixed flames. Glassman [Glassman, 1979; Glassman & Yaccarino, 1981] reported that the soot volume fraction increased with an increasing temperature field in non-premixed flames while it decreased in premixed flames. In premixed flames, the oxidation of soot precursors increased at a faster rate than precursor formation, leading to a reduction of soot. On the other hand, no oxidation took place during preheating. Increases in non-premixed flame temperatures promoted fuel pyrolysis rates which gave rise to the increase of soot precursor formation. Wey *et al.* [1984] also pointed out that an increase in temperature field resulted in a considerable increase in local soot volume fraction and aggregate diameters due to an effective growth of residence time for soot.

Temperature usually varies from 300 K to 2500K in diffusion flames but the soot formation process is limited by the range of 1000K to 2000K [Mansurov, 2005]. The peak soot formation rates occur in a temperature range of 1500K to 1600K. Kent and Honnery [1990] described the dependence of soot formation rate on temperature as an approximate parabolic trend, which is consistent with Warnatz's research [Warnatz, *et al.*, 2006]. The soot oxidation rates increase with increasing temperature, but the relative increase rate of soot oxidation depends on the fuel type.

3.2.3.3 Dilution

Dilution affects soot formation rates due to thermal and kinetic effects. The addition of an inert gas decreases the flame temperature and the probability of chemical reaction by decreasing probability of collisions.

Gülder *et al.* [1996] investigated the influence of hydrogen and helium dilution on soot volume fraction in counter-flow diffusion flames. If moderate amounts of hydrogen or helium were added to fuel, the changes in temperature field were negligible. The soot formation rates slightly reduced in ethylene diffusion flames but there were no noticeable changes in propane and butane flames. They also carried out two experiments on soot volume fraction by either

cooling the reactants from the base temperature of 600K or by diluting the reactants with an inert gas. The soot generation rate was observed to decrease in both experiments. The effect of dilution on the maximum soot volume fraction is greater than that of temperature when the amounts of dilution is moderate.

Axelbaum [Axelbaum, 1988; Axelbaum & Law, 1991] used two different methodologies to investigate the effects of dilution and temperature change by diluting the fuel with nitrogen and argon or adjusting temperatures. They found that soot generation rates behaved nearly linearly with fuel concentration in the diffusion flame. The soot generation rates and maximum soot yield in a 50% methane flame was about half of that in a pure fuel flame. As moderate amounts of inert gas caused only a very small reduction of temperature, the soot yield decreased mainly due to the dilution rather than the reduction of temperature. However, when large amounts of inert gas were added, it was found that temperature effects may dominate soot reduction, in an absolute sense, dilution effects could still be important because fuel concentrations were low.

3.3 Soot generation models

Although the mechanisms of soot generation are still not fully understood, a large number of models have been developed to describe the generation of soot in various combustion situations. As reported by Kennedy *et al.* [Kennedy, 1997; Moss, *et al.,* 1995; Dederichs, 2004], existing soot models can be classified into the following three categories: Empirical models, semi-empirical models and detailed chemistry models. The sections that now follow will discuss each of these models in more detail.

3.3.1 Empirical models

Based completely on experimental results, empirical models are designed to model a certain combustion situation without describing combustion processes in general.

Soot generation is expected to begin at a critical ratio (C/O ratio) or threshold equivalence ratio χ_C . Experiments show that soot emission sometimes occurs even at C/O = 0.5. Takahashi and Glassman [1984] proposed an effective equivalence ratio χ_C for the onset of sooting, which were applied to both premixed and diffusion flames:

$$\chi_C = \frac{2C + H}{2O} \tag{3.13}$$

And they also pointed out that the sooting of a fuel was determined by temperature, the C/H ratio and the number of C atoms in the fuel molecule.

Calcote and Manos [1983] first defined a threshold soot index (TSI) as a way to remove any system or apparatus dependence of the sooting tendency of a fuel in a diffusion flame, as a function of the equivalence ratio:

$$TSI = a + b\chi_C \tag{3.14}$$

where a and b were empirical apparatus dependent constants, and χ_C was the critical threshold of equivalence ratio.

Olson *et al*. [1985] extended TSI for a wide variety of fuels in laminar diffusion flames. They provided a useful way to assess the sooting thresholds for fuel mixtures by using individual TSIs of each component. The averaged TSI value of a mixture was given by:

$$TSI_{mix} = \sum_i X_i TSI_i \tag{3.15}$$

where X_i was the mole fraction of component i and TSI_i was the corresponding TSI for the component.

Khan *et al*. [1971] proposed a model to describe soot emissions in diesel engines. They assumed that the size of soot was constant in engines and soot generation was the results of particle inception alone. The particle inception was defined as a function of pressure, the equivalence ratio of the unburned gases and temperature:

$$\frac{dC_s}{dt} = c\frac{V}{V_{NTP}} p_u \chi_u{}^n \exp\left(\frac{-E}{R_u T_u}\right) \tag{3.16}$$

where C_s was the soot concentration in (kg/m^3), c was a modelling parameter, V and V_{NTP} were the volume of the soot formation zone and cylinder contents at normal temperature and pressure. P_u was the partial pressure of unburned fuel, χ_u was the local unburned equivalence ratio, T_u was the local temperature. The constant parameters c, n and E were gauged by experiments with general values of 0.468 kg.N^{-1}m^{-1}sec^{-1}, 3 and 1.7×10^5 kJ kmol^{-1} respectively. The results of the model showed a good agreement with experiments for a direct injection diesel over a range of frequency of rotation (1100 RPM to 2700RPM).

Edelman and Harsha [1977] developed a more sophisticated model:

$$\frac{dC_s}{dt} = aTX_{fu}^{b} X_{ox}^{c} \exp\left(\frac{-E_a}{R_u T}\right) \tag{3.17}$$

where X_{fu} and X_{ox} were the molar concentrations of unburned fuel and oxygen respectively. E_a was the activation energy and a, b c were constant parameters.

In 1990s, Rizk and Mongia [1990; 1991] built empirical correlations between soot production and inputs through detailed predictions of the flow field within a combustor. The inputs include pressure (p), residence time (through mass flow rate of air m_A), gas temperature (T) and fuel composition. Although the model tended to under-predict the soot emission, reasonable predictions were achieved compared with experimental measurements for three-dimensional gas turbine combustors. This model handled soot formation and oxidation separately. Soot formation was expressed as:

$$\dot{w}_{soot}(mg/kg) = cp^2(18 - m_H)^{1.5}\left[\frac{(F/A)m_{fu}}{Tm_A C_{k-\varepsilon}^{0.25}}\right] \tag{3.18}$$

where c was a modelling constant, m_H was the mass percentage of hydrogen in the fuel, F/A was overall fuel-air ratio, m_{fu} was the mass fraction of fuel that was burned in the computational zone, and $C_{k-\varepsilon}$ was a turbulence modelling constant describing the rate of turbulent mixing. The soot oxidation rate was modelled as:

$$\dot{w}_{ox}(mg/kg) = a\frac{p^2}{V}\left(\frac{F/A}{T}\right)_{pz}\left[\frac{Ve^{0.001\,\mathrm{IT}}}{m_A(F/A)}\right](18 - m_H)^{1.5} \tag{3.19}$$

where a was a constant, V was combustion volume and subscript pz referred to the primary zone, where the majority of the fuel combustion takes place.

Empirical models do not require complex modelling and are thus easy to develop and require little CPU time. However, these models fail to describe the combustion process in a general way. Thereby the applicability of empirical models is restricted to the exact conditions of a particular combustion process.

3.3.2 Semi-empirical models

Semi-empirical models develop mathematical descriptions of soot generation supplemented with data originating from experimental results. Compared with empirical correlations, semi-

empirical models are generally valid for a wide range of combustion applications as they can describe part of the physical and chemical aspects of soot phenomenology.

Tesner *et al.* [1971] proposed a simple kinetics model based on two-step mechanisms for soot generation. The mechanisms included a branch-chain process and a destruction of active particles on the surface of soot particles being formed. It described the formation rate of radical nuclei density *n* (radical nuclei per volume) as:

$$\frac{dn}{dt} = n_0 + (f - g)n - g_0 Nn \tag{3.20}$$

where n_0 was the initial number of nuclei which was temperature dependent, f and g were branching and terminating coefficient respectively, g_0 was the rate of loss of nuclei due to collisions with soot particles, and *N* was the number density of soot particles (particles per unit volume) which was solved by:

$$\frac{dN}{dt} = (a - bN)n \tag{3.21}$$

Here *a* and *b* were adjustable parameters. This model has been applied widely over years and is considered as a foundation of many later soot models.

Surovikin [1976] developed a more detailed model to describe the soot generation. It included four steps: formation of radical nucleus n, growth of nucleus to incipient particles, growth of incipient particles into carbon particles and oxidation of soot particles with O_2. The rate of formation of radical nucleus was given as:

$$\frac{dn}{dt} = R_H + fn - g_0 n^2 - K_l \tag{3.22}$$

Here R_H was the rate of decomposition of hydrocarbon molecules with an activation energy that corresponds to energy of a C-C or C-H bond. f was the coefficient of branching of nucleus formation reaction, and g_0 was the rate of loss of nuclei due to collisions with soot particles. The third term in the right side was the loss of nucleus due to the collisions of one with another and the last term was the loss of nucleus on the surface of particles.

Magnussen *et al.* [1979] extended Tenser's model [Tesner *et al.*, 1971] with the oxidation step and applied it to a generalized eddy dissipation model to a turbulent acetylene flame. Soot oxidation was calculated to be proportional to the combustion rate of fuel. Here the reactants were assumed to be perfectly mixed and chemical reactions took place in fine

structures in the flow. Brown and Heywood [1988] improved the mixing properties to predict soot emission in a diesel engine.

Hiroyasu *et al.* [1983a; 1983b] proposed a simple soot model in diesel engine which expressed net rate of soot mass (m_s) generation as the difference between the rates of formation and oxidation:

$$\frac{dm_s}{dt} = \left(\frac{dm_s}{dt}\right)_{formation} - \left(\frac{dm_s}{dt}\right)_{oxidation} \tag{3.23}$$

Arrhenius expressions are used to calculate the rates of soot formation and oxidation:

$$\left(\frac{dm_s}{dt}\right)_{formation} = A_{fu} m_{fu} p^{0.5} \exp\left(\frac{-E_{fu}}{RT}\right) \tag{3.24}$$

$$\left(\frac{dm_s}{dt}\right)_{oxidation} = A_{ox} m_{ox} p^{1.8} \exp\left(\frac{-E_{ox}}{RT}\right) \tag{3.25}$$

where A_{fu} and A_{ox} were model experimentally-determined constants. m_{fu} and m_{ox} were the masses of vaporized fuel and oxygen, *p* was the pressure in the cylinder. Activation energies were $E_{fu} = 8\times10^4$ J/mol and $E_{ox} = 12\times10^4$ J/mol respectively. Kouremenos *et al.* [1990] employed the model to predict soot emission from a single cylinder under different pressures. The simple model was demonstrated useful as the errors between measured and predicted exhaust soot were within about 20% or better.

Assuming the collision of soot particles were coalescent and self-preserving size distribution was maintained, Graham [1981] developed a model to simulate the growth of soot during the pyrolysis and partial oxidation of aromatic hydrocarbons. Self-preserving size distribution led to coagulation as:

$$\frac{d\overline{V}_s}{dt} = k_p f_v \overline{V}_s^{1/6} \tag{3.26}$$

where $\overline{V}_s$ was mean soot particle volume, f_v was the particle volume fraction and the rate constant k_p was calculated as:

$$k_p = \frac{1}{2}\left(\frac{3}{4\pi}\right)^{1/6}\left(\frac{6K_B T}{\rho}\right)^{1/2} \alpha G_e \tag{3.27}$$

where K_B was the Boltzmann's constant, α was a factor related to the polydisperse nature of the system and was suggested to use a value α =6.55. G_e was the enhancement of the collision

rate by long range dispersion forces with a typical value of 2. The effect of nucleation and condensation led to a rate of change of mean soot particle volume as:

$$\frac{d\overline{V}_s}{dt} = k_p f_v \overline{V}_s^{1/6} + \left(\frac{\overline{V}_s}{f_v}\right)\frac{df_v}{dt} \tag{3.28}$$

Graham gauged the value of the constants such as the soot density and the collision enhancement factor by using shock tube experiments. His results shown that nucleation was physical rather than chemical and particles were part soot and in part liquid poly-nuclear aromatic compounds.

Mulholland [1986] proposed a simple scheme in which soot nucleus were generated by pyrolysis of the fuel investigated. The production rate of soot nucleus was written in an Arrhenius form. The surface growth rate was assumed to be proportional to the soot particle surface area. It was found that the satisfactory time dependence of various parameters such as the number density and size distribution, could not be obtained compared with experiments due to the simplified nature of the model.

Many models of soot formation are facilitated by the use of mixture fraction as it provides a very useful method to describe the local thermochemical state in diffusion flame. Delichatsios [1994] formulated a theoretical model which scaled the soot formation with flame height and pressure. The soot mass fraction Y_s along the axis of a laminar diffusion flame was:

$$\left(\rho u \frac{dY_s}{dx}\right) = \dot{w}_s \tag{3.29}$$

where the reaction rate $\dot{w}_s$ was a function of the mixture fraction ξ, temperature T and fuel mass fraction Y_{F0} at the nozzle exit:

$$\dot{w}_s = c\rho^2 (Y_{F,0} \frac{\xi - \xi_{st}}{1-\xi_{st}}) exp(-E_a / R_u T) \qquad \xi > \xi_{st} \tag{3.30}$$

where E_a is activation energy with a value of 163,540 J/mol and R_u is the specific gas constant for dry air. The model assumed that soot mass growth was controlled solely by the availability of fuel and independent of particle surface area and number density of particles. However, Lindstedt [1994] found that the peak soot volume fractions were predicted more close to the experimental results if the growth rate was a function of the soot number density.

Kennedy *et al.* [1990] attempted to use only one equation to describe soot formation and oxidation in which the number density was assumed to be constant. Said and Borghi [1997]

improved the model by postulating the existence of a hypothetical species, intermediate between the fuel and soot. Two rate equations were formulated, one described the rate of formation and oxidation of the intermediate species, I, and the other described the conversion rate from I into soot and oxidation of soot.

$$\frac{dY_I}{dt} = k_A Y_{fu} Y_{ox}^{\alpha} \exp\left(\frac{-T_{A1}}{T}\right) - k_B Y_I Y_{ox}^{\beta} \exp\left(\frac{-T_{A2}}{T}\right) - k_I T Y_I \tag{3.31}$$

$$\frac{dY_s}{dt} = k_s T Y_I - \frac{k_{ox}}{\rho_s d_p} Y_{ox} Y_s P T^{-1/2} \exp\left(\frac{-T_{A3}}{T}\right) \tag{3.32}$$

where Y_{fu}, Y_{ox}, Y_s and Y_I were the mass fractions of fuel, oxidizer, soot and the intermediate species respectively. Soot particle diameter d_p was taken to be a constant value of 1 nm in Equation (3.32). This value may be appropriate to freshly formed soot but it is much smaller than the majority of the soot at the tip of a diffusion flame. The other parameters were determined empirically. Good agreement between the predicted and measured soot volume fractions was achieved for turbulent ethylene diffusion flames.

Moss *et al.* [1995] proposed a flamelet approach to describe four main soot mechanisms: nucleation, heterogeneous surface growth, coagulation and oxidation. Two conservation equations were solved for soot volume fraction, f_v, and particle number density, N.

$$\frac{d}{dt}(\rho_s f_v) = \gamma(\xi) N + \delta(\xi) \tag{3.33}$$

$$\frac{d}{dt}(N / N_0) = \alpha(\xi) - \beta(\xi)(N / N_0)^2 \tag{3.34}$$

Equation (3.33) represented the increase in soot volume fraction due to surface growth (first term) and nucleation of new particles (second term). Equation (3.34) represented the increase in soot particle number density as a result of particle inception (first term) and the loss of particle number due to coagulation. The source terms (γ, δ, α, β) were functions of mixture fraction and temperature:

$$\gamma = C_\gamma \rho T^{1/2} X_{fu} \exp(-T_\gamma / T) \tag{3.35}$$

$$\alpha = C_\alpha \rho^2 T^{1/2} X_{fu} \exp(-T_\alpha / T) = \delta / 144 \tag{3.36}$$

$$\beta = C_\beta T^{1/2} \tag{3.37}$$

where the activation temperature T_a and T_γ, the constants C_γ, C_α, C_β were gauged to achieve satisfactory agreement with the measured peak soot particle size and number density in the diffusion flames for several fuels, including ethylene, kerosene and methane.

Lindstedt and co-workers [Leung, *et al.,* 1991] developed another approach to predict the soot volume fractions in co-flow and counter-flow laminar diffusion flames. They modelled that the acetylene was primarily responsible for the nucleation and surface growth of soot. The nucleation step for acetylene was simplified as a one step process: $C_2H_2 \rightarrow 2C_{soot}+H_2$. The rate of nucleation was proportional to acetylene concentration $C_{C_2H_2}$ (kmol/m^3):

$$\dot{w}_n = 10^4 e^{-21{,}100/T} C_{C_2H_2} \tag{3.38}$$

The rate of surface growth was also assumed to be proportional to acetylene concentration and to the square root of the total aerosol surface area:

$$\dot{w}_g = k(T) C_{C_2H_2} C_s^{1/3} (\rho N)^{1/6} \tag{3.39}$$

where

$$k(T) = 6\times10^3 (\pi (6M_c / \pi\rho_s)^{2/3})^{1/2} e^{-12{,}100/T} \tag{3.40}$$

M_c was the molecular weight of carbon and N was the number of soot particles per unit mass of soot/gas mixture.

The oxidation rate in this model was derived from the method of Lee *et al.* [1962]. It assumes O_2 was the main oxidant and OH• was ignored for oxidation. The oxidation reaction was treated as $C_s + \frac{1}{2}O_2 \rightarrow CO$ and the rate was calculated as:

$$\dot{w}_{ox} = k(T) \frac{\pi}{M_c} \left(\frac{6M_c}{\pi\rho_s} \right)^{2/3} C_{ox} C_s^{2/3} (\rho N)^{1/3} \tag{3.41}$$

where

$$k(T) = 1.25\times10^5 T^{1/2} e^{-19{,}680/T} \tag{3.42}$$

Lindstedt and co-workers [Leung *et al.*, 1991] applied the model in a co-flowing, axisymmetric methane air flame. Generally a good agreement was obtained for the distribution of soot volume fraction, but discrepancies appeared near the nozzle. Fairweather *et al*. [1992] extended the model to turbulent flames with a similar method of Syed *et al*. [1991]. Lindstedt [1994] later improved the calculation of soot nucleation and mass growth by adding a kinetic mechanism for the soot nucleation. He also studied the dependence between soot mass growth, surface area, and number density of soot particles. The models which assumed soot mass growth to be proportional to number density achieved better results than

other models. It was noted that these models neglect OH• as an oxidant which was potentially important in the oxidation process.

3.3.3 Models with detailed chemistry

Both empirical and semi-empirical models rely on pre-determined empirical inputs, which limits their application within certain combustion conditions and fuel types. Hence, it is not easy to extend these models to general applications. A complete description of the soot generation is required to gain more generality in soot prediction. Detailed chemistry models have been developed over the last decade or so to solve the rate equations for the elementary reactions that lead to soot generation.

Frenklach *et al*. [Frenklach, *et al.*, 1985; Frenklach & Wang, 1991; Frenklach & Wang, 1994] had proposed sophisticated detailed soot models, which modelled the full panoply of soot phenomena, from the initial pyrolysis of fuel, nucleation of soot particles, surface growth and coagulation, to final oxidation. They modelled soot generation during the shock tube pyrolysis of acetylene. The model used Tanzawa and Gardiner's pyrolysis mechanism [Tanzawa & Gardiner, 1980] to describe the early hydrocarbon chemistry. The dominant precursor was the formation of the first aromatic from aliphatic fuel (PHAs). The aromatic ring then grew through HACA route and the coagulation related to PAH was also important in soot growth processes.

The formation of soot particles can be broken down to an infinite number of collision processes between particles of all sizes. The number density N_i of particles of all size classes ($i = 1,2,\cdots,\infty$) could be described by particle size distribution function. The concentration variation could be solved using the statistical method of moments. The k^{th} moment of concentration is defined as:

$$M^k = \sum_{i=1}^{\infty} m_i^k N_i \tag{3.43}$$

where M^k was the k^{th} concentration moment, N_i was the number density of class i and m_i was the mass of particles. The size moments were defined as normalized concentration moment:

$$\mu^k = \frac{M^k}{M^1} \tag{3.44}$$

Rate of nucleation, coagulation and surface reactions were used to describe the changes in the moments equations.

The forming of a soot particle was described as two PHA molecules that combined to form a dimer. The addition of acetylene to radical 'arm chair' site on a particle gave rise to the particle surface growth as shown below:

$$C_i - H + H \leftrightarrow C_i + H_2 \tag{3.45}$$

$$C_i \bullet + H \rightarrow C_i - H \tag{3.46}$$

$$C_i \bullet + C_2H_2 \leftrightarrow C_{i+2} - H + H \tag{3.47}$$

Oxidation by O_2 was also included:

$$C_i \bullet + O_2 \rightarrow products \tag{3.48}$$

The rate of surface growth was calculated as:

$$\dot{w}_g = aC_g \alpha \Psi_{Csoot} \cdot S_p n \tag{3.49}$$

where a was the per-site rate coefficient, C_g was the concentration of the growth species, α was the fraction of surface sites available for a given reaction, S_p was the surface area of a spherical particle and n was the number density of particles of given size class, factor $\Psi_{Csoot} \cdot$ accounted for the number of surface radicals per unit area and was derived from a steady state assumption applied to reactions (3.45)-(3.48).

The soot oxidation was assumed to be the consequence of reaction of oxygen with a radical site of a soot particle (Equation 3.48) and attachment of OH• on the surface:

$$C_i - H + OH \bullet \rightarrow products \tag{3.50}$$

As the present understanding of the details of OH• reactions with soot was deficient, the reaction probability of OH• with soot was an experimental factor with the value of 0.13.

Markatou *et al.* [1993] examined the model of Frenklach *et al*. [1985; 1991; 1994] with detailed chemistry for its ability to predict the critical equivalence ratio in acetylene, ethylene and ethane premixed flames. The critical equivalence ratio is the C/O ratio at which soot first appears. The model used 32 species and 139 reactions to calculate the early chemistry (C_1 to C_4 chemistry) and 70 species and 337 reactions to calculate the production of PAH up to coronene. The agreement between predicted critical equivalence ratios and the measurements was remarkably good. Beltrame *et al*. [2001] suggested 361 reactions involving 61 species in the detailed chemical mechanism while Wang and Frenklach [1997] included an even more elaborate reaction mechanisms with 99 chemical species and 527 reactions. Mauss *et al.*

[1994] modified the PAH growth and soot growth approach of Frenklach and his co-workers [Frenklach & Wang, 1991] with particular interest in the role of aerosol surface area and acetylene concentration in controlling soot growth.

Although these detailed chemistry models are generally valid for most combustion conditions, the high computational expenses limit their application by the current computer capacities. In order to simplify these models, efforts have been focused on using smaller sets of equations to describe soot generation, mainly to the processes of nucleation, surface growth and oxidation.

3.3.4 Two semi-empirical analytical soot models

Recently, two semi-empirical soot models were proposed to predict soot generation in diffusion flames. Both models estimate soot generation rates with analytical functions of mixture fraction, temperature and other global species. The sections that now follow describe these two models in more detail.

The analytical model of Lautenberger *et al.*

Lautenberger *et al*. [2005; 2002] proposed a simplified model for soot formation and oxidation in CFD simulation of non-premixed flames. Soot generation processes had been divided into two major mechanisms: formation and oxidation. The net rate of soot generation was:

$$\omega_s''' = \omega_{sf}''' + \omega_{so}''' \tag{3.51}$$

Soot formation rate was calculated as an approximately parabolic trend in local mixture fraction and a less-discernible trend in temperature. Soot oxidation was assumed to be controlled by the diffusion of molecular oxygen into the oxidative zone rather than reaction of OH• radicals with the available surface. Thus soot oxidation was modelled as a fuel-independent and surface area-independent function of mixture fraction and temperature.

$$\omega_{sf}''' = f_{sf}'''(\xi) g_{sf}'''(T) \tag{3.52}$$

$$\omega_{so}''' = f_{so}'''(\xi) g_{so}'''(T) \tag{3.53}$$

$f_{sf}'''(\xi)$ and $f_{so}'''(\xi)$ had units of kg/m^{3}s and accounted for mixture fraction-dependency of soot formation and oxidation respectively. Analytical forms of these functions were selected as a third order polynomial as shown in Figure 3.2(a). Temperature functions $g_{sf}'''(T)$ and

$g'''_{so}(T)$ were dimensionless. $f'''_{so}(Z)$ was chosen similar to the formation functions while temperature function $g'''_{so}(T)$ was assumed to be linearly proportional to temperature (see Figure 3.2(b)).

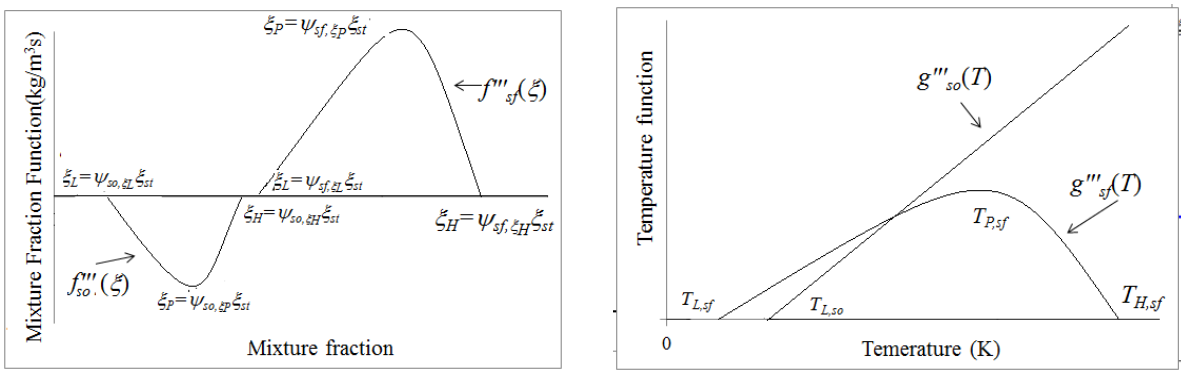

(a) (b)

Figure 3.2 (a) Mixture fraction polynomials; (b) Dimensionless temperature polynomials (reproduced from the work of Lautenberger *et al.* [2005]).

In Figure 3.2, ξ_{st} is the fuel's stoichiometric mixture fraction. Function $f'''_{sf}(\xi)$ assumes that soot formation starts at mixture fraction $Z_L = \psi_{z_L}\xi_{st}$ and reaches the peak rate at mixture fraction $Z_P = \psi_{z_P}\xi_{st}$, then falls back to zero at a mixture fraction of $Z_H = \psi_{z_H}\xi_{st}$. The parameters ψ_{z_L}, ψ_{z_P} and ψ_{z_H} are assumed to be fuel-independent and the values are obtained through manual calibration exercises for methane, ethylene and propane flames. The parameter constants for 212 W ethylene flame are listed in Table 3.1. Although there are 13 constants required in the model, only peak soot formation rate $f(\xi_p)$ is fuel-dependent.

Table 3.1 Optimal mixture fraction and temperature polynomial constants in the soot model of Lautenberger *et al.* [2005]

Parameter	ψ_{z_L}	ψ_{z_P}	ψ_{z_H}	$f(\xi_P)$	T_L	T_P	T_H	$dg_{so}(T_P)/dT$
Soot formation	1.05	1.77	2.15	1.10 kg/m^{3}s	1375K	1625K	1825K	----
Soot oxidation	0.56	0.84	1.05	-0.85 kg/m^{3}s	1375K	----	----	0.006K^{-1}

The model was generalized to other hydrocarbon fuels by relating the fuel's peak soot formation rate $f(\xi_{sf,P})$ to its laminar smoke point height. The laminar smoke point (L_{sp}) height is defined as the maximum height of the fuel's laminar flame burning in air at which

soot is not released from the flame tip. Lautenberger [2005] expressed the peak soot formation rate as:

$$\omega'''_{sf,p} = 1.1\left(\frac{0.106}{L_{sp}}\right)\left(\frac{28}{M_F}\right)^a\left(\frac{p_0}{p^o}\right)Y_{F0} \tag{3.54}$$

The above equation shows the peak soot formation rate is related to the background pressure p_0 normalized by the reference pressure p^o (101.3 kPa), the fuel's molecular weight M_F, and the mass fraction of fuel in the fuel supply stream Y_{F0}. The value of constant *a* is set to 0 or 1.

The analytical model of FireSERT

Delichatsios and co-workers [Delichatsios *et al.*, 1994] first proposed a simple soot formation model. Later, the model was further developed by Beji *et al.* [2008] based on the laminar smoke point concept. Then Yao *et al*. [2011b; 2010] applied the oxidation model proposed by Leung *et al*. [1991] to complete a global soot generation model. In a different development, Chen *et al*. [2014] took a similar approach of modelling soot formation but with a different soot oxidation model to complete their global soot generation model.

This model assumed that the soot started to form due to condensation of PAHs at a critical mixture fraction ξ_c and ended at ξ_{so} (slightly lean to the fuel's side). The oxidation zone was limited between 0 and ξ_{so}. The soot production rate can be calculated as:

$$\omega'''_s = \begin{cases} \omega'''_{sf} - \omega''_{so}\rho A_s Y_s & \xi \in [\xi_{so}, \xi_c] \\ -\omega''_{so}\rho A_s Y_s & \xi \in [0, \xi_{so}] \end{cases} \tag{3.55}$$

where ω'''_{sf} was volumetric soot formation rate, ω''_{so} was surface oxidation rate, ρ was gas-phase density, ξ was local mixture fraction, Y_s was local soot mass fraction and A_s was soot particulate surface area with a value of 160 m^2/g.

The volumetric soot formation rate (kg/m3 s) was expressed by an Arrhenius equation:

$$\omega'''_{sf} = A_f \rho^2 T^\gamma Y_{F0} \frac{\xi - \xi_{st}}{1 - \xi_{st}} e^{-T_a/T} \qquad \xi \in [\xi_{so}, \xi_c] \tag{3.56}$$

where A_f was the pre-exponential factor accounting for the soot propensity of a specific fuel. Y_{F0} was the fuel concentration in the fuel supply, which had a value of 1 for pure fuel. The temperature exponent was γ =2.25 and activation temperature was T_a=2000K for all fuels and combustion conditions.

The soot surface oxidation rate (kg/m^2 s) was developed initially by Leung *et al.* [1991].

$$\omega''_{so} = A_{ox} C_{O_2} \sqrt{T} e^{-E_{a,0}/R_u T} \qquad \xi \in [0, \xi_{so}] \tag{3.57}$$

where A_{ox} was a pre-exponential factor in the oxidation rate and was calibrated to be 120, $E_{a,0}$ was activation energy for soot oxidation rate with a value of 163,540 J/mol and R_u was the specific gas constant for dry air.

The pre-exponential factor A_f is a fuel-dependent parameter in the model and a value of 4.0×10^{-5} is obtained for ethylene (C_2H_4) by numerical calibration [Delichatsios, 1994]. A_f for other fuels are calculated based on the assumption that the sooting propensity of each fuel is inversely proportional to its L_{sp} (smoke point height):

$$\frac{A_{f,Fuel}}{A_{f,C_2H_4}} = \frac{L_{sp,C_2H_4}}{L_{sp,Fuel}} \tag{3.58}$$

Soot inception limit ξ_c is related to the stoichiometric mixture fraction:

$$\xi_c = \psi_c \xi_{st} \tag{3.59}$$

where ψ_c is a fuel-independent constant and is determined to be 2.5 [Beji, *et al*., 2008]. The value of ξ_{so} for a fuel with a molecular form C_xH_y is calculated from the critical ratio $(C/O)_c$:

$$\xi_{so} = \frac{(C/O)_c}{(C/O)_c + (1/\xi_{st} - 1)/(2 + y/2x)} \tag{3.60}$$

Applications of the model in laminar flames achieved good predictions [Beji, *et al*., 2008] and Yao *et al.* [2010; 2011a] also extended the model to turbulent flames via alternative conditional source-term estimation (A-CSE) approach to model the interaction between combustion and turbulence.

3.4 Soot particle transport mechanism

3.4.1 Forces on particle

This section discusses the forces and mechanisms that can cause particles to make movements relative to the fluid stream along which they travel. Sippola and Nazaroff [2002] summarised these forces in their review. All equations developed in this section are based on the assumption that the particles are in a spherical solid shape.

Brownian diffusion

Brownian motion describes the random movement of particles suspended in a fluid as the result of their random collision with the molecules in the fluid. Based on Fick's law of diffusion, Brownian diffusion of the particle flux in one dimension can be calculated as:

$$J_B = -D_B \frac{\partial C_p}{\partial y} \tag{3.61}$$

where J_B is the Brownian diffusive particle flux in the *y*-direction, $\partial C_p / \partial y$ is the *y*-component of the particle concentration gradient. D_B is the Brownian diffusivity which can be calculated by the Stokes-Einstein relation as [Crocker, 1997]:

$$D_B = \frac{C_c k_B T}{3\pi d_p \mu} \tag{3.62}$$

where Boltzmann's constant $k_B = -1.38 \times 10^{-23}$ J/K, C_c is the Cunningham slip corrector and T is the absolute temperature. Brownian diffusion is generally a weak mechanism for particles larger than 0.1 μm.

Drag force

Whenever there is a relative motion between a particle and its surroundings, the particle experiences a drag force from the fluid to reduce the relative motion. The drag force can be written as a function of the particle's size, relative velocity, and fluid's density and viscosity:

$$F_D = C_D \rho_f A_c |u_f - u_p|^2 / 2 \tag{3.63}$$

where A_c is the cross sectional area of particles, u_f and u_P are the velocities of the fluid and particle respectively. The drag coefficient C_D depends on particle Reynolds number [Sippola & Nazaroff, 2002] and can be calculated approximately as follows if particle Reynolds number $\mathrm{Re}_P < 0.5$:

$$C_D = 24 / \mathrm{Re}_P \tag{3.64}$$

where particle Reynolds number Re_P is calculated as:

$$\mathrm{Re}_p = \frac{d_p |u_f - u_p|}{\nu} \tag{3.65}$$

Here d_P is the diameter of the particle and *v* is the kinematic viscosity of the fluid. The above equation shows Re_P varies proportionally to $|u_f - u_p|$. The particle Reynolds number is usually small as particles relax towards the fluid velocity.

Gravitational force

Gravitational force on particles leads them to fall towards the floor. The net gravitational force on a particle is:

$$F_G = \frac{\pi}{6} d_p{}^3 \rho_p g \tag{3.66}$$

where g is the gravitational acceleration with an approximately value of 9.81 m/s^2. The gravitational force can be a dominant force on particles larger than 0.1 μm in a laminar fluid.

Buoyancy force

Buoyancy force is the product of the mass of the fluid displaced by the particle and the acceleration from the external force on the particle, such as gravitational or centrifugal force. It acts parallel with the external force but in the opposite direction. Based on Archimedes' law, it could be calculated as:

$$F_B = \frac{m_p}{\rho_p} \rho_f g \tag{3.67}$$

where $\frac{m_p}{\rho_p}$ is the volume of the particle.

Shear-induced lift force

A particle entrained in a shear flow field may experience a lift force which is perpendicular to the main flow direction. Saffman [1965; 1968] first evaluated the magnitude of this shear-induced lift force for particles in a constant shear flow away from walls:

$$F_L = \frac{1.62 \mu d_p (du_f / dy)}{\sqrt{\nu | du_f / dy |}} \left(u_f - u_{px} \right) \tag{3.68}$$

where du_f / dy is the fluid velocity gradient normal to the duct wall and u_{px} is the stream-wise velocity of a particle. Equation (3.68) was derived on the constrains:

$$\frac{d_p (du_f / dy)}{\nu} < 1 \text{ and } \mathrm{Re}_p < \frac{d_p (du_f / dy)}{\nu} \tag{3.69}$$

The direction of the lift force is determined by the relative velocity between the particle and fluid in stream-wise. The particle will experience a lift force towards the wall if $u_{px} > u_f$, otherwise, it is away from the wall.

Theoretical analysis on the lift force was investigated with equation (3.68) and a modification of Saffman's calculation can be found in [McLaughlin, 1993; Wang, *et al*., 1997]. It suggests that the lift force arises with particle inertia and becomes very important for large particles very close to the wall ($y^+ < 20$).

Thermophoresis

If there exists a temperature gradient in the fluid, the average strike force of molecules on the warm side is higher than those on the cooler side, which causes a particle to move towards the cooler region. Talbot *et al.* [1980] evaluated the force by balancing a drag force with the thermophoretic force and obtained the expression as:

$$F_T = \frac{3\pi\mu^2 d_p H}{\rho_f}\frac{dT}{dy} \tag{3.70}$$

where dT/dy is the y-component of the temperature gradient. The thermophoretic force coefficient H is calculated as:

$$H = \left(\frac{2.34}{1+3.42Kn}\right)\left(\frac{k_f/k_p + 2.18Kn}{1+2k_f/k_p + 4.36Kn}\right) \tag{3.71}$$

where k_f and k_p are the thermal conductivities of the fluid and the particle respectively. Kn is the Knudsen number, defined as a ratio of the mean free path of gas molecules λ (λ=0.065 um at T=298K and P=1 Pa) and the particle diameter :

$$Kn = \frac{2\lambda}{d_p} \tag{3.72}$$

In a given temperature gradient, the thermophoresis force is nearly independent of particle size for those smaller than 1 μm. For large particles, the thermophoresis velocity decreases with the increase of particle size if k_f/k_p <0.2.

3.4.2 Other transport mechanisms

There are other forces to transport particles such as pressure gradient force, the Basset force, and the Magnus force due to particle spin. Zhao, *et.al*. [2004] pointed out that the ratio of the pressure gradient force F_p to an external force exerted on the particle F_e is approximately equal to

$$\frac{F_P}{F_e} \approx \frac{\rho_f a_f}{\rho_p a_p} \tag{3.73}$$

As the acceleration rates of fluid a_f and particle a_p are in the same order in many circumstances, the ratio of F_P / F_e is determined by the ratio of fluid density to particle density ρ_f / ρ_p . The pressure gradient force F_p can be ignored compared with the external force F_e due to $\rho_f << \rho_p$. The other forces such as Basset force can be neglected because of the small fluid density compared with particle density [Zhao, *et al.,* 2004].

3.5 Soot particle transport models

The ability of correctly predicting soot levels within compartment fires is crucial for fire simulations as soot plays a significant role in fire development and may severely impede the ensuing occupant evacuation. Soot is a particle phenonmenon and the transport mechanisms of soot are different from those of gas species. Therefore, it is necessary to develop soot transport model to predict the soot layers in fires.

3.5.1 Conventional model

Most of soot particles have diameters less than about 1.0 μm and the geometric mean diameters are less than 2 μm. Murakami *et al.* [1989] investigated the diffusion characteristics of airborne particles with the size increasing from 0.3 μm to 100 μm. The results show that the particles smaller than 4.5 μm move in the similar way as those in the case of zero gravitational settling velocity. When the particle size increases to 10 μm, the effects of gravitational sedimentation starts to appear, and becomes significant if the sedimentation time scale is larger than or on the same order as the characteristic diffusion time scale.

Conventional soot transport modelling simply treats soot as being in a gaseous state [Rubini, *et al*., 2007; Galea, *et al*., 2008], assuming soot movement in the same manner of other gaseous combustion products without considering any of the movement mechanisms of particles, except Brownian diffusion and turbulent diffusion.

The instantaneous soot particle concentrations C_s in turbulent flows can be expressed as the sum of a time averaged concentration $\overline{C_s}$ and a fluctuating concentration C_s'. The total particle diffusive flux J_{diff} (average over turbulent fluctuations) is:

$$J_{diff} = -D_B \frac{\partial \overline{C_s}}{\partial y} - \overline{v' C_s'} \tag{3.74}$$

where D_B is the Brownian diffusion coefficient. The second term on the right side, $\overline{v'C'_s}$, is the contribution to the total diffusive flux from turbulent fluctuations. It is commonly modelled for homogeneous turbulence:

$$\overline{v'C'_s} = \varepsilon_p \frac{d\overline{C}_s}{dy} \tag{3.75}$$

where ε_p is the eddy diffusivity of the particles, often use the same value as the eddy viscosity of fluid ε_f . $\varepsilon_p = \varepsilon_f$ means there is no slip velocity between the particle and fluid stream, which is reasonable for particles with small relaxation time (with an upper bound 10^{-3} s) [Hinze, 1975].

The governing equation for soot movement is expressed the same as other gaseous products:

$$\frac{\partial C_s}{\partial t} + div(\vec{U}C_s) = div((D_B + \varepsilon_p)\nabla C_s) + S_{Y_s} \tag{3.76}$$

where C_s is the soot mass fraction. This modelling approach simplifies the soot behaviour and sometimes fails to reproduce the observed heavy soot presence in the lower layer of the fire enclosures [Blomqvist, 2003].

3.5.2 Particle transport models

Generally, there are two approaches to analyse the particle transport process with computational fluid dynamics (CFD) namely the Lagrangian method and Eulerian method. Both approaches are theoretically based on particle movement mechanisms. The Lagrangian approach considers the air as a continuous phase and the trajectory of a single particle through the airflow is affected by the sum of all forces acting on the particle. The concentration of particles should be analysed before statistical conclusions can be drawn. The Eulerian approach treats both the particles and the air as separate continuous phases. The overall behaviour of an ensemble of particles, instead of individual trajectories of particles, is predicted through the solution of conservation equations for the particle concentration.

Comparisons between these two methods have been made in the literature [Durst, *et al*., 1984; Gouesbet & Berlemont, 1998]. The high computational cost of the Lagrangian method limits its application in soot simulations within large-scale enclosure fires as statistically stable particle concentrations require a large number of particle tracks. Compared with the expensive

computational requirement of the Lagrangian method, the computational cost of the Eulerian method for simulating particle movement is significantly low.

Most models are based on some common assumptions to simplify the simulations. One such assumption is that particle concentrations are sufficiently low to ignore the effect on the structure of air turbulence and particle-particle interactions. Also, forces on the particles due to pressure gradient and thermal gradients are not included as the density of air is small compared with density of soot particles.

3.5.2.1 Lagrangian models

Based on Newton's law, the momentum equation of each particle is:

$$m_p \frac{d\vec{u}_p}{dt} = -\vec{F}_D + \vec{F}_G - \vec{F}_B + \vec{F}_a \tag{3.77}$$

where m_p and $\vec{u}_p$ are the mass and velocity vector of the particle respectively. The forces accounted for particle motion are drag force $\vec{F}_D$, gravitational force $\vec{F}_G$, buoyancy force $\vec{F}_B$, and additional forces $\vec{F}_a$. Zhao *et al*. [2004; 2008] pointed out that the forces caused by the pressure gradient and the virtual mass are negligible compared with drag force. However, Saffman's lift force $\vec{F}_L$ may be relatively large for fine particles. Thus this force is included in this model. Substituting the forces in Equation (3.77) with their expressions, the finial trajectory equation is:

$$\frac{du_p}{dt} = \frac{3\mu C_D \,\mathrm{Re}_p}{4\rho_p d_p^{\,2}}(\vec{u}_p - \vec{u}_a) + \frac{\vec{g}(\rho_p - \rho_f)}{\rho_p} + \frac{\vec{F}_L}{m_p} \tag{3.78}$$

The mean path of particles is determined by the time-average flow field while each particle's turbulent dispersion from the mean trajectory is governed by the instantaneous flow field. The discrete random walk model (DRW) is used to simulate the stochastic velocity fluctuations in the airflow. It assumes that the fluctuating velocities follow a Gaussian probability distribution and the fluctuating velocity components could be calculated as:

$$\overrightarrow{u'_a} = \zeta\sqrt{\overrightarrow{u'^2_a}} = \zeta\sqrt{2k/3} \tag{3.79}$$

where *k* is the turbulent kinetic energy and ζ is the Gaussian distribution random number.

Particle positions are recorded at the end when the air flow computation has converged. The trajectories terminate if the particles escape the computational region or reach rigid surfaces

since the rebound energy accumulated by particles are usually not sufficient to overcome adhesion [Hinds, 1982].

To express the Lagrangian trajectory information in the form of particle concentration distribution, the particle concentration in the cell (PSI-C) method is applied here:

$$C_j = \frac{\dot{M} \sum_{i=1}^{m} dt_{(i,j)}}{V_j} \tag{3.80}$$

where C_j is the mean particle concentration in a cell j, $\dot{M}$ is the flow rate of each trajectory, V_j is the volume of the cell and $dt_{(i,j)}$ is the particles residence time at i^{th} trajectory in j^{th} cell.

Zhang and Chen [2006] used Lagrangian DRW model with the PSI-C scheme to simulate the particle concentration fields in ventilated rooms and found that the concentration results became statistically stable if sufficient number of trajectories were tracked. The predictions of particles dispersion in a ventilated room using 16,000 tracks [Zhao, *et al*., 2008] showed that the Lagrangian DRW model provided good agreements with the measured particles dispersion in the room except that at locations near the ceiling and inlet.

3.5.2.2 Eulerian models

Mixture model

As the air phase and the particle phase move at different velocities, the model views the motion of the particle to the mixture phase as the diffusion of the particle phase [Zhao, *et al*., 2008]. The velocities and the volume fraction of the two interpenetrating continua (fluid phase and particle phase) are solved through differential equations for the volume fraction of the particle coupled with the mixture.

Governing continuity equation for the mixture is:

$$\frac{\partial}{\partial t}(\rho_{mix}) + \nabla(\rho_{mix}\overrightarrow{u_{mix}}) = \dot{m} \tag{3.81}$$

Governing equation of momentum for the mixture is:

$$\begin{aligned}\frac{\partial}{\partial t}(\rho_{mix}\overrightarrow{u_{mix}}) + \nabla(\rho_{mix}\overrightarrow{u_{mix}}\overrightarrow{u_{mix}}) = -\nabla p + \nabla[\mu_{mix}(\nabla\overrightarrow{u_{mix}} + \nabla\overrightarrow{u_{mix}}^{T})] \\ + \rho_{mix}\vec{g} + \vec{F} + \nabla(\alpha_p\rho_p\vec{u}_{dr,p}\vec{u}_{dr,p} + \alpha_f\rho_f\vec{u}_{dr,f}\vec{u}_{dr,f})\end{aligned} \tag{3.82}$$

Governing equation of volume fraction for the particles is:

$$\frac{\partial}{\partial t}(\alpha_p \rho_p) + \nabla(\alpha_p \rho_p \overrightarrow{u_{mix}}) = -\nabla(\alpha_p \rho_p \vec{u}_{dr,p}) \tag{3.83}$$

If the volume fraction of the particle phase and fluid phase are α_p and α_f, the density, viscosity and mass averaged velocity of the mixture can be defined as:

$$\rho_{mix} = \alpha_p \rho_p + \alpha_f \rho_f \tag{3.84}$$

$$\mu_m = \alpha_p \mu_p + \alpha_f \mu_f \tag{3.85}$$

$$\vec{u}_{mix} = \frac{\alpha_p \rho_p \vec{u}_p + \alpha_f \rho_f \vec{u}_f}{\rho_{mix}} \tag{3.86}$$

Drift velocity of the particle $\vec{u}_{dr,p}$ is defined with respect to the velocity of mixture phase:

$$\vec{u}_{dr,p} = \vec{u}_p - \vec{u}_m = \vec{u}_{ap} - \frac{\alpha_f \rho_f}{\rho_{mix}} \vec{u}_{ap} \tag{3.87}$$

where $\vec{u}_{ap}$ is the slip velocity of the particles with respect to the fluid phase and is a function of particle acceleration $\vec{a}_p$ and particulate relaxation time τ_{ap} in this model [Manaul, 2005]:

$$\vec{u}_{ap} = \tau_{ap} \vec{a}_p \tag{3.88}$$

The acceleration $\vec{a}_p$ and relaxation time τ_{ap} are calculated as:

$$\vec{a}_p = \vec{g} - (\vec{u}_{mix} \cdot \nabla)\vec{u}_{mix} - \frac{\partial \rho \vec{u}_{mix}}{\partial t} \tag{3.89}$$

$$\tau_{ap} = \frac{(\rho_m - \rho_p) d_p^2}{18 \mu_f C_D} \tag{3.90}$$

According to Equation (3.86), drift velocity of air $\vec{u}_{dr,f}$ can be derived from the drift velocity of the particle $\vec{u}_{dr,p}$ as:

$$\vec{u}_{dr,f} = \vec{u}_f - \vec{u}_m = -\frac{\alpha_f \rho_f}{\rho_{mix}} \vec{u}_{dr,p} \tag{3.91}$$

Drift flux model

Another Eulerian model called drift flux model was developed to take full advantages of the extremely low volume fraction of particles. The model is one-way coupling that ignores the effect of particles movement on turbulence. Particle phase and air phase are assumed well coupled and a small drift flux velocity exists between the two continua. The drift flux velocity

of a particle is derived by equalling the fluid drag force and buoyant force on the particle with the gravitational force.

The governing equation for particle transport is given as :

$$\frac{\partial C_p}{\partial t} + div((\vec{U} + \vec{v}_s)C_p) = div((D_B + \varepsilon_p)\nabla C_p) + S_{C_p} \tag{3.92}$$

where C_p is the particle mass concentration (or number density) , ε_p is the particle eddy diffusivity and D_B is the Brownian diffusion coefficient. $\vec{v}_s$ is the particle settling velocity, which is derived by balancing the drag force, buoyant force on particles with the gravitational force:

$$|\vec{v}_s| = \left[\frac{2(\rho_p - \rho_f)gV_p}{C_D A_p \rho_f}\right]^{1/2} \tag{3.93}$$

The model is widely applied to predict indoor particle distributions [Chen, *et al*., 2004; Chen, *et al*., 2006; Zhao, *et al*., 2008; Holmberg & Chen, 2003; Zhao, *et al*., 2004] and achieved good agreements with experimental data.

3.5.3 Models without solving soot equation

An approach was developed by calculating soot extinction coefficient through the predicted temperature or CO_2 concentration or O_2 concentration. This approach can be easily incorporated in CFD fire models. However, low precision may be achieved as temperature or gas concentration cannot fully describe the characteristics of transport of soot particles.

Estimate soot layer by temperature

Evans and Stroup [1986] developed a model which assumed the optical density (D) is related to the temperature rise:

$$\frac{D}{\Delta T} = \frac{3330 \cdot \rho \cdot c_p \cdot Y_{yield}}{\dot{Q}} \tag{3.94}$$

where ρ and c_p were density and specific heat capacity of air respectively, Y_{yield} was the soot yield value of a fuel and $\dot{Q}$ was the convective heat release rate per kg fuel burnt.

The soot concentration C_s (kg/m^3) can be expressed as a function of optical density per meter and optical path length l:

$$C_s = \frac{D/l}{K_m} \tag{3.95}$$

where K_m was the specific extinction coefficient (m^2/kg).

He [He, 1997; He, *et al*., 1998] also proposed a method to determine the soot-layer height from temperature profile data. The soot layer interface height H_{int} was calculated in a two-zone model as follows:

$$H_{\text{int}} = \frac{T_l(I_1 I_2 - H^2)}{(T_l^2 I_2 + I_1 - 2HT_l)} \tag{3.96}$$

where T_l was the lower layer temperature, H was the height of the region, I_1 and I_2 were the integral ratio for heat and mass respectively. The integral ratio for parameter *p(y)* was written as:

$$I = \frac{1}{(H - H_{\text{int}})^2}\int_{H_{\text{int}}}^{H} p(y)dy \int_{H_{\text{int}}}^{H} \frac{1}{p(y)}dy + \frac{1}{H_{\text{int}}^2}\int_{0}^{H_{\text{int}}} p(y)dy \int_{0}^{H_{\text{int}}} \frac{1}{p(y)}dy \tag{3.97}$$

3.6 Conclusion

Soot is a major contributor to the radiation characteristics of large scale fires, and therefore its generation and transport is of great importance in fire simulations. In this chapter, the mechanisms of soot generation and transport were presented, and the progresses of modelling the phenomena were summarized.

Detailed chemistry models are the most accurate, but they are seldom used in practice due to their high computing expenses and being involved with a great number of species and reactions. Semi-empirical models describe the major processes of soot evolution supplemented with experimental data. Despite a lot of constants required, semi-empirical soot models are widely used in fire simulation because the chemistry of practical fuels is generally unknown. However, the predicted soot field needs to be calibrated under unique experimental conditions in most cases.

Until now it is still not possible to accurately predict the soot emission from different combustion configurations because of the complexity of the chemical processes of soot generation. Yet, these existing soot models and improvements have to be achieved with better understanding on the effect of flame characteristics on soot generation processes. The challenge of modelling soot generation in the future is to generalize any new models for a

wide range of fuel and combustion conditions, especially in turbulent diffusion flame. The new models also should be able to improve the efficacy of prediction.

This chapter provided a comprehensive discussion of soot transport and pointed out intensive development was required to improve the prediction of soot movement. Due to a large majority of soot particles with sizes in the magnitude of nanometres, the soot movement is often modelled as other gaseous species in practice. In real fires, however, the gravitational sedimentation of soot particles makes their behaviours, in particular of large particles with diameter more than 4.5 μm, differ from gases and their motion should be modelled differently with particle characteristics. The next generation of soot transport models should consider the effects of wide size ranges of soot particles on soot particle movement.

Chapter 4

Multi-Particle-Size soot transport model

In Computational Fluid Dynamics (CFD) based fire simulation, the particle-laden soot is usually assumed to be in a gaseous state. This assumption ignores the forces and mechanisms influencing soot particle motion which can lead to severely under-predicted soot levels in the lower layer at remote locations from the fire source. This, in turn, has a significant impact on the assessment of survivability of evacuees and evacuation simulation outcomes when the CFD predictions of fire hazards are used in the evacuation simulations. In this chapter, a soot transport model, namely Multi-Particle-Size model (MPS model), is developed to improve the prediction on soot particle transportation. The MPS model was original proposed in my work [Hu, *et al*., 2011]. This model adopts the drift flux method in considering of the impact of soot mass size distribution on particle settling velocity. Soot particles are divided into several groups by size in this model. Several soot particle grouping strategies are developed with a compromise between computational efficiency and performance accuracy. The performance of this model when different grouping strategies are applied is investigated through the comparison of the predicted movement of soot particles generated from several burnable materials.

4.1 Size distribution of soot particle

Soot is mainly composed of carbon and it varies in structure and size. Generally, the diameter of soot particles produced in fire ranges from 10^{-2} μm to 10 μm [Hertzberg & Blomqvist, 2003], while the smallest soot particle detected can be as small as 20 nm in size [Thomas & Howard, 1992]. Particle size distribution is one of the primary physical properties of soot. The particle size distribution functions can be expressed in a number of different ways. Of them the widely used are the number size distribution and mass size distribution [Chen, *et al.*, 2006; Murakami, *et.al.*,1992].

4.1.1 Number size distribution

The number size distribution is defined as a function of the number of particle (N) against particle diameter (d), usually expressed as $\Delta N / \Delta d$ (or $\Delta N / \Delta \log d$). ΔN is the number of particles per unit volume, with diameter in the size range of a class, while the discrete size range Δd (or $\Delta \log d$) is defined as $\Delta d^i = d^i_{\max} - d^i_{\min}$ (or $\Delta \log d^i = \log d^i_{\max} - \log d^i_{\min}$) for particle class i .

As an example, Figure 4.1 shows the number size distribution of soot produced by a smouldering incense stick, which is reproduced from the work in [Mulholland, 2002]. The size distribution is approximately log-normal. The geometric mean diameter d_{gn} and geometric standard deviation δ_{gn} are the most important characteristics for log-normal distribution as 68.3% of total particles are within the size range $d_{gn} \pm \log_{10} \delta_{gn}$ for this kind of distribution [Holgate, 1989]. In the size distribution plotted in Figure 4.1, the geometric mean diameter of soot d_{gn} is 0.072 μm, and the geometric standard deviation δ_{gn} is 1.75 μm, thus 68.3% of the total particles are within the size range [0.041 μm, 0.126 μm]. For a variety of widely used building materials, the geometric mean diameters are mainly within the range [0.3 μm, 2μm] and the geometric standard deviations are within the range [1.8μm, 2.4μm] [Mulholland, 2002].

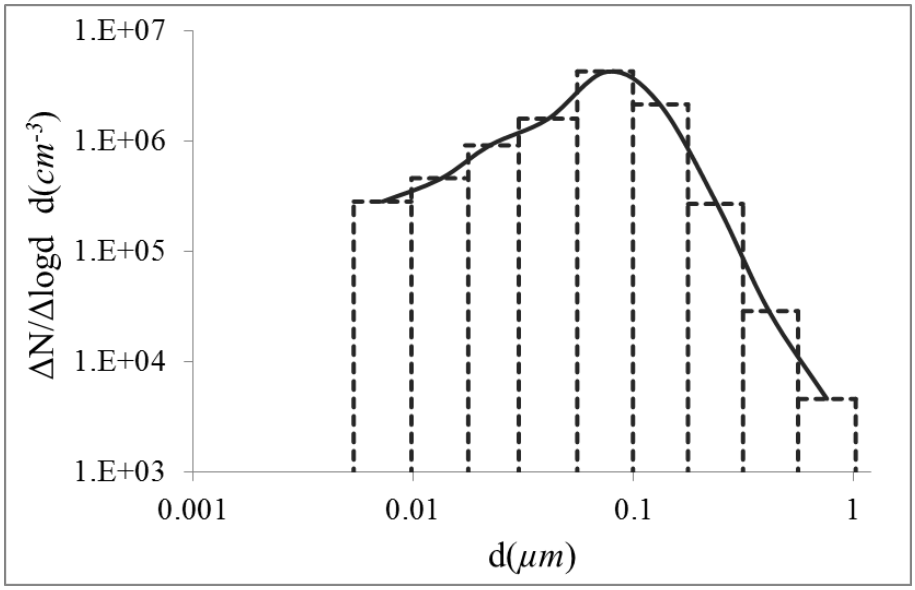

Figure 4.1 The number size distributions of soot generated by smouldering incense stick (reproduced from [Mulholland, 2002]).

4.1.2 Mass size distribution

The mass size distribution is defined as the mass of particles per unit volume, against diameter in the size range of a particle class. The soot particle mass size distributions of a wide range of building materials have been experimentally derived [Hertzberg & Blomqvist, 2003; Mulholland, 2002; Butler & Mulholland, 2004; Rhodes, *et.al.*, 2011]. To facilitate the discussion in Section 4.3, the soot mass fraction distribution instead of mass distribution is represented here. The mass fraction is the ratio of the mass of soot particles of a size class to the total mass of soot particles of all size classes. Figure 4.2 shows the soot mass fraction distribution of some building materials derived from [Hertzberg & Blomqvist, 2003]. Note that although the mass fraction of soot particles smaller than 2 μm accounts for a large proportion, the mass fraction of soot particles larger than 5 μm are more than 5 % for most of the materials.

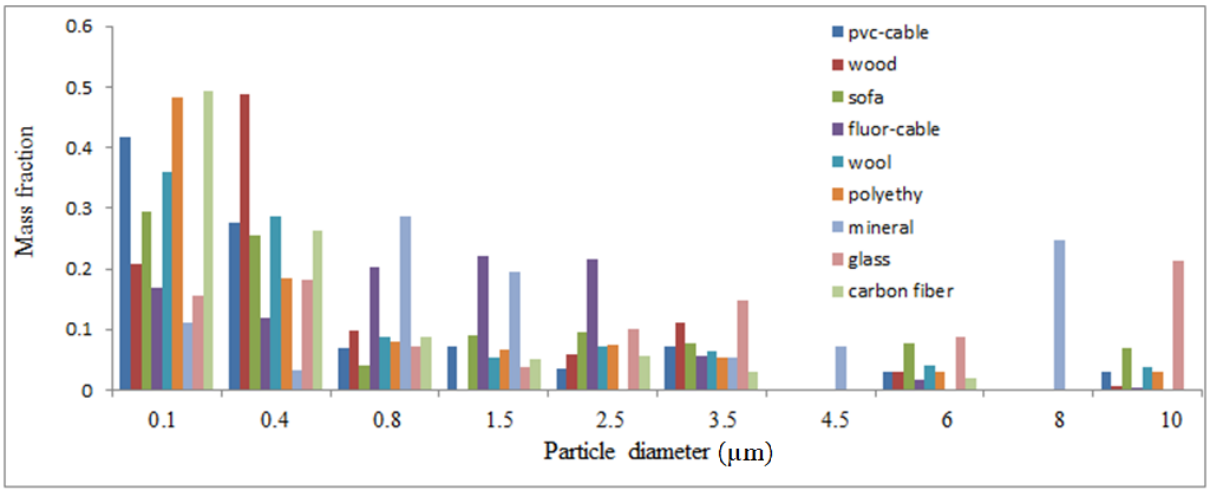

Figure 4.2 Mass fraction against the discrete particle size (reproduced from the work in [Hertzberg & Blomqvist, 2003]).

Soot mass fraction distributions of some combustible materials are shown in Figure 4.3, which is reproduced from the work of Hertzberg and Blomqvist [Hertzberg & Blomqvist, 2003]. For carbon fibre and wood, the majority of soot mass is from small particles. More than 94% soot mass of carbon fibre and 80% soot mass of wood are from particles smaller than 1 μm. Mineral wool and glass wool have a more even soot mass size distribution trend. The mass fractions from particles smaller than 1 μm, between 1 to 5 μm and larger than 5 μm are around 40%, 20%~30% and more than 30% respectively. For soot produced from optical cable and polystyrene, mass fractions from particles larger than 6 μm account for a large proportion (more than 40% for polystyrene and 24% for optical cable respectively).

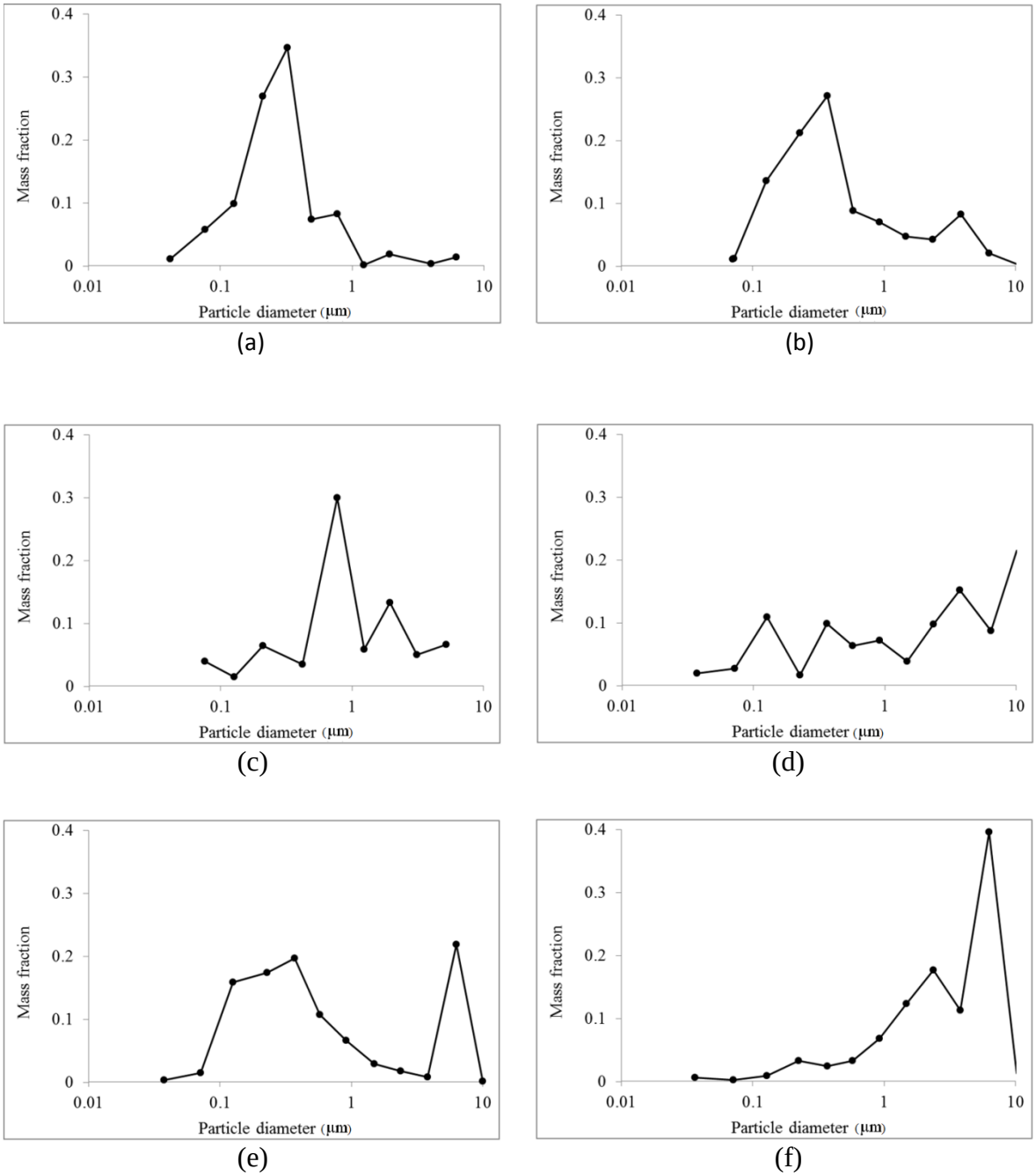

Figure 4.3 Soot mass fraction in terms of soot particles size for (a) carbon fibre, (b) wood, (c) mineral wool, (d) glass wool, (d) optical cable, and (e) polystyrene (reproduced from the work in [Hertzberg & Blomqvist, 2003]).

From the above discussion, it can be seen that the mass fraction of soot particles with size larger than 5 µm accounts for a large portion of the total particle mass for materials like glass wool, polystyrene, etc.. For the soot produced from materials like carbon fibre, although the majority of soot particles are smaller than 1 µm, the mass fraction of particles larger than 5 µm is near 5 %.

4.1.3 Changes in size distribution due to coagulation

Soot particles undergoing Brownian motion collide and stick together. The most important process is known as coagulation which is the process that particle-particle collision, followed by coalescence into a single particle.

The coagulation of soot particles reduces the number of particles and increases the size of particles while the total mass of the soot particles remains unchanged. Theoretically, the change of the soot number can simultaneously cause the change of the soot mass size distribution during the coagulation process. However, this change in a real fire situation is not significant and hence is negligible.

By assuming a size-independent coagulation coefficient Γ_c, Friedlander [Friedlander, 2000] developed an equation to express the rate of change of total number concentration N in coagulation:

$$\frac{dN}{dt} = -\Gamma_c N^2 \tag{4.1}$$

where Γ_c is about 4×10^{-10} cm^3/s for soot produced from incense sticks, 1×10^{-9} cm^3/s for soot from flaming α-cellulose [Mulholland, *et al*., 1977] and 1.5×10^{-9} cm^3/s for soot produced from burning of crude oil [Dobbins, *et al*., 1994].

Integrating Equation (4.1) over time, the total number concentration as a function of time is obtained with an initial total number concentration N_0:

$$N = \frac{N_0}{1+\Gamma_c N_0 t} \tag{4.2}$$

The soot number concentrations released from flames for most combustible materials were measured to be on the order of 10^5 to 10^8 particles/cm^3 [Hertzberg & Blomqvist, 2003]. However, soot concentrations in a fire are being continuously diluted by fresh air while soot particles travel from the region near a fire source to a remote location. The coagulation coefficient also drops significantly with the decreasing temperature [Butler & Mulholland, 2004]. Therefore, the coagulation process does not cause a significant change in the size distribution. Using the coagulation coefficient of 10^{-10}, for example, the change in the number concentration with an initial value 10^6 particles/cm^3 over a 10-second time interval is only 0.1% according to Equation (4.2).

4.2 Settling velocity and drift flux model

The forces exerted on particles cause particles to make movements relative to the fluid streams. The relative velocity between the particle phase and fluid phase, called settling velocity, is considered in the drift flux model by adding an extra drift term in the governing transport equation of the particle phase.

4.2.1 Settling velocity

The forces influencing particle motion can be described as [Zhang, 1998]:

$$\text{Force exerted on particle} = F_G - F_B - F_D \tag{4.3}$$

where F_G is the gravitational force, F_B is the buoyancy force and F_D is the drag force. The calculation of these forces has been discussed in detail in Chapter 3.

The buoyancy force F_B and drag force F_D act in the opposite direction to the gravitational force F_G. Assuming the particle travels in a homogeneous surrounding medium, the drag force increases with the increase of the particle's relative velocity to its surrounding while the gravity and buoyant force exerted on the particle are constants. Thus the acceleration decreases with time and eventually reaches zero. Therefore, there are two stages of particle movement relative to the surrounding: acceleration and then movement at a constant velocity. The constant velocity is also called terminal velocity or free settling velocity [Maxey, 1987]. When the particle reaches the terminal value, the combination of the three forces on the particle is equal to zero:

$$F_G - F_B - F_D = 0 \tag{4.4}$$

The settling velocity has the same direction as the gravity. By substituting equations for calculating the three forces (Equation (3.63), (3.66) and (3.67)) into Equation (4.4), the magnitude of the settling velocity is:

$$|\vec{v}_s| = \left[\frac{2(\rho_p - \rho_f) g V_p}{C_D A_p \rho} \right]^{1/2} \tag{4.5}$$

where ρ_p and ρ_f are density of particle and fluid respectively, C_D is drag coefficient, A_P is the cross-sectional area of the particle and V_P is the volume of the particle. If the particle is a sphere with diameter d_P, then:

$$V_P = \frac{\pi}{6} d_P^{\,3} \tag{4.6}$$

$$A_P = \frac{\pi}{4} d_P^{\,2} \tag{4.7}$$

Substitution of Equation (4.6)-(4.7) into Equation (4.5) gives another form of the magnitude of settling velocity:

$$|\vec{v}_s| = \left[\frac{4g(\rho_p - \rho_f)d_p}{3C_D\rho_f} \right]^{1/2} \tag{4.8}$$

Zhang [1998] proposed a way to calculate the drag coefficient:

$$C_D = 24/\mathrm{Re}_P \qquad \mathrm{Re}_P \le 0.5 \tag{4.9}$$

$$C_D = 26.5/\mathrm{Re}_P \qquad \mathrm{Re}_P \le 800 \tag{4.10}$$

$$C_D = 0.44 \qquad \mathrm{Re}_P \le 200{,}000 \tag{4.11}$$

where Re_P is the particle Reynolds number and is defined in Equation (3.65).

The particle Reynolds number Re_P is usually very small as the size of particles is in the order of 10^{-6} m. Therefore, the drag coefficient for soot particles is calculated from Equation (4.9). Substituting Equation (4.9) into Equation (4.8), the magnitude of settling velocity is

$$|\vec{v}_s| = \frac{g(\rho_p - \rho_f)d_p^{\,2}}{18\mu} \tag{4.12}$$

4.2.2 Drift flux model

The drift flux model [Zhao, *et.al*., 2008] is an Eulerian method which treats both the particles and the fluid as separate continuous phases. The two phases are assumed to be well coupled but particles have a small drift velocity relative to the fluid due to the gravitational settling and diffusion.

The drift flux model integrates the gravitational settling effects of particles into the concentration equation of particles. In this model, the governing equation for particle transport in a turbulent flow field is expressed as:

$$\frac{\partial \rho Y_p}{\partial t} + div(\rho(\vec{U} + \vec{v}_s)Y_p) = div((D_B + \varepsilon_p)\nabla Y_p) + S_Y \quad (4.13)$$

where Y_p is the particle mass fraction, $\vec{v}_s$ is the settling velocity of particles, ε_p is the particle eddy diffusivity and D_B is the Brownian diffusion coefficient. The particle eddy diffusivity ε_p is assumed to equal the fluid turbulent viscosity, v_t, in enclosed fire environments for soot particles [K Lai & Nazaroff, 2000].

Equation (4.13) shows that the drift flux model improves the traditional transport model by adding the drift term $\nabla\vec{v}_s$ into the convection term. There are several assumptions in the drift flux model [Zhao, *et.al*., 2008]:

1) The impact of particles on turbulence is not considered, as the low particle loadings and comparatively small particle settling velocities have a negligible impact compared to the high inflow turbulence levels.
2) The particle number/mass size distributions are not altered by coagulation.
3) The body force due to particle/fluid density difference is neglected.

4.3 Multi-Particle-Size soot transport model

In this section, the methodology of Multi-Particle-Size model is developed by considering the mass size distribution and gravitational settling effect on the movement of soot particles, in order to improve the prediction on soot particle transport. Strategies of grouping soot particles based on their size for the model are derived, with a compromise between computational efficiency and performance accuracy. Then the strategies are tested through examining the movement of soot particles of several materials, of which soot mass distributions are representative among a variety of burnable building materials.

4.3.1 Gravitational settling effect against soot particle size

Most soot particles are sized less than 1 μm and the movement of those particles are similar to that of gaseous fire products [Murakami, *et.al*., 1992]. In most soot transport models, soot is often either ignored, such as the methods using oxygen depletion or temperature to predict soot levels [Isaksson, *et.al*., 1999], or simply treated as being in a gaseous state [Rubini, *et.al*., 2007; Galea, *et.al*., 2008], assuming soot movement in the same manner as the other gaseous

combustion products. However, this simplification sometimes causes under-prediction of the soot levels, especially in the lower layer of an enclosed fire.

Gravitational settling and deposition are the important characteristics that distinguish particles from gases, and besides, both effects become increasingly important as particle size increases [Chen, *et.al.*, 2006]. As discussed in Section 4.1.2, the mass fraction of soot particles larger than 5 μm accounts for a non-negligible proportion of the total soot mass over the spectrum of particle size. Therefore, the settling velocity of large particles should be considered in soot transport simulations, in particular within large enclosures. Murakami [Murakami, *et.al.*, 1992] drew a similar conclusion that the effect of gravitational settling made the behaviour of the particles larger than 4.5 μm differ from the gas phase.

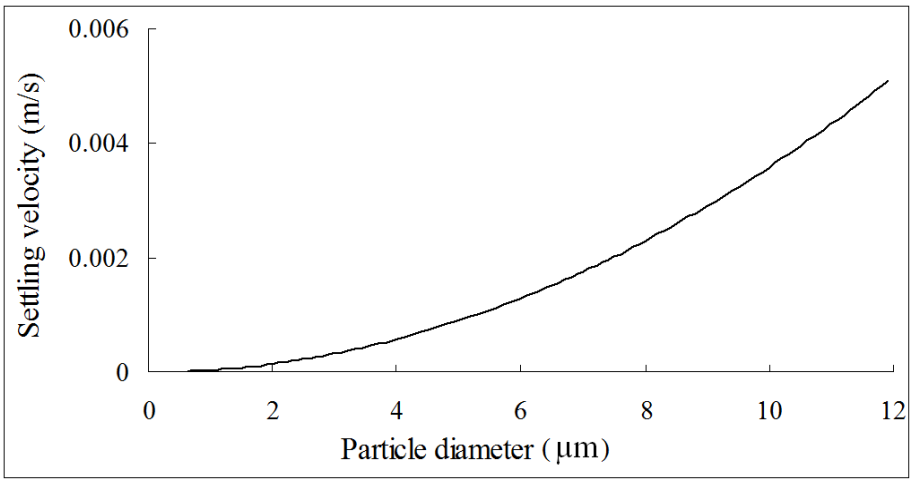

Figure 4.4 Gravitational settling velocity as a function of particle diameter.

Figure 4.4 shows the relationship between settling velocity and particle size derived from Equation (4.8) in air. The gravitational settling velocity increases with the increase of particle size. For particles smaller than 1.5 μm, the settling velocity is smaller than 10^{-5} m/s, which can be ignored compared with the velocity of the air flow within fire enclosures. However, the settling velocity of larger particles cannot be completely ignored. For example, the settling velocities are approximately 10^{-4} m/s for particles sized of 2 μm and 10^{-3} m/s for particles sized of 5 μm respectively. This velocity magnitude is comparable with the velocity in the gravitational direction of gas flow in the remote locations in fire enclosures. At this magnitude of velocity, the accumulative gravitational settling effect over a long period of time can be significant within a large fire enclosure as the residence time of soot particles within the

enclosure can be very long. Therefore, the settling velocities of large soot particles must be considered as they may account for a significant fraction of the total mass of soot particles.

A simple test was carried out in a 2 dimensional chamber to investigate the effect of settling velocity on particle movement. The geometry of the chamber was 30 m (length) × 10 m (height). There were no fans or ventilation in the chamber. A simple heat source with size 30 m×1 m was placed under the ceiling. The heat source released constant heat 10 kW/s and soot 0.0025kg/s for the first 100 seconds. The initial velocity of soot particles was set to be zero and soot density was assumed to be constant with a value of 1800 kg/m^3. The drift flux model was used twice to simulate soot movement with soot particles of two different sizes (1 μm and 10 μm).

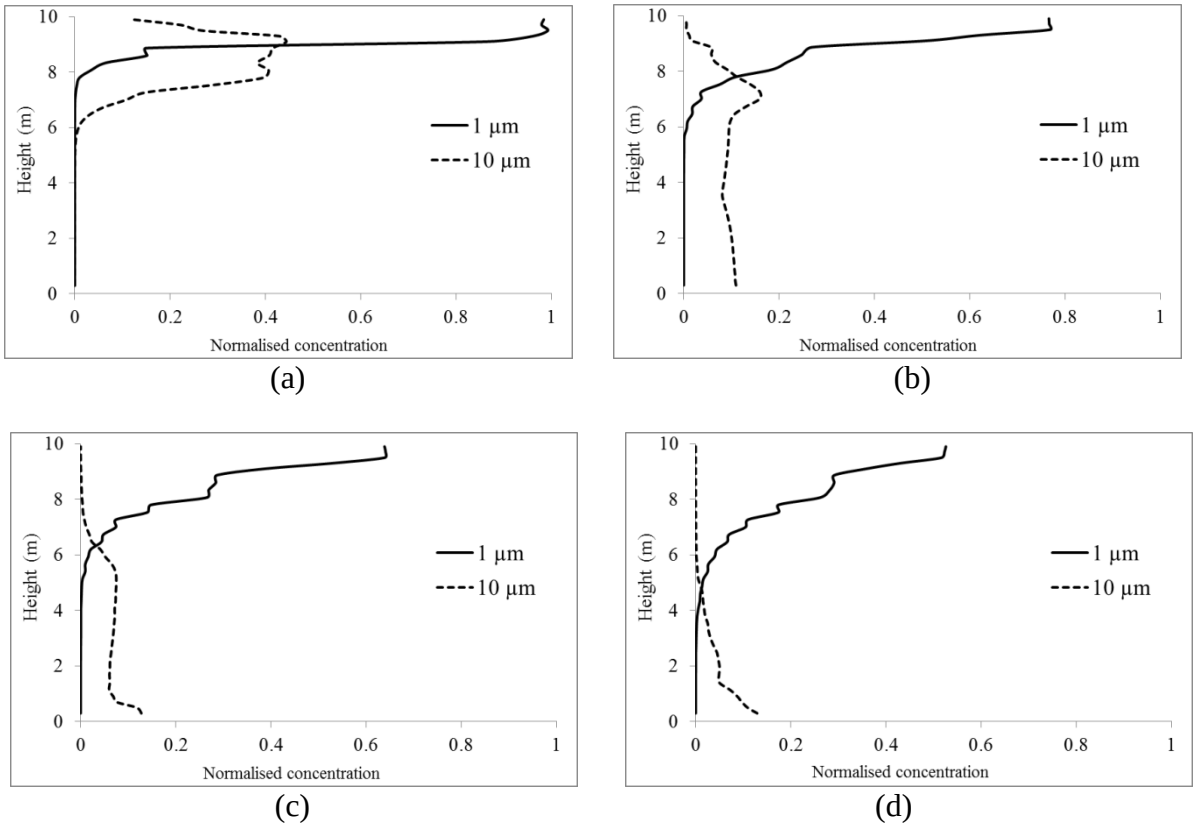

Figure 4.5 The normalised soot concentration along the central vertical line at (a) 180 seconds, (b) 600 seconds, (c) 1200 seconds, and (d) 1800 seconds.

Figure 4.5 shows the normalised soot concentrations along the vertical central line. The concentration of soot was normalised by a maximum concentration of 8.04×10^{-3} kg/m^3 appeared in the chamber. For soot particles sized of 1 μm, the soot particles stayed in the upper layer during the whole simulation. Almost no particles reached the low layer even after 1800 seconds. For soot particles sized of 10 μm, however, most of them travelled downwards

to approximately 8 m height within a short period of time (180 s). These soot particles kept moving towards the floor and most of them deposited on floor after 1800 s. It can be seen the settling velocity plays an important role in soot transport for large soot particles.

4.3.2 Multi-particle-size soot transport model

As reviewed in Section 4.1, the sizes of soot particles mainly vary between 0.01 μm and 10 μm. Such a large variation in particle size makes it difficult to simulate the movement of soot particles as particle size has a significant impact on particle movement. A grouping strategy is required to represent the effect of settling velocity for particles of different size. Therefore, soot particles are divided into several groups according to their mass size distribution. For each group, a representative soot size is used to calculate the settling velocity. The transport of the soot particles for i^{th} group is defined by a governing equation in the form:

$$\frac{\partial \rho Y_{s,i}}{\partial t} + div(\rho(\vec{U} + \vec{v}_{s,i})Y_{s,i}) = div((D_B + \varepsilon_p)\nabla Y_{s,i}) + S_{Y_{s,i}} \tag{4.14}$$

The settling velocity $\vec{v}_{s,i}$ has the same direction as the gravitational force and its magnitude is calculated by Equation (4.8). The calculation of the volume and cross-sectional area of particles in each group in Equation (4.8) are determined by the representative particle size of the particles in the group. Let $Y_{s,i}$ denote the mass fraction of the i^{th} soot group within a control volume. The total soot mass fraction in this control volume, Y_s, is then given by:

$$Y_s = \sum Y_{s,i} \tag{4.15}$$

Based on the particle grouping concept, the Multi-Particle-size model is depicted in Figure 4.6.

With this approach, the criterion for dividing soot particles into groups and the method for determining a representative soot size for each group need to be discussed. The number of soot groups should be determined in consideration of both the particle mass size distribution of the material in question and the variation of settling velocity via particle size. The strategy for grouping soot particles is discussed in the next section.

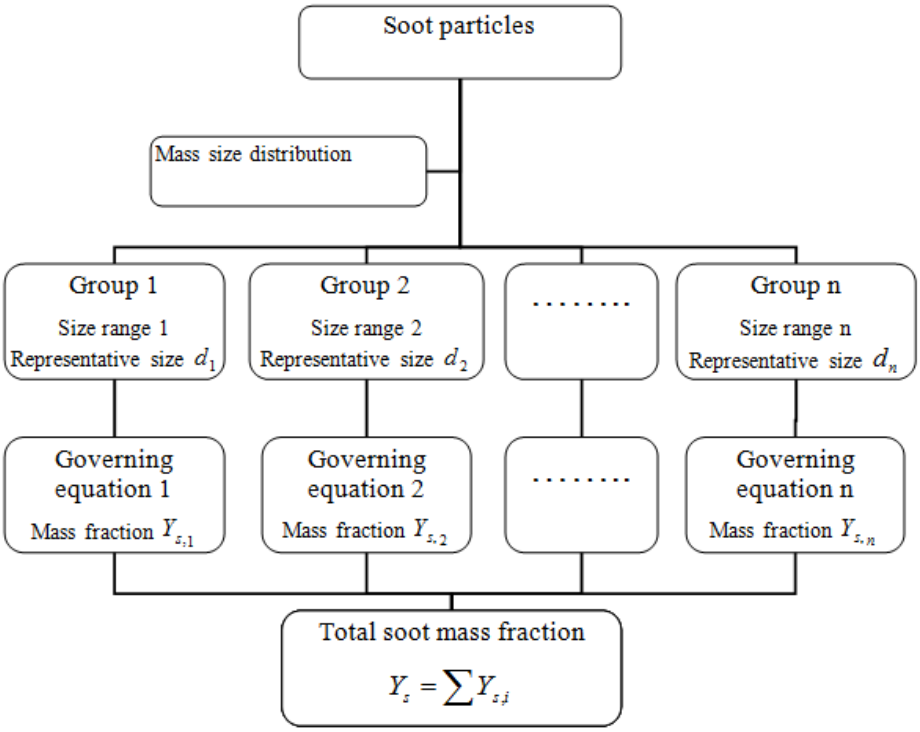

Figure 4.6 The Multi-Particle-Size Model.

This modelling approach was first presented in my publication [Hu, *et al*., 2011]. It was later adopted in the study by Floyd, *et al*.[2014] within the framework of the widely used CFD fire simulation tool FDS.

4.3.3 Soot particle grouping strategy

Although the prediction of soot particle movement by taking into account the settling velocity based on particle size might become more accurate with the increasing group number, a pragmatic consideration is the computational expense. In this section, several soot particle grouping strategies are discussed with consideration of both computational efficiency and performance accuracy.

In experiments, soot particles are collected and assigned into *n* classes according to their size (see Figure 4.2-4.3). The i^{th} class contains soot particles sized within a small range and the representative size for this class is d_i . The sizes for all classes are $d_1, d_2, \cdots, d_n$ ($d_1 > d_2 > \cdots > d_n$) and the corresponding global mass fractions for these classes are $m_1^0, m_2^0, \cdots, m_n^0$ ($\sum_{i=1}^{n} m_i^0 = 1$), which are assumed to be constants as the changes in soot mass size

distribution due to coagulation and so on are ignored. The density of soot particle is assumed to be a constant.

Method 1

The simplest method of grouping soot particles is to assign them into one group (the mass fraction is 1) with a representative size $\bar{d}$ to quantify the effect of gravitational settling on soot movement. The total mass of soot particles in a volume is assumed to be m. The momentum of the representative particles with size $\bar{d}$ should be equal to that of all classes:

$$m\bar{\vec{v}}_s = \sum_{i=1}^{n} (mm_i^0)\vec{v}_{s,i} \tag{4.16}$$

where $\bar{\vec{v}}_s$ and $\vec{v}_{s,i}$ are the settling velocities for soot particles of size $\bar{d}$ and d_i respectively. Substituting of Equation (4.12) into Equation (4.16), we get:

$$\bar{d}^2 = \sum_{i=1}^{n} m_i^0 d_i^2 \tag{4.17}$$

The representative soot size calculated by Equation (4.17) is valid only if the soot mass fractions of all classes in a volume at any instant are the same as the global mass fractions.

Method 2

The assumption of Method 1 cannot be held for a material that has a large variation in soot particle size and mass size distribution. It can be very crude to have one single group to represent all soot particles in this situation. Using settling velocities calculated from several representative sizes to describe the soot movement is a more accurate way. The soot size range and the representative size for each group need to be defined for this method. Two issues need to be considered when dividing soot particles into groups:

- The representative size of the group can describe the gravitational settling effect on soot particles within this group with a reasonable accuracy.
- The way of grouping soot particles should guarantee that the settling velocity calculated from the representative size of the group can be used to quantify the soot momentum of the group in a reasonable accuracy in local volumes.

For the first issue, the representative size of a group is derived in the similar way as Method 1. Assuming soot particle classes with size $d_k, d_{k+1}, \cdots, d_{k+p}$ ($d_k > d_{k+1} > \cdots > d_{k+p}$) and corresponding mass fractions $m_k^0, m_{k+1}^0, \cdots, m_{k+p}^0$ are assigned to one group. The soot momentum of this group equals to the soot momentum calculated from the group representative size.

Then the representative size of the group is calculated in the similar way as in Equation (4.17):

$$\bar{d}_k^{\,2} = \frac{\sum_{j=k}^{k+p} m_j^0 d_j^{\,2}}{\sum_{j=k}^{k+p} m_j^0} \tag{4.18}$$

The settling velocity $\bar{\vec{v}}_{s,k}$ of soot particles with the representative size $\bar{d}_k$ can be calculated by Equation (4.12). According to the Equation (4.18), the representative size is in the range $d_{k+p} \le \bar{d}_k \le d_k$, regardless of the particle mass fraction distribution.

Before addressing the second issue, the characteristic of soot particle transport is discussed first. As the soot particles in a group consisting of a number of particles classes have different settling velocities, these soot particles travel different distances in the same time. Thus the mass fractions of these classes in a small volume are dynamic while the global soot mass fractions are constant. Therefore, the soot particle size $\bar{d}_k$ derived from the global mass fractions might not be an accurate representative in the local volume if the sizes of the particles in this group have a large variation. It is necessary to define some criteria to restrict the size range of the group in order that the settling velocity $\bar{\vec{v}}_{s,k}$ calculated from size $\bar{d}_k$ can be used to quantify the soot momentum of the group in local volumes with a reasonable accuracy. Two criteria are considered here. The first criterion restrict the maximum possible error of under-estimation of the soot momentum by the representative size $\bar{d}_k$. The second criterion is to restrict the variation of the settling velocities in the group.

Our study concerns on the soot movement in the lower layer where soot levels affect the evacuation and damage the respiratory system of occupants. Because there are more large soot particles moving downwards than small soot particles, the soot momentum of a group in the lower layer might be under-estimated by the settling velocity $\bar{\vec{v}}_{s,k}$. As the settling velocities among the group are no more than the largest settling velocity $\vec{v}_{s,k}$, the soot momentum of this group calculated from $\bar{\vec{v}}_{s,k}$ is no more than the momentum which is calculated from the same amount of soot mass and the settling velocity $\vec{v}_{s,k}$. Assume the total soot mass of the group in a volume is m_{gk}.

$$1 \ge \frac{m_{gk}\bar{\vec{v}}_{s,k}}{m_{gk}\vec{v}_{s,k}} = \frac{\bar{\vec{v}}_{s,k}}{\vec{v}_{s,k}} \tag{4.19}$$

Substituting of the settling velocities in the above inequality with Equation (4.12), we have

$$1 \geq \frac{m_{gk}\bar{\vec{v}}_{s,k}}{m_{gk}\vec{v}_{s,k}} = \frac{\bar{\vec{v}}_{s,k}}{\vec{v}_{s,k}} = \frac{\bar{d}_k^2}{d_k^2} \tag{4.20}$$

The above inequality shows that the larger the ratio, $\bar{d}_k^2 / d_k^2$, is, the less possible the momentum of the group is under-estimated in the local volumes in the lower layer if the settling velocity is calculated from the representative size $\bar{d}_k$. Define Cr_1 as follows:

$$Cr_1 = 1 - \frac{\bar{d}_k^2}{d_k^2} < t_1 \tag{4.21}$$

Cr_1 should be smaller than a given tolerance t_1 so that the momentum of the group is not severely under-estimated in the lower layer.

The next criterion is related to the change in the representative size if an additional soot class is merged into the current group. Assuming that soot particles with size $d_k, d_{k+1}, \cdots, d_{k+p}$ ($d_k > d_{k+1} > \cdots > d_{k+p}$) are assigned into one group, and the representative size $\bar{d}_k$ (μm) of the current group is calculated using Equation (4.18). An additional soot class with a smaller size d_q ($d_q < \bar{d}_k$) and mass fraction m_q^0 is merged into the current group. The mass fraction of the newly added soot particle class to that of the whole new group is:

$$m_q^* = \frac{m_q^0}{m_q^0 + \sum_{j=k}^{k+p} m_j^0} \tag{4.22}$$

Then the mass fraction of the original group to the new group is $1 - m_q^*$. The representative size $\bar{d}_k^*$ of the new group is calculated by Equation (4.18) as:

$$\bar{d}_k^{*2} = m_q^* d_q^2 + (1 - m_q^*)\bar{d}_k^2 \tag{4.23}$$

Here another criterion related with the change of the representative size is defined as:

$$Cr_2 = \bar{d}_k - \bar{d}_k^* < t_2 \tag{4.24}$$

where t_2 is a given tolerance. For particles smaller than 5 μm, $Cr_2 \leq 1$ μm is acceptable as the change in the representative settling velocity is less than about 5×10^{-4} m/s. Similarly, for particles smaller than 10 μm and larger than 5 μm, $Cr_2 \leq 0.5$ μm is acceptable.

Criterion 1 (Cr_1) is used to restrict the soot particle size range of a group so that the under-estimation of the soot momentum of the group is always in the acceptable tolerance even if there is a large variation in the settling velocities among the group (usually larger than 10^{-3} m/s). Criterion 2 (Cr_2) is used to restrict the soot particle size range of a group so that there is

no great change in the settling velocity calculated from the representative size if an additional class is merged into the group. Criterion 1 restricts the error estimation of soot momentum if there is a great variation in settling velocities among the group while Criterion 2 avoids a great variation in the settling velocities among the group. Therefore, a class of soot particles is combined with the group if one of the criteria is met. In practice, Criterion 1 is normally applied for particles larger than 5 μm while Criterion 2 is applied for particles size of 1.5 μm to 5 μm.

For soot particles smaller than 1.5 μm, the magnitude of settling velocity is 10^{-5} m/s. The effect of gravitational settling on these particles can be ignored compared with the fluid flow. Thus grouping these small soot particles without considering the above two criteria is reasonable.

Based on the above discussion, a method to group the soot particles is developed and the procedure is outlined as follows:

Step 1: Sort the ungrouped soot particles by size from largest to smallest. This results in soot classes as $d_1, d_2, \cdots, d_n$ ($d_1 > d_2 > \cdots > d_n$) and the corresponding global mass fractions for these classes are $m_1^0, m_2^0, \cdots, m_n^0$ ($\sum_{i=1}^{n} m_i^0 = 1$);

Step 2: Set $k = q = 1$;

Step 3: If d_q<1.5 μm, go to step 6; otherwise, set $S_k = \{d_q\}$ and $\bar{d}_k = d_q$. Set $q = q + 1$. If $q \le n$, go to step 4. Otherwise go to step 7;

Step 4: Add the soot class with size d_q to $S'_k = S_k \cup \{d_q\}$, calculate the criterion Cr_1 (Equation 4.21) and Cr_2 (Equation (4.24) over S'_k.

If (d_q>=5 μm) and (Cr_1<30% or Cr_2<0.5 μm), add the soot class q to group k, i.e., $S_k = S_k \cup \{d_q\}$. Go to step 5;

If (d_q<5 μm) and (Cr_1<30% or Cr_2<1 μm), add the soot class q to group k, i.e., $S_k = S_k \cup \{d_q\}$. Go to step 5;

Otherwise, set k = k + 1, go to step 3;

Step 5: Calculate the representative size of S_k by Equation (4.18). Set $q = q + 1$; go to step 4;

Step 6: Combine all the remaining classes into one group as S_k and calculate the representative size by Equation (4.18).

Step 7: Stop.

Method 3

Method 2 is developed to divide the soot particles into several groups with the principle of a reasonably accurate representation of the group soot momentum. However, this method does not consider the computation cost, which can be high if a large number of groups are produced. To limit the number of groups and hence reduce the potential computational cost, a simple way is to merge some groups. Thus one issue needs to be considered: which groups are selected to be merged.

For most combustible materials, the mass fraction of soot particles smaller than 1.5 μm is usually very large (see Figure 4.2). Among the soot groups produced by Method 2 for the combustible materials studied in [Hertzberg & Blomqvist, 2003], the mass fractions of larger particles, especially for particles larger than 5μm, are very small for some materials. For example, after grouping soot particles produced from wood by Method 2, the mass fraction for soot groups with soot particles larger than 7 μm is only 0.39%, and the mass fraction for soot groups with particles sized between 4μm and 7 μm is 2.1%. Combining these soot groups with small mass fractions with other groups is a reasonable way to reduce the number of soot groups.

Suppose there are two groups produced by Method 2. The mass fractions and representative sizes for the two groups are $m_{g1}, \bar{d}_{g1,}$ and $m_{g2}, \bar{d}_{g2,}$ respectively. If the two groups are merged into one new group, the mass fraction m_{gn} for the new group is

$$m_{gn} = m_{g1} + m_{g2} \tag{4.25}$$

As the soot momentum of the new group equals to the sum of the soot momentums of the two groups, the representative size can be calculated in similar way as Equation (4.18):

$$\bar{d}^2_{s,gn} = \frac{m_{g1}\bar{d}^2_{s,g1} + m_{g2}\bar{d}^2_{s,g2}}{m_{gn}} \tag{4.26}$$

Based on the above discussion, a strategy to reduce the number of soot groups is developed. First, the soot particles are grouped by Method 2, and then the groups are sorted in the order of the representative size from largest to smallest. If the number of soot groups is over 3, it is suggested that:

- If a group with large soot particles (representative size > 5μm) has a small mass fraction (<0.05), the group is combined with next group which has a smaller

representative size. The representative size of the new group is calculated by Equation (4.26).

- If a group with the representative soot particle smaller than 5 μm has a mass fraction <0.1, the group is combined with the next group which has a smaller representative size. The representative size of the new group is calculated by Equation (4.26).

Method 2 normally divides the soot particles produced from the combustible materials studied in [Hertzberg & Blomqvist, 2003] into 3 to 4 groups, only a few of them into 5 to 6 groups. With the above strategy, the soot particles from all of these materials are divided into 3 groups. In practice, the computational cost is acceptable if the number of groups is no more than 3.

4.3.4 Performance of the grouping strategies

The strategies to group soot particles have been discussed in Section 4.3.3. In order to examine the performance of these grouping strategies, soot transport in the chamber (the same as section 4.3.1) for six building materials (listed in Figure 4.3) has been simulated.

Four simulations for each material were carried out with different grouping strategies. First, the original soot group division (10 to 13 groups) was used. Then the soot groups derived by Method 1 to Method 3 were applied respectively. The predicted soot concentrations along the vertical central line at different times were compared with the results of the original groups in order to examine the reliability and accuracy of the three soot grouping strategies.

The soot groups and their representative sizes are listed in Table 4.1. The materials were chosen from the materials shown in Figure 4.3. Carbon fibre and wood have similar soot mass size distributions, of which mass fraction of small soot particles (smaller than 2 μm) accounts for around 90%. Glass wool and mineral wool have more even soot mass size distributions. For soot produced from polystyrene and optical cable, the mass fraction of particles larger than 6 μm accounts for a large proportion.

Table 4.1 The soot groups derived from Method 1, Method 2 and Method 3 for six representative materials

Materials	Method 1		Method 2		Method 3	
	Representative size(μm)	Mass fraction	Representative size(μm)	Mass fraction	Representative size(μm)	Mass fraction
carbon fibre	2.1838	1	7.1944	0.0385	7.1944	0.0385
			1.2054	0.0207	1.2054	0.0207
			0.3236	0.9408	0.3236	0.9408
Wood	2.9188	1	10.1499	0.0039	7.013	0.0249
			6.2597	0.0210		
			2.9974	0.1734	2.9974	0.1734
			0.3566	0.8017	0.3566	0.8017
Mineral wool	4.3443	1	7.1576	0.3531	7.1576	0.3531
			1.7604	0.1927	1.7604	0.1927
			0.4231	0.4542	0.4231	0.4542
Glass wool	5.3152	1	9.1658	0.3026	9.1658	0.3026
			3.0733	0.2895	3.0733	0.2895
			0.2938	0.4079	0.2938	0.4079
Optical cable	3.0563	1	10.000	0.002	6.0872	0.2469
			6.0448	0.2449		
			0.8757	0.2039	0.8757	0.2039
			0.1199	0.5422	0.1199	0.5422
Polystyrene	4.4617	1	10.1517	0.01347	10.1517	0.01347
			5.1463	0.6863	5.1463	0.6863
			0.6169	0.3022	0.6169	0.3022

Figure 4.7 shows the normalised soot concentration along the vertical central line at 180 seconds. The soot concentrations were normalised by the maximum value 8.04×10^{-3} kg/m^3. The normalised soot concentrations near the ceiling for all the materials reduced slightly along the vertical direction in a short period of time (see Figure 4.7).

The predictions from the three grouping methods show good agreement with that from the original soot group division. The results of Method 1 slightly over-predicted the soot dropping movement of wood, mineral wool and glass wool and slightly under-predicted the soot dropping movement of polystyrene at a few locations. The reason is that the settling velocity calculated from a single representative size for soot particles is not sufficiently accurate to

describe the behaviour of soot particles with a large variation in size. Using one single representative size might over-predict the settling velocities for small particles and under-predict the settling velocities for large particles. As the majority of soot particles produced from wood, mineral wool and glass wool are much smaller than the representative soot particle, these soot particles drop more slowly than the representative soot particle. So the concentrations near the ceiling predicted by Method 1 are lower than the predictions by all groups for these materials.

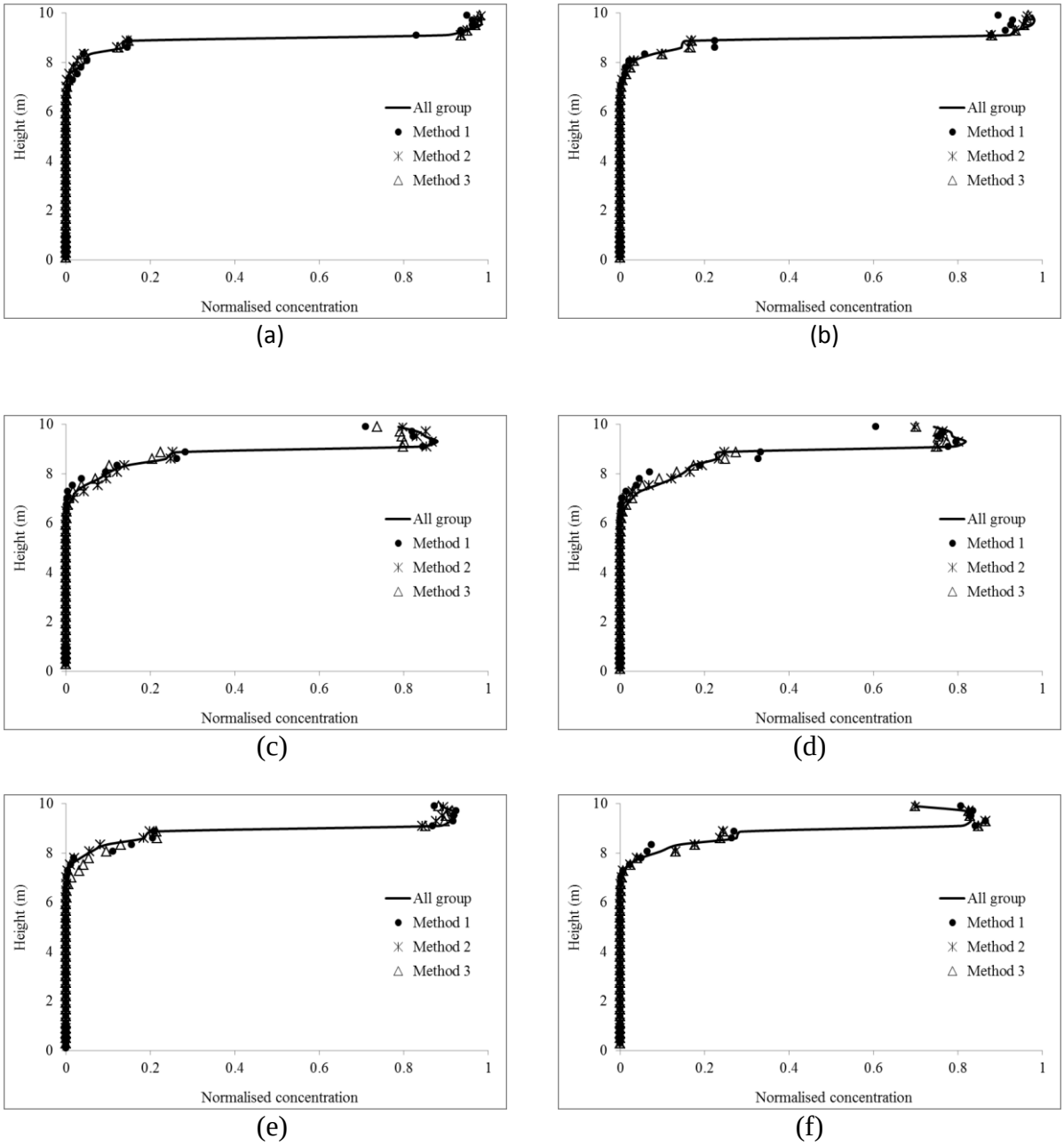

Figure 4.7 Predicted normalised soot concentration along the vertical line at 180 seconds with different particle group divisions for (a) carbon fibre, (b) wood, (c) mineral wool, (d) glass wool, (e) optical cable, and (f) polystyrene.

Figure 4.8 shows the normalised soot concentrations of the six materials along the vertical central line at 600 seconds. After soot particles travelled for 600 seconds, the concentrations near the ceiling decreasd and the concentrations at 6-8 m height increased for all materials. However, the change in soot concentrations differs from one material to another due to the different mass size distributions. The normalised soot concentrations of carbon fibre and wood decreased only by around 20% because more than 80% of the soot mass comes from particles smaller than 1 μm. However, the soot concentrations near the ceiling decreased to around 50% for the mineral wool, glass wool and polystyrene, of which mass fractions of soot particle smaller than 1 μm are less than 45%. For these three materials, a great proportion of soot particles transported to the height of 6-8 m and some even reached the floor.

The concentrations predicted by Method 2 and Method 3 are very close to that predicted by all groups for the first five materials. For polystyrene, the predicted normalised concentration at 0.01 m below the ceiling was under-predicted by 18% compared with the prediction by all groups. The reason might be the majority of soot particles in the third group (size in the range of 0-1 μm) are smaller than the representative size (0.6169 μm). Thus these small soot particles (much smaller than 0.6169 μm), which should stay close to the ceiling, were predicted to fall downwards at a velocity higher than it should be.

For Method 1, the predictions of mineral wool and glass wool are very poor. As these two materials have relatively even soot mass distributions, one representative soot size is not sufficiently accurate to describe the settling velocities for all sizes. A single representative size causes over-estimation of settling velocity for small soot particles and under-estimation of settling velocity for large soot particles. Therefore, more soot particles were predicted to move from the ceiling to the height of 6-8 m and less soot particles were predicted to reach the lower layer compared with the predictions from all groups.

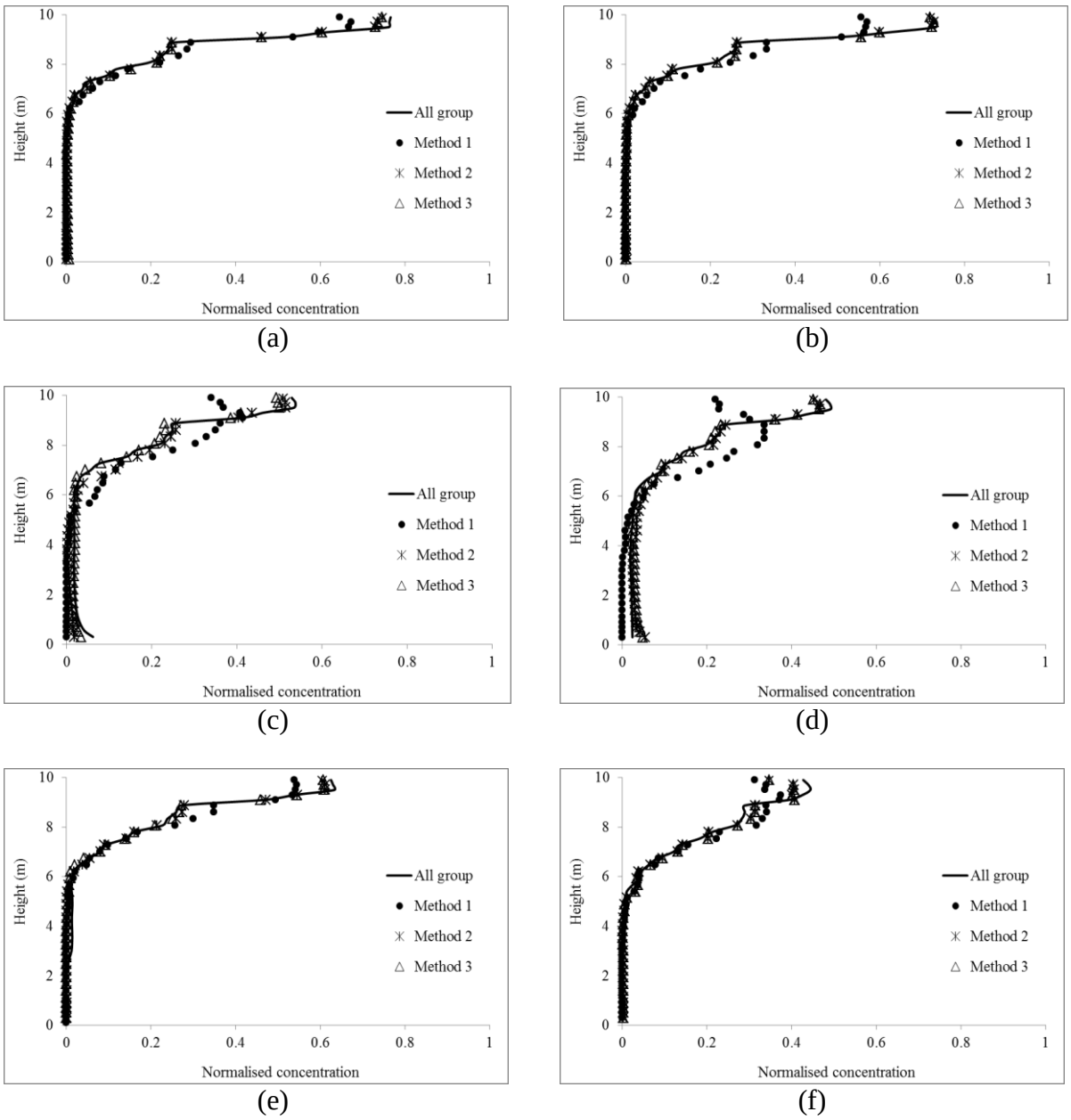

Figure 4.8 Predicted normalised soot concentration along the central vertical line at 600 seconds with different particle group divisions for (a) carbon fibre, (b) wood, (c) mineral wool, (d) glass wool, (e) optical cable, and (f) polystyrene.

Figure 4.9 shows the normalised soot concentration of the six materials at 1200 seconds at the central vertical line. The normalised concentrations near the ceiling decreased further and the concentrations near the floor increased further compared with the normalised concentrations at 600 seconds. The tendency appears more clearly for polystyrene because the mass proportion of soot particles smaller than 1 μm for polystyrene is small (17 %). The larger soot particles all dropped away from the ceiling after 1200 seconds. The increases of soot concentration near the floor are very clear for the last four materials, because the mass of soot particles larger than 6 μm accounts for large proportions for these materials.

Again the predicted soot concentrations by Method 2 and Method 3 are in good agreement with those predicted by all groups, but it is not the case for Method 1. After a long period of time, the deviations between the predictions by Method 1 and by all groups become significant.

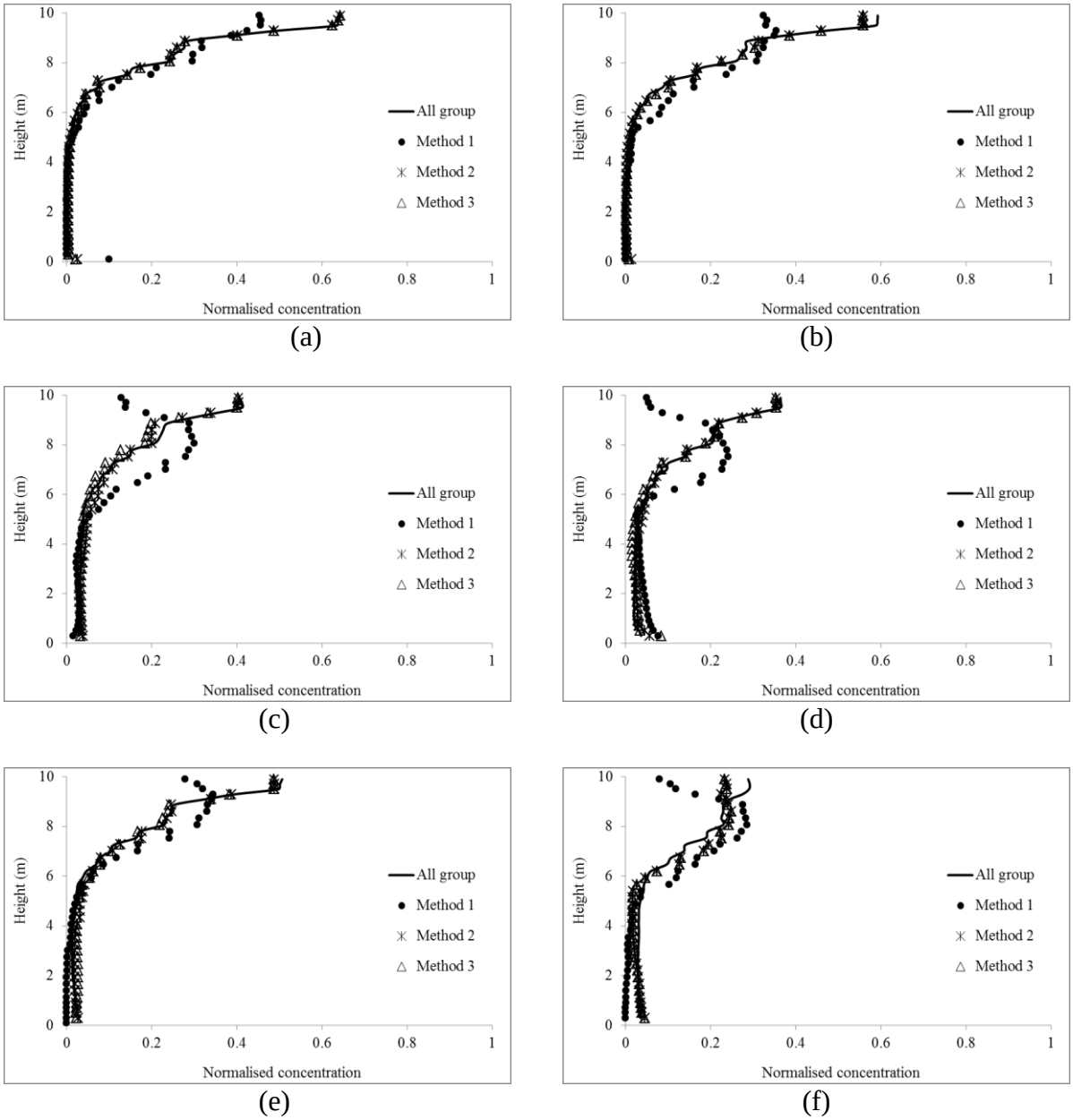

Figure 4.9 Predicted normalised soot concentration along vertical line at 1200 seconds with different particle group divisions for (a) carbon fibre, (b) wood, (c) mineral wool, (d) glass wool, (e) optical cable, and (f) polystyrene.

Figure 4.10 shows the normalised soot concentration of the six materials at 1800 seconds at the central vertical line. It shows the majority of soot particles of carbon fibre and wood would remain near the ceiling even after a very long period of time. The reason is that a large

proportion (96% of carbon fibre, 89% of wood respectively) of the soot mass fraction are from small soot particles (smaller than 2 μm), of which settling velocity is less than 2×10^{-4} m/s. Even after 1800 seconds, these soot particles travelled less than 1 m. In contrast, significant proportions of soot particles larger than 6 μm (24% of mineral, 30% of glass wool, 24% of optical cable and 42% of polystyrene respectively) travelled downwards to the lower layer with settling velocity higher than 2×10^{-3} m/s, and some of soot particles even reached the floor.

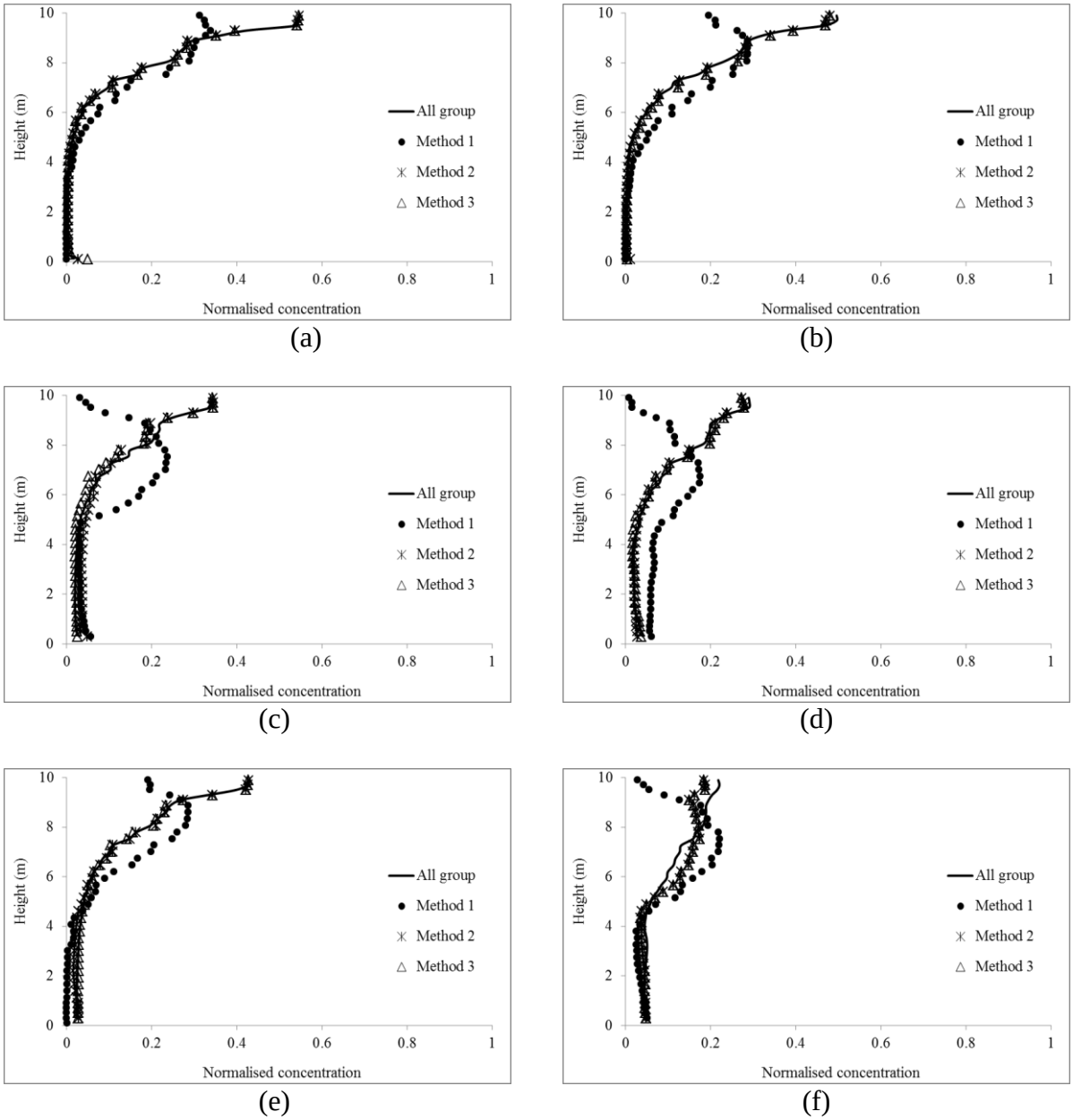

Figure 4.10 Predicted normalised soot concentration along the central vertical line at 1800 seconds with different particle group divisions for (a) carbon fibre, (b) wood, (c) mineral wool, (d) glass wool, (e) optical cable, and (f) polystyrene.

Figures 4.7-4.10 examine the capabilities of the three soot particle grouping methods in predicting soot particles movements. The predictions derived from Method 2 and Method 3 match reasonably well with the prediction from the original soot particle groups. However, Method 1 failed to correctly describe the settling velocities for soot particles, especially after 180 seconds.

These figures also demonstrate that the gravitational settling plays a significant role in the soot movement even for those materials which produce a large proportion of very small soot particles. The downward travelling phenomenon of small soot particles is not very noticeable within a short period of time, but the accumulative effect over a long period of time is still significant.

4.3.5 Group divisions for some combustible materials

The previous section shows that Method 2 and Method 3 both can be used to classify soot particles with a reasonable accuracy in the prediction of soot movemtn. Compared with Method 2, Method 3 can be more computationally efficient as the method also tries to reduce the grouping numbers as few as possible. Table 4.2 presents the representative sizes of soot particle groups and their corresponding soot mass fractions produced by Method 3 for a number of combustible materials.

Table 4.2 Soot representative sizes and its mass fractions derived by Method 3

Material	Representative size(μm)			Mass fraction		
	$\bar{d}_1$	$\bar{d}_2$	$\bar{d}_3$	m_1	m_2	m_3
Carbon fiber	7.1944	1.2054	0.3236	0.0385	0.0207	0.9408
Glass wool	9.1658	3.0733	0.2938	0.3026	0.2895	0.4079
Mineral wool	7.1576	1.7604	0.4231	0.3531	0.1927	0.4542
Polyethylene-cable	8.4415	1.2387	0.2373	0.1635	0.1392	0.6973
Polystyrene	10.1517	5.1463	0.6169	0.01347	0.6863	0.3022
PVC	9.3053	2.3703	0.3949	0.0168	0.1013	0.8819
Sofa(Room Corner)	10.1498	2.6468	0.3050	0.1459	0.2643	0.5898
Wood	7.0130	2.9974	0.3566	0.0249	0.1734	0.8017
Wool	8.1233	2.7345	0.3594	0.082	0.1884	0.7314
Bitumen	8.7325	1.5680	0.3112	0.09855	0.2167	0.6848
Fluoropolymer-cable	7.1240	1.1269	0.2547	0.0682	0.5409	0.2949
Fluoropolymer	9.3365	2.4816	0.3758	0.0294	0.0486	0.9220
FR 4	8.960	2.4270	0.5024	0.0368	0.1938	0.7694
Hard board	9.0354	2.2382	0.2938	0.020	0.0987	0.8813
Melamine	7.8010	1.9044	0.3212	0.3095	0.3173	0.4394
Nitrile rubber	9.5060	2.5407	0.3759	0.0276	0.0450	0.9274
Optical cable	6.0872	0.8757	0.1199	0.2469	0.2039	0.5422
PUR	9.2763	2.7938	0.3639	0.0510	0.1929	0.7561
PVC+fluoropolymer cables	9.0138	2.5854	0.3656	0.0398	0.1649	0.7953
PVC-cable	8.4415	1.2387	0.2373	0.1635	0.1392	0.6973

4.4 Conclusion

This chapter presents the first original contribution in the dissertation and address objectives 1(a) and 1(b). The Multi-Particle-Size model is an improvement to the drift flux model by considering the uneven mass size distribution of soot particles and the gravitational settling. The drift flux model can be deemed as a particular case of the Multi-Particle-Size model with just one single size group of particles. In the Multi-Particle-Size model, the soot particles are divided into several groups with various size ranges. The transport of soot particles in each group is represented by a governing equation, in which the gravitational settling effect is addressed by adding a correction into the convection term.

Although the prediction of soot concentration may become more accurate with a large group division number, the computational cost can be high. Strategies for better grouping soot particles are developed based on cost-benefit balance between the prediction accuracy and the computational power required. Method 1 assigns all soot particles into one group and the representative soot size is calculated by the conservation of soot momentum. Method 2 divides soot particles into several groups with a guarantee that the settling velocity calculated from the representative soot size can be used to quantify the momentum of the group in local volumes with a reasonable accuracy. Method 3 is developed based on Method 2 by reducing the group number to an acceptable value without remarkably lowering the prediction accuracy.

In order to examine the performance of these grouping strategies, the soot particle movement in a big chamber produced from six materials was simulated with these three strategies. The predicted soot concentrations in a central vertical line by the three methods were compared with those predicted by the original soot particle groups (10-13 groups). Results shows Method 1 failed to produce reasonable predictions on soot concentration, especially after some times (after 600 s). However, the predictions made by Method 2 and Method 3 are in good agreement with those from the original soot particle groups for the whole simulation time (up to 1800 seconds).

The Multi-Particle-Size soot model will be applied to simulate soot movement in full-scale fire tests in Chapters 5 and 6.

Chapter 5
Simulating soot transport in Large-scale enclosure fires

In this chapter, soot movements in two large-scale corridor fires are simulated with the Multi-Particle-Size soot model developed in Chapter 4 and the Conventional soot model. The predicted soot levels within the large enclosure of the fire tests are compared with measured values and observed soot (smoke) movement phenomena in detail.

5.1 Fire Experiment

Fire statistics suggests that the most commonly identified cause of death during fire incidents is being overcome by soot and toxic gases[Chowdhury *et.al.*, 2013]. For life safety assessment it is important to accurately predict soot levels within compartment fires. However, most of the existing soot models under-predict soot levels in the lower layer at remote locations from the fire source by simply assuming soot as being in a gaseous state. This simplification to the particulate nature of soot is reasonable in regions near the fire source where the gravitational settling of soot particles can be ignored compared with the strong momentum of the flow. At remote regions from the fire source, however, the flow momentum decays and the gravitational settling become important. Thus the treatment of soot as gas can result in poor predictions of soot levels at remote locations in fire scenarios. The Multi-Particle-Size soot model was developed in the last chapter to address this weakness. In this study the efficiency of the model is examined by simulating two large scale enclosure fires.

A series of large-scale cable fire tests in a full scale corridor were conducted by the Department of Fire Technology at SP Swedish National Testing and Research Institute with assistance from Fire Safety Engineering Group, the University of Greenwich in 2006 [Persson, 2006; Mahalingam, 2007; Mahalingam *et.al.*, 2007]. Two of the tests were selected here to validate the Multi-Particle-Size soot model . The cables burnt in the two tests were PVC cable and polyethylene (PE) cable respectively.

5.1.1 Corridor layout

The tests were conducted indoors in a large fire test hall with dimensions of 18 × 22 × 20 m^3. Inside the hall, a U-shaped corridor with a total length of 44.6 m (centreline) was constructed. There were one inlet and one exit at the start and end of the corridor (see Figure 5.1). The nominal inner height of the corridor was 2.4 m and the nominal inner width was 2.0 m. At the inner corner, between the Middle and the Inlet Corridor, a room with size of 3.0 m ×4.0 m was connected to the corridor through a 2 × 0.4 m^2 opening at ceiling level.

Four soffits were installed by extending 0.4 m from the ceiling at positions as shown as red lines in Figure 5.1. In the Exit Corridor, an exit was positioned below a calorimeter system making it possible to measure the heat release rate and collect soot. In order to obtain a restricted air flow, some tests were performed with the inlet closed and a 1.00 m weir was also built up from the floor, below soffit 2.

The wall of the corridor and the ceiling of the room were covered with 10 mm Promatect-H, non-combustible boards. The ceiling of the corridor was covered with a 6 mm Masterboard, non-combustible board. To reinforce the wall and ceiling which were close to the fire source, extra 10 mm Pormatect-H board with 2.4 m height were used in 1.2 m width of the wall behind the cable tray. The 2-metre-wide ceiling close to the fire source was reinforced with extra pormatech-H board. The first 2 m section of the ceiling in the Inlet Corridor was constructed of 10 mm board, followed by a 3 m section with 30 mm board, then the remainder with 10 mm board. The properties of those materials are given in detail in Table 5.1.

Table 5.1 The properties of non-combustible boards [Persson, 2006]

	Promatek H	**Masterboard**
Density (kg/m^3)	870	1100
Thermal conductivity (W/m ^oC)	0.188 (250^oC)	0.13(dry condition)
Specific heat capacity (kJ/kg ^oC)	1.13	---

There were two ventilation arrangements used for the tests. One arrangement designated an inlet opening of 1.0 m^2 (1 ×1 m^2) at the corridor gable upstream from the fire. In the other arrangement, the inlet opening was completely closed and a 1.0 m high weir was installed

from the floor, below soffit #2. The exit door with size 1 ×2.4 m^2 was positioned at floor level at the end of corridor for all tests (Figure 5.1).

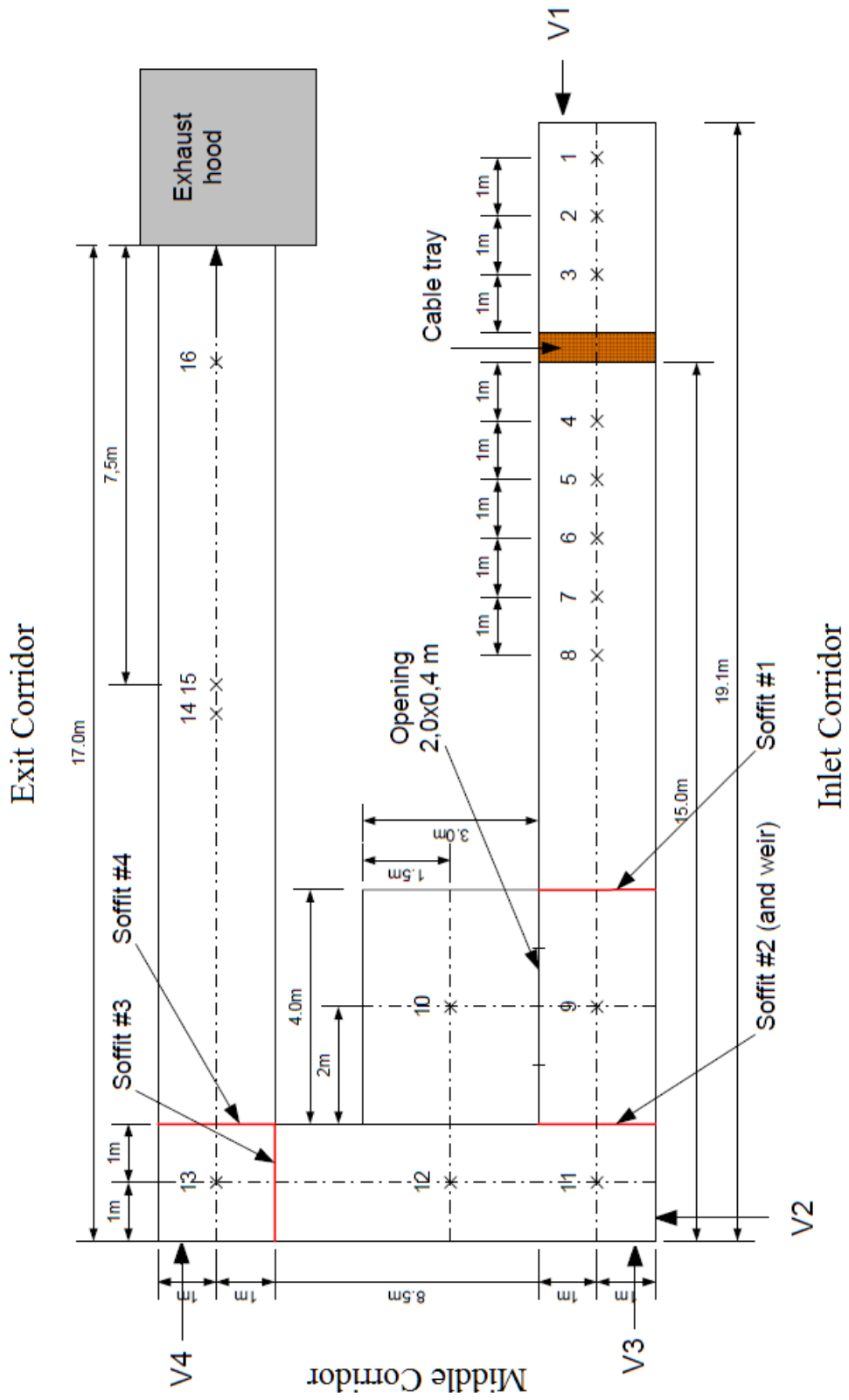

Figure 5.1 General layout of the test corridor (reproduced from [Persson, 2006]).

5.1.2 Fire source

The fire source consisted of a L-shaped cable tray arrangement as shown in Figure 5.2. the cable tray had one vertical (1.95 m) section and one horizontal (1.8 m) section (see Figure 5.2 (b)). The fire source was located at a distance of 3.9 m from the inlet. The vertical cable tray section was 0.25 m above from the floor and 0.06 m from the corridor wall in the Inlet Corridor. The horizontal tray was located nominally 0.15 m from the ceiling. In order to expose the lower part of the cables to the ignition source, the cover plate at the bottom of the vertical tray was cut by 0.2 m (see Figure 5.2 (a)).

(a) (b)

Figure 5.2 (a) Cable tray before being mounted in the corridor (b) Both vertical and horizontal cable tray engulfed in flames [Persson, 2006].

The cable tray was ignited by a propane sand burner with size 0.1 × 0.4 × 0.1 m^3. The burner had a heat output of approximately 30 kW and lasted for 30 minutes. The top of the gas burner was located 0.195 m above the floor and 0.06 m from the wall. The burners in the two tests were ignited 3 minutes after the start of switching on the system for gas sampling.

There were a total of 10 experiments (three different cables with or without weir on the floor, and closed or open inlet) conducted and two of them were selected to be simulated because there was a great amount of soot released during the two fire tests.

Table 5.2 Summary of the two fire tests

	Test Ⅰ	**Test Ⅱ**
Test no. in [Person, 2006]	Test no. 5	Test no. 8
Type of cable	NYM	NHMH
bedding of cable	PVC	Chalk filled polyethylene (PE)
Corridor ventilation	Inlet closed +1m weir	Inlet ($1m^2$) opening + 1m weir

In Test II, it was noticed that plastics were dropping down to the floor from the horizontal tray during the test which were not fully combusted at the time of the weight loss (see Figure 5.3 (a)). The amount of dripping plastic that was not weighted in the test might be significant compared to the total recorded mass loss . However, in another test with the same kind of cable, the remaining plastic on the floor was measured after the test to be about 23% of the total mass loss.

(a) **(b)**

Figure 5.3 (a) melted, burning plastics starts to drip down to the floor, (b) residual of plastic on the floor after the test [Person, 2006].

5.1.3 Measurements and recordings

In order to record the fire development and the generation and transport of fire gases, extensive measurements were made along the corridor during each test.

Temperatures were measured at 27 positions in total. Thermocouples were mounted at 1.0m and 2.2m above floor for position 2, 5, 7, 9, 10, 12, 15, 16 in Figure 5.1 and additional thermocouples were mounted at 0.5 m, 1.5 m and 2.0 m for position 2, 5 and 7 in Figure 5.1.

The soot obscuration across the corridor was measured at a total of six positions at 2.2 m above the floor at positions no. 6, 9 and 10 (inside the corner room), and at 2.0 m above the floor at positions no. 12, 13 and 15 (see Figure 5.1 for the positions). In these positions, lasers were mounted on one side of the corridor wall and detectors were mounted on the opposite wall, giving a beam length of 2.0 m. Four video cameras (V1-V4) (see Figure. 5.1 for positions) were placed outside the corridor and faced into the corridor through glass to record the soot movement. They were positioned about 0.5 m above the floor except for Camera V3 which was placed 1.3 m above the floor. In order to clearly see the soot filling, reflective markings were mounted on poles along the corridor wall at position 6, 9, 12, 13 and 15 and two lights were located on the floor in the Exit Corridor.

An exhaust/calorimeter system was located at the corridor exit to measure the combustion gases, which were used to calculate the total heat release rate. The mass loss of the burning cables was measured by positioning the entire cable tray arrangement on a load cell platform. In Test II, the melting and dripping plastic on the floor caused inaccuracy in calculating the effective heat of combustion with the measured mass loss.

5.2 Numerical details

5.2.1 Heat release rate

The eddy dissipation combustion model (EDM) was used to simulate the burning of the combustible gases released from the ignited materials. The cable used in Test Ⅰ was made of PVC material which contained pure PVC, plasticizer and chalk. The cable in Test Ⅱ was NHMH, the main part of which was polyethylene (PE). In the simulations, the average heat of combustion was 9.66 MJ/kg in Test I and 21 MJ/kg in Test Ⅱ respectively, which were derived from the measured fuel loss rate and heat release rate. The mass loss rate curves for both the tests derived from the measured load cell data are given in Figure 5.4. But there were some visible plastic dripping in Test Ⅱ. As the amount of unburned plastic was not measured in the test II and there was 23% plastic measured to have been dripped on the floor in another test with the same kind of cable, the mass loss rate was multiplied by a factor 0.77 in Test II [Mahalingam, 2007]. A multi-ray radiation model was used to simulate radiative exchange.

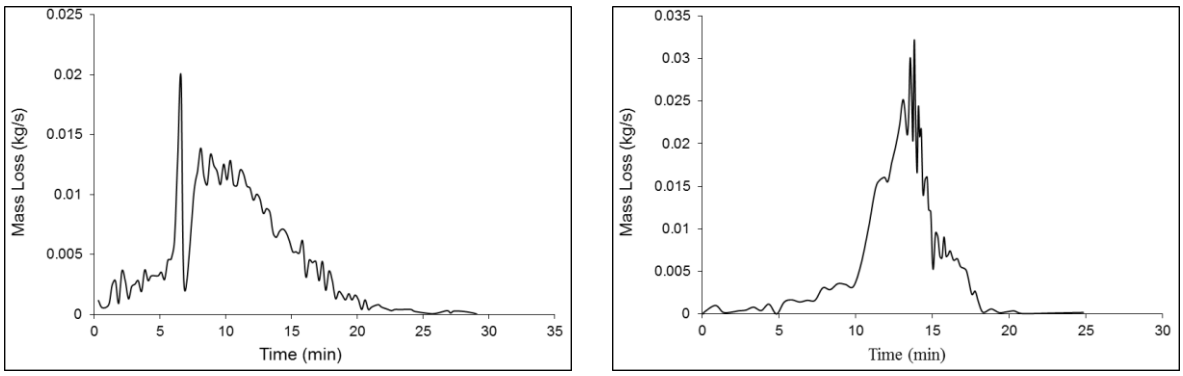

(a) (b)

Figure 5.4 The mass loss rate for (a) Test I and (b) Test II.

5.2.2 Mesh sensitivity analysis

A non-uniform Cartesian mesh consisting of 132,411 cells was used in the discretization of the geometry. The mesh was finer in the flame region with size 10 cm and gradually changed to coarser with a maximum size around 30 cm. For mesh sensitivity analysis, a finer mesh consisting of 573,000 cells was also created. The variation of the predicted peak temperatures at position 5 in Test Ⅰ with the two meshes is less than 1.7% (see Figure 5.5), thus it is reasonable to assume that the mesh consisting of 132,411 cells is adequate for producing mesh independent simulation results. The following discussed results are therefore of the coarser mesh.

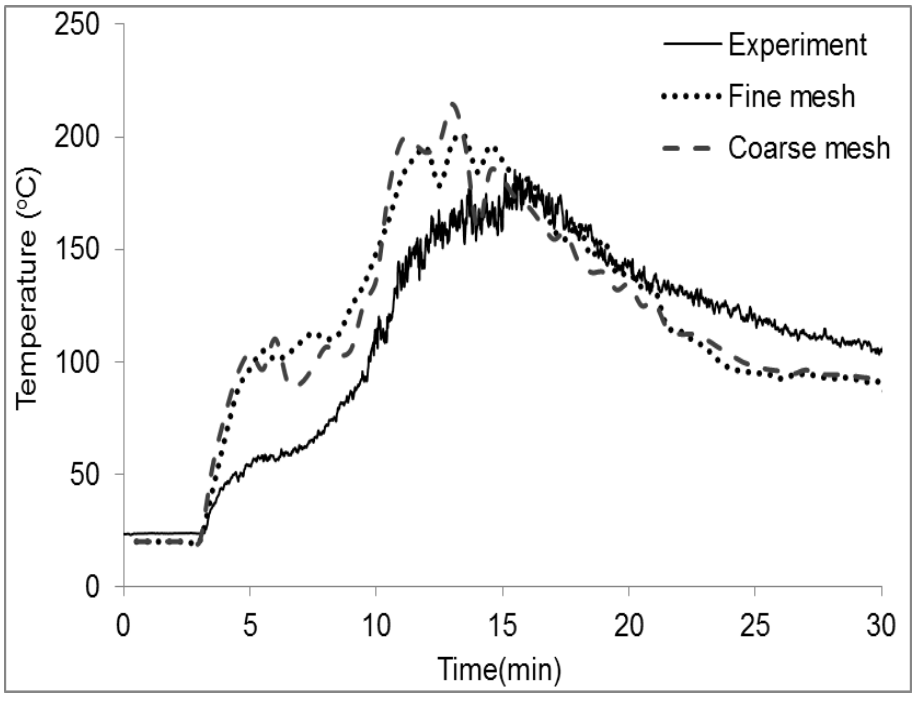

Figure 5.5 Measured and predicted temperatures at position 5-2.2 m

5.2.3 Soot yield and group division

The mechanisms of soot production are very complex and beyond the scope of the present study so far. Therefore, the generation of soot was not modelled and constant soot emission factors of 0.12 in Test I [Mulholland, 2002] and 0.06 in Test II [Butler & Mulholland., 2004] were instead applied to calculate the total soot generation rate, i.e., the soot yield was the product of the fuel loss rate and the soot emission factor.

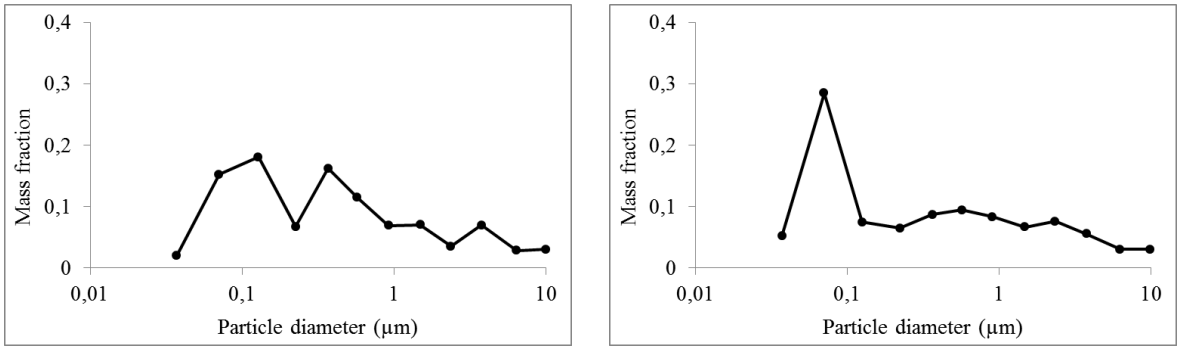

(a) (b)

Figure 5.6 Soot mass fraction in terms of soot particles size for (a) PVC cable, (b) Polyethylene

For the two materials PVC cable and Polyethylene, the soot mass fractions in terms of soot particles size have been measured in [Hertzberg, *et.al*., 2003] and the distributions are shown in Figure 5,6. Soot particles were grouped into three groups of three different sizes with Method 3 described in the preceding chapter. Among the three grouping strategies discussed in Chapter 4, Method 3 shows the best performance regarding the computational efficiency and the prediction accuracy. The mass fraction in the soot generation of each particle group is listed in Table 5.3, which were derived from the mass size distributions of soot produced from PVC cable and Polyethylene [Hertzberg, *et.al*., 2003]. The source for each of the three soot governingequations was the product of the total soot yield and the mass fraction of the corresponding group.

Table 5.3 The soot representative sizes and the corresponding mass fraction

Fire source	Representative size (μm)	Mass fraction
Pvc cable	8.4415	0.1635
	1.2387	0.1392
	0.2373	0.6973
Polyethylene	9.0334	0.0609
	2.6067	0.1998
	0.2620	0.7413

5.2.4 Boundary condition

In order to complete the setup of the simulation to the corridor fire scenario, it was necessary to specify a proper set of boundary conditions. A wall emissivity of 0.8 was used for all solid surfaces. The thickness of the walls was those described previously. The thicknesses of the wall patches near the fire source were set to be either 0.02 or 0.03 m in correspondence with the actual thickness of the wall and others were set to be 0.01 m. The density, conductivity and specific heat were 870 kg/m^3, 0.18 W/m·K, 1130 J/kg·K respectively for Promatect-H, and were 1100 kg/m^3, 0.22 W/m·K, and 1130 J/kg·K for the Masterboard respectively. At the exit, the solution domain was extended by 2.1 m and the boundaries at the extension were set as outlet from the floor. The ambient temperature was set to be 20 $^{\circ}$C. As the $k-\varepsilon$ turbulence model is applicable only in regions with high Reynolds numbers, close to the walls, where viscous effects become dominant, wall functions were applied. Details of the wall functions implemented in SMARTFIRE can be found in [Ewer, *et al*., 2008].

5.2.5 Time step size

The duration of the fire was approximately 1800 s and simulations were carried out with a time step size of 2 s.

5.3 Results

The fire tests were conducted within a large enclosure (the total length of the corridors is 44.6 m), hence it was very suitable to observe the soot movements in weak turbulence environments, especially in the Exit Corridor, where the temperature rise was not high. In the following discussion, the predictions of the Multi-Particle-Size model and the Conventional Model in which soot is treated as a gas species are compared with the experimental data and

observations of soot movement at locations of interest. Position 6 and 15 were chosen because the soot movements at these two locations were representative of those in the near field and far field respectively. In addition, the videos recorded at these two positions were of high quality, showing clear soot movement.

5.3.1 Light extinction at the upper layer

Figure 5.6 and Figure 5.7 show the measured and calculated light extinctions at 2.2 m above the floor at position 6 (near the fire) and 2.0 m above the floor at position 15 (far away from the fire) for the two tests. The calculation of light extinction is discussed in detail in section 3.1.2. The calculated light extinctions were derived from Equation (3.5) from the predicted soot concentrations from the Conventional Model and the Multi-Particle-Size soot model respectively.

Test I

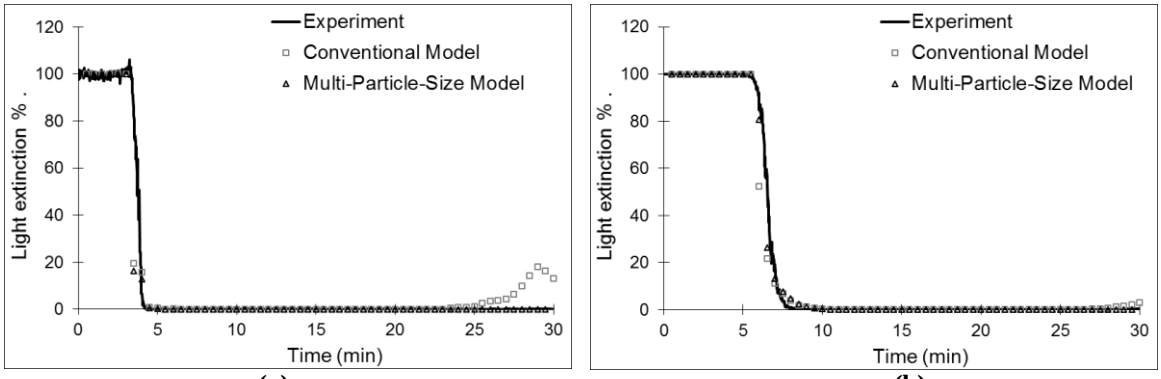

(a) **(b)**

Figure 5.7 The measured and predicted light extinction at (a) position 6 and (b) position 15 for Test Ⅰ

The cable used in Test Ⅰ was NYM whose major component is PVC. A significant amount of soot was generated during the test. In the test, the measured light extinctions decreased from 100% to nearly 0% very rapidly in a short period of time at both positions. The sharp decrease period was between 3.3 minutes to 4.2 minutes for position 6 (Figure 5.7(a)) and was between 5.6 minutes to 7.8 minutes for position 15 (Figure 5.7 (b)). It is obvious that the simulations of those two soot models reproduce the phenomena accurately at both positions.

Test II

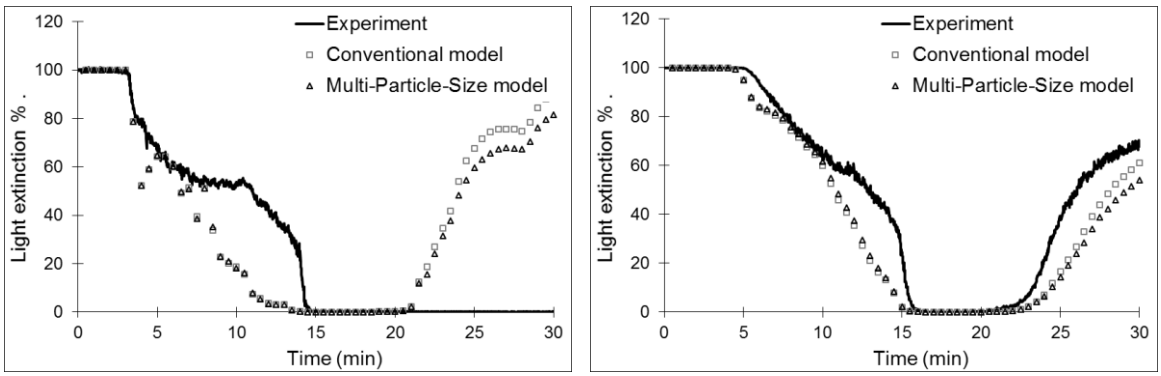

Figure 5.8 The measured and predicted light extinction at (a) position 6 and (b) 15 for Test II

In Test Ⅱ, the cable burnt was NHMH. The soot release rate in this test was smaller than that of Test Ⅰ, therefore the light extinctions decreased slowly compared with Test I (Figure 5.8). The two models predicted similar trends of light extinction at position 6 and position 15. The predictions of both models drop from 100% to 0% in 13 minutes and remain 0 for another 5 minutes in position 6. At position 15 which was far away from the fire source, the predicted curves of light extinction from both models decrease to zero at 15 minutes and start to increase after 21 minutes. The under-prediction on light extinction between 8 minutes to 15 minutes in two positions means the over-prediction on soot concentration. The reason is the constant soot yield valueis higher than the real soot yield valuein this time, which will be discussed in Chapter 9. After 20 minutes, the measured zero light extinction in position 6 was not reliable because it did not match with the video records. The fire in the vertical cable tray was almost self-extinguished at 18 minutes and the remaining fire at the horizontal cable tray was also self-extinguished at 23 minutes. In the video, the markings at 2.0 m above the floor at positions 6 can be clearly seen after 21 minutes. Therefore, the light extinctions at position 6 in Test II should be greater than zero after the fire was extinguished, which were predicted by the two models.

It is obvious that both models are capable of producing reasonably accurate predictions of light extinction in the upper layer.

5.3.2 Visibility distance at the lower layer

In the experiments, a bright light was located on the floor near the exit and the visibility of it could be watched through Camera V4 (Figure 5.9 (a)). Camera V4 was placed at the start of the Exit Corridor, opposite to the exit (See Figure 5.1 for position). The distance between Camera V4 and the light source was approximately 17 m. The visibility distance referred in

the later discussion starts from Camera V4 which was pointed towards the exit. The simulation calculated the visibility distance from the position of Camera V4 by Equation (3.12), which was discussed in detail in section 3.1.2. In this section, the calculated visibility of light near the exit in the Exit Corridor was compared with the experimental observations.

Test I

In Test Ⅰ, camera V4 recorded that the light source became very dim at about 9 minutes and was completely obscured at about 10.6 minutes. For the remaining 20 minutes of the test, the light source remained completely obscured (see Figure 5.9).

(a) **(b)**

Figure 5.9 Observed light at the exit in Test I at (a) 7 min and (b) 9 min

In the simulations, the visibility distance calculated by Equation (3.12) was based on the average concentration of soot between Camera V4 and the light source at the height of 0.3 m above the floor. In Equation (3.12), the constant C_V takes the value of 8 which was derived from the condition of illumination of the exit sign while the light used in the experiment was much brighter than that of common exit signs, which might cause the calculated distance to be smaller than it should be. Figure 5.10 shows the predicted visibility distances of both models during the test.

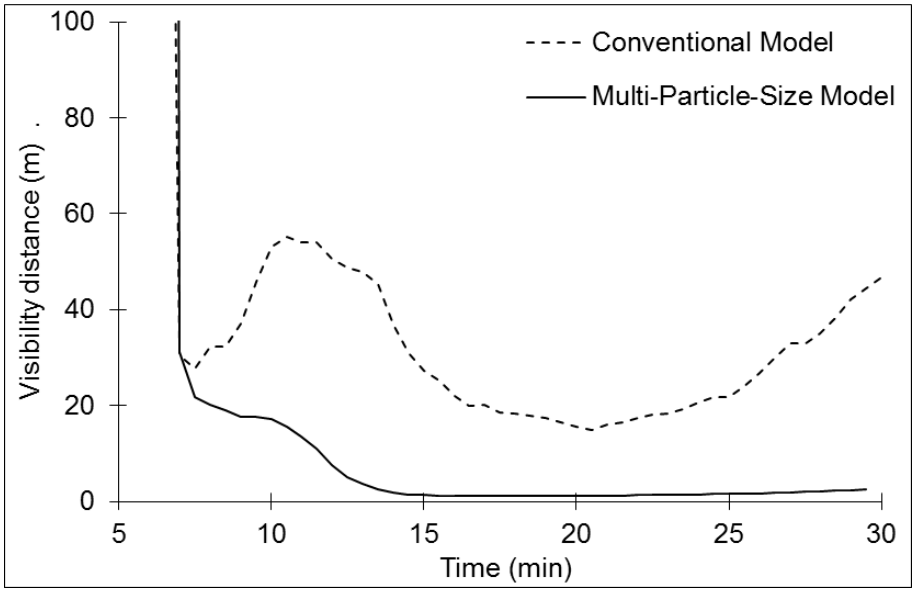

Figure 5.10 Predicted visibility distance from Camera V4 to the light source near the exit for Test Ⅰ.

In Figure 5.10, the Conventional Model predicted a visibility distance of less than 17 m only at 20 minutes, which is approximately 9.4 minutes later than the observed obscuration time or an over-prediction of 89%. Furthermore, the Conventional Model predicted that the period of obscuration of the light source lasted for only 1.5 minutes and then the predicted visibility distance became greater than 17 m, indicating that the light source was visible again. However, the visibility distance derived from the Multi-Particle-Size soot model decreases to 17 m at approximately 10 minutes, which is approximately 0.6 minutes earlier or an under-prediction of 6%. Considering that the light source used in the test was much brighter than those used for common exit signs, the constant value of 8 in Equation (3.12) used in the calculation may be too low for the source used in the experiment. The calculated visibility distance therefore decreases more quickly than it should. With this in mind, the predicted time of 10 minutes is in a reasonably good agreement with the measured time of 10.6 minutes. The model also correctly predicted the obscuration of the light in the remaining 20 minutes.

Test II

In Test Ⅱ, although the light remained visible during the whole experimental period, it was very dim between about 18.5 minutes and 28 minutes. During this period of time, the exit near the light could not be seen from the position of Camera V4 (Figure 5.11). At 21 minutes, the light looked very obscured as shown in Figure 5.11(b).

(a) (b) (c)

Figure 5.11 Observed light at the exit in Test Ⅱ at (a) 18.5 minutes, (b) 21 minutes and (c) 28 minutes.

Figure 5.12 shows the predicted visibility distances by both models for the test. It shows that the visibility distances predicted by the Conventional Model are larger than 20 m in the whole duration of the experiment, which means the light remains very clear all the time. Thus the Conventional Model failed to accurately predict the soot concentrations at the lower layer in this simulation. However, the Multi-Particle-Size Model predicted the visibility distance to be less than 17 m between 18 minutes and 25.5 minutes. As the same reason discussed in the above paragraph, the visibility distance calculated from Equation (3.12) is shorter than it should be. Considering this reason, the predicted disappearance time for the light by the Multi-Particle-Size Model is in reasonable agreement with the observed phenomenon.

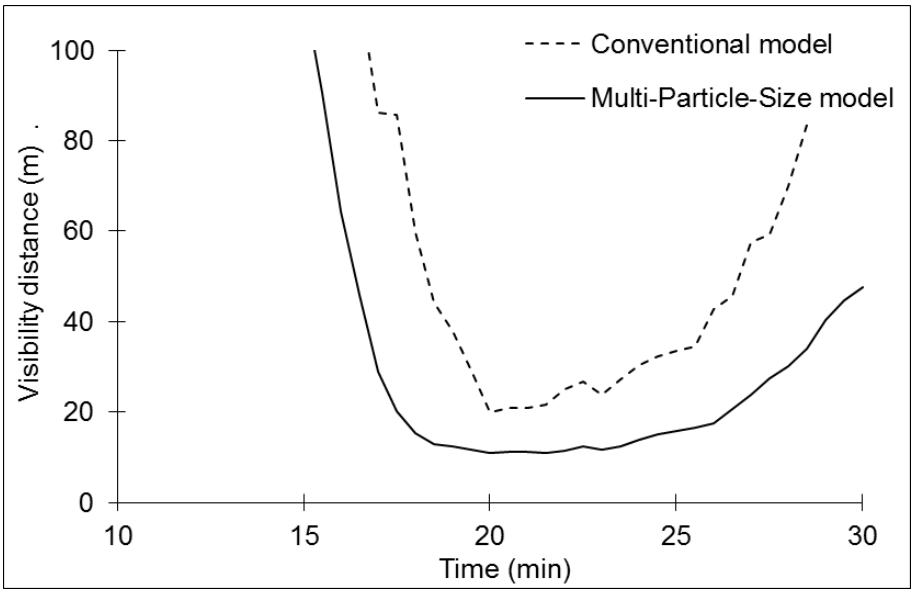

Figure 5.12 Predicted visibility distance from Camera V4 to the light source near the exit for Test II.

5.3.3 Visibility of Markings in the Exit Corridor

In the experiments, reflective markings were mounted on poles at several positions with a vertical spacing of 0.5 m and starting from 0.5 m above the floor (Figure 5.13(a)). The

observed and predicted disappearing times of the markings at position 15 were compared. The distance between Position 15 and Camera V4 was approximately 10 m. The observed obscuration times of the four markings at position 15 were all approximately estimated from the video recordings of Camera V4 in the two experiments.

Test I

In Test Ⅰ, all the markings on the pole at position 15 were no longer visible after 9.5 minutes (Figure 5.13(b)).

(a) **(b)**

Figure 5.13 Observed soot movement in the Corridor at (a) 6 minutes at position 15 and (b) 9.5 minutes at position 15 for Test Ⅰ.

The predicted obscuration time is defined as the time when the visibility distance is less than the distance between the markings and the camera. Table 5.4 presents the observed and predicted obscuration time of each marking. From the table, it is clear that the predictions of the obscuration times by both models are in good agreement with the observed times in the upper (2.0 m above the floor) and middle layers (1.5-1.0 m above the floor). However, the Conventional Model predicted that the marking in the lower layer (0.5 m above the floor) remained visible 7.6 minutes longer than the observation in the test, an over-prediction of 81% while the prediction from the Multi-Particle-Size model was only 2 minutes longer, or an over-prediction of 20%. The marking at the lower layer was predicted to become visible again at 21.5 minutes by the Conventional Model while this marking remained obscure after 9.4 minutes in the test. The Multi-Particle-Size Model also predicted the marking remains obscure once it became invisible. Obviously the Multi-Particle-Size Model performs much better in predicting the visibility of the marking than the Conventional Model does.

Table 5.4 Obscuration times (minutes) of the markings at position 15 in Test I

Height of markings	Observation	Conventional	Multi-Particle-Size
2.0 m	6.8	5.8	6.9
1.5 m	7.5	7.2	7.0
1.0 m	8.3	7.8	7.9
0.5 m	9.4--	17-21.5	11.5--

Figure 5.14 presents the predicted iso-surfaces of soot concentrations predicted by the two soot models for Test Ⅰ with a value of 8.8×10^{-5} kg/m^3 at 12 minutes in the Exit Corridor. At this time, the marking at the height of 0.5 m was obscured in the test. With soot concentrations at this value, the visibility distance calculated from Equation (3.12) with constant C_V value of 8 is 10 m. As seen in Figure 5.14(a), the marking at 0.5 m above the floor is obscured by this iso-surface while the marking in Figure 5.14(b) is much lower than the iso-surface. At 0.5 m above the floor, the average soot concentration from Camera V4 to the marking derived from the Multi-Particle-Size model is higher than 8.8×10^{-5} kg/m^3 indicating a visibility distance less than 10 m. On the other hand, the marking is below the iso-surface predicted by the Conventional Model, indicating the marking is visible from Camera V4 at this time.

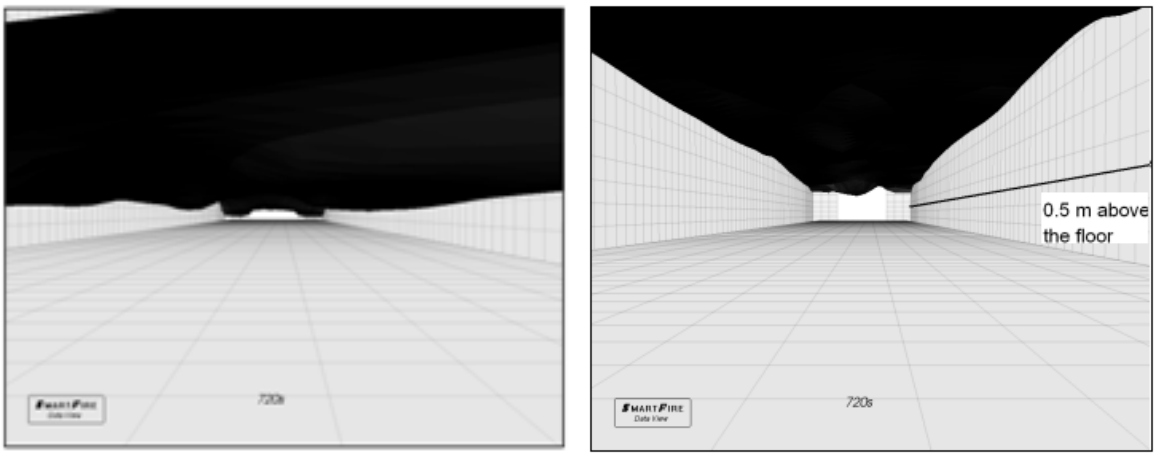

(a) **(b)**

Figure 5.14 Predicted iso-surface of soot concentration in the Exit Corridor at 12 minutes for Test Ⅰ from (a) the Multi-Particle-Size model and (b) the Conventional Model.

Test II

In Test Ⅱ, the upper marking at position 15 became obscure at 11.5 minutes and the bottom marking disappeared after 16.3 minutes. However, the markings all became visible again at

round 29 minutes and the Exit Corridor became very clear after 32 minutes. Table 5.5 shows that the predicted obscured time of the markings between 1.0 to 2.0 m above the floor by both models are approximately 1.0 minute sooner than the observed, or under-predicted by 8%. However, for the marking at 0.5 high above the floor, the Conventional Model predicted that the obscuration times were between 20.5 and 22 minutes while the observed obscuration times were between 16.3 and 28.5 minutes. The predicted obscuration time is 4 minutes later than the observation and the reappearing time is around 6 minutes earlier than the observation by the Conventional Model. By contrast, there are only 1.7 minutes difference in the obscuration time and 2.5 minutes difference in the reappearing time respectively between the predictions of the Multi-Particle-Size model and the observations in the test. In addition, the Multi-Particle-Size Model produces reasonable predictions in the obscuration times for all the markings at position 15.

Table 5.5 Obscuration times (minutes) of the markings at position 15 in Test II

Position of markings	Observation	Conventional	Multi-Particle-Size
2.0 m	11.5-29	10.5-27	11-28
1.5 m	12.5-29	11.5-27.5	11.5-29
1.0 m	14.3-28.5	14.5-28	14.3-29
0.5 m	16.3-28	20.5-22	18-25.5

Figure 5.15 shows the predicted iso-surfaces of soot concentrations predicted by the two soot models with a value of 8.8×10^{-5} kg/m^3 at 18 minutes in the Exit Corridor. At this time, the marking at the height of 0.5 m was invisible at Camera 4. Under the iso-surface, the visibility distance from Camera V4 is more than 10 m. The marking at 0.5 m above the floor was predicted to be obscured by the Multi-Particle-Size Model as the marking is above the iso-surface predicted (Figrue 5.15(a)). On the other hand, the marking was predicted to be visible at this time by Conventional Model as the marking is much lower than the iso-surface (Figure 5.15(b)).

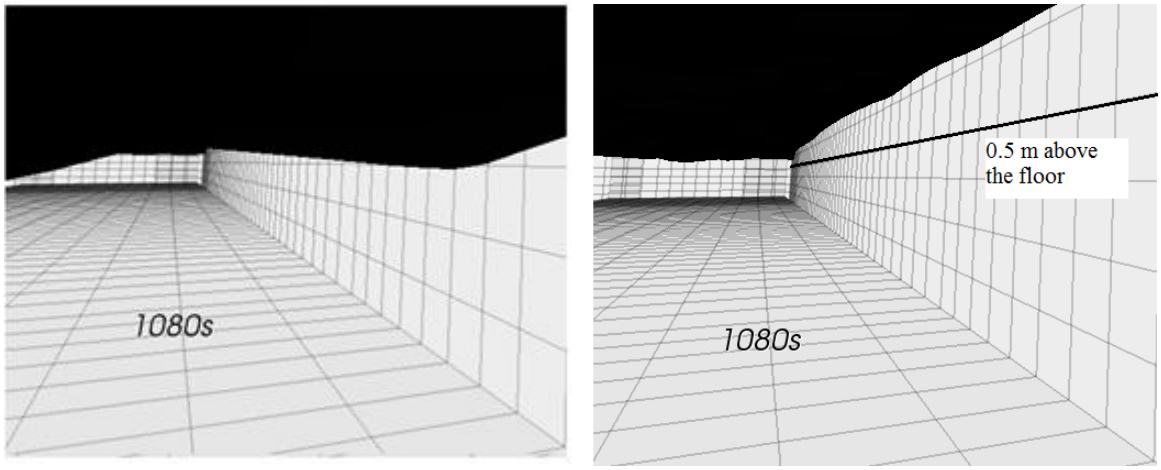

(b) **(b)**

Figure 5.15 Predicted iso-surface of soot concentration in the Exit Corridor at 18 minutes for Test II from (a) the Multi-Particle-Size model and (b) the Conventional Model.

5.4 Deficiency of using Temperature to estimate soot levels

Finally, the deficiency of using temperature to estimate soot levels was highlighted by comparing the visibilities produced from the temperature approach with the observations in Test I.

Evans and Stroup [Evans, 1986] reported a model that the optical density (D) was related to the temperature rise (ΔT) by Equation (3.94), which was discussed in section 3.5.3 in detail. By using approximate values (density of air 1.165 kg/m^3, specific heat capacity of air 1 kg/kgK, yield of soot 0.12 kg/kg and heat release rate 1×10^4 kJ/kg) for the parameters, Equation (3.94) can be expressed as $D/\Delta T \approx 0.046$. Thus the visibility distance can be calculated from Equation (3.12).

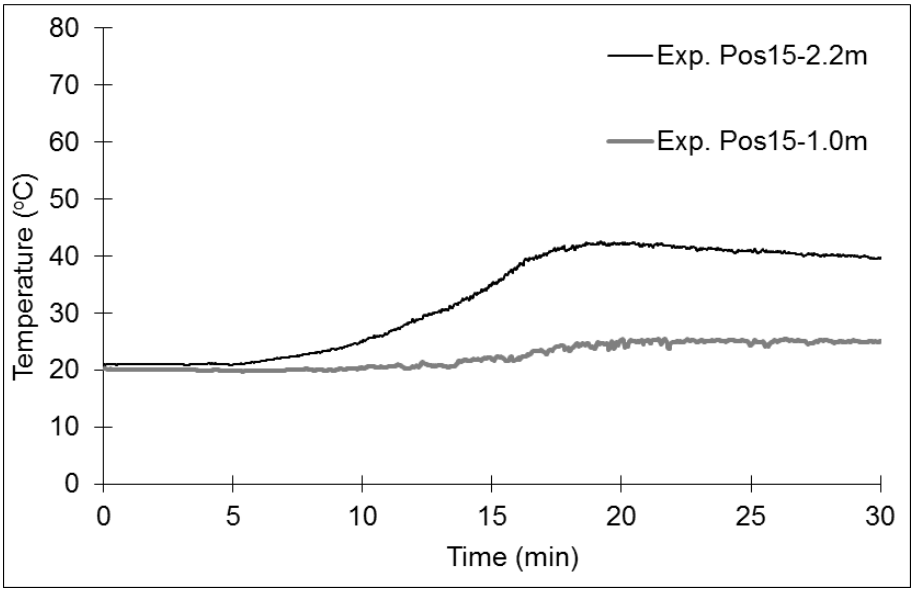

Figure 5.16 Measured temperatures (a) at position 15 in Test I.

At position 15 in Test Ⅰ, the measured temperatures are as high as 40 ^{O}C at 2.2 m above the floor, while they are close to the ambient value of 20.0 ^{O}C at 1.0 m above the floor during the entire 30 minutes of the test time (see Figure 5.16). Based on Equation (3.94), the visibilities at the two different heights at 12 minutes are approximately 5.1 m and over 16.1 m respectively. It is clear that the soot layer predicted from this approach is at least 1.0 m above the floor at position 15. Furthermore, the predicted visibility distance, based on the measured peak temperature at 1.0 m above the floor during the entire 30 minute test period, is more than 10 m, which suggests that the marking at this height is always visible during the entire test. However, as observed in the experiment and predicted by the Multi-Particle-Size model, the soot layer moved below the marking at position 15 in the lower layer, 0.5 m above the floor, within 12 minutes.

This difference between the predictions by the temperature estimation method and the experimental observation highlights the deficiency of that approach. Before soot moves to remote locations, a lot of heat has already been lost via radiation or through the confining walls. Therefore, temperature is not a good indicator of the soot movement at remote locations.

5.5 Investigation of group division performance and computational cost

There are some issues relating to the Multi-Particle-Size model that need to be considered. The rationality of the three-group division had already been discussed based on the

simulations in a chamber in Chapter 4. In order to further examine the reliability of this group division, a finer division including 10 groups with particle sizes between 0.1 μm and 10 μm were investigated for Test I. The soot concentrations predicted from the two group divisions are compared at position 6 and 15 (Figure 5.17).

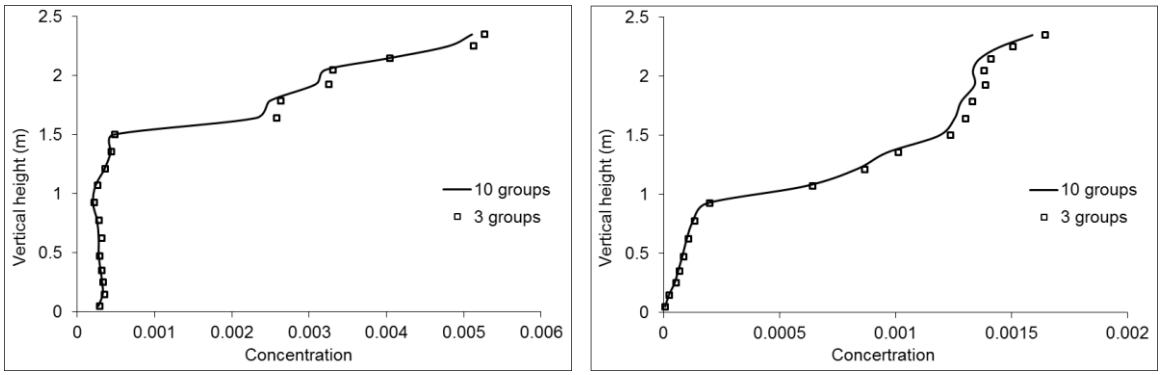

(a) **(b)**

Figure 5.17 Predicted soot mass fractions along vertical line at (a) position 6 and (b) position 15 at 12 minutes in Test I with the two different particle group divisions.

The soot mass fractions along the vertical line at position 6 and 15 at 12 minutes predicted from the Multi-Particle-Size model with the two soot group divisions are compared with each other (Figure 5.17). From the figure, obviously the predictions with the two different soot group divisions are very close at both positions, especially in the lower layer. It shows that the use of three groups for categorizing soot particles are sufficient to describe the effect of soot particle size on the transportation of soot for cable fires.

Then the computational cost of the simulations are discussed. Compared with the Conventional Model, two additional conservation equations must be solved in the Multi-Particle Size soot model when three particle groups are represented. This increase in the number of governing equations might incur additional computational costs. Furthermore, some additional computational effort is required for the convection correction for each of the three conservation equations associated with each particle group. The 1800 second simulation of the PVC-cable fire scenario, involving 132,411 computational cells was carried out using a computer with 4-cores/8-threads 3.06 GHz processors and a memory of 24.0 GB. Using the Conventional Model, the simulations required approximately 32 hours. The simulation using the Multi-Particle Size model took approximately 35 hours, which was 3 more hours or 9% longer – a modest increase in computational time for the improved accuracy.

5.6 Conclusion

This chapter addresses Objectives 1(b) and 1(c) by validating the MPS model using experimental data. In order to investigate the accuracy and efficiency of the new modelling approach, the Multi-Particle-Size model and the Conventional model were both used to simulate two large-scale cable fire experiments, one was with a PVC-cable and the other was with a polyethylene -cable. The predictions of soot transport were compared with measured data and observed phenomena from video recordings of the two tests:

- In the upper layer, the predicted light extinctions by both models were in good agreement with the measured experimental data.

- In the lower layer, the measured obscuration time for the light source in the corner near the exit was compared with the predictions by the two models. The newly developed model more accurately predicted the observed obscuration time. These results show that the Multi-Particle-Size method greatly improved the prediction precision for the soot movement in the lower layer compared with the Conventional Model.

- The predicted obscuration times of reflecting markings at different levels at the position 15 also showed the Multi-Particle-Size method improved the prediction precision for the soot movement in the lower layer compared with the Conventional Model.

    - In Test Ⅰ, the Conventional model over-predicted the starting time of obscuration for the marking 0.5 m above the floor (which was 9.4 minutes in the test) by 81% (17 minutes) while the newly developed model over-predicted the starting time by only 12% (11.5 minutes). More importantly, the new model correctly predicted that the marking remained invisible in the remainder of the test while the Conventional model predicted that it remained invisible for only 4.5 minutes.

    - In Test Ⅱ, The Multi-Particle-Size model significantly improved the accuracy of the prediction on the obscuration times of the markings 0.5 m above the floor at Position 15.

The present study also highlighted the deficiency of estimating soot levels by the temperature approach. The predicted soot layers using the temperature approach for Test I were significantly different from those observed in the test. In the Exit Corridor in Test Ⅰ, predicted soot layer was at least 1.0 m above the floor during the entire simulation time while the observed soot layer descended below 0.5 m above the floor within 12 minutes. Therefore, it is potentially problematic to represent the soot layer by the hot layer at remote regions from the fire source.

The accuracy of the three-group division method was investigated by comparing with a finer division of ten-group. The predicted mass fractions at positions near the fire and far away from the fire were very close for both division methods. Thus the three groups might be adequate to represent the effect of soot particle size on soot transportation for the cable fires.

While the Multi-Particle-Size model appears promising, further validation is required involving more experimental data, especially the light extinction data in the lower layer. Furthermore, the simulations model the soot yield valueas constants, which are derived from experiments. The constant rates capture the global soot yield trends, but may not be capable of accurately reproducing detailed soot yield, for example, the soot yield between 8 to 15 minutes in Test II. This problem will be discussed in Chapter 9.

The outcome of the simulation of Test I has been presented in [Hu, *et al*., 2011].

Chapter 6
Simulating soot transport in a building with high ceiling

In this chapter, soot transport in an industrial building with high ceiling is simulated by the Multi-Particle-Size model and Conventional Model. The obscuration profiles derived from the predictions of both models are compared with each other. The obscuration tendency at several positions is compared with the experimental data detected by soot lasers and detectors.

6.1 Introduction

The buildings with high ceilings, such as industrial units and warehouses, are often densely packed with stacked goods or high-bay racking systems. Fires in these buildings are potentially devastating, causing not only casualties and damage to the stocked goods and the building, but also business interruption cost and sometimes loss of customers. The security of these buildings today relies heavily on the smoke detection system to be fast enough. If a fire occurs, it is desirable that the fire detection and warning arrangements in large buildings give such early warning that the staff is able to escape to a safe area and the fire fighting service arrives in time to extinguish the fire before the damage is severe.

Early detection in buildings with high ceilings is a difficult task. When a fire starts or the fire is small, the soot concentration is very low and the soot movement is sensitive to the airflow pattern. Thus it is important for computer simulations to provide detailed and accurate information on soot movement to determine the best placement of the detectors so that the detection system will give sufficient early warning.

In this study, the newly developed soot model - Multi-Particle-Size model - is used to simulate the soot transport in an industrial building with high ceiling. In order to further compare the performance of the model with the Conventional Model, the latter is also used to simulate the same case. The predicted soot obscuration profiles at a vertical cut plane from

both models are compared with each other. Then the predicted tendencies of soot obscuration at several positions are also compared with the measurements.

6.2 Experiments and measurements

The experiments were conducted in an industrial building called Fläkt Woods in Enköping [Blomqvist, 2003]. The tests were performed during normal operation of the facility, which means the experiments were not fully controlled. The normal working activities included gates' opening and closing, machines starting and switching off, forklifts' driving around etc.

6.2.1 Displacement system

Fläkt Woods was a large scale enclosure with a width of 171×90 m and a height of 7.25 m. Goods were stacked in high-bay racking systems, which were not described in detail in the experimental report [Blomqvist, 2003]. During the experiments, a ventilation system was operated to maintain the temperature in the building. A thermocouple tree was mounted in the building to record temperature every half meter from 2.2 m to 7.2 m in height and it was shown that the temperature varied approximately between 23 to 26 degrees centigrade. The air velocity in the room was measured to be between 0.1 to 0.2 m/s and it would be somewhat higher close to the air inlets.

The building was heavily equipped with 13 optical point detectors APS006 (warning, pre-alarm and alarm activated at 1%/m, 2%/m and 3%/m respectively) and 3 lasers with a wavelength of 670 nm. The laser measured the mean obscuration in one meter while a detector measured the obscuration at a single point. The laser beams were parallel to the floor and the position of midpoint of each laser beam was the closest point to the soot source in the beam. The soot generator SG3000 was used here as the soot source, which could yield the amount of soot as required. The soot generator was placed on the floor and released soot upward. The origin of the coordinates was defined as the position 7 m away from the soot source in x direction and 6 m away from the soot source in y direction at floor level. The third coordinate, z, is the height above the floor. The locations of the soot source and the items of the experimental equipment are given in Table 6.1.

Table 6.1 Coordinates of equipment and soot source

Instrument/fire	coordinates	Comments
SG3000	(7, 6, 0)	Soot source
thermocouples	(6.7, 5.35, 2.2-7.2)	One thermocouple every half meter
Detector 1	(6.2, 6, 7.1)	
Detector 2	(6.2, 6, 6.2)	
Detector 3	(2.25, 6, 7.1)	
Detector 4	(2.25, 6, 6.2)	
Detector 5	(6.2, 12.4, 7.1)	
Detector 6	(6.2, 12.4, 6.2)	
Detector 7	(11.25, 6, 7.1)	
Detector 8	(11.25, 6, 6.2)	
Detector 9	(15.75, 6, 7.1)	
Detector 10	(15.75, 6, 6.2)	
Detector 11	(11.25, 12.4, 7.1)	
Detector 12	(11.25, 12.4, 6.2)	
Detector 13	(11.25, 6, 4.7)	
Laser 1	(7.4, 5.7, 4.8)	Midpoint of measuring beam
Laser 2	(6.3, 10.7, 6.25)	Midpoint of measuring beam
Laser 3	(10.8,10.7, 6.25)	Midpoint of measuring beam

6.2.2 Measurements and observations

The experiment was repeated three times using the soot generator SG3000 and the soot obscuration was measured by the detectors and the lasers. For Detector 13, no test results were provided. Due to some problem with the signal register system, the signals of Detector 1-6 in the first test were not recorded. Based on the detail of the measured data given in [Blomqvist, 2003], some conclusions of the experimental results can be made:

- The uncontrolled circumstances made the timings of warning, pre-alarm and alarm for all detectors in the three tests were totally unmatched. But some detectors mounted at 1.1 m below the ceiling gave warning and pre-alarmed activation (pre-alarm at 2 %/m) in the three repeat tests, which indicated that the soot obscuration at these points at this layer should be more than 2 %/m. It was also observed that the soot remained hanging in the air and moved downwards to the people working in the building.

- For most detectors, the recorded soot obscuration shown a great difference between the three repeat tests. However, the Detector 8 and Detector 10, which were mounted far away from the soot source and at 1.1 m below the ceiling, recorded similar tendency of soot obscuration in the three tests. Figure 6.1 shows the soot obscuration measured by Detector 10 for the three repeat tests.

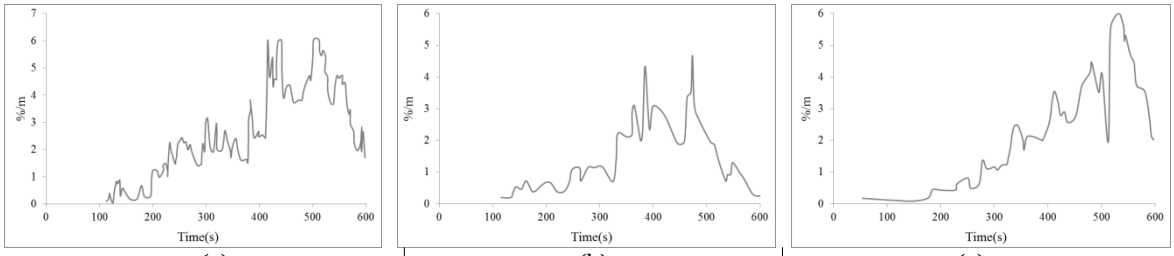

Figure 6.1 The measured soot obscuration by Detector 10 for (a) test 1, (b) test 2, and (c) test 3 [Blomqvist, 2003].

- There are great fluctuations in the soot obscuration measured by the lasers, especially for laser 1. However, for each laser, the measured soot obscuration in the three repeat tests follows a similar tendency. Figure 6.2 shows the soot obscuration measured by laser 1 for the three repeat tests.

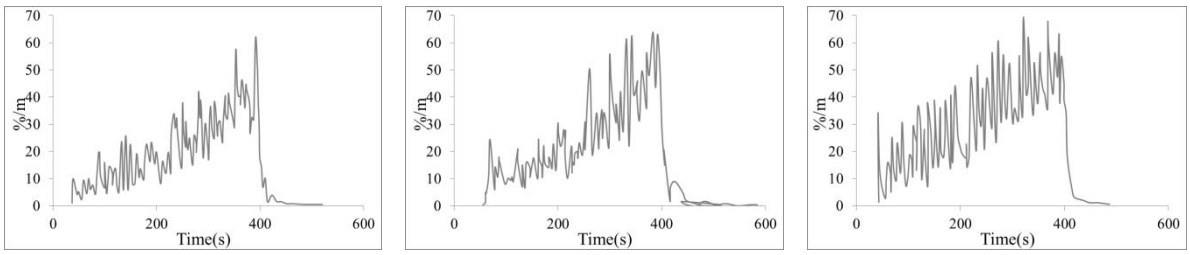

Figure 6.2 The measured soot obscuration by laser 1 for (a) test 1, (b) test 2 and (c) test 3 [Blomqvist, 2003].

The detailed soot obscuration measured by all of the detectors and lasers can be found in [Blomqvist, 2003]. The fact that the soot obscuration at a single point varied significantly in the three tests was probably caused by that the tests were not fully controlled. The normal working activities were going on, which causes the change of airflow pattern during the experiments. It further caused the difference of soot concentrations between the three repeat tests.

6.3 Numerical details

Blomqvist conducted a numerical simulation of the experiments [Blomqvist, 2003]. The simulation set-up in this study was very similar to that of the Blomqvist simulation as there was a lack of detailed information on the report of the experiment, such as the soot release

rate and velocity, ventilation system, temperature gradient, disturbances caused by the normal operation at the facility [Blomqvist, 2003].

The computational region was a cuboid of 20 m by 15 m with a height of 7.3 m, a cut-out space within the building. A non-uniform mesh consisting of 192,000 cells was applied to discretise the region. The smallest mesh size of 0.1×0.1×0.2 m^3 was applied to the region near the soot source and the largest mesh size of around 0.3×0.3×0.2 m^3 was applied to the region far away from the soot source. The four vertical boundaries of the cuboid were set to be free flow (outlet) as the industry building was much bigger than the computational region and the operational detail of the ventilation system was unknown. As there was only a variation of 3 degrees in the temperature in the building, the temperature was assumed be constant with a value of 297 K.

The soot source SG3000 was modelled as an inlet on the floor, with a conservative inlet velocity of 1.5 m/s through a 0.2 m squared hole at temperature 340 K. According to the simulation of Blomqvist, the soot release rate was set as follows:

$$\textit{Soot release rate} = 10\ g/s \quad \textit{if} \quad t \leq 10\ s \tag{6.1}$$

$$\textit{Soot release rate} = 0.1\ g/s + (t-10) \times 0.02\ g/s \quad \textit{if} \quad 10s < t \leq 360\ s \tag{6.2}$$

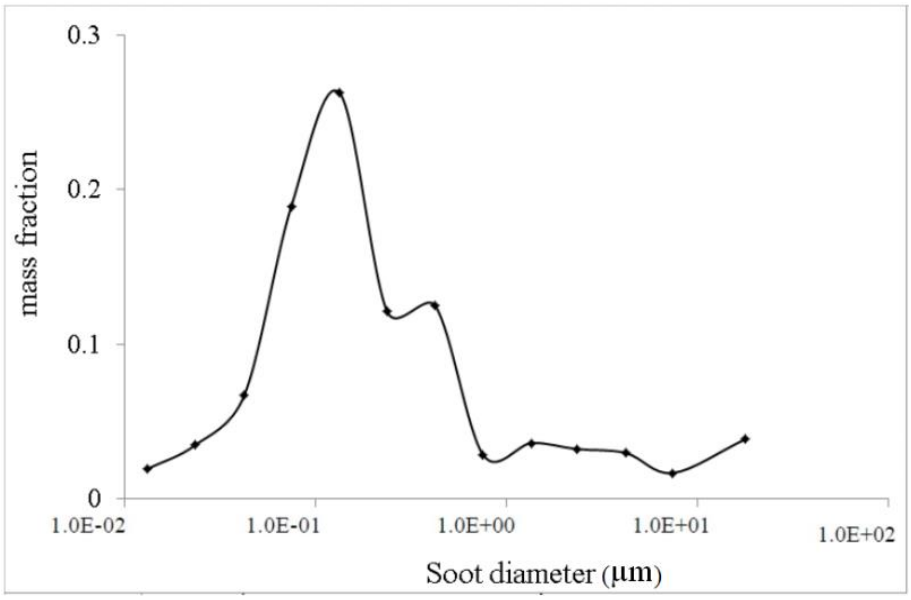

Figure 6.3 The mass size distribution of soot generated from diesel [Kittelson *et al.*, 2002].

The Multi-Particle-Size model was used to simulate the soot transport in the computational region. The fuel used in the soot generator SG3000 is diesel [Thermo, 2014] but the soot

particle distribution was not mentioned in the experimental report. According to the research work in [Kittelson *et al*., 2002], the mass fraction distribution against particle size of soot generated from diesel is shown as Figure 6.3.

Using the strategy Method 3 in the Multi-Particle-Size model, the soot particles generated from diesel can be divided into three groups. The representative size and the corresponding mass fraction of each group are shown in Table 6.2.

Table 6.2 The representative size and the corresponding mass fraction for soot particles generated from diesel

Representative size (μm)	Mass fraction
15.4643	0.0553
2.8052	0.1050
0.2021	0.8397

The simulations were carried out with a time step size of 2 second for 600 seconds.

6.4 Results and discussion

The normal operation of the facility caused the measured data different between the tests. However, section 6.2.2 shows that there are still some measurements that have the same tendency for the repeat tests, including the obscuration tendency measured by the three lasers and two detectors (Detector 8 and Detector 10), and the soot obscuration at some positions at 1.1 m below the ceiling that should be over 2 %/m according to the activation of the detectors at these positions. In this section, the predicted soot obscuration profiles on the vertical cut plane across the soot source at several time points were shown, and the predicted obscuration tendencies at five positions were compared with measurements.

6.4.1 Obscuration profile

In the experiments, it was observed that a non-negligible amount of soot moved down away from the ceiling. According to the experimental report, most detectors mounted at 1.1 m below the ceiling were activated during the tests. Some detectors (Detector 8, 10 and 12) were activated for all the three repeat tests and some detectors (Detector 2 and 4) were activated at least once. The timings of activation of these detectors are mainly in the range of 250 s to 500

s. Therefore, the soot obscuration at these detector positions should be over 1 %/m, and sometimes even be over 3 %/m between 250 s and 500 s.

In order to have an overview of the soot movement, the obscuration distribution on the vertical cut plane across the soot source is displayed. The obscuration is calculated from Equation (3.10). A particular mass optical density $D_{m,0}$ (ob m^3/kg) is defined as [Husted, 2004]:

$$D_{m,0} = \lim_{L\to 0} -\frac{10}{L}\log_{10}\left(\frac{I_\lambda}{I_\lambda^0}\right)\frac{V_c}{\Delta m} \tag{6.3}$$

where I_λ, I_λ^0, L , Δm and V_c have the same definitions as those in Section 3.1.2.1. The ratio of soot mass rate Δm to the volume flow rate V_c can be calculated from:

$$\frac{\Delta m}{V_c} = \frac{\rho_s f_v V_c}{V_c} = \rho_s f_v \tag{6.4}$$

Substituting Equation (6.3)-(6.4) into Equation (3.10), the obscuration can be calculated as:

$$\textit{obscuration per meter}\ (\%/m) = 100(1-10^{-\frac{D_{m0}\rho_s f_v L}{10}})/L \tag{6.5}$$

By setting the soot density to be a constant ρ_s =1800 kg/m^3, the particular mass optical density per meter $D_{m,0}$ =1.9×10^4 ob m^3/kg, and the distance L to be unit length, the obscuration is calculated as [Blomqvist, 2003]:

$$\textit{obscuration per meter}\ (\%/m) = 100\left(1-10^{-\frac{1.9\times10^4\times1.8\times10^3\ f_v}{10}}\right) \tag{6.6}$$

Equation (6.6) shows the obscuration increases with the increasing of soot volume fraction.

Figure 6.4 shows the obscuration profile at 300 seconds calculated from the predictions by the Multi-Particle-Size model and Conventional Model. At 300 seconds, the soot generator released soot continually. Soot was predicted to spread and stay under the ceiling by both models. The obscuration in the region 0.8 m below the ceiling was predicted to be over 4 %/m. However, there is a remarkable difference in the soot obscuration in the region below the ceiling 0.8 m to 2 m predicted by the two models. The obscuration in this region was predicted to decrease gradually and the obscuration value in most part of the region was near or over 1 %/m according to the prediction from the Multi-Particle-Size model. But the obscuration was predicted to be near zero in this region by the Conventional Model.

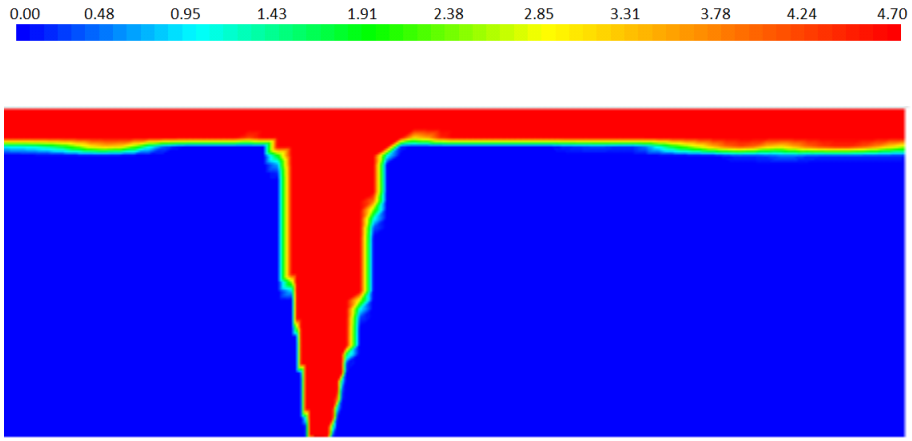

(a)

(b)

Figure 6.4 The obscuration profile on the vertical cut plane across the soot source at 300 seconds derived from the prediction of (a) Conventional Model and (b) Multi-Particle-Size model.

The obscuration profile at 400 seconds is shown in Figure 6.5. The soot generator stopped releasing soot at 360 second. Soot was predicted to move away in the horizontal direction by the Conventional Model. However, the Multi-Particle-Size model predicted soot to move away in both the horizontal and vertical directions. Soot obscuration in the region below the ceiling 2 m to 3 m was predicted to be over 1 %/m at some positions by the Multi-Particle-Size model.

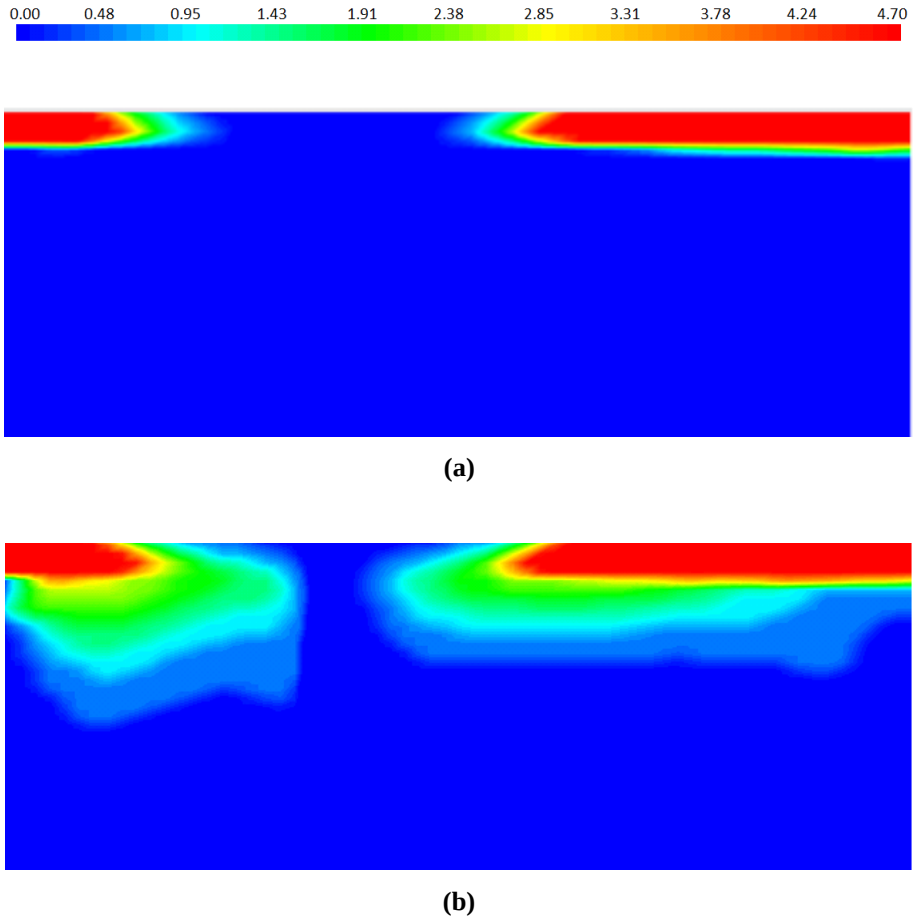

Figure 6.5 The obscuration profile on the vertical cut plane across the soot source at 400 seconds derived from the prediction of (a) Conventional Model and (b) Multi-Particle-Size model.

Figure 6.6 shows the obscuration profiles at the cut plane at 480 seconds. At this time, only a small amount of soot was predicted to stay in a small region just below the ceiling by the Conventional Model. However, a significant portion of soot was predicted to descend and the obscuration at some positions 3 m below the ceiling was predicted to be over 1 %/m by the Multi-Particle-Size model.

From the above comparison, it can be seen the Conventional Model predicted soot hanging below the ceiling and travelling along the horizontal direction during the simulation. The simulation performed by Blomqvist [2003] showed similar soot obscuration profiles as those from the Conventional Model. The soot was observed hanging in the air and moving downwards to the people working in the building during the tests. Blomqvist pointed out that the descent of soot layer was not captured at all in his simulation. However, the Multi-Particle-Size model predicted soot hanging in the air and moving downwards during the simulation.

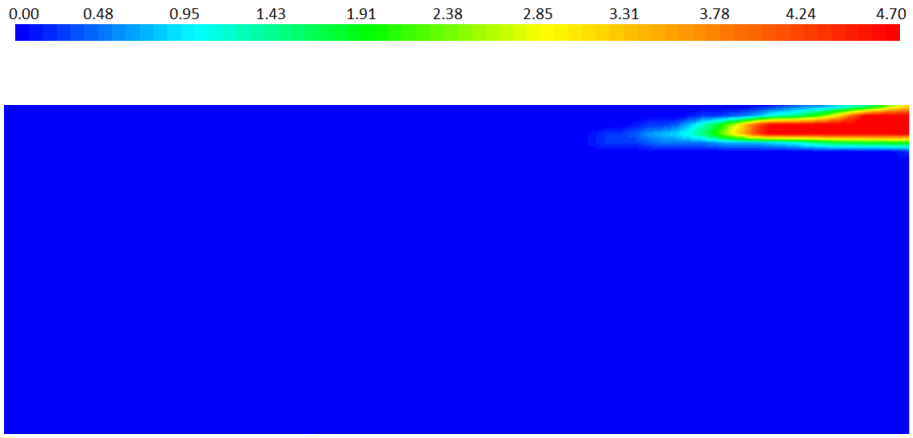

(a)

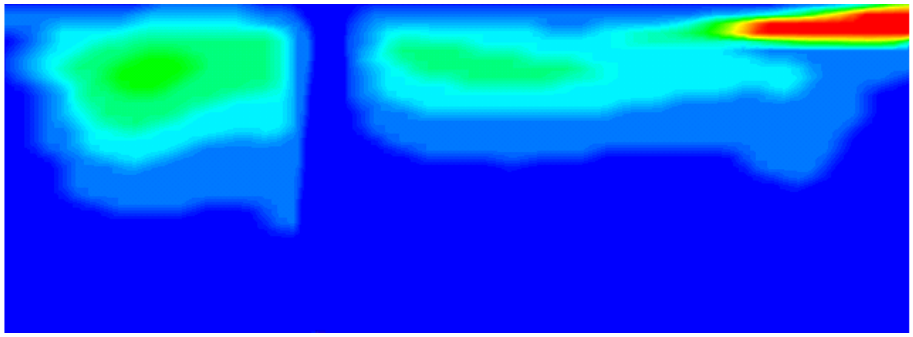

(b)

Figure 6.6 The obscuration profile on the vertical cut plane across the soot source at 480 seconds from (a) Conventional Model and (b) Multi-Particle-Size model.

6.4.2 Obscuration at positions of the lasers

The obscuration at two heights was measured by three lasers. The positions of the three lasers are presented in Table 6.1. Laser 1 was mounted at 4.8 m high above the floor and the midpoint of the laser beam was only 0.5 m away from the centre line of the soot plume. Laser 2 and Laser 3 were both mounted at 6.2 m above the floor. The midpoint of Laser 2 beam and the midpoint of Laser 3 beam were 5 m and 6 m away from the centre line of the soot plume respectively.

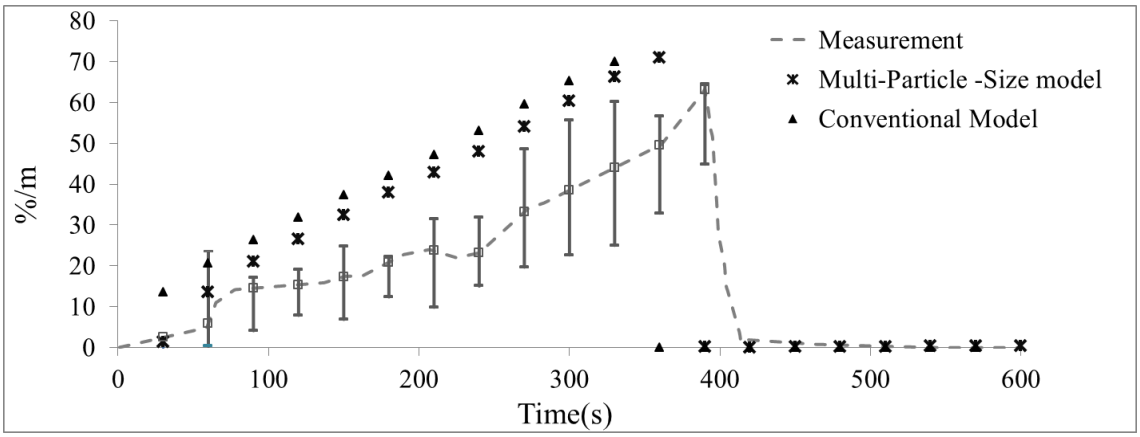

(a)

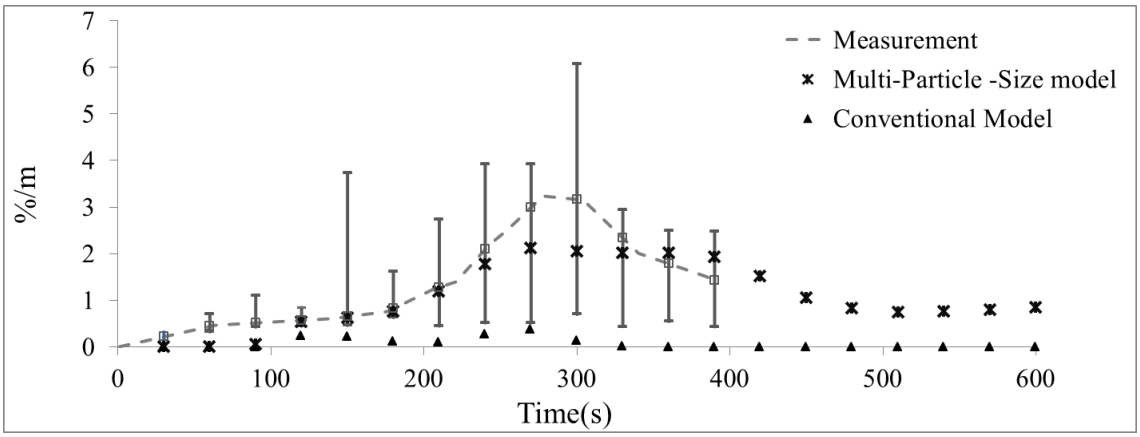

(b)

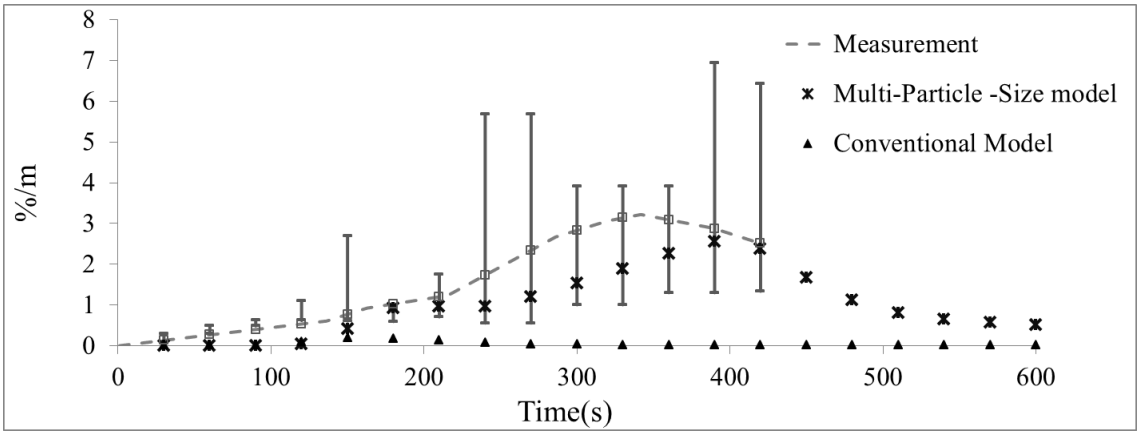

(c)

Figure 6.7 The measured and predicted obscuration tendency at positions of (a) Laser 1, (b) Laser 2 and (c) Laser 3.

Figure 6.7 shows the soot obscuration measured by the three lasers in test 2 and calculated from the predictions of the Multi-Particle-Size model and the Conventional Model. The obscuration measured in the three repeat tests shows great fluctuations, but has a similar

tendency. Here the measured obscuration from test 2 (dash lines) is used to compare with the predictions as the results from this test are more stable than those from the other two tests. In order to show the obscuration fluctuations, the upper and lower bounds of the measured obscuration at every 30 seconds are also presented (vertical lines).

Laser 1 was close to the central line of the soot plum, thus a large amount of soot might have crossed the laser beam. Figure 6.7(a) shows the measured obscuration increases gradually to about 60 %/m in the first 390 second, with significant fluctuations during the whole period. But it drops to nearly zero after 390 second as no soot was released after 360 second. The fluctuation in obscuration might be caused by the uncontrolled ventilation in the building. The obscuration tendencies calculated from both models are similar to each other. However, both models over-estimated the obscuration at this position. The reason might be that the soot concentration at the height of the laser was easily diluted by the air flow which was caused by the normal operations within the building and was not considered in the study.

Laser 2 measured the soot obscuration at the height of 6.2 m. The obscuration at this position shows an increasing tendency in the first 300 seconds. The Multi-Particle-Size model predicted the tendency at this position and the predicted level of obscuration is in reasonably good agreement with the measured data. However, the Conventional Model failed to reproduce it with an almost flat obscuration level. The peak obscuration from the prediction of the Conventional Model is only about 0.38 %/m, lying outside the range of the measured obscuration fluctuations.

Laser 3 measured a tendency of soot obscuration that slightly increased in the first 360 seconds. Same as the other two lasers, significant fluctuation was observed during this period of time. The obscuration tendency was reasonably reproduced by the Multi-Particle-size model while the Conventional Model failed again to predict the tendency.

6.4.3 Obscuration at positions of the detectors

The soot obscuration was measured by 13 detectors during the tests. For most detectors, the measured obscuration at its position in the three repeat tests is totally unmatched because the environment of the tests was not fully controlled. However, the soot obscuration measured from the Detector 8 and 10 shows a similar tendency in the three tests. The Detector 8 and 10

were both mounted at 1.1 m below the ceiling and they were 4.25 m and 8.75 m away from the central line of the soot plume respectively.

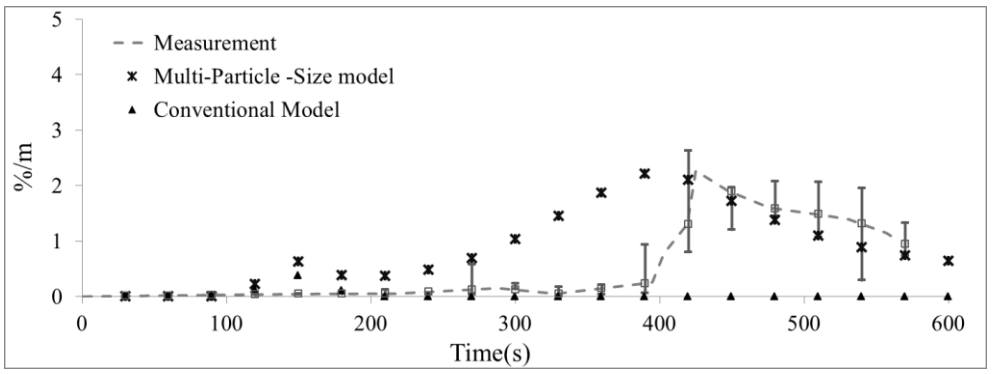

(a)

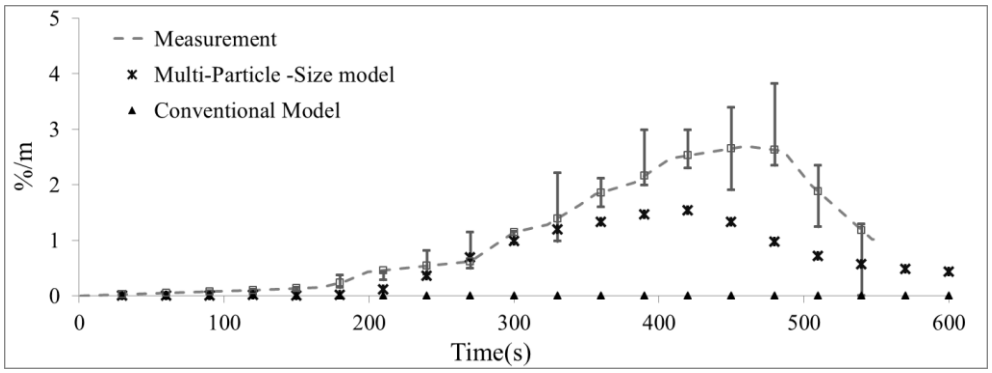

(b)

Figure 6.8 The measured and predicted obscuration tendency at position of (a) Detector 8, and (b) Detector 10.

Figure 6.8 shows the tendency of soot obscuration measured by the detectors (Detector 8 and 10) and calculated from the predictions of the Multi-Particle-Size model and the Conventional Model. The measured tendencies (dash lines), the upper and lower bounds of the measured obscuration at every 30 seconds (vertical lines) are derived from test 2.

The measured soot obscuration at Detector 8 was about 0.24 %/m at 390 s and 2.1 %/m at 420 s. As there was a sharp increase in the measured obscuration between 390 second and 420 second while the soot generator stopped releasing soot during this period of time, it was likely the soot concentration before 420 second at this position was diluted by the air flow which was unable to model in the simulations. Both models over-predicted the obscuration before 420 second. However, the obscuration tendency after 420 seconds predicted by the Multi-Particle-Size model matches the measurement very well while the Conventional Model predicts almost zero obscuration, far too low compared with the measurement.

Figure 6.8(b) shows that the Detector 10 recorded that the soot obscuration increased gradually before 420 s, then decreased gradually after that. The Multi-Particle-Size model captured the tendency of the obscuration reasonably well while the Conventional Model predicted a flat obscuration close to zero (in the order of 10^{-3} %/m) during the whole simulation.

Considering that these tests were not fully controlled and barriers for soot movement (stacked goods, racks, *etc.*) were unknown, only qualitative match of the model predictions with the measured obscuration can be expected. The prediction from the Multi-Particle-Size model shows the ability to provide a reasonable description of the soot obscuration at these two positions.

6.5 Conclusion

Fire safety of large buildings relies heavily on the smoke detection system. It is desirable that computer simulations can provide reasonable predictions on soot movement. Therefore, reliable information can be obtained for determining the best position for placing soot sensors of the detection system.

In this chapter, the movement of soot particles released from a smoke source in a large industrial building with a high ceiling was simulated using the Multi-Particle-Size model and Conventional Model. The timings of the activation of the soot detectors were observed to be mainly between 250 s and 500 s. Thus the predicted soot obscuration profiles in the vertical cut plane through the centre of the smoke source were presented at 300 s, 400 s and 480 s. The simulation results show that the Conventional Model did not predict the downward movement of the soot layer while the Multi-Particle-Size model predicted the soot descent phenomenon that was observed during the experimental tests. The obscuration values measured by three lasers and two detectors (Detector 8 and 10) were also compared with the model predictions. The Multi-Particle-Size model was able to produce reasonably well predictions on the tendency of the obscuration at these positions. However, the Conventional Model greatly under-predicted the obscuration at four of the positions. This chapter further addresses Objective 1(c) by validating the MPS model using the soot data of a large scale experiment.

Chapter 7

Beta soot generation model

In this chapter, a global approach to modelling soot generation rate in non-premixed combustion flames is developed. This new model has only one extra fuel-specific parameter—peak soot formation rate. By making use of the characteristics of the probability density function of the beta distribution in the PDF approach of simulating turbulent combustion, the model is of low cost in terms of computational resources. The new soot generation model is incorporated into the CFD fire tool—SMARTFIRE.

7.1 Introduction

The way in which a fire model deals with the soot generation greatly alters the prediction of thermal radiation, therefore has a profound influence on predicting fuel burning, flame spread and fire growth. Thus it is desirable to predict the soot production in flames with reasonable accuracy and relatively low computational cost.

Over the few last decades, considerable progress has been achieved in understanding soot evolution and a lot of effort has been dedicated to modelling soot generation in fires. Generally, the existing soot generation models can be classified in the following three categories: empirical models, semi-empirical models and detailed chemistry models. Empirical models rely heavily on empirical data and thus are only appropriate for specific combustion conditions. Detailed chemistry models pursue accurate predictions by describing the soot evolution with a large number of intermediate species and chemical reactions. However, the chemical mechanism responsible for soot generation has not yet been unambiguously identified and the complexity of this type of model requires large computational resources, which limits their application to laboratorial experiments. Semi-empirical models describe a limited number of phenomena which are usually considered to be important for soot generation. The parameters in these models are adjusted to obtain reasonable agreement with empirical data. This type of models provides a good compromise between detailed chemistry and empirical models in terms of generality and computational cost. One shortcoming of this approach is that they are usually designed for a specific fuel and

extension of this type of model beyond the operating conditions for which it was developed may lead to unreliable predictions. Kennedy *et. al* [1997] provided a succinct review on the work done before 1997 and pointed out that the current soot models had not yet been universally accepted to use in diffusion flames.

At the stage where many components of soot processes have not yet been unravelled, the semi-empirical approach with acceptable computational cost and a small set of empirical parameters remain the most practical way to estimate soot production for fire safety science. Recently, two semi-empirical analytic models were developed to estimate soot generation rate as a source term in a conservation equation for soot mass fraction [Yao, *et al*., 2011a; Yao, 2010; Lautenberger, 2005; Lautenberger, 2002]. The local mixture fraction, temperature and other global species information are required as inputs. Both models were established on ethylene laminar flames and generalized to other hydrocarbon fuels by using the fuel's laminar smoke point height (L_{sp}) which is a fuel-dependent and measurable parameter. To extend models of this kind to turbulent combustion, conditional source-term estimation or conditional moment closure were proposed. The two models have been successfully applied to predict soot generation rates in several fires. However, the validation cases were laboratory-scale fires and the simulation regions were discretized with meshes with cell size less than 1 mm, which limits their application in large-scale fire simulations.

The above discussion shows that practicality is still crucial to the application of soot generation models in fire simulations. The aim of this study is to develop a general and computationally efficient semi-empirical soot model for non-premixed flames, especially for large-scale turbulent flames. To achieve the goal, the issues below have to be addressed.

Firstly, the rate of soot generation should be modelled as a function of mixture fraction and other global species information rather than detailed intermediate species information, such as cyclic poly-aromatic hydrocarbons. This leads to minimized computational expense and simplifies the soot model. More importantly, estimating soot generation rates from global species information may globalize the model and avoid solving intermediate incipient species, which are usually not fully identified, in particular in fires where in most of the cases the fuels are in the condensed phase.

Another issue is to generalize the model to an arbitrary hydrocarbon fuel with fuel-specific measurable constants. The above two analytical models both assume that 'sooting' propensity

of a fuel of interest is inversely proportional to its laminar smoke point height (L_{sp}), which has been measured for a variety of fuels.

The applicability of a soot model relies heavily upon its ability to deal with a variety of flame types with computational cost kept to a minimum. In turbulent combustion, it is a challenge to model a chemical reaction source term because it is a highly nonlinear function of scalars (temperature, species concentration etc.) and the fluctuations of these scalars are usually not ignorable. The scalars in a highly turbulent reacting flow usually deviate greatly from their mean scalar values, which cause large errors by estimating the source term from the mean values. One solution is to introduce a statistical approach to calculate the source term using a probability density function (PDF) for fluctuating scalars. It is necessary to find a way to incorporate a soot generation model with the PDF approach considering both the accuracy and computational efficiency.

In this chapter, experimental findings and the existing soot models are exploited in the development of a new approach to modelling the soot generation rate in non-premixed ethylene laminar flames. Then the new model is generalized to other hydrocarbon fuels and their fuel-specific model constants are listed. The methodology of incorporating the new model and the PDF approach is presented in detail in this chapter.

7.2 Soot generation and modelling approaches

A number of phenomena are usually considered to be important for soot generation in diffusion flames. Most semi-empirical models treat the soot evolution as processes of nucleation/inception, surface growth, coagulation/agglomeration and oxidation. Incipient soot particles are formed by inception or nucleation in slightly fuel-rich regions of the flame. It is generally agreed that PAHs (Polycyclic aromatic hydrocarbons) are important precursors of primary particles. These primary particles may undergo surface growth by HACA (hydrogen abstraction with acetylene addition) chemical mechanism, with H• atoms impacting on the soot surface to activate acetylene addition, thereby increasing the mass of existing soot particles [Lautenberger *et al.*, 2005]. The small particles coalesce to form larger primary particles by the process of coagulation and line up end-to-end to form larger structures resembling a string of pearls by agglomeration. The physical processes of agglomeration and coagulation increase the particle diameter and decrease the number density while not changing the soot mass/volume fraction. Finally the soot particles transport towards the flame

front where oxidation reduces the mass of soot and the soot not completely oxidized is released from the flame envelope as soot.

7.2.1 Physical and chemical factors affecting soot formation

Section 3.2.3 showed how the soot formation rate is affected by many factors, including pressure, temperature, and gas-phase composition. These factors alter the soot formation rate through changing the circumstances of soot chemical reactions.

Soot formation contains at least two main chemical mechanisms—HACA and PAHs. In hydrocarbon-rich regions, fuel pyrolysis results in particle inception which forms the first soot precursors. The candidates proposed as precursors include a large number of positive hydrocarbon ions, reactive free radicals such as $C_2H\bullet$, $C_2\bullet$, poly-aromatic hydrocarbons (PAH). When H• atom concentration generally exceeds equilibrium values, HACA becomes competitive with PAHs. Hwang *et. al.* [2001] examined counter-flow ethylene diffusion flames and reached a similar conclusion that hydrocarbon radicals played an important role in soot growth when H• atoms were nearly absent in this region. HACA mechanism was the dominant mode of soot formation in the high temperature regions while coagulation of PAHs with soot became important in low temperature regions.

Therefore, soot particles are nucleated in the main heat-release reaction-zone and then transported by convection and thermophoresis into the fuel-rich regions wherein soot mass growth occurs mainly by surface reaction. Traditional models consider that soot growth is controlled by the available surface area. It is the case in premixed flames because the large concentrations of free radicals make the gas-phase reaction rates relatively fast and thus available soot surface area becomes the limit on the formation of soot.

However, soot formation in non-premixed flames is usually not controlled by the soot surface area. Delichatsios [1994] pointed out that the experimental results cannot be readily explained by assuming that the soot formation is dependent on the specific surface area. Lindstedt [1994] modelled soot mass growth proportional to soot surface area and poor agreements were obtained between the predictions and measured soot volume fractions. His predictions on three counter-flow ethylene flames also cast doubt on whether the nucleation is part of the controlling mechanism of soot formation in non-premixed flames as soot volume fractions are

insensitive to the particular form of the nucleation model. Reaction rates are slowed by the presence of hydrocarbons that tend to scavenge H• atoms and other free radicals.

From the above discussion, soot formation rates in non-premixed flames are anticipated to be gas-phase controlled on the fuel-rich side wherein abundant hydrocarbons may exist and temperature is appropriate for chemical reactions.

7.2.2 Physical and chemical factors affecting soot oxidation

Soot oxidation reactions reduce soot mass when soot particles are transported towards the high-temperature and oxygen-rich combustion zone. The species linked to soot oxidation in hydrocarbon flames, most notably OH•, O_2 and O•, play controversial roles in oxidation reaction in non-premixed flames. Most oxygen molecular doesn't react with soot directly. When the temperature is sufficiently high (above 1300 K), molecular oxygen diffused to the reaction zone with super-equilibrium concentration of radicals is immediately consumed by radicals (i.e. O_2+H• $\rightarrow$OH• +O•). Radical OH• is one of the important oxidants and becomes the principal oxidant under a fuel-rich condition and at high temperatures. The molecular oxygen become important only for the O_2 concentration above approximately 5% [Neoh, 1981].

The soot oxidation is a mixing controlled process, of which the oxidation rate is highly dependent on the temperature field, concentration distribution of oxidizing species and soot surface area. The coupled effect of the concentration of oxidizer, flame temperature and soot mass fraction is complicated. Increasing the concentration of oxidizing species increases the number density of oxidizer molecules to contact the soot surface. Temperature of the flame, as an exhibition of enthalpy, controls the momentum and frequency of collision of oxidizer molecules to soot surface and hence also controls the oxidation reaction. Meantime, the flame temperature decreases by the radiation of soot. When the flame is cooled below approximately 1300K, the oxidation slows to the point of releasing soot.

7.3 Beta soot generation model

In this section, a new soot model is developed with global information in non-premixed ethylene laminar flames. The model is generalized to hydrocarbon fuels with smoke point height. Then the new model is combined with the beta probability density function (PDF) for

turbulent combustion simulations. The model has been incorporated in to the frame work of SMARTFIRE.

7.3.1 Basic model

From an engineering standpoint, soot evolution can be simplified into two processes—formation and oxidation—one increases soot mass and the other reduces soot mass. This simplification not only decreases computational expense but also reduces the number of conservation equations. For example, the conservation equation for soot number density is not required to quantify the nucleation/inception process.

As discussed in Section 7.2, it is likely that the dominant factor affecting soot formation is the gas-phase process instead of soot surface area in non-premixed flames. The formation controlled by soot surface is only in the narrow heat-release reaction-zone where the concentrations of free radicals are high. In order to retain simplicity, the model proposed here considers the soot formation to be only homogeneously (volume) gas-phase controlled. Consumption of soot is dependent on the concentration of oxidizing species and surface area of soot. Here soot oxidation is modelled as a surface-area controlled mechanism.

The net rate of soot generation ω_s''' (kg/m^3s) is calculated as:

$$\omega_s''' = \omega_{sf}''' + \omega_{so}'' A_s \rho Y_s \tag{7.1}$$

where ω_{sf}''' (kg/m^{3}s) is the volumetric soot formation rate and ω_{so}'' (kg/m^{2}s) is the surface soot oxidation rate. Here the triple superscript means the volumetric rate while double superscript means the surface rate. Y_s is the soot mass fraction. A_s is the soot particulate surface area and ρ is the flame density. Soot formation rate is a positive term as the process increases the soot mass while oxidation rate is a negative term as the process decreases the soot mass. The analytical forms of these functions for non-premixed ethylene laminar flame will be discussed in the next section.

7.3.2 Analytic soot formation function

Soot is formed during combustion of hydrocarbons under fuel-rich conditions at high temperature. The soot formation rate is determined from the composition of fuel-air and temperature. In the adiabatic condition, the values of temperature, species concentrations and

so on appear to depend strongly on the local instantaneous value of some variables, such as mixture fraction within the mixing field between fuel and oxidation zone. Bilger [1990] pointed out that all information on the elemental composition and enthalpy (temperature) at any point at any instant could be derived from local instantaneous mixture fraction if there is no significant differential molecular diffusion in the turbulent flame. Therefore, the soot formation rate in the adiabatic condition can be calculated as a function of mixture fraction ξ:

$$\omega_{sf}''' = f_{sf}'''(\xi) \tag{7.2}$$

Function $f_{sf}'''(\xi)$ has unit of kg/m^{3}s.

However, fire flames always accompany with radiation, fluid diffusion and so on, which alter the combustion condition and further alter the soot formation rate. To include these effects, the function of soot formation rate is adjusted as:

$$\omega_{sf}''' = g_{sf}(T, T(\xi)) h_{sf}(Y_{ox}, Y_{ox}(\xi)) f_{sf}'''(\xi) \tag{7.3}$$

where T and $T(\xi)$ are the temperatures in non-adiabatic conditions and adiabatic conditions respectively. Y_{ox} and $Y_{ox}(\xi))$ are the mass fractions of oxygen derived from non-adiabatic conditions and adiabatic conditions respectively. $g_{sf}(T, T(\xi))$ and $h_{sf}(Y_{ox}, Y_{ox}(\xi))$ are dimensionless functions that account for the effects on soot formation due to the difference of temperature/oxygen mass fraction between adiabatic and no-adiabatic combustion condition.

Function $f_{sf}'''(\xi)$

Santoro [1994] did experiments for hydrocarbon diffusion flames and examined the relation between the soot formation rate and a global equivalence ratio Φ, which is defined as:

$$\Phi = \frac{A/F_{Stoi}}{A/F} = \frac{1-\xi_{st}}{1-\xi} \tag{7.4}$$

where A/F_{Stoi} is the stoichiometric air and fuel flow rate ratio and A/F is the actual air and fuel flow rates.

Some of the measurements of soot yield value are listed in Table 7.1.

Table 7.1 Measured soot yield value (g/g) against Φ in different ethylene diffusion flames

Fire source \ Φ	0.50	1.00	1.52	2.52	4.00
Ethylene 6.4 cm^3/s, N2 dilution 590 cm^3/s, Fuel tube 22 mm	1.00E-5	1.25E-2	1.29E-2	9.30E-3	1.96E-3
Ethylene 6.4 cm^3/s, N2 dilution 590 cm^3/s, Fuel tube 29 mm	6.40E-3	1.36E-2	1.36E-2	6.22E-3	1.79E-3
Ethylene 3.2 cm^3/s, N2 dilution 590 cm^3/s, Fuel tube 29 mm	3.00E-5	8.33E-3	4.43E-3	7.60E-4	2.00E-5

Table 7.1shows that soot formation starts at the value of around Φ=0.5, and the peak soot yield is produced at the value of Φ between1.00 to 1.52. When the value of Φ is over 4, the formation of soot tends to stop. As mixture fraction ξ has the same monotonicity as Φ, the trend of soot formation rate against mixture fraction is similar to that of Φ.

Similar conclusions have been made by Kent & Honnery [1990] and Warnatz, *et al.*[2006]. They stated that the soot formation rate map is approximately a parabolic curve in a limited range of mixture fraction. Lautenberger *et. al.*[2005] modelled soot formation rate in terms of mixture fraction as a third order polynomial function.

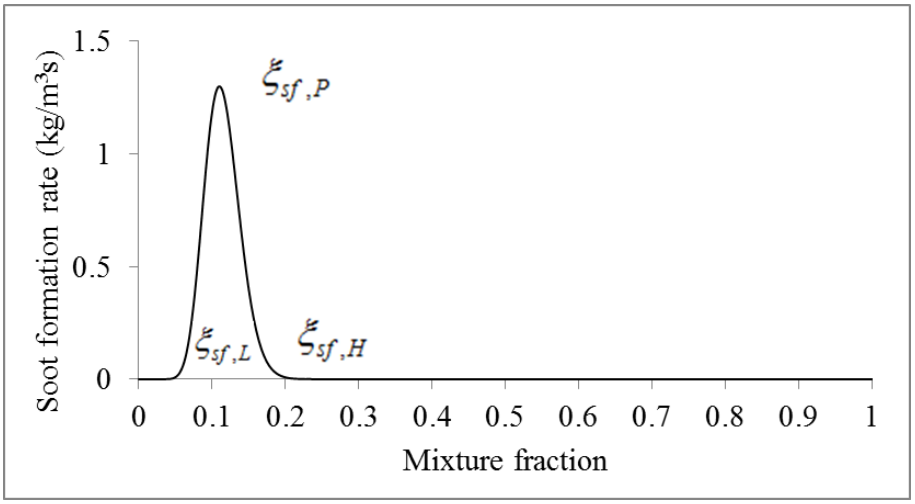

Figure 7.1 Function for soot formation rate.

From the above discussion, it is likely that soot formation rate rises from around zero at a mixture fraction of $\xi_{sf,L}$ to a peak rate at mixture fraction $\xi_{sf,P}$ and then falls back to around zero at mixture fraction $\xi_{sf,H}$ (see Figure 7.1). In this study, a function inspired from the form of beta distribution density function is chosen to describe the soot formation trend. $f_{sf}'''(\xi)$ is written as:

$$f_{sf}'''(\xi) = P_f \frac{\xi^{a_{sf}}(1-\xi)^{b_{sf}}}{\xi_{sf,P}^{\ a_{sf}}(1-\xi_{sf,P})^{b_{sf}}} = P_f' \xi^{a_{sf}}(1-\xi)^{b_{sf}} \tag{7.5}$$

where P_f is the peak soot formation rate with unit kg/m^{3}s and $P_f' = P_f \frac{1}{\xi_{sf,P}^{\ a_{sf}}(1-\xi_{sf,P})^{b_{sf}}}$.

Parameters a_{sf}, b_{sf} are calculated from the value of mixture fraction $\xi_{sf,L}$, $\xi_{sf,P}$. Mixture

fraction $\xi_{sf,H}$ is not considered here as it varies greatly with fuel [Lautenberger, 2002], which will be discussed in Section 7.3.4 and Appendix A.

The function $f_{sf}'''(\xi)$ is a continuous derivative function in the range $0<\xi<1$. To guarantee the shape of the function $f_{sf}'''(\xi)$ in accordance with the changing trend of the function shown in Figure 7.1, the ranges of parameters a_{sf}, b_{sf} must be limited.

Figure 7.1shows $f_{sf}'''(\xi)$ should have one single maximum at $\xi_{sf,P}$. Therefore, the derivative of Equation (7.5) should be zero at $\xi_{sf,P}$:

$$a_{sf}(1-\xi_{sf,P})-b_{sf}\xi_{sf,P}=0 \tag{7.6}$$

From Figure 7.1, the soot formation rate at mixture fraction $\xi_{sf,L}$ is very small compared with that at $\xi_{sf,P}$. The following equation stands at $\xi_{sf,L}$:

$$\frac{\xi_{sf,L}^{\ a_{sf}}(1-\xi_{sf,L})^{b_{sf}}}{\xi_{sf,P}^{\ a_{sf}}(1-\xi_{sf,P})^{b_{sf}}}=\sigma \tag{7.7}$$

where σ is a small value. The value of 0.01 is used for σ here.

To simplify the calculation, logarithm is applied to Equation (7.7):

$$a_{sf}\ln(\frac{\xi_{sf,L}}{\xi_{sf,P}})+b_{sf}\ln\left(\frac{1-\xi_{sf,L}}{1-\xi_{sf,P}}\right)=\ln\sigma \tag{7.8}$$

Equation (7.6) and (7.8) are combined to have a linear equation set for the two variables a_{sf}, b_{sf}, and it is easy to get a solution for a_{sf} and b_{sf}:

$$a_{sf}=\frac{\xi_{sf,P}\ln\sigma}{C_{sf}} \tag{7.9}$$

$$b_{sf}=\frac{(1-\xi_{sf,P})\ln\sigma}{C_{sf}} \tag{7.10}$$

where

$$C_{sf}=\xi_{sf,P}\ln(\frac{\xi_{sf,L}}{\xi_{sf,P}})+(1-\xi_{sf,P})\ln\left(\frac{1-\xi_{sf,L}}{1-\xi_{sf,P}}\right) \tag{7.11}$$

The value of $f_{sf}'''(\xi)$ is calculated from Equation (7.5) and (7.9)-(7.11) with two inputs $\xi_{sf,L}$ and $\xi_{sf,P}$, whose values will be discussed in Section 7.3.4. The value ranges of a_{sf}, b_{sf}, and the formation rate $f_{sf}'''(\xi)$ at mixture fraction greater than $\xi_{sf,P}$ will be discussed in appendix A.

Function $g_{sf}(T, T(\xi))$

Soot formation process depends on temperature in an approximately parabolic form and the peak formation rate occurs over temperatures approximately 1600K [Kent & Honnery, 1990]. In the adiabatic condition, the temperature could be calculated just from the mixture fraction as $T(\xi)$. However, it drifts away from $T(\xi)$ due to radiation or other physical factors in non-adiabatic conditions. Here one variable T_{sf}' is introduced to describe the difference between the temperature T in a non-adiabatic condition and the temperature $T(\xi)$ in the adiabatic condition. Assuming T_P is the temperature at which the soot formation rate reaches the peak, a value of 1625K is used in this study [Lautenberger *et. al.*, 2005]. T_{sf}' is defined as:

$$T_{sf}'(\xi) = \frac{abs(T - T_P) - abs(T(\xi) - T_P)}{T} \tag{7.12}$$

When T_{sf}' >0, the temperature T is farther away from T_P than $T(\xi)$, which means the actual soot formation rate should be smaller than that in the adiabatic condition. When T_{sf}' <0, the temperature T is closer to T_P than $T(\xi)$, which means the actual soot formation rate should be greater than that in the adiabatic condition. Therefore, the variable T_{sf}' has an inverse effect on soot formation rate.

Inspired by the work of Delichatsios [1994], $g_{sf}(T, T(\xi))$ is written as:

$$g_{sf}(T, T(\xi)) = e^{(-T_a T_{sf}'(\xi)/T)} \tag{7.13}$$

where T_a is the activation temperature with a value of 2000 K.

Function $h_{sf}(Y_{ox}, Y_{ox}(\xi))$

In an adiabatic condition, the oxygen mass fraction depends strongly on the local instantaneous value of mixture fraction. Therefore, the oxygen mass fraction in the adiabatic condition can be modelled as a function of mixture fraction $Y_{ox}(\xi)$. The calculation of $Y_{ox}(\xi)$

will be discussed in section 7.3.4. In a non-adiabatic condition, the mass fraction of oxygen Y_{ox} drifts away from $Y_{ox}(\xi)$ because of fluid diffusion and other factors. The difference of oxygen mass fractions between the adiabatic and a non-adiabatic condition is described by $Y'_{ox,\,sf}$.

$$Y'_{ox,\,sf} = \frac{Y_{ox}(\xi) - Y_{ox}}{M_{sf}(\xi)} \tag{7.14}$$

If $\xi \le \xi_{st}$, $M_{sf}(\xi)$ is calculated as

$$M_{sf}(\xi) = Y_{ox}(\xi) \tag{7.15}$$

If $\xi > \xi_{st}$, $Y_{ox}(\xi)$=0. Based on the soot map for a laminar ethylene flame [Kent, & Honnery, 1990], the soot generation region is limited in a small range of mixture fraction. There is no soot generation if the mixture fraction is over about 0.2 or about $3\xi_{st}$. $M_{sf}(\xi)$ is defined as:

$$M_{sf}(\xi) = \frac{\xi - \xi_{st}}{3\xi_{st}}, \text{ if } \xi_{st} < \xi < 3\xi_{st} \tag{7.16}$$

$$M_{sf}(\xi) = 1, \quad \text{if } \xi \ge 3\xi_{st} \tag{7.17}$$

To avoid $M_{sf}(\xi) = 0$ when $\xi = \xi_{st}$, the value of $M_{sf}(\xi)$ is reset as $M_{sf}(\xi) = \max(M_{sf}(\xi), 10^{-3})$.

As oxygen mass fraction has an negative impact on soot formation, the function $h_{sf}(Y_{ox}, Y_{ox}(\xi))$ is expressed as:

$$h_{sf}(Y_{ox}, Y_{ox}(\xi)) = (1 - Y'_{ox,sf})^{-Ro} \tag{7.18}$$

where *Ro* is the stoichiometric molar coefficient for oxygen in the chemical reaction equation of fuel and oxygen.

7.3.3 Analytical soot oxidation function

From the discussion in Section 7.2.2, it shows that soot oxidation in non-premixed flames is controlled by the concentration of the oxidizer and available soot surface in high temperature zones. Therefore, the soot oxidation surface rate is modelled as a function of concentration of oxidant, temperature and mixture fraction. In a adiabatic condition, the information of the oxidant and enthalpy (temperature) can be derived from the local instantaneous mixture fraction, therefore the soot oxidation surface rate is modelled as a mixture fraction dependent function:

$$\omega''_{so} = f''_{so}(\xi) \tag{7.19}$$

In a non-adiabatic condition, however, mixture fraction alone is not sufficient to describe all the information in flames. Some commonly used models [Lee, 1962; Fenimore, 1967; Leung, *et al.*, 1991; Kent, 1985] calculate the oxidation rate as functions of oxygen and temperature. In this model, the factors accounting for the effect of non-adiabatic conditions on the oxidation rate are introduced and included in equation (7.20), it is:

$$\omega''_{so} = g_{so}(T, T(\xi))h_{so}(Y_{ox}, Y_{ox}(\xi)))\, f''_{so}(\xi) \tag{7.20}$$

The function $f''_{so}(\xi)$ has unit of kg/m^{2}s while the other two functions are dimensionless functions. Function g_{so} accounts for the effect on soot oxidation due to the temperature difference between the adiabatic and non-adiabatic conditions. Function h_{so} accounts for the effect on soot oxidation due to the difference of oxygen mass fraction between the adiabatic and non-adiabatic conditions.

Function $f''_{so}(\xi)$

The range of mixture fraction related to soot oxidation has been investigated in a number of previous researches. Smyth [1999] found that the upper limit of mixture fraction range is relative to the stoichiometric mixture fraction. Lautenberger [2005] and Yao *et al.* [2011a] both pointed out that soot is oxidated in a flame region where the mixture fraction is limited in a small range. Lautenberger [2005] modelled soot oxidation rate as a parabolic function of mixture fraction.

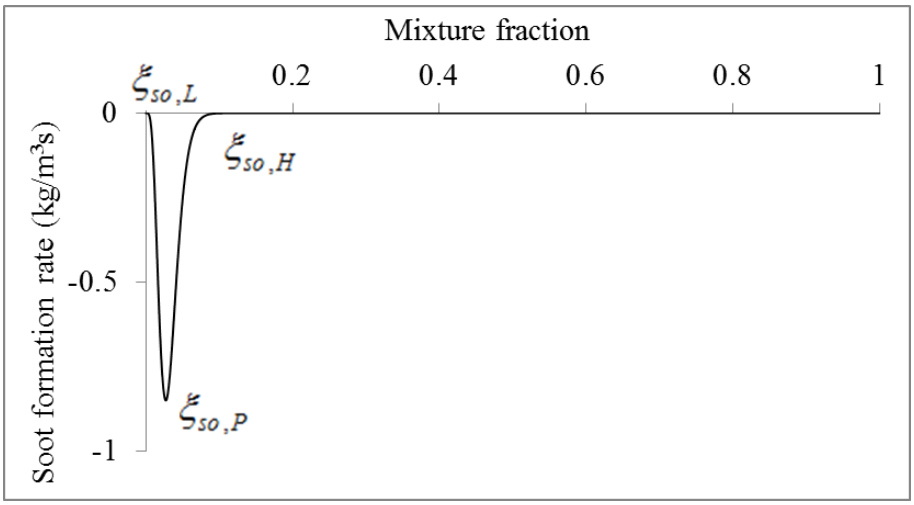

Figure 7.2 Function for soot formation rate.

In this study, similar to the soot formation function, soot oxidation surface rate is modelled to fall from around zero at mixture fraction $\xi_{so,L}$ to its peak negative rate at $\xi_{so,P}$, and then rises to around zero at $\xi_{so,H}$ (see Figure 7.2). A function in the form of the beta distribution density function is chosen to describe the soot oxidation trend:

$$f''_{so}(\xi) = P_o \frac{\xi^{a_{so}}(1-\xi)^{b_{so}}}{\xi_{so,P}{}^{a_{so}}(1-\xi_{so,P})^{b_{so}}} = P'_o \xi^{a_{so}}(1-\xi)^{b_{so}} \tag{7.21}$$

where P_o is the peak negative soot surface oxidation rate with unit kg/m^{2}s and $P_o' = P_o \frac{1}{\xi_{so,P}{}^{a_{so}}(1-\xi_{so,P})^{b_{so}}}$. Parameters $a_{so,}\, b_{so}$ are calculated from the values of mixture fraction $\xi_{so,P}$ and $\xi_{so,H}$. Mixture fraction $\xi_{so,L}$ is not used to determine the parameters and the value of function $f''_{so}(\xi)$ at mixture fraction between $\xi_{so,L}$ and $\xi_{so,P}$ will be discussed in appendix A.

The parameters $a_{so,}\, b_{so}$ are obtained in the similar way to that in the derivation of the soot formation rate in Section 7.3.2. The soot oxidation surface rate ω''_{so} reaches its peak value at $\xi_{so,P}$, and the soot oxidation rate at mixture fraction $\xi_{so,H}$ is relatively small compared with that at $\xi_{so,P}$. The two facts can be expressed in Equations (7.22) and (7.23) as the zero derivative of Equation (7.21) at $\xi_{so,P}$ and a small ratio of the soot oxidation rate at $\xi_{so,H}$ to the peak negative soot oxidation .

$$a_{so}(1-\xi_{so,P}) - b_{so}\xi_{so,P} = 0 \tag{7.22}$$

$$\frac{\xi_{so,H}{}^{a_{so}}(1-\xi_{so,H})^{b_{so}}}{\xi_{so,P}{}^{a_{so}}(1-\xi_{so,P})^{b_{so}}} = \sigma \tag{7.23}$$

The solution of the above simultaneous equations is:

$$a_{so} = \frac{\xi_{so,P}\ln\sigma}{C_{so}} \tag{7.24}$$

$$b_{so} = \frac{(1-\xi_{so,P})\ln\sigma}{C_{so}} \tag{7.25}$$

where

$$C_{so} = \xi_{so,P} \ln(\frac{\xi_{so,H}}{\xi_{so,P}}) + (1-\xi_{sf,P}) \ln\left(\frac{1-\xi_{so,H}}{1-\xi_{so,P}}\right) \quad (7.26)$$

The soot oxidation rate is calculated from Equation (7.21) and (7.24)-(7.26) with two inputs $\xi_{so,P}$. and $\xi_{so,H}$, which are related with the stoichiometric mixture fraction and is discussed in Section 7.3.4.

Function $g_{so}(T, T(\xi))$

In the adiabatic condition, the temperature can be calculated just from mixture fraction as $T(\xi)$. The differences between the adiabatic and non-adiabatic conditions is described by T'_{so}, which is defined as:

$$T'_{so} = \frac{T(\xi) - T}{T} \quad (7.27)$$

In general, soot oxidation increases with the increase of temperature but the accelerated increase slows down with the increasing temperature. When T'_{so} >0, the temperature T is smaller than $T(\xi)$, which means the actual soot oxidation rate should be smaller than that in the adiabatic condition. When T'_{so} <0, the temperature T is larger than $T(\xi)$, which means the actual soot oxidation rate should be greater than that in the adiabatic condition. Therefore, the variable T'_{so} has an inverse effect on soot formation rate.

An expression derived from the work of Delichatsios [1994] is used to describe the effect of T'_{so} on soot oxidation:

$$g_{so}(T, T(\xi)) = (1+T'_{so})^3 e^{(-EaT'_{so}/R_uT(\xi))} \quad (7.28)$$

where R_u is the gas constant with the value of 8.3144 J/mol K. E_a is the activation energy. The value of E_a used in soot models varies from 110 KJ/mol to 164.5kJ/mol [Lall & Zachariah, 2009; Lee, *et.al.*, 1962]. In this study, the value of 143 KJ/mol is used for the activation energy E_a [Nagle, *et.al.*, 1962], which is more appropriate for oxidation reactions in low temperatures.

Function $h_{so}(Y_{ox}, Y_{ox}(\xi))$

In the adiabatic condition, the oxygen mass fraction can be calculated just from the mixture fraction as $Y_{ox}(\xi)$. The difference of oxygen mass fractions between the adiabatic and a non-adiabatic conditions is described by $Y'_{ox,\,so}$, which is defined by Equation (7.14).

If $Y'_{ox,\,so} < 0$, the actual oxygen mass fraction Y_{ox} is greater than $Y_{ox}(\xi)$. Higher mass fraction of oxygen increases soot oxidation rate. If $Y'_{ox,\,so} > 0$, the actual mass fraction of oxidant Y_{ox} is less than $Y_{ox}(\xi)$ which makes the soot oxidation rate lower than that in the adiabatic condition. So soot oxidation surface rate is inversely proportional to $Y'_{ox,\,so}$. Inspired by the work of Lautenberger [2005], the function $h_{so}(Y_{ox}, Y_{ox}(\xi))$ is expressed as:

$$h_{so}(Y_{ox}, Y_{ox}(\xi)) = (1 - Y'_{ox,so}) \tag{7.29}$$

7.3.4 Determination of the soot model parameters

7.3.4.1 Soot model constants

The new model contains six adjustable constants (Four critical mixture fraction $\xi_{sf,L}$, $\xi_{sf,P}$, $\xi_{so,P}$, $\xi_{so,H}$, peak soot volumetric formation rate P_f and soot surface oxidation rate P_o) and one constant (soot surface area A_s**)**. Adjusting the combination of the parameters to achieve reasonable predictions in soot generation is impracticable. Fortunately, the four critical limits of mixture fraction are found to be related to the stoichiometric mixture fraction ξ_{st} and fuel molecular structure according to the studies in [Lautenbergers, 2002; Yao, *et al*., 2011a; Yao, 2010]. Although the model may not be capable of accurately predicting detailed soot volume fraction profiles in flames, it should be capable of capturing global trends of soot generation.

Mixture fraction $\xi_{sf,L}$

The value of $\xi_{sf,L}$ is linked to the position where soot formation starts to dominate soot evolution in the adiabatic condition. Yao's model [2011a; 2010] suggests the critical limit $\xi_{sf,L}$ is calculated for a hydrocarbon fuel in the chemical form C_xH_y with a critical ratio $(C/O)_c$ which is defined by Kumfer et.al [2006]. Lautenbergers [2002] calculates $\xi_{sf,L} = 1.05\xi_{st}$. The values used in these two models are derived from a non-adiabatic condition. In this study, soot is assumed to be formed in fuel rich regions. The value of $\xi_{sf,L}$ is thus defined as:

$$\xi_{sf,L} = \xi_{st} \tag{7.30}$$

Mixture fraction $\xi_{sf,P}$

The value of $\xi_{sf,P}$ is linked to the position where soot formation rate reaches its peak. It is between $\xi_{sf,L}$ and $\xi_{sf,H}$. $\xi_{sf,H}$ is the position where soot formation is assumed to end and is calculated as $\xi_{sf,H} = \psi_{sf,H}\xi_{st}$ in some models [Lautenbergers, 2005; Yao, *et al.*, 2011a;Yao, 2010]. $\psi_{sf,H}$ is assumed to be a fuel-independent constant. The value of $\psi_{sf,H}$ is set to be around 2.15 in Lautenberger's model [2005] and 2.5 in Yao's model [2011a; 2010]. In the early work of Lautenberger [2002], the value of $\psi_{sf,H}$ varies from 1.9 to 3.0 for different fuels. In this study, $\xi_{sf,H}$ is not used to determine the value of $\xi_{sf,P}$ as the value tends to vary with fuel.

The value of $\xi_{sf,P}$ is calculated as:

$$\xi_{sf,P} = 1.9\xi_{st} \tag{7.31}$$

It is a slightly greater than $\xi_{sf,P} = 1.77\xi_{st}$, which was used in a non-adiabatic condition in Lautenberger's model [2005].

Mixture fraction $\xi_{so,P}$

The value of $\xi_{so,P}$ represents the position where soot oxidation surface rate reaches its peak, and can be derived from ξ_{st} by:

$$\xi_{so,P} = 0.85\xi_{st} \tag{7.32}$$

The coefficient in the above equation was set to be 0.84 in Lautenberger's model [2005]. The slight difference in the coefficient between the two models is due to the fact that the one in this study is used in the adiabatic condition and the other is for a non-adiabatic condition.

Mixture fraction $\xi_{so,H}$

Soot oxidation usually occurs on the oxygen-rich side, so the oxidation starts to dominate the soot evolution when mixture fraction falls down to ξ_{st}, therefore, $\xi_{so,H}$ is defined as:

$$\xi_{so,H} = \xi_{st} \tag{7.33}$$

The position of mixture fraction $\xi_{so,L}$ where soot oxidation starts, is not used here to model soot oxidation. Lautenberger [2005] suggested that $\xi_{so,L} = 0.56\xi_{st}$ while Yao [2011a; 2010] set the lower limit $\xi_{so,L} = 0$. As there is a lack of experiments to investigate $\xi_{so,L}$, the lower limit $\xi_{so,L}$ is not applied in this model. The value of $f''_{so}(\xi)$ at mixture fraction less than $\xi_{so,P}$ will be discussed in appendix A.

Soot surface area A_s

Equation (7.1) contains a soot particulate surface area A_s. Studies show that A_s varies from 20 m^2/g to 270 m^2/g [Fairchild, *et.al.*, 1983; Kennedy, *et.al.*, 1991]. The value used in Yao's work [2011a] is applied here.

$$A_s = 1.60 \times 10^5 \quad m^2 / kg \tag{7.34}$$

Peak soot surface oxidation rate P_o

There is no experimental data to determine the peak soot oxidation surface rate. It is assumed to be fuel-independent and a constant value is applied in some models [Lautenbergers, 2002; Yao, *et al.*, 2011a]. This study applies the same value as that used in Lautenbergers' work [2002],

$$P_o = -0.007 \ \ kg / m^2 s \tag{7.35}$$

Peak soot formation rate P_f

Peak soot formation rate P_f is a fuel-dependent parameter in this model. It is found to be 1.1 kg/m^3s [[Lautenbergers, 2005] and 1.0 kg/m^3s [Yao, *et.al.*, 2011b] for a laminar ethylene flame. The value of P_f for an ethylene flame applied in this study is:

$$P_f = 1.0 \, kg / m^3 s \tag{7.36}$$

A method is required to determine the peak soot formation rate for other hydrocarbon fuels.

7.3.4.2 Adiabatic temperature and oxygen mass fraction

Adiabatic temperature

In a mixture of gases, the mass fraction of i^{th} species is Y_i ($i = 1,2,3,\cdots, n$). The enthalpy of the mixture is:

$$h = \sum_i Y_i h_i = \sum_i Y_i \left(h_i^0 + \int_{T_0}^{T} c_{p_i}(T) dT \right) \tag{7.37}$$

where h_i^0 is the enthalpy of the formation of the i^{th} species at the reference temperature T_0, and c_{p_i} is heat capacity of the i^{th} species.

In an adiabatic non-premixed combustion system at initial temperature T_0, reactants (the mass fraction of r^{th} reactant is Y_r) form products (the mass fraction of p^{th} product is Y_p). As no energy is lost/gained in the adiabatic condition, the total energy is perfectly conserved:

$$\sum_r Y_r h_r^0 = \sum_p Y_p h_p \tag{7.38}$$

The enthalpy of the products on the right hand side of Equation (7.38) can be calculated according to Equation (7.37)

$$\sum_p Y_p h_p = \sum_p Y_p \left(h_p^0 + \int_{T_0}^{T} c_{p\,p}(T) dT \right) \tag{7.39}$$

The enthalpy of the reactants can be expressed as a function of mixture fraction by assuming that the fuel and oxidant have equal diffusivities:

$$\sum_r Y_r h_r^0(\xi) = \xi h_{fu}^0 + (1-\xi) h_{ox}^0 \tag{7.40}$$

Therefore, the temperature of an adiabatic combustion system can be expressed as a function of mixture fraction:

$$T(\xi) = T_0 + \frac{\xi h_{fu}^0 + (1-\xi) h_{ox}^0 - \sum_p Y_p h_p^0}{\overline{c_p}} \tag{7.41}$$

where

$$\overline{cp} = \frac{\sum_p Y_p \int_{T_0}^{T} c_{p\,p}(T) dT}{T - T_0} \tag{7.42}$$

An approximate solution is achieved by using constant values of specific heat capacity and the temperature can be expressed as a linear function of the mixture fraction:

$$T(\xi) = T_0 + (T_{ad} - T_0) \frac{1-\xi}{1-\xi_{st}} \quad \text{if } \xi > \xi_{st} \tag{7.43}$$

$$T(\xi) = T_0 0 + (T_{ad} - T_0) \frac{\xi}{\xi_{st}} \quad \text{if } \xi \le \xi_{st} \tag{7.44}$$

where T_{ad} is the adiabatic flame temperature that results from a complete combustion taken place adiabatically. It can be calculated from Equation (7.41) with $\xi = \xi_{st}$.

Adiabatic oxygen mass fraction

The chemical reaction is assumed to be a global one-step, infinitely fast process, where the fuel reacts with the oxidant in the stoichiometric proportions to form products:

$$1\,kg\,of\ \ fuel + s\,kg\,of\ \ o\text{xidant} \rightarrow (1+s)\,kg\,of\ \ p\text{roducts}$$

where $s = (1-\xi_{st})/\xi_{st}$.

If mixture fraction $\xi \le \xi_{st}$, then there is an excess of oxidant and no fuel is present in the mixture. Hence $Y_{fu} = 0$. According to Equation (2.69),

$$Y_{ox}(\xi) = Y_{ox,0} - \xi(sY_{fu,1} + Y_{ox,0}) \tag{7.45}$$

where suffix 0 denotes the oxidant stream and 1 denotes the fuel stream. The local value of ξ equals 0 if the mixture at a point contains only oxidant and equals 1 if it contains only fuel.

If $\xi > \xi_{st}$, then there is an excess of fuel in the mixture and there is no oxidant:

$$Y_{ox}(\xi) = 0 \tag{7.46}$$

7.3.5 Determination of P_f for a hydrocarbon fuel

In order to use the new model with respects to other fuels than ethylene in fires, a procedure is required to determine the peak soot formation rate P_f of the fuel concerned. For engineering applications, it is necessary to estimate the peak soot formation rate from some fuel-specific constants.

A fuel's laminar smoke point (L_{sp}) is the maximum height of its laminar flame burning in air at which soot is not released from the flame tip. It is a fuel-specific measurable constant. Lautenberger [2005] drew a conclusion that the peak soot formation rate could be expressed as:

$$P_f = P_{f,C_2H_4}\left(\frac{L_{sp,C_2H_4}}{L_{sp}}\right)\left(\frac{M_{C_2H_4}}{M_f}\right)^a\left(\frac{p_0}{p^o}\right)^2 Y_{FT} \tag{7.47}$$

where M_f is the fuel's molecular weight and $M_{C_2H_4}$ is the molecular weight of ethylene, p_0 is the background pressure and p^0 is the reference pressure (101.3 kPa). Y_{FT} is the mass fraction of fuel in the fuel supply stream. The value of the exponent *a* is uncertain, but set 0 for mixtures of hydrocarbon fuels.

Delichatsios [1994] pointed out that the peak soot formation rate is inversely proportional to the smoke point height (L_{sp}), which is consistent with Equation (7.47) with *a*=0:

$$L^{-1}{}_{sp} \propto P_f \tag{7.48}$$

In this work, the above relation between the smoke point height L_{sp} and peak soot formation rate is used to calculate P_f. As the peak soot formation rate for ethylene is known as P_{f,C_2H_4}=1 kg/m^{3}s, $P_{f,fuel}$ for any other fuel can be deduced by

$$\frac{P_{f,fuel}}{P_{f,C_2H_4}} = \frac{L_{sp,C_2H_4}}{L_{sp,fuel}} \tag{7.49}$$

L_{sp} is a characteristics of 'sooting' propensity for each hydrocarbon fuel and the value of some common fuels can be found in [Hunt, 1953; Yao, 2010].

For multi-component fuels, $P_{f,total}$ is estimated as the mean of each of component's $P_{f,k}$ weighted by its mole fraction M_k:

$$P_{f,total} = \sum P_{f,k} \times M_k \tag{7.50}$$

The peak soot formation rates for a variety of fuels are listed in Table 7.2 which is derived by the laminar smoke point heights (L_{sp}) of the fuels published in [Hunt, 1953; Tewarson, 1988]. The corresponding peak soot formation rates P_f for these fuels are calculated from Equation (7.49).

Table 7.2 Laminar smoke point height and peak soot formation rate for hydrocarbon fuels

Fuel		L_{sp} (mm)	P_f
Aliphatic hydrocarbon	Methane	--	0.0177
	Acetylene	19	5.5790
	Ethylene	106	1.0000
	Propane	162	0.6543
	Propylene	29	3.6552
	n-Hexane	149	0.7113
	2-Methylpentane	137	0.7737
	3-Methylpentane	135	0.7852
	2,2-Dimethylbutane	114	0.9298
	2,3-Dimethylbutane	120	0.8833
	n-Heptane	147	0.7212
	2-Methylhexane	136	0.7793
	2,4-Dimethylpentane	117	0.9060
	n-Octane	149	0.7113
	2-Methylheptane	137	0.7737
	3-Methylheptane	126	0.8413
	3-Ethylhexane	117	0.9060
	2,2-Dimethylhexane	100	1.0600
	2,3-Dimethylhexane	123	0.8618
	2,2,4-Trimethylpentane	86	1.2325
	n-Decane	139	0.7627
	n-Undecane	142	0.7465
	n-Dodecane	137	0.7737
	n-Tetradecane	137	0.7737
	1-Hexene	88	1.2045
	1-Heptene	96	1.1042
	2-Heptene	91	1.1648
	1-Octene	99	1.0707
	2-Octene	99	1.0707
	1-Decene	94	1.1277
	1-Dodecene	96	1.1042
	1-Tetradecene	91	1.1648
	1-Hexadecene	94	1.1277
	1-Octyne	24	4.4167
	1-Dodecyne	36	2.9445
	Cyclohexane	117	0.9060
	Methylcyclohexane	94	1.1277
	Ethylcyclohexane	96	1.1042
	Cyclopentane	84	1.2618
	Bicyclohexyl	56	1.8928
	Decalin	38	2.7895
	Cyclohexene	47	2.2553
Aromatic hydrocarbon	Benzene	66	1.6060
	Toluene	48	2.2083
	Ethylbenzene	64	1.6563
	p-Xylene	56	1.8928
	n-Propylbenzene	78	1.3590

Table 7.3 Laminar smoke point height and peak soot formation rate for hydrocarbon fuels (continue)

	Cumene	71	1.4930
	Mesitylene	56	1.8928
	Mixed trimethylbenzenes	56	1.8928
	p-Cymene	61	1.7377
	n-Butylbenzene	80	1.3250
	Isobutylbenzene	68	1.5588
	sec-Butylbenzene	76	1.3947
	tert-Butylbenzene	63	1.6825
	sec-Amylbenzene	81	1.3087
	tert-Amylbenzene	66	1.6060
	Mixed diethylbenzenes	58	1.8277
	Tetralin	48	2.2083
	Naphthalene	42	2.5238
	1-Methylnaphthalene	37	2.8648
	2-Methylnaphthalene	37	2.8648
	Diphenyl	44	2.4092
	Styrene	56	1.8928
	Phenylcyclohexane	66	1.6060
Sulfur and Nitrogen hydrocarbon	n-Hexyl mercaptan	102	1.0392
	n-Heptyl mercaptan	132	0.8030
	n-Decyl mercaptan	119	0.8908
	Benzyl mercaptan	6	17.6667
	o-Thiocresol	3	35.3333
	Thiophenol	5	21.2000
	n-Hexyl sulphide	114	0.9298
	n-Heptyl sulphide	104	1.0192
	n-Octyl sulphide	87	1.2183
	n-Decyl sulphide	51	2.0785
	Phenyl sulphide	4	26.5000
	p-Cresolmethyl sulfide	3	35.3333
	Thiophene	33	3.2122
	Diethylamine	103	1.0292
	Triethylamine	122	0.8688
	n-Butylamine	104	1.0192
	Di-n-butylamine	112	0.9465
	sec-Butylamine	114	0.9298
	Aniline	15	7.0667
	n-Butylaniline	17	6.2353
	Pyridine	29	3.6552
	α-Picoline	19	5.5790
	β-Picoline	13	8.1538
	γ-Picoline	19	5.5790
	Quinoline	6	17.6667
	Isoquinoline	5	21.2000

7.3.6 Application in turbulent flames

There are fluctuations for the scalars (mixture fraction, temperature, species concentrations etc.) in turbulent reacting flow. Generally, these scalars are calculated in the form of Favre mean, which eliminates the fluctuations using a density weighted average. However, Favre means cannot include all the information of instantaneous scalars at any point at any instant. Soot generation reaction rate is a highly nonlinear function of these scalars. So the calculation of soot generation rate in turbulent combustion is not as straightforward as that in laminar combustion.

Sections 7.3.2-7.3.3 estimate soot formation volume/oxidation surface rate in laminar flames as:

$$\omega_{sf}''' = g_{sf} h_{sf} f_{sf}'''(\xi) \tag{7.51}$$

$$\omega_{so}'' = g_{so} h_{so} f_{so}''(\xi) \tag{7.52}$$

$f_{sf}'''(\xi)$ and $f_{so}''(\xi)$ are functions of mixture fraction. $g_{sf}(T, T(\xi))$ and $g_{so}(T, T(\xi))$ are functions of temperature difference between the adiabatic and non-adiabatic conditions. $h_{sf}(Y_{ox}, Y_{ox}(\xi))$ and $h_{so}(Y_{ox}, Y_{ox}(\xi))$ are functions with the difference of oxygen mass fraction between the adiabatic and non-adiabatic conditions.

The variables in Equations (7.51)-(7.52) should be local instantaneous scalars if these equations are applied in turbulence. To simplify the problems, some assumptions are made:

- The effect on soot generation due to different temperature/oxygen mass fraction between the adiabatic and non-adiabatic conditions is independent of the fluctuation of mixture fraction.
- Fluctuations of soot mass fraction is independent of the fluctuation of mixture fraction

The four functions $g_{sf}(T, T(\xi))$, $g_{so}(T, T(\xi))$, $h_{sf}(Y_{ox}, Y_{ox}(\xi))$ and $h_{so}(Y_{ox}, Y_{ox}(\xi))$ are used to describe the effect on soot generation due to a non-adiabatic condition. Based on the above assumptions, the effect on soot generation due to a non-adiabatic condition is independent of the fluctuation of the mixture fraction. Therefore, the Favre means, instead of local instantaneous values for the scalars (temperature, oxygen mass fraction and mixture fraction), are applied in the four functions. The functions in Equations (7.51)-(7.52) can be written as follows in a turbulent flame:

$$f_{sf}'''(\xi) = P_f' \xi^{a_{sf}} (1-\xi)^{b_{sf}} \tag{7.53}$$

$$f''_{so}(\xi) = P'_o \xi^{a_{so}} (1-\xi)^{b_{so}} \tag{7.54}$$

$$g_{sf}(T, T(\xi)) = e^{(-T_a T'_{sf}(\tilde{T},\tilde{\xi})/\tilde{T})} \tag{7.55}$$

$$h_{sf}(Y_{ox}, Y_{ox}(\xi)) = (1 - Y'_{ox,so}(\tilde{Y}_{ox}, \tilde{\xi}))^{-Ro} \tag{7.56}$$

$$g_{so}(T, T(\xi)) = (1 + T'_{so}(\tilde{T}, \tilde{\xi}))^3 e^{(-EaT'_{so}(\tilde{T},\tilde{\xi})/R_u T(\tilde{\xi}))} \tag{7.57}$$

$$h_{so}(Y_{ox}, Y_{ox}(\xi)) = (1 - Y'_{ox,so}(\tilde{Y}_{ox}, \tilde{\xi})) \tag{7.58}$$

Equation (7.55)-(7.58) are functions with the Favre means of the mixture fraction, temperature and oxygen mass fraction. The mixture fraction in Equation (7.53)-(7.54), however, is an instantaneous value.

The mixture fraction in functions $f'''_{sf}(\xi)$ and $f''_{so}(\xi)$ are local instantaneous values. Soot formation/oxidation reactions occur within very small ranges of mixture fraction, thus accurate prediction of the mixture fraction is essential to estimate the soot generation in a flame. The first problem that needs to be addressed is how to describe the mixture fraction fluctuations if the flow is turbulent. In Chapter 3, the probability density function (PDF) method presents a very general statistical description of turbulent reacting flows. The density-weighted PDF $\tilde{P}(\xi)$ for the mixture fraction ξ is chosen to be the beta distribution, which has been proved to be an accurate description of fluctuations in turbulent combustion:

$$\tilde{P}(\xi) = \frac{\xi^{\alpha-1}(1-\xi)^{\beta-1}}{B(\alpha,\beta)} \tag{7.59}$$

where $B(\alpha,\beta) = \int_0^1 x^{\alpha-1}(1-x)^{\beta-1}dx$ denotes the beta function. The two constants in the distribution are derived from the Favre mean of mixture fraction ($\tilde{\xi}$) and Favre-average variance ($\tilde{\xi}''^2$):

$$\alpha = \tilde{\xi}\left(\frac{\tilde{\xi}(1-\tilde{\xi})}{\tilde{\xi}''^2} - 1\right) \tag{7.60}$$

$$\beta = \alpha\frac{(1-\tilde{\xi})}{\tilde{\xi}} \tag{7.61}$$

Both $\tilde{\xi}$ and $\tilde{\xi}''^2$ are positive quantities and $0 < \tilde{\xi}''^2 < \tilde{\xi}(1-\tilde{\xi})$ should be checked before the beta PDF is used.

The main problem of the soot model in turbulent combusting flows arises from calculating the average soot formation/oxidation terms $\overline{\omega_{sf}'''}$ and $\overline{\omega_{so}''}$ from the Favre mean of mixture fraction by the PDF method. The source term is averaged by PDF-weight as:

$$\overline{\omega_{sf}'''} = \left\langle \omega_{sf}''' \mid \xi \right\rangle = \int_0^1 \omega_{sf}'''(\xi)\tilde{P}(\xi)d\xi = g_{sf}h_{sf}\int_0^1 f_{so}'''(\xi)\tilde{P}(\xi)d\xi \tag{7.62}$$

$$\overline{\omega_{so}''} = \left\langle \omega_{so}'' \mid \xi \right\rangle = \int_0^1 \omega_{so}''(\xi)\tilde{P}(\xi)d\xi = g_{so}h_{so}\int_0^1 f_{so}''(\xi)\tilde{P}(\xi)d\xi \tag{7.63}$$

By substituting the soot formation rate (Equation (7.5)) and beta PDF (Equation (7.59)) in the conditional formation source term (Equation (7.62)), we get:

$$\begin{aligned}\overline{\omega_{sf}'''} = \left\langle \omega_{sf}''' \mid \xi \right\rangle &= g_{sf}h_{sf}\int_0^1 P_f'\xi^{a_{sf}}(1-\xi)^{b_{sf}} \cdot \frac{\xi^{\alpha-1}(1-\xi)^{\beta-1}}{B(\alpha,\beta)}d\xi \\ &= \frac{g_{sf}h_{sf}P_f'}{B(\alpha,\beta)}\int_0^1 \xi^{\alpha+a_{sf}-1}(1-\xi)^{\beta+b_{sf}-1}d\xi\end{aligned} \tag{7.64}$$

The integration term in the above Equation (7.64) is a beta function:

$$B(\alpha+a_{sf},\beta+b_{sf}) = \int_0^1 \xi^{\alpha+a_{sf}-1}(1-\xi)^{\beta+b_{sf}-1}d\xi \tag{7.65}$$

Equation (7.64) is simplified to:

$$\overline{\omega_{sf}'''} = \left\langle \omega_{sf}''' \mid \xi \right\rangle = \frac{g_{sf}h_{sf}P_f'}{B(\alpha,\beta)} \cdot B(\alpha+a_{sf},\beta+b_{sf}) \tag{7.66}$$

Similarly, soot oxidation rate can be expressed as

$$\overline{\omega_{so}''} = \left\langle \omega_{so}'' \mid \xi \right\rangle = \frac{g_{so}h_{so}P_o'}{B(\alpha,\beta)} \cdot B(\alpha+a_{so},\beta+b_{so}) \tag{7.67}$$

From Equation (7.66) and (7.67), the average soot formation volume/oxidation surface rates are related to the two beta functions. As there are several methods with low computational cost for calculating the beta function, the turbulent soot model is computationally efficient.

7.3.7 Incorporating the soot generation model within SMARTFIRE

The soot model proposed in the previous sections is incorporated in to the commercial CFD package SMARTFIRE.

In flows with large variations of density, such as a flow with combustion, the Favre-averaged transport equations are used to describe the conservation of scalars. The equations of mixture fraction, mixture fraction variance, enthalpy and soot mass fraction are solved in conjunction with the k-ε turbulence model, which involves two additional partial differential equations for the turbulent kinetic energy k, and the energy dissipation rate ε. The general form of the Favre-averaged transport equation for any scalar ϕ can be expressed as:

$$\frac{\partial(\overline{\rho}\widetilde{\phi})}{\partial t} + div(\overline{\rho}\widetilde{\phi}\widetilde{\vec{U}}) = div(\Gamma grad\widetilde{\phi}) + \overline{S}_{\phi} \tag{7.68}$$

where $\widetilde{\phi}$ and $\widetilde{\vec{U}}$ represent the Favre-averaged of the scalar ϕ and the flow velocity respectively. $\overline{S}_{\phi}$ is the mean source term of scalar ϕ. Γ is the diffusion coefficient of scalar ϕ. The detail of coefficients Γ and source term $\overline{S}_{\phi}$ for various equations are presented in Table 7 .3.

Table 7.4 Diffusion coefficient and source term in the transport equation of variable ϕ

ϕ	Γ_{ϕ}	$\overline{S}_{\phi}$
k	$\mu + \frac{\mu_t}{\sigma_k}$	$G_k + G_B - \overline{\rho}\varepsilon$
ε	$\mu + \frac{\mu_t}{\sigma_{\varepsilon}}$	$C_{1\varepsilon}\frac{\varepsilon}{k}G_k - C_{2\varepsilon}\overline{\rho}\frac{\varepsilon^2}{k}$
$\widetilde{\xi}$	$\mu + \frac{\mu_t}{\sigma_t}$	0
$\widetilde{\xi}''^2$	$\mu + \frac{\mu_t}{\sigma_t}$	$C_{g1}\mu_t\left(\frac{\partial\widetilde{\xi}^2}{\partial x_i}\right)^2 - C_{g2}\overline{\rho}\frac{\varepsilon}{\kappa}\widetilde{\xi}''^2$
$\widetilde{h}$	$\frac{k}{C_p} + \frac{\mu_t}{\mathrm{Pr}_t}$	$\overline{S}_{rad}$
$\widetilde{Y}_s$	$\frac{\mu_t}{\sigma_t}$	$\overline{\omega}_s$
σ_k=1, σ_{ε}=1.3, σ_t=0.85, $C_{\varepsilon 1}$=1.44, $C_{\varepsilon 2}$=1.92, C_{g1}=2.0, C_{g2}=2.8		

In Table 7.3, $\widetilde{Y}_s$ is the Favre mean soot mass fraction. As soot particles are much heavier and larger than gas-phase molecules, soot diffusivity is neglected. The soot source term $\overline{\omega}_s$ is calculated from Equation (7.1) and (7.66)-(7.67).

The density $\overline{\rho}$ is two-phase (total) density:

$$\overline{\rho}^{-1} = \frac{\widetilde{Y}_s}{\rho_{soot}} + \frac{1-\widetilde{Y}_s}{\rho_{gas}} \tag{7.69}$$

The source term for the total enthalpy equation $\overline{S}_{rad}$ accounts for the enthalpy gain/loss due to radiation. The effect of soot concentrations on radiation is included by adding the absorption coefficient of soot into that of gas

$$\kappa = \kappa_g + \kappa_s \tag{7.70}$$

Generally, soot contribution to the total absorption coefficient is an order of magnitude greater than that of gas species. The soot absorption coefficient is approximately proportional to the soot volume f_v as the majority of soot particles has a size in the range of 10^2 nm:

$$\kappa_s = C f_v T \tag{7.71}$$

where C =1226.0 $(mK)^{-1}$ and the mean soot volume f_v is calculated from the mass fraction $\widetilde{Y}_s$:

$$f_v = \frac{\overline{\rho}\widetilde{Y}_s}{\rho_s} \tag{7.72}$$

Here the soot particle density ρ_s =1800.0 kg/m^3.

7.4 Conclusion

This chapter presents the second original contribution to the dissertation and addresses Objectives 2(a) to 2(c). In this chapter, a global soot model has been developed to estimate soot generation rate in the non-premixed flames in an efficient way.

The BSG model simplifies soot evolution into two processes: formation which increases soot mass and oxidation which reduces soot mass. The net rate of soot generation ω_s''' (kg/m^3s) is calculated from the volumetric soot formation rate ω_{sf}''' (kg/m^3s) and the surface soot oxidation rate ω_{so}'' (kg/m^2s) as Equation (7,1).

The model first developed an approach to calculate the formation rate and oxidation rate for adiabatic laminar flames, and then it was extended to non-adiabatic laminar flames. By making use of the characteristics of the probability density function of the beta distribution in the PDF approach, the BSG model can be applied to turbulent flames with relatively low cost

in terms of computational resources. The method of calculating soot formation rate and oxidation rate for different flames is outlined as follows.

BSG model for adiabatic laminar flames

As all information on the elemental composition and enthalpy (temperature) at any point at any instant can be derived from local instantaneous mixture fraction in laminar flames [Bilger, 1990], the rate in the adiabatic condition can be calculated as functions of mixture fraction:

$$\omega_{sf}''' = f_{sf}'''(\xi) = P_f' \xi^{a_{sf}} (1-\xi)^{b_{sf}} \quad (7.73)$$

$$\omega_{so}'' = f_{so}''(\xi) = P_o' \xi^{a_{so}} (1-\xi)^{b_{so}} \quad (7.74)$$

P_f' is a fuel-specific parameter. a_{sf}, b_{sf} $a_{so,}$ b_{so} and P_o' are related to the stoichiometric mixture fraction ξ_{st} and fuel molecular structure.

BSG model for non-adiabatic laminar flames

In a non-adiabatic condition, however, mixture fraction alone is not sufficient to describe all the information in flames. To include these effects such as radiation, fluid diffusion, the rates are adjusted as:

$$\omega_{sf}''' = g_{sf} h_{sf} f_{sf}'''(\xi) \quad (7.75)$$

$$\omega_{so}'' = g_{so} h_{so} f_{so}''(\xi) \quad (7.76)$$

g_{sf} / g_{so} and h_{sf} / h_{so} are dimensionless functions that account for the effects on soot formation/oxidation due to the difference of temperature/oxygen mass fraction between adiabatic and no-adiabatic combustion conditions.

BSG model for turbulent flames

The soot generation rate defined in Equations (7.75) and (7,76) is calculated from highly nonlinear functions of the scalars (mixture fraction, temperature etc.), which intensely fluctuate in the turbulent reacting flow. Generally, these scalars are calculated in the form of Favre mean, which cannot include all the information of instantaneous scalars at any point at any instant. The BSG model applies the probability density function (PDF) method to describe the fluctuations of turbulent flows. The PDF for the mixture fraction ξ is chosen to be the beta distribution. The source term is averaged by PDF-weight and simplified by the characteristics of beta PDF as:

$$\overline{\omega_{sf}'''} = \left\langle \omega_{sf}''' \mid \xi \right\rangle = \frac{g_{sf} h_{sf} P_f'}{B(\alpha,\beta)} B(\alpha + a_{sf}, \beta + b_{sf}) \tag{7.77}$$

$$\overline{\omega_{so}''} = \left\langle \omega_{so}'' \mid \xi \right\rangle = \frac{g_{so} h_{so} P_o'}{B(\alpha,\beta)} B(\alpha + a_{so}, \beta + b_{so}) \tag{7.78}$$

The two constants α,β are derived from the Favre mean of mixture fraction ($\tilde{\xi}$) and Favre-average variance ($\tilde{\xi}''^2$). *B* denotes the beta function.

This semi-empirical model involves 7 parameters, but only the peak soot formation rate P_f is a fuel-specific measureable parameter. As 'sooting' propensity of a fuel is related to its laminar smoke point height (L_{sp}), the model is extended to any hydrocarbon fuel by assuming the peak soot formation rate is inversely proportional to L_{sp}. The values of L_{sp} for a variety of fuels have been listed in Table 7.2.

The most outstanding feature of the model is how it can be coupled with the PDF approach in turbulent combustion simulation without a significant increase of computational cost. In next chapter, the performance of the Beta soot generation model is investigated by simulating two turbulent pool fires.

Chapter 8
Simulating turbulent flames using the Beta soot generation model

In this chapter, simulations of two buoyant turbulent diffusion flames are performed using the Beta soot generation model proposed in Chapter 7. It begins with the introduction of the experiments, followed by the numerical model set up together with the comparison between predictions and measurements.

8.1 Introduction

Modelling soot generation rate in turbulent flames is greatly different from that in laminar ones because the soot generation rate is very sensitive to the changes of scalars, such as mixture fraction, temperature, and there are usually non-negligible fluctuations in these scalars. Some soot generation models close the soot generation chemical source term with the CMC method. However, they are likely to be mesh sensitive and computationally expensive.

The soot generation rate in the Beta soot generation model, which was developed in the last chapter, is modelled as a global function of the mixture fraction, temperature and oxygen mass fraction in the laminar flames. The function is a combination of several power functions and exponential functions, of which calculation cost is very low. It is extended to turbulent flames with a PDF approach. The additional computation is just one conservation equation of mixture fraction variance and computation of two beta functions, with just a slight increase in the computational cost compared with the calculation in laminar flames.

In this chapter, we apply the Beta soot generation model to predict soot distribution in two turbulent methane and ethylene pool fires. The details of the experiments and measurements are introduced first, followed by the numerical details of the soot model. Then the predictions are compared with the experimental data. In addition, the computational cost of the model is compared with the Conventional Model for the methane fire.

8.2 Experiments and measurements

The turbulent buoyant diffusion flames were established on a diffuser burner with exit diameter D= 7.1 cm fuelled by methane or ethylene [Xin & Gore, 2005; Xin, *et al.*, 2005]. The burning occurred in quiescent ambient air in an open environment and planar laser-induced incandescence (LII) technique was used to obtain data for soot model validation. The gaseous fuel was adjusted along the burner and formed a uniform velocity distribution of 3.14 cm/s at the burner exit in the methane fire. The fuel velocity for ethylene is not provided directly but could be derived from the fuel flow rate. The information of the fuel flow rates and the visible flame heights in the two flames are listed in Table 8.1.

Table 8.1 Fuel flow of methane and ethylene fire

Experiment	Fuel velocity (m/s)	Fuel flow rate (kg/s)	Visible flame height (m)
Methane	0.0314	8.43×10^{-5}	0.364
Ethylene	0.0190	7.28×10^{-5}	0.388

Instantaneous LII images of 2 cm high were collected to observe the instantaneous soot distributions at 20 evenly spaced elevations which cover the entire flame height. Then, 3500 samples of the soot volume fraction were measured to study the statistics and the average soot volume fractions at each of the five elevations of H=1/2D, 1D, 2D, 3D, and 4D were obtained. H is the elevation above the burner exit and D is the diameter of the burner. However, the information at 1/2D couldn't be found in the publications [Xin & Gore, 2005; Xin, *et al.*, 2005].

Except for soot volume fractions in the mathen fire, the measurements included the vertical and horizontal velocities, concentration of species such as CH_4, C_2H_2, H_2, CO, O_2 and N_2. Assuming an adiabatic condition, the mean temperature was calculated from the mean species concentrations without considering the effects of cross correlation between species, temperature and specific heat. The mean mixture fraction was computed from the mean species concentrations based on its definition. For the ethylene fire, neither species concentrations nor temperature was provided.

8.3 Numerical details

8.3.1 Simulations

The commercial fire simulation tool—SMARTFIRE—was used to simulate the two flames. The fuel exit was modelled as an inlet with a constant fuel rate as shown in Table 8.1. In these simulations, the *k*-*ε* model was used to describe the turbulence of the flow field. Combustion of the gaseous fuel was modelled with the eddy dissipation combustion model (EDM). The methane fuel was commercial grade 1.3 with purity not less than 93% (mole fraction). The average heat of combustion for the commercial methane fuel was 5.0MJ/kg, which was derived from the measured total heat release rate 4.2 kW. The ethylene fuel was commercial grade 2.5, whose purity was not less than 99.5 %. Thus heat of combustion for purity ethylene 5.0 MJ/kg was used here for the ethylene fuel. A multi-ray radiation model was used to represent the exchange of heat due to radiation. The newly proposed soot model—Beta soot generation model— was applied to calculate the soot generation rate.

It was observed that the fires were very weak, and sensitive to any small disturbance. In order to successfully model the fire flow field, a computational domain was required to be sufficiently large to exclude the negative effect of boundary entrainment. The whole computation domain used in the simulation of Yao [2010] was a 30×30 cm^2 with 60 cm height cylinder. In order to save computation cost, the computation domain was defined as a 30×15×60 cm^3 rectangular cuboid in this study. The burner exit was modelled as a square inlet rather than a circular section, which is located on the centre of the cuboid's bottom. The size of the side of the square inlet was 7 cm. The face of the cuboid on the end of the shortest side passing through the centre of the inlet was set as a symmetric boundary. As the fires occurred in an open environment, the boundaries except the symmetric face in the computation domain, are treated as outlet.

8.3.2 Mesh sensitive analysis

To analyse the mesh sensitivity of the model, two meshes were used in discretization of the computational domain.

The coarse Cartesian mesh was unevenly distributed in the cuboid domain. The total number of cells was 71,200 and the minimum cell size was 4×3.5×5 mm^3. The mesh was finer in the combustion region and gradually changes to coarser from the centre to the edges of the

computation domain. The finer mesh contains total 324,000 cells and the minimum cell size was 1.4×1.4×2 mm^3.

The mesh sensitivity of the simulations was analysed by comparing the predictions of the temperatures and mixture fractions at 0.1 m height above the burner exit in the methane fire.

Temperature

Figure 8.1shows the temperatures at 0.1 m above the burner exit predicted with the two meshes. The temperature derived from the coarse mesh dovetails nicely with that from the finer mesh at most locations, with a variation of about 7% between the two predictions.

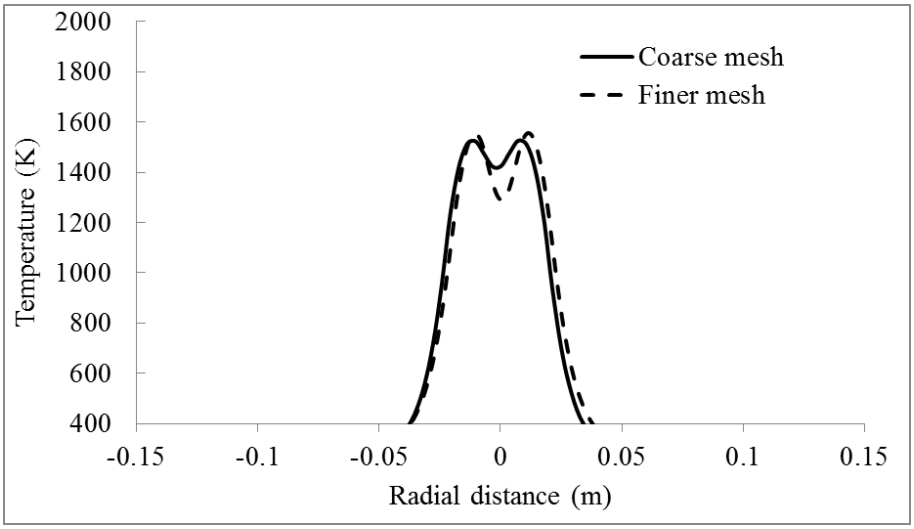

Figure 8.1. Temperature at 0.1 m height above the burner exit with the coarse mesh and the finer mesh.

Mixture fraction

The predicted mixture fractions at 0.1 m height above the burner exit are shown in Figure 8.2. Both meshes give similar distributions of mixture fraction at this height, except the peak value in the centreline. The peak mixture fraction with the coarse mesh was predicted to be about 10% less than that with the fine mesh at this height.

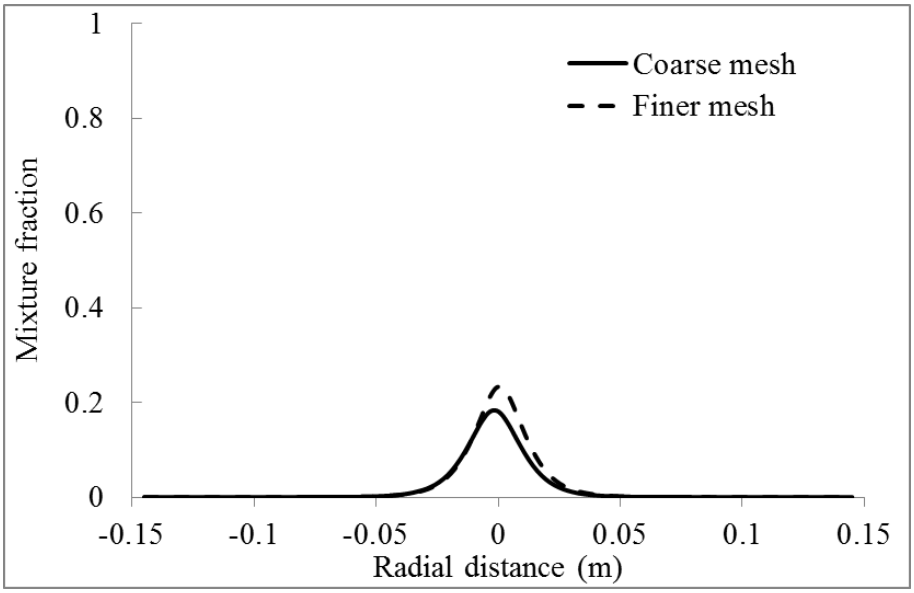

Figure 8.2. Mixture fraction at 0.1 m height above the burner exit with the coarse and the finer mesh.

Thus it is reasonable to assume that the accuracy of the numerical results of the simulation cannot be significantly improved with a further finer mesh and the coarse mesh is adequate to provide a solution with a satisfactory accuracy. The following discussion is therefore based on the results from the simulations with the coarse mesh.

8.3.3 The parameters in the Beta soot generation model

Although there are 7 parameters in the Beta soot generation model, most of them are constant or determined by the stoichiometric mixture fraction, except the peak soot formation rate. The Beta soot generation model calculates the peak soot formation rate as inversely proportional to the smoke point height L_{sp}, of which value is listed in Table 7.2 for some widely used combustible materials.

The peak soot formation rate for methane cannot directly be applied in this simulation as the commercial methane fuel contains some other heavy 'sooting' gases. The methane gas used in the methane fire is commercial grade 1.3, whose purity is not less than 93%. The composition of the impurity is not exactly known, but ethylene or acetylene is empirically included in industrial gas. According to Yao's simulations [Yao, *et al*., 2011a; Yao, 2010], the possible mole fractions of ethylene and acetylene in the methane fuel mixture are 5% and 2% respectively. For a multi-component mixture, the $P_{f,\,total}$ is the mean of each component's P_f

weighted by its mole fraction, calculated as Equation (7.50). $P_{f,\ total}$ for the methane fire is hence calculated as:

$$P_{f,total} = P_{f,CH_4} \times 0.93 + P_{f,C_2H_4} \times 0.05 + P_{f,C_2H_2} \times 0.02 = 0.3236 \quad (8.1)$$

The above calculation suggests that the 'sooting' characteristic of the impure methane is quite different from that of the pure methane gas. The fuel gas used in the ethylene fire was commercial Grade 2.5, whose purity was not less than 99%. So the peak soot formation rate for pure ethylene is applied here.

8.4 Results and discussion

Before comparing predictions of the soot volume fraction with the experimental results, the other numerical predictions which influence the predictions of the soot generation or distribution, are first discussed in the methane fire. These predictions include the mixture fraction and temperature. For the ethylene fire, only the prediction of soot volume fraction was compared with the experimental data as no other information was provided in the publications for this test [Xin & Gore, 2005; Xin, *et al.*, 2005].

8.4.1 Methane fire

To have an overview of the flame, the predicted Favre mean mixture fraction field and temperature field in the central vertical cut plane of the methane flame are shown in Figure 8.3. The flame height was observed to be 0.364 m in the experiment. Heskestad [1997] adopted a criterion of 793K as defining the flame tip temperature. The temperatures in the centreline were predicted to be 840 K at 0.36 m height and 780 K at 0.38 m height above the burner exit. So the predicted flame height is between 0.36m-0.38m, which is close to the observed flame height of 0.364 m.

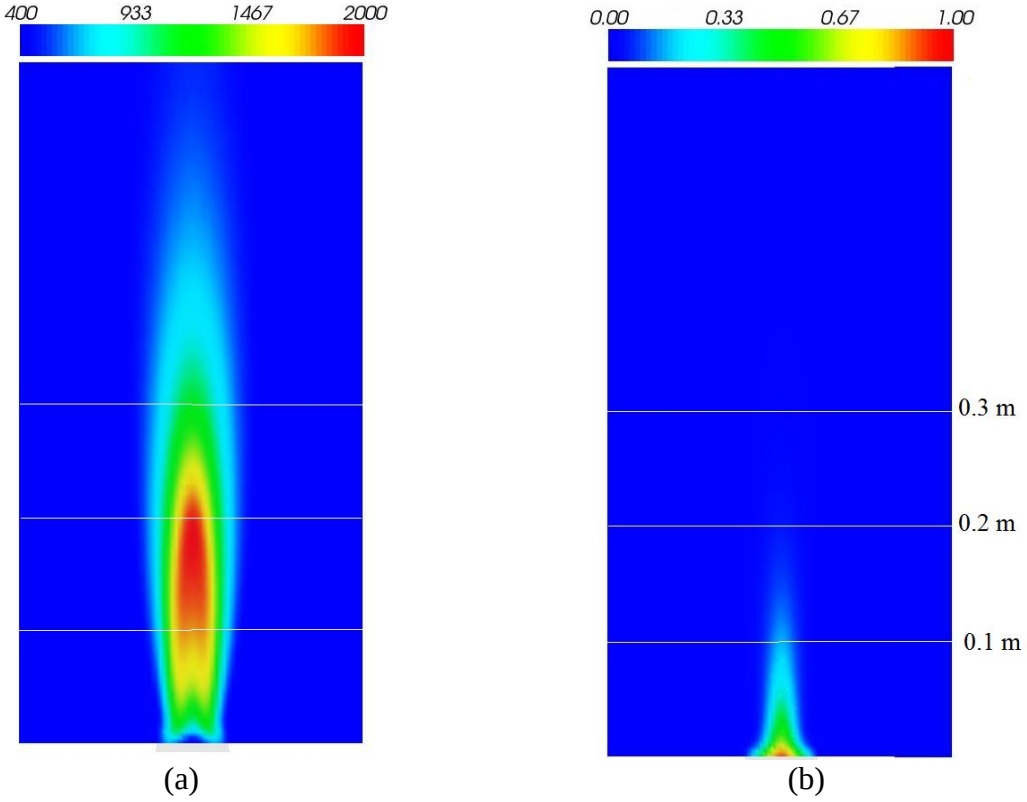

Figure 8.3. Predicted (a) temperature field and (b) mixture fraction field on the central vertical cut plane of the methane flame.

In Section 3.2.3.2, it was pointed out that soot formation is limited in the temperature range of 1000 K to 2000 K and mainly in the range of 1300 K to 1800 K. The predicted high temperature region (greater than 1300 K) is in the region between 0.03 m and 0.3 m height above the burner exit. The predicted mixture fraction in the central line decreases sharply from near 1 at the exit to about 0.05 at 0.2 m height above the burner exit. Generally, soot is formed at mixture fraction with values slightly greater than the stoichiometric mixture fraction ($\xi_{st} = 0.0544$ for methane). From the temperature field and mixture fraction field, it can be seen that the majority of soot should appear above 0.03 m and below 0.2 m height. The experimental data shows the majority of soot appear at about 0.5 D -3 D (0.035 m - 0.213 m) (see Figure 8.4(a)).

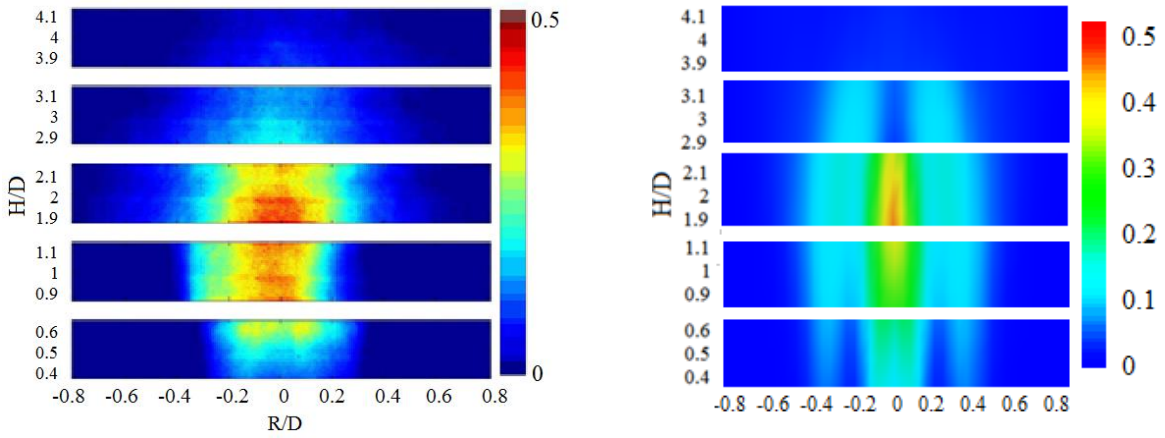

(a) (b)

Figure 8.4 (a) observed averaged soot volume fraction [in ppm] [Xin & Gore, 2005] and (b) predicted soot volume fraction field [in ppm] on the central cut plane of the methane flame.

Figure 8.4 shows the observed and the predicted soot volume fraction field at five downstream locations , i.e., 0.5 D, 1 D, 2 D, 3 D and 4 D (0.028 m to 0.291 m). The field of soot volume fraction was reproduced reasonably well by the prediction. The soot was predicted to be concentrated at the height of 0.5 D to 2.1 D and the peak value of soot volume fraction was predicted to be 0.49 ppm (1 ppm=0.0001 %) at the height of about 2.0 D, which matches the observations (Figure 8.4(a)). There are some disagreements in the two figures: there is an under-prediction of soot volume fraction in the centreline at the height of about 3 D; the predicted soot profile appears wider than the observation, especially at the height of 0.5 D and 1.0 D. The reason for the above disagreements will be discussed in the illustration of Figure 8.7.

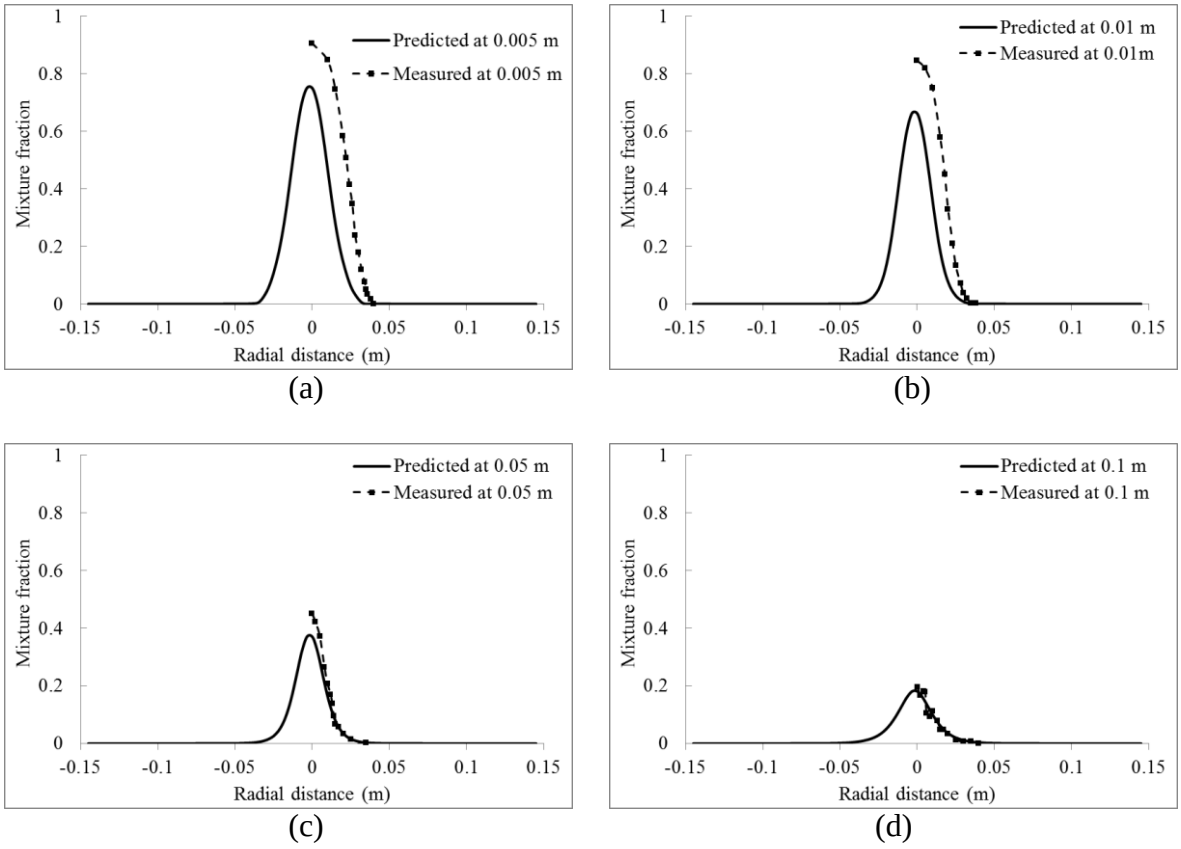

Figure 8.5 Measured and predicted mixture fraction profiles in the methane fire at different elevations above the burner exit: (a) 0.005 m, (b) 0.01 m, (c) 0.05 m and (d) 0.1 m.

Accurate predictions of the mixture fraction are an important premise for soot predictions by a global soot model such as the Beta soot generation model. Figure 8.5 shows the predicted and measured mixture fraction profiles at four different elevations above the burner exit. The predicted mixture fractions are in overall agreement with the measurements at height 0.05 m and 0.1 m, but smaller than the measurements at height 0.005 m and 0.01 m. There are several possible explanations which may account for these differences between the predictions and measurements at the two low elevations. The circular fuel inlet was modelled as a square rather than a circular section, which might alter the distribution of fuel field and further influence the mixture fraction field, especially near the burner exit. Another source of error in deriving the predicted values at the said elevations was that the elevations were not right at a cell centre and the predicted values have to be averaged with the values at two adjacent cell centres closest to the elevations. In the simulation, the flame region was discretized into small volumes with size no less than 0.005 m in height. The predicted value at 0.005 m height was determined from averaging the values of mixture fraction between 0 m to 0.01m height.

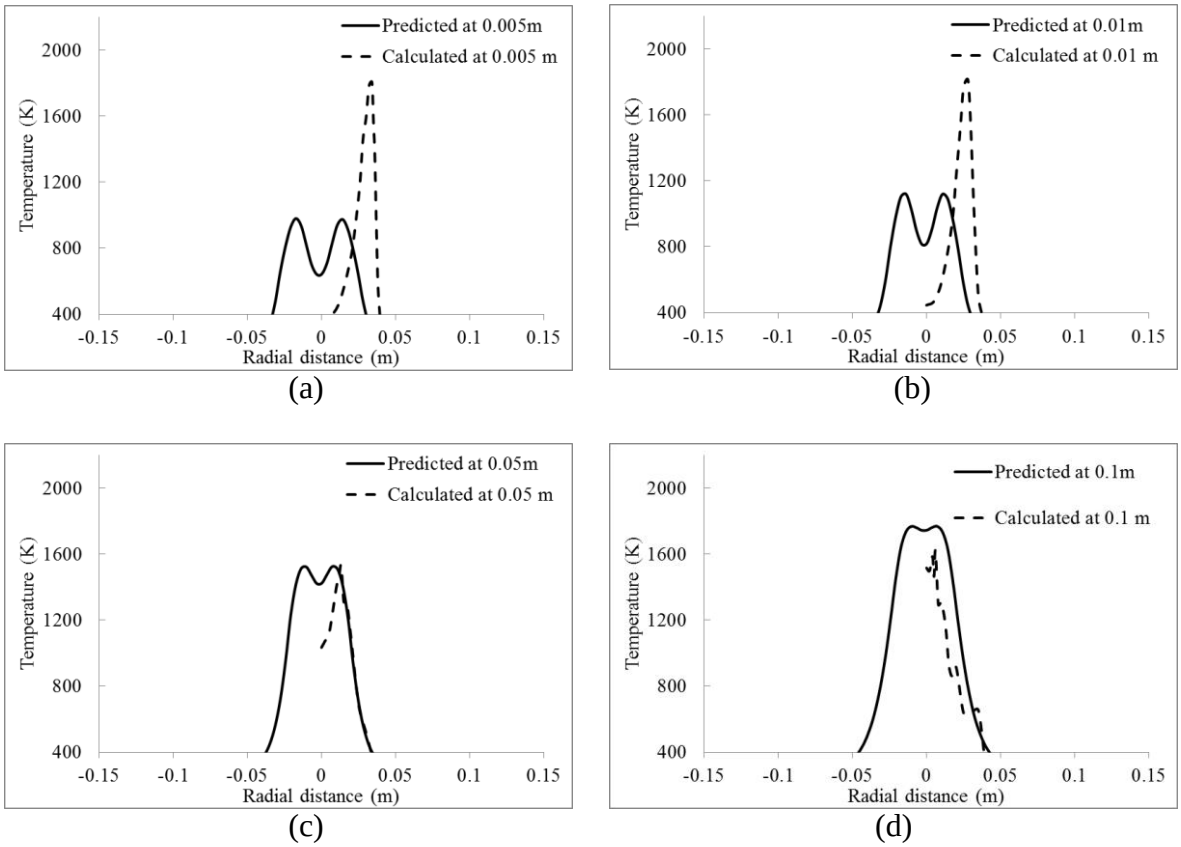

Figure 8.6 Calculated and predicted temperature profiles in the methane fire at different elevations above the burner exit: (a) 0.005 m, (b) 0.01 m, (c) 0.05 m, and (d) 0.1 m.

Figure 8.6 shows the comparison of the predicted temperatures and the calculated mean temperatures at the same four elevations as those in Figure 8.5. The temperatures were not measured in the experiment but calculated from the mixture fraction, assuming an adiabatic flame with measured species concentrations, ignoring the effects of cross correlations between species, temperature and specific heat. At the height of 0.005 m and 0.01 m, the predicted temperatures are higher than the calculated temperatures in the flame centre but lower than the calculated temperatures on the wings. At 0.05 m and 0.1 m, the temperature profiles are predicted to be reasonably close to the calculations except in the flame centre. However, the accuracy of the calculated temperatures is questionable as they were calculated under the assumption of the adiabatic condition and also relied on the accuracy of other measurements.

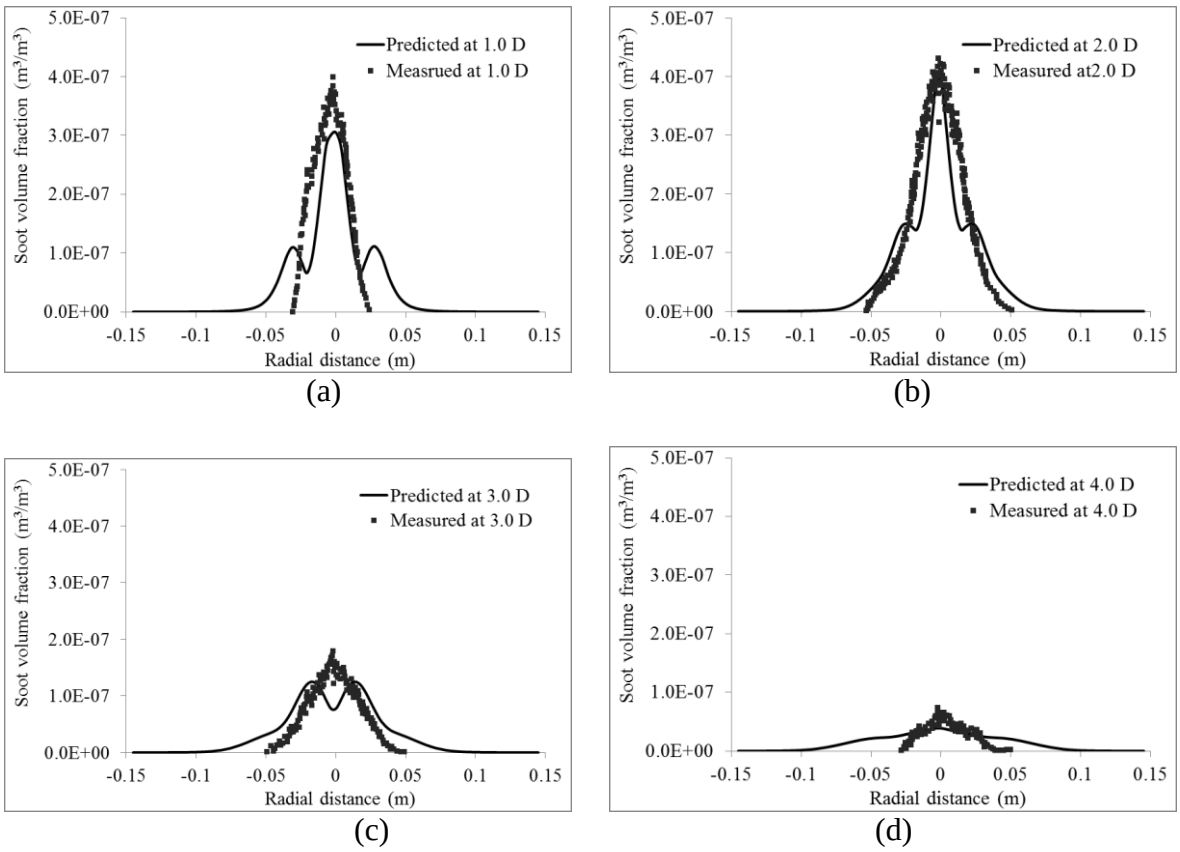

Figure 8.7 Measured and predicted soot volume fraction profiles in the methane fire at different elevations above the burner exit: (a) 1.0 D, (b) 2.0 D, (c) 3.0 D and (d) 4.0 D.

Figure 8.7 shows the comparison of the predicted and measured soot volume fraction profiles at four downstream elevations. The figure shows that the predicted soot distribution trends are in reasonable agreement with the measured mean soot field. At the two low elevations, the predicted peak soot volume fractions are in reasonable agreement with the measurement. However, there are some disagreements:

- At 1.0 D (0.071 m), the predicted soot volume fraction profile is wider than the measured one at radial distance 0.02-0.04 m from the flame centre.
- At 3.0 D (0.213 m), there is a dip in the predicted soot profile in the flame centre and the peak soot volume fraction is under-predicted by 24%.
- At 4.0 D (0.284 m), the predicted soot profiles appear wider than the measurement.

The above disagreements also appear in the Figure 8.4(b). These disagreements might be caused by the errors in the temperature predictions:

- Figure 8.4 (b) and Figure 8.7 (a) show that the soot volume fraction was over-predicted in the region from an elevation of 0.4D/0.028m to 1D/0.071m and at radial distance 0.02-0.04 m from the flame centre. In this region, the mixture fraction was less than the stoichiometric mixture fraction (see Figure 8.3 (b) and

Figure 8.5 (c)), thus soot evolution was predicted to be dominated by the oxidation process. The soot oxidation rate decreases with decreasing temperature and it decreases to near zero if the temperature is below 1300K. The temperature in this region was predicted to be less than 1300K (see Figure 8.3(a)), which was likely to be under-predicted. The under-predicted temperature might reduce the soot oxidation rate at this region.

.

- Figure 8.4(b) and Figure 8.7(c) show that the soot volume fraction was under-predicted in the region at about elevation of 3D/0.213m and in radial distance 0-0.02 m. The soot evolution was predicted to be dominated by the oxidation process in this region where the mixture fraction was predicted to be less than the stoichiometric mixture fraction and the temperature was predicted to be in the range of 1500K-1800K (see Figure 8.3(b)). It is likely the soot was over-oxidized in this region.

The reason causing the soot profile at 4.0 D wider is uncertain.

8.4.2 Ethylene fire

Soot was measured at the same four elevations in the ethylene fire as in the methane fire, however, no information on the species and temperature were provided by the experimenters.

Figure 8.8 shows the predicted temperature field, mixture fraction field and soot volume fraction field in the ethylene flame. The visible flame height in the ethylene flame was observed to be 0.388 m in the experiment. The temperature in the centreline was predicted to be 806 K at a height of 0.388 m and 773 K at a height of 0.40m. With the flame tip temperature of 793 K defined by Heskestad [1997], the predicted flame height should be between 0.388m and 0.400m, which is very close to the observation of 0.388m.

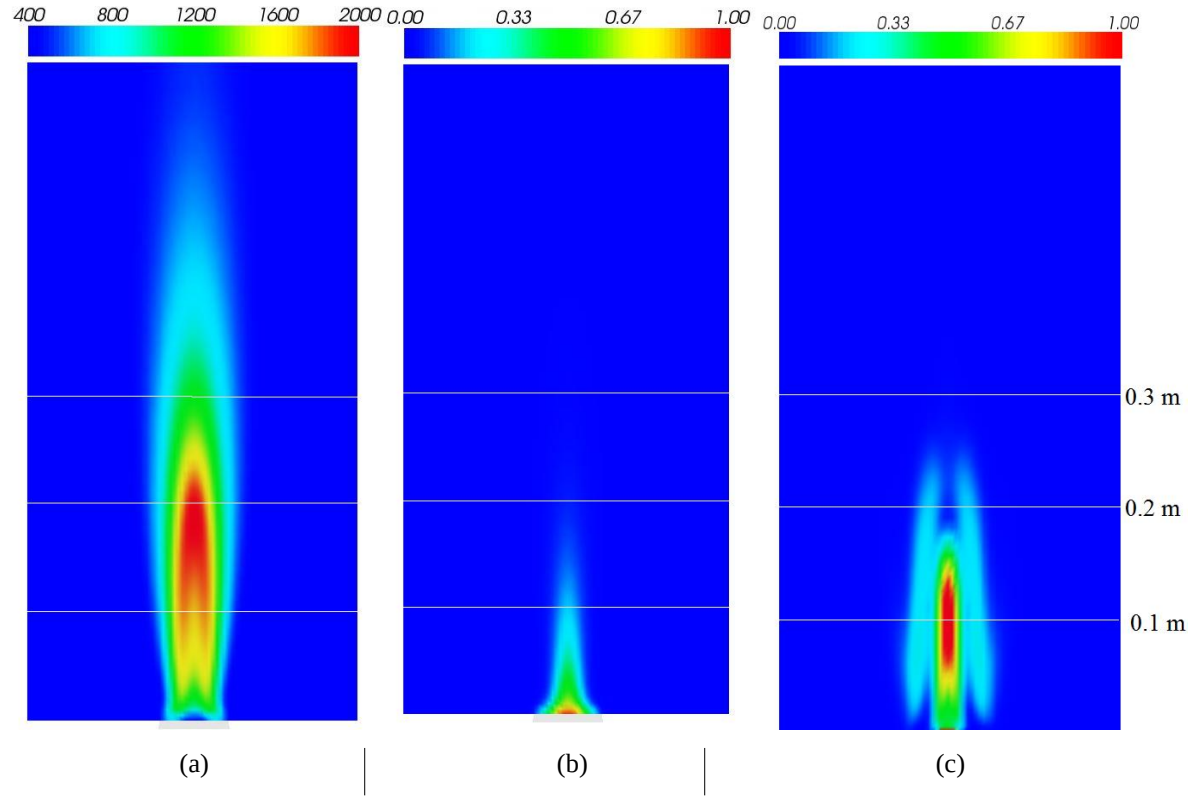

Figure 8.8 Predicted (a) temperature field, (b) mixture fraction field and (c) soot volume fraction field on the central vertical cut plane of the ethylene flame.

The temperature in the central line reaches 1300 K at a height of 0.03 m , increases to a peak value at approximately 0.19 m high and falls down to less than 1300 K at 0.27 m. The mixture fraction in the central line is less than 0.2 at the height of 0.1m and less than 0.06 at the height of 0.2 m respectively. The stoichiometric mixture fraction is 0.0629 for ethylene. From the temperature field and mixture fraction field, it can be concluded that the majority of soot should appear at the height below 0.2 m and above 0.03 m as indicated by the predicted soot volume fraction field (Figure 8.8 (c)).

Figure 8.9 shows the predicted and ensemble-averaged measured soot volume fractions at four downstream elevations in the ethylene fire. The soot profiles generally follow the measured trends at all elevations. However, the following disagreements exist:

- At 1.0 D (0.071 m) and 2.0 D (0.142 m), the predicted peak soot volume fractions are higher than the measured one and the predicted soot profiles are wider than the measured ones at radial distance 0.02-0.04 m from the flame centre.
- At 3.0 D (0.213 m), there is a dip in the predicted soot profile at the flame centre, which does not appear in the measured one.

As it lacks the information of the measured temperature and mixture fraction, the underlying reasons for the disagreements are uncertain.

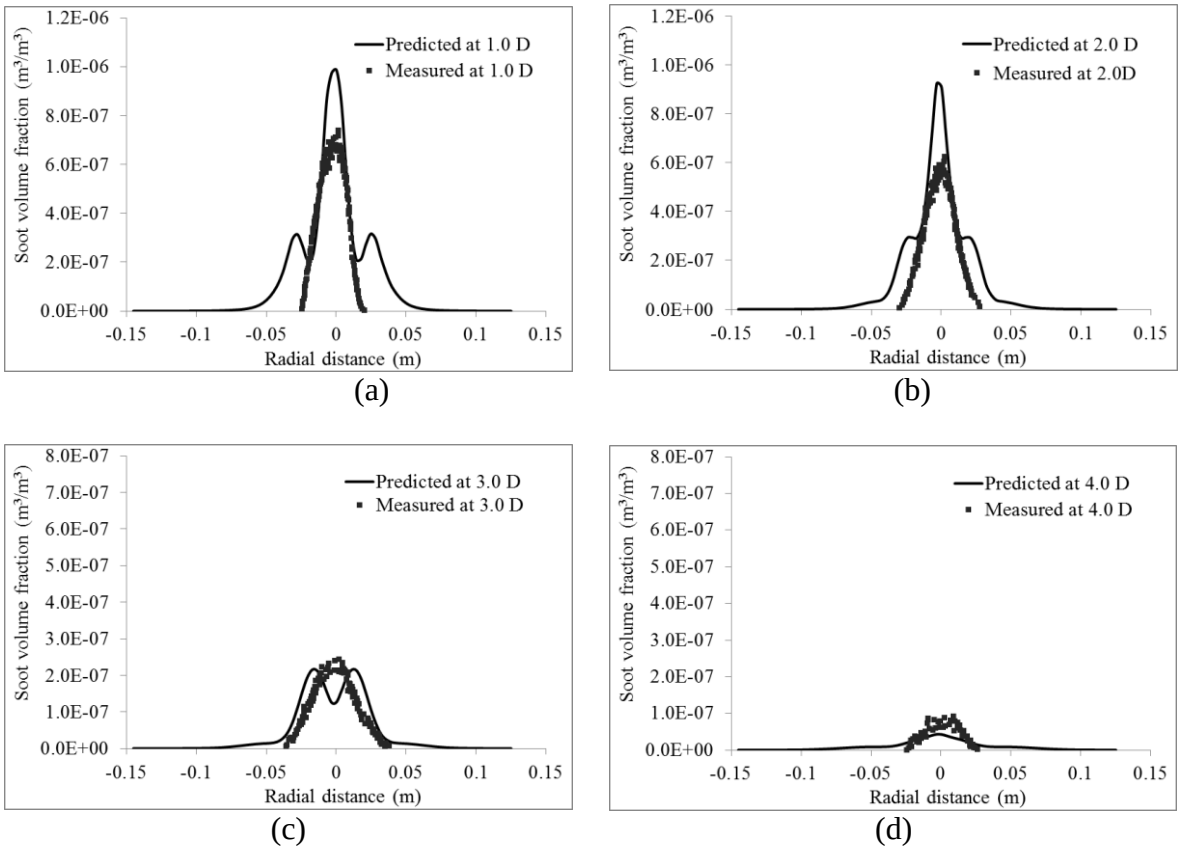

Figure 8.9. Measured and predicted soot volume fraction profiles in the ethylene fire at different elevations above the burner exit: (a) 1.0 D, (b) 2.0 D, (c) 3.0 D and (d) 4.0 D .

Figure 8.10 compares the predicted and measured soot volume fraction on the axis of the ethylene fire. While the changing trend of the soot volume fraction along the axis was predicted, the soot volume fraction was poorly predicted at the height of approximately 0.1 m. However, the prediction becomes closer to the measured soot volume fraction with the axial distance increasing. Generally, the axial soot prediction matches with the experimental data.

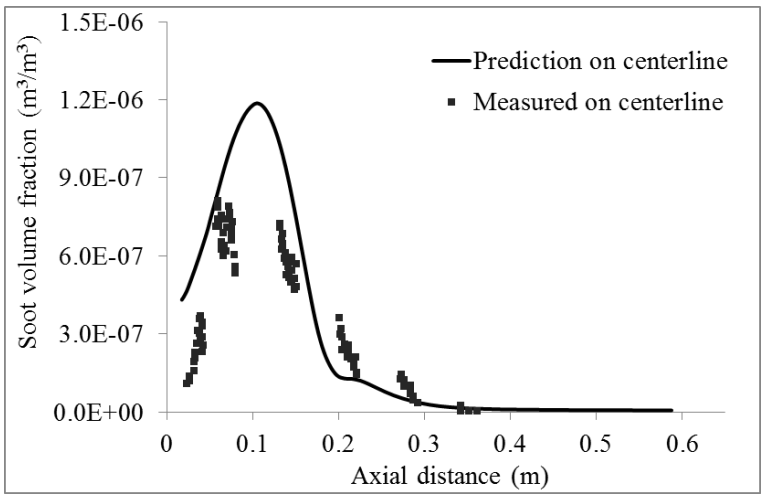

Figure 8.10 Measured (square symbols) and predicted (solid line) soot volume fraction profiles on the axis of the ethylene fire

8.5 Computational cost

The simulations were carried out on one workstation with 3.0GHz dual core processor and 4GB memory. Using the Beta soot generation model, the simulation of the methane fire took 57.5 minutes. The fire was also simulated with the Conventional soot generation model, which treats soot yield as a constant. It took 54.5 minutes for the Conventional soot generation model. Therefore, the Beta soot generation model took 3 more minutes or 5.5% longer than the Conventional model - not a significant increase in computational cost.

8.6 Conclusion

This chapter addresses Objectives 2(c) and 2(d) by validating the Beta soot generation model using experimental data. The Beta soot generation model developed in Chapter 7 was used to simulate soot formation in two turbulent flames with methane and ethylene respectively. The simulations were carried out using a mesh with a minimum cell size in the range of 4×3.5×5 mm^3. The results showed that:

- Figure 8.3, Figure 8.4 and Figure 8.8 demonstrated that the predicted distribution of the soot volume fraction in both fires qualitatively matched with the possible distribution indicated by the values of temperature and mixture fraction according to the mechanisms of soot generation.

- For the methane fire, the predicted mixture fraction and temperature at the heights over 0.1 m (Figure 8.5-8.6) were in good agreement with the measurements. The predicted soot volume fraction profiles generally follow the measured trends (Figure 8.7).

- For the ethylene fire, the predicted soot volume fraction profiles generally follow the measured trends (Figure 8.9). The peak soot volume fractions are over-predicted in the centreline at low elevations (Figure 8.9 (a) - (b), and Figure 8.10).

- For both fires, the soot volume fraction profiles at 1.0 D (0.071 m) and 2.0 D (0.142 m) are wider than the measurement at radial distance 0.02-0.04 m from the centre of the fires (Figure 8.7 (a) and Figure 8.9(a)). There is also a dip in the predicted soot profile at the flame centre at 3.0 D (0.213 m) (Figure 8.7(c) and Figure 8.9(c)). The explanation of these disagreements requires the further information of the temperature profile and mixture fraction profile at these elevations.

It takes 55 minutes to run the simulation on one workstation with a 3.0 GHz dual core CPU and 4GB memory. Compared with the simulation time with the Conventional soot generation model, only 3 more minutes is required. The increase in computational cost is considered acceptable.

Chapter 9
Simulating soot generation and transport in a large-scale enclosure fire

The Beta soot generation (BSG) model and the Multi-Particle-Size (MPS) soot transport model developed in the previous chapters are integrated into a soot model in this chapter. This integrated model is hereafter called BSG+MPS model. This model is used to simulate a large-scale enclosure cable fire conducted in a long corridor which has been simulated in Chapter 5. The performance of the model on reproducing soot generation and transport is investigated by comparing the predictions with the measured data and observation of soot movement in the experiment. The results are also compared with the predictions of the constant yield (CY) +MPS model in which the soot generation is modelled with a constant soot yield value.

9.1 Introduction

The soot released in the initial stage of a fire is expected to be detected by the soot detectors sufficiently early, so that the occupants can escape to safety and the fire can be extinguished in time before the damage is severe. Moreover, the soot movement is expected to be controlled by the building emergency ventilation, so that the visibility of the exit routes would not decrease significantly to delay the evacuation of occupants. Therefore, the accurate prediction on the amount of soot released from fires and the soot level in buildings can provide useful information on the design of the fire detection system, ventilation system and evacuation route in a building. Until now, most of the existing soot models focus on modelling soot generation or soot transport but not both.

A soot transport model called Multi-Particle-Size (MPS) model and a soot generation model called Beta soot generation (BSG) model were developed in Chapter 4 and Chapter 7 respectively. The two models were integrated into one soot model called BSG+MPS model. In this chapter, the performance of the BSG+MPS model is investigated by simulating a large-scale enclosure corridor fire which had been simulated in Chapter 5. In this chapter, first is the outline of the integration of the soot BSG model and MPS model. Then the experiment

and the numerical details of soot modelling are introduced in brief. Finally, the predictions derived from the BSG+MPS model and the constant yield (CY) +MPS model are compared with the experimental measurement and observation of soot movement.

9.2 Integration of soot generation and transport model

The MPS model is a further development of the drift flux model in which the gravitational force on soot particles is taken into account. The model divides the soot particles into several groups according to the soot mass size distribution. The strategy of grouping soot particles and calculating the representative size and the mass fraction for each group has been discussed in Section 4.3.3. If there are n groups of soot particles and the representative size for group i^{th} is $\overline{d}_i$ ($i \le n$), the general soot Favre mean transport equation for group i^{th} is expressed as:

$$\frac{\partial \overline{\rho} \widetilde{Y}_{s,i}}{\partial t} + div(\overline{\rho}(\widetilde{\vec{U}} + \overline{\vec{v}}_{s,i})\widetilde{Y}_{s,i}) = div(\overline{\rho}(D + \varepsilon_p)\nabla \widetilde{Y}_{s,i}) + \overline{S}_{Y_{s,i}} \qquad i = 1,2,\cdots,n \tag{9.1}$$

where $\widetilde{Y}_{s,i}$ is the soot Favre mean mass fraction of group i, $\overline{\vec{v}}_{s,i}$ is the settling velocity calculated from the representative size $\overline{d}_i$, and $\overline{S}_{Y_{s,i}}$ is the mean source term of group i^{th}. The number of the soot particle groups, n, is usually no more than 3 for many combustible materials, thus there is no significant increase in computational cost.

The total source term for all groups $\overline{S}_{Ys}$ is modelled by the BSG model which has been discussed in Chapter 7. The soot generation rate is a function of mixture fraction, temperature and oxygen mass fraction. The source term $\overline{S}_{Y_{s,i}}$ for each group is calculated as the product of the mass fraction of this group and the total source term:

$$\overline{S}_{Y_{s,i}} = m_i \overline{S}_{Y_s} \tag{9.2}$$

where m_i is the mass fraction of the i^{th} soot group to the total soot mass and $\sum_{i=1}^{n} m_i = 1$.

9.3 Experiment and numerical details

9.3.1 Experiment

Test II, one of the two large scale corridor fire tests that were simulated in Chapter 5, used NHMH cables as the fire source. The main component of NHMH cables was polyethylene (PE). The soot release rate was very small in the first 15 minutes, and then dramatically increased in the next 3 minutes. Test II with this very uneven soot yield was simulated again in this chapter to investigate the performance of the soot models.

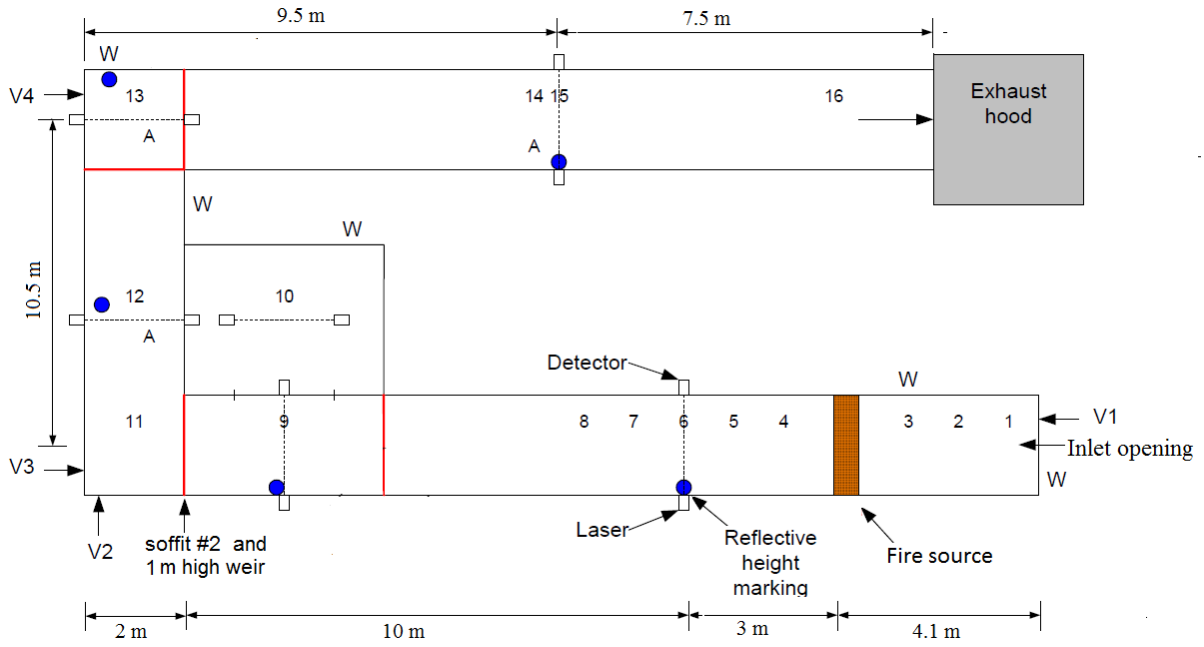

Figure 9.1 Locations of lasers, video cameras (V1-V4), reflective height markings and windows (W) for observation during the test [Persson, 2006].

The layout of the test, the locations of the fire source, lasers, reflective markings, video cameras and windows are shown in Figure 9.1. There was a 1.0 m high weir built from the floor and just below soffit #2. Six lasers with 650 nm wavelength were mounted on one side wall of the corridor and the corresponding detectors were mounted on the opposite wall. The lasers measured soot obscuration at 2.2 m above the floor at Position 6, 9, 10 and at 2.0 m above the floor at Position 12, 13, 15. Reflective markings were mounted on poles at every 0.5 m above floor at Position 6, 9, 12, 13 and 15. Four cameras were used to record the soot generation and movement. The Camera V3 was positioned about 1.3 m above the floor to avoid the light to be blocked by the weir. Other cameras were positioned about 0.5 m above the floor.

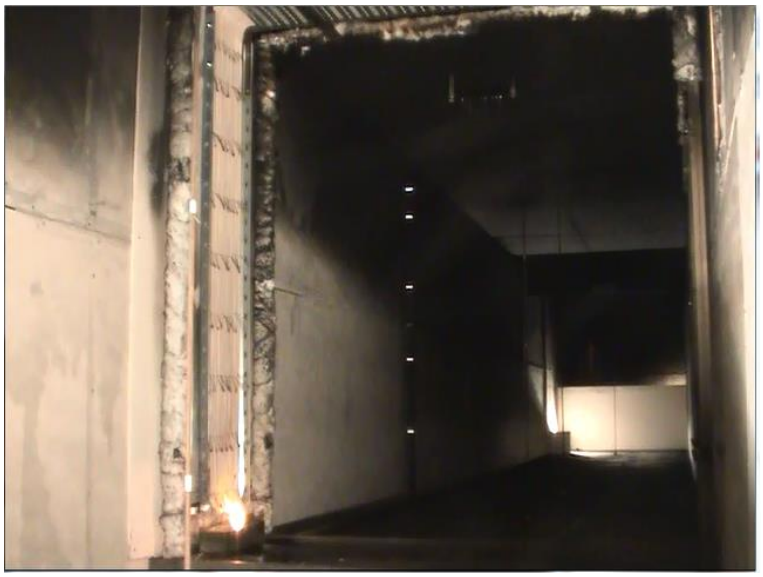

Figure 9.2 The fire source, reflective markings at Position 6 and 1.0 m high weir at the end of the corridor

Camera V1 was positioned at the Inlet opening (see Figure 9.1), which recorded the fire development and soot release clearly during the test. Table 9.1 presents the observation according to the video clips of Camera V1.

Table 9.1 Observation of Camera V1

Time (min:s)	Observation
03:00	The ignition source (a propane sand burner) was ignited.
12:45	Light soot kept hanging below the horizontal cable tray.
14:30	Entire vertical and horizontal cable tray were involved in fire. 3-4 m long flames were noticed along the ceiling on the right side of the corridor.
15:00	Plastic dripping was noticed. A significant amount of soot was released. (Figure 9.6(a)).
15:30	The right half of the horizontal cable tray became invisible due to the presence of heavy soot.
16:30	The upper layer became very dark. The entire horizontal cable tray and the fire flame along the ceiling both became invisible (Figure 9.6 (b)).
17:00	The fire flame on the upper right corner became visible again (Figure 9.6(c)).
18:00	The fire in the vertical cable tray was almost self-extinguished, but a fire of intense burning was still present along the horizontal cable tray.
20:20	Fire was only on the right half of the horizontal cable tray (Figure 9.6(d)).
23:00	Fire was only on the right end of the horizontal cable tray.

In the later stage of the test (after 15 minutes), there was a small distortion in the corridor construction due to the thermal forces. Therefore, the laser at Position 6 was not aligned with the detector sensor and other lasers were also noticed to have small movements in the later stages of the test. The misalignment of the lasers and the detectors caused the measuring error in visibility. However, this was not judged to influence the measurements during the initial part of the test, until transmission was reduced to 0%.

9.3.2 Numerical details

The numerical model set up, including the heat release rate, discretization of the geometry, boundary conditions and time step size, was exactly the same as that in Chapter 5.
. Two simulations were run with different soot generation models in this chapter. Both simulations used the same MPS model for the soot transport.

The CY+MPS model used a constant yield of soot, 0.06 kg/kg, in one of the simulations. In the other simulation, however, the BSG model was used to model soot generation rate. The peak soot formation rate is the only input parameter required in this model. According to Equation (7.49), the peak soot formation rate for polyethylene can be calculated from a fuel-specific constant—smoke point height L_{sp}, which is 29 mm in Table 7.2,

$$P_{f,C_3H_6} = \frac{L_{sp,C_2H_4}}{L_{sp,fuel}} P_{f,C_2H_4} = 3.6552(kg/m^3 s) \tag{9.3}$$

The soot particles were divided into 3 groups for the MPS soot transport model. The representative size and the corresponding mass fraction for each group were presented in Table 5.3 in Chapter 5.

Compared with the simulation in Chapter 5, the division of the fire source patches was changed in the two simulations in this chapter. The fire source consisted of one vertical (1.95 m) cable tray and one horizontal (1.80 m) cable tray. The fire source was modelled as one vertical patch and one horizontal patch in Chapter 5. In a SMARTFIRE simulation, once a volume patch is ignited, the whole volume patch is considered to be involved in the fire. However, the video recording showed the fire flame moved along the cable trays very slowly in the initial stage of the test, especially for the vertical cable tray. It took more than 11

minutes for the fire to reach the horizontal cable tray. In order to provide a more accurate description of the combustion development along the cables, the vertical tray was modelled as 5 patches and the horizontal tray was modelled as 2 patches in the two simulations. For the vertical cable tray, the bottom patch was one ninth and the other patches are two ninth of the vertical section. The horizontal tray was divided into two sections with one half of the length of the horizontal tray for each section. The patches in the vertical tray were ordered from bottom to top (Patch 1-5) and the patches in the horizontal tray were ordered from left to right (Patch 6-7). According to the video recording, the start and end combustion times for each patch are listed in Table 9.2.

Table 9.2 start and end combustion times for patches

	Patch 1	**Patch 2**	**Patch 3**	**Patch 4**	**Patch 5**	**Patch 6**	**Patch 7**
Start	3:00	6:20	10:20	12:20	13:20	14:20	14:50
End	18:00	18:00	18:00	18:00	18:00	20:20	24:50

9.4 Results and discussion

To investigate the performance of the BSG+MPS model in the cable fire, the predictions from the BSG+MPS model and the CY+MPS model are compared with the measurements or observation of the test.

9.4.1 Light extinction at the upper layer

The soot light extinction at the upper layer (2.0-2.2 m above the floor) was measured at six positions. The measured light extinctions at Position 6 (near the fire source) and Position 15 (far away from the fire source) are compared with the predictions from the BSG+MPS model and the CY+MPS model.

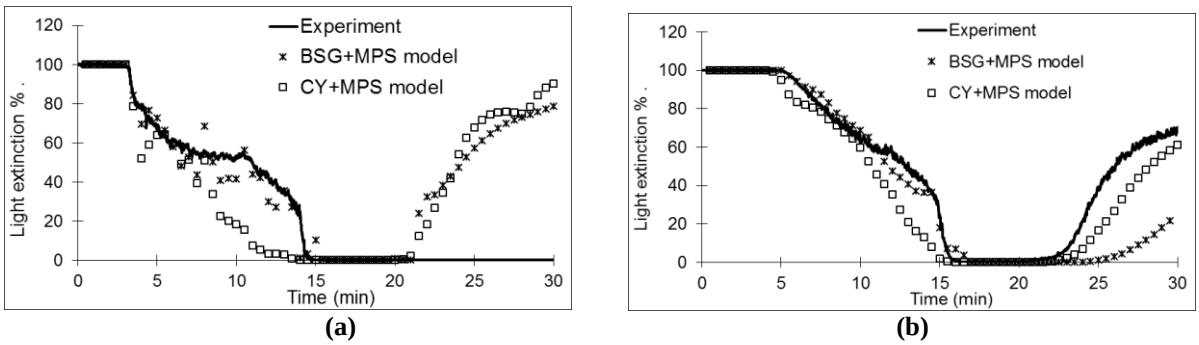

(a) **(b)**

Figure 9.3 The measured and predicted light extinction at (a) Position 6, and (b) Position 15.

The measured light extinction decreased slowly from 100% to near 0% between 3 minute and 14 minute at Position 6 and between 5 minute and 15.5 minute at Position 15 (see Figure 9.3). The figure shows that the BSG+MPS model predicted the light extinction at the two positions in good agreement with the measurements in the first 15 minutes, with the exception of some fluctuations between 8 and 15 minute at Position 6, and a slight over-estimation before 11 minute and a slight under-estimation after 11 minute at Position 15. The light extinction at Position 6 predicted by the CY+MPS model matches the measurement in the first 7 minutes but is much lower than the measured light extinction between 7 minute to 15 minute, which indicates the soot generation rate was over-estimated between 7 minute to 15 minute by the CY+MPS model.

Figure 5.7 shows that the predictions from the CY+MPS model and Conventional Model in Chapter 5 match each other for the first 15 minutes very well. However, the predicted light extinction using the BSG+MPS model is remarkably different from the predictions by the CY+MPS model at Position 6 between 5 minute and 15 minute. Therefore, it is very likely that the soot generation model used in the simulations played a dominant role in determining the predicted levels of the soot concentration in the upper layer near the fire source. The more accurate predictions of the light extinction at Position 6 by the BSG model show that it more accurately predicted the soot generation rate for the test in the first 15 minutes.

After 20 minutes, all of the predictions from the two models do not match the measurements, especially at Position 6. The test report pointed out that there were movements for all lasers in the later stage of the test and the measurements of light extinction are not reliable any more. Especially at Position 6, the laser beam and the detector sensor in the later stage were not aligned, which caused zero visibility in the measurements.

The upper layer in the Inlet Corridor was observed to be very clear after the fire almost extinguished at 23 minute. The predicted light extinctions by the two models at position 6 increased gradually after 20.5 minute, which matches the video recording. To further check the reliability of the predicted light extinction after 20 minute by the BSG+MPS model, the prediction is compared with the video recording at a given time. The video shows the visibility of the Inlet Corridor at 24 minute is similar to the visibility at 11 minute, which means the actual light extinction at 24 minute should be close to the measured light extinction of 44% at 11 minute. The predicted light extinction at Position 6 is 47.8% at 24 minute, which

is close to 44.0%. Therefore, the light extinction of 47.8% at 24 minute is a reasonable prediction.

(a) **(b)**

Figure 9.4 The observation of Inlet Corridor by Camera V1 at (a) 11 minute and (b) 24 minute

9.4.2 Soot mass flux at the end of Inlet Corridor

Camera V1 recorded that the cable fire started to release heavy soot at 15 minute and the soot yield in the next 5 minutes varied significantly (Table 9.1). These observations are used to examine the performance of the BSG+MPS model and the CY+MPS model during this period of time. The variations in the average soot mass flux predicted from the two models crossing a cut plane at the end of the Inlet Corridor are expected to match the timing of these observations if the models are capable of producing reasonably accurate predications in soot generation rates and movement.

Because there were very intense turbulent eddies near the fire source, a cut plane at the end of the Inlet Corridor is selected to avoid the strong fluctuations in the soot mass flux. The normal direction of the plane is parallel to the floor and points to the end of Inlet Corridor. The plane is just below the 0.2 m soffit #2 and beyond the 1.0 m high weir (see Figure 9.2). It is about 13 m away from the fire source (see Figure 9.1).

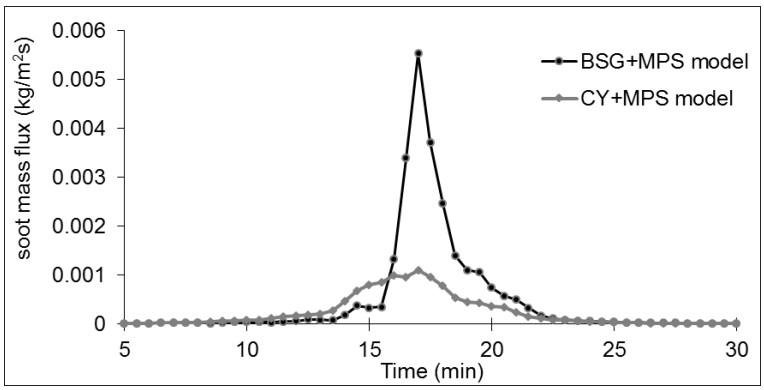

Figure 9.5 the average soot mass flux across the plane at the end of Inlet Corridor

Figure 9.5 shows the predicted average soot mass flux across the plane at the end of the Inlet Corridor. The figure shows that the average soot mass flux predicted by the BSG+MPS model increases very slowly in the first 15.5 minute, then increases dramatically to 5.2 $\times 10^{-3}$ kg/m^{2}s in just one and a half minutes and decreases quickly to about 1.1 $\times 10^{-3}$ kg/m^{2}s in the next 2 minutes. The average soot mass flux predicted by the CY+MPS model is higher in the first 15.5 minutes, but much lower between 16 minute to 21 minute than the predicted flux by the BSG+MPS model. The peak soot mass flux predicted by the CY+MPS model is 1.08 $\times 10^{-3}$ kg/m^{2}s at 17 minute, which is nearly one fifth of the peak value predicted by the BSG+MPS model. Therefore, compared with the constant soot yield value, it is likely that the predicted soot yield valueby the BSG+MPS model is smaller in the intial stage, but much higher in the later stage.

The constant yield value0.06 kg/kg is the mean soot yield valueof a polyethylene (PE) fire with fuel size in the order of 0.1m in width and 0.6 m in height under the well-ventilated flaming condition [Tewarson. 2002]. It is also found that the soot generation rate under ventilation-controlled conditions might increase by up to 2.8 times for PE [Tewarson, *et,al*., 1993]. Generally, the soot yield of a fuel increases moderately with the increase of the fuel size. Evans and his co-workers [Walton, *et al*., 1992] pointed out that soot poduction might increase from 0.06 g to 0.13 g per gram of crude oil if the fuel size increased from 0.085 m to 2 m. In this test, the cable fire is nearly 4 m long and the fire occurred in an enclosed corridor, thus the peak soot yield valuein this test should be much higher than the constant yield value0.06 kg/kg.

As the plane is at the end of the Inlet Corridor, 13 m away from the fire source, it took time for the soot generated from the fire source to reach it. Therefore, the time to the peak soot

yield might be a little earlier than the time to the peak soot mass flux at the plane (17 minute). From the video recording of Camera V1, the soot yield reached the peak value at about 16.5 minute (see Figure 9.6(b)), thus both models predicted the time to peak soot mass flux at the plane (17 minute) reasonably well.

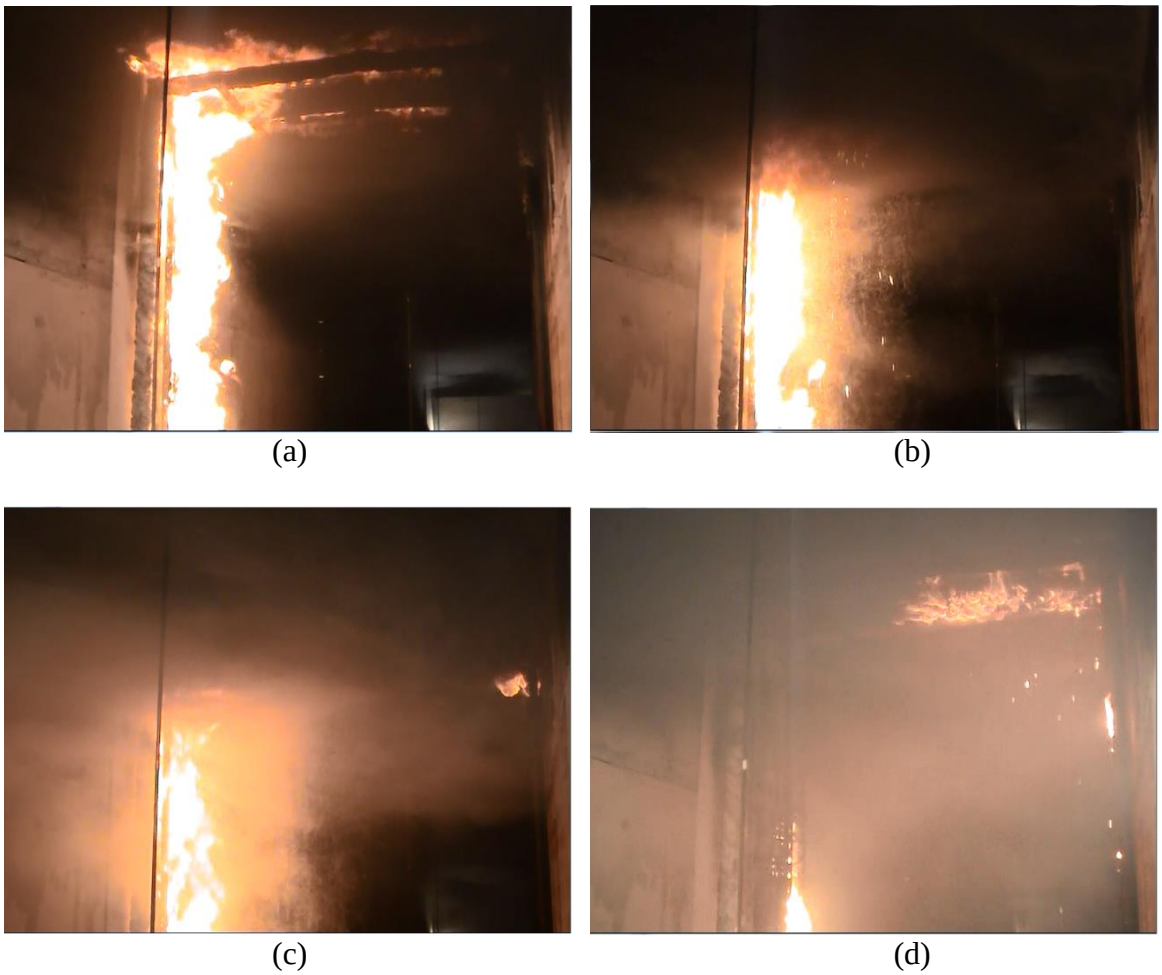

Figure 9.6 observed burning at (a) 15 minute, (b) 16.5 minute, (c) 17 minute, and (d) 20 minute.

The dramatic changes of the soot yield between 15 minute and 20 minute predcited by the BSG+MPS model can be corroborated by the fire scene recorded by Camera V1 at 15 minute, 16.5 minute, 17minute and 20 minute that are shown in Figure 9.6. Both the vertical tray and horizontal tray were involved in combustion at 15 minute and the horizontal tray could be seen very clearly at this time. However, the horizontal cable tray and the fire flame along the horizontal cable tray both became invisible at 16.5 minute due to the presence of heavy smoke. At 17 minute, the upper layer was not as dark as that at time 16.5 minute and the fire flame on the upper right corner became visible again. At 20 minute, most part of the horizontal tray became visible again. The changes of the visibility around the fire source

coincides with the dramatic changes of the predicted soot mass flux through the plane at the end of Inlet Corridor.

9.4.3 Visibility distance at the lower layer

The distance between Camera V4 and the light source 0.3 m above the floor in the Exit Corridor was approximately 17 m. The visibility distance from the Camera V4 was estimated roughly to be less than 17 m between 18.5 minute and 28 minute as the light source was invisible or obscured during this period of time according to the video recording.

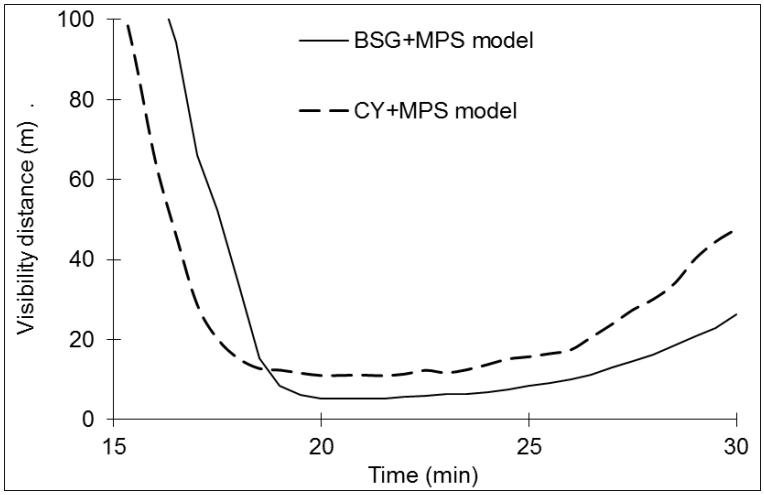

Figure 9.7 Predicted visibility distance from Camera V4

Figure 9.7 shows the predicted visibility distances from the Camera V4 towards the exit. The light was predicted to be obscured if the predicted visibility distance was less than 17 m. Thus, the predicted start and end obscuration time of the light can easily be calculated from Figure 9.7. Then, the predicted and observed obscuration times are compared in Table 9.3.

Table 9.3 The obscuration time of the light source

Obscuration time	Begin(min)	End(min)
Observation	18.5	28
CY+MPS model	18	25.5
BSG+MPS model	18.5	28

The CY+MPS model predicted that the end of the obscuration time was at 25.5 min, which was 2.5 min earlier than the observation. However, the obscuration time predicted by the BSG+MPS model match the observation very well.

9.5 Computational cost

The two simulations were run by the same computer as that used for the simulations in Chapter 5. The running times are listed in Table 9.4. The CY+MPS model took approximately 35 hours while the BSG+MPS model took approximately 35 hours 40 minutes in simulating the corridor fire. Compared with the running time of the Conventional model in Chapter 5, the CY+MPS model took extra 9.37% time and the BSG+MPS model took extra 11.46% time. Therefore, the computational cost of the BSG+MPS model is a modest increase for the improved accuracy.

Table 9.4 The running times of soot models

Models	Running time	Incremental time
Conventional model	32 hours	----
CY+MPS model	35 hours	9.37%
BSG+MPS model	35 hours 40 minutes	11.46%

9.6 Conclusion

This chapter addresses Objective 3(a) and 3(b). In this chapter, the BSG model and MPS soot model were integrated into one single soot model (BSG+MPS). The performance of the model was examined by predicting the soot generation and transport in a large-scale enclosure corridor which has been simulated in Chapter 5. The predictions of BSG+MPS model were compared with the predictions of CY+MPS model and the measurement and video observations.

The predicted upper light extinction at two positions by the BSG+MPS model and the CY+MPS model was compared with the measurements. It shown that the prediction of the BSG+MPS model was in good agreement with the measurement. It was also found that the soot generation rate was smaller than the constant yield (0.06kg/kg) in the initial stage of the test (the first 15 minutes).

The predicted soot mass flux through a cut plane at the end of Inlet Corridor by the BSG+MPS model and the CY+MPS model were compared with each other. The BSG+MPS

model predicted a sharp increase in soot mass flux between 15.5 minute to 17 minute, which matched the observed dramatic change of visibility around the fire source during the same period of time. However, the CY+MPS model failed to reproduce the phenomenon.

The visibility distance of the light near the floor adjacent to the exit door was discussed again in this chapter. The prediction of the obscuration time of the light using the BSG+MPS model matched very closely the video recording of Camera VI and improved the prediction of the CY+MPS model.

In this chapter, two interesting points are found:

- The actual soot yield valuein the initial stage of a large-scale fire can be smaller than the mean yield valuewhich is measured in a small fire under the well-ventilated condition.
- A significant amount of soot can be released in a very short period of time, which decreases the visibility rapidly in a large fire in a few seconds.

These two observations demonstrate that a constant soot yield value might be not adequate to describe the actual varying soot yield. The results of this chapter demonstrate that the soot BSG+MPS model is a promising approach resulting in an improved prediction of soot generation and transport compared to the CY+MPS model

Chapter 10
Conclusions and future work

In this chapter, the soot modelling development work in this study is initially summarised, together with the validations. It is demonstrated that all the research objectives set out for the work in Chapter 1 have been meet. Then, the direction of potential future work is discussed.

10.1 Concluding Comments

There are great concerns about the effects of soot on fire evacuation, human health, fire spread and growth, and combustion efficiency. To minimize these negative effects, it is desirable to be able to predict soot (smoke) levels in fires to determine the safe design of a building, best placement of the detection system , evacuation path, the location and type of evacuation signage.. Both the amount of soot generated in a fire and the transport of soot should be considered in order to accurately predict the soot concentration distribution within the fire building enclosure.

The soot generation mechanism is very complex and there are still gaps in understanding. Further, soot movement is more a particle phenomenon than a gas-phase phenomenon. Until now, there are no models that have been widely applied in practical large-scale fire simulations. Modelling soot generation and transport is still at the stage of intensive development and validation. The concerns about the effectiveness and accuracy of modelling soot generation and transport in practice provided the direction for the research in this dissertation.

In the following sections, the major outcomes of the theoretical development along with the validation are outlined.

10.1.1 Development of a soot transport model and its validation

Particle-laden soot is usually assumed to be in a gaseous state because the majority of soot particles have a size of less than 1.0 μm and so the small particle movement mechanism can

be ignored in the intensive turbulent fire gas flow. However, this simplification can sometimes lead to severe errors in the predictions of soot levels in fire simulation because, for some combustible materials, there is a non-negligible mass fraction of soot particles with settling velocities which are comparable to the gas flow velocity. Due to the movement mechanism of these large soot particles, soot transportation behaves differently to the transportation of fire gases. Soot size varies typically between 0.01 μm and 10 μm. Such a large variation in particle size makes it difficult to simulate the movement of soot because particle size has a significant influence on the manner of particle movement. This problem was addressed in this study through the development of a soot transport model called Multi-Particle-Size (MPS) model.

10.1.1.1 Multi-Particle-Size (MPS) soot transport Model

The MPS model was developed by considering the particle movement mechanism for soot and the uneven mass size distribution of soot particles (see Chapter 4). The result of gravitational force, drag force and buoyant force exerted on soot particles leads the soot particles to move in a relative velocity, called settling velocity, to its surroundings. The settling velocity is heavily dependent on soot particle size. To take into account the effect of particle size on the settling velocity, the MPS model divides the soot particles into several groups. Each group has a size range and a representative size is used to calculate the settling velocity of the group. The transport of soot particles in each group is represented by a governing equation, in which the impact of the settling velocity on particle movement is addressed by adding a correction into the convection term.

Increasing the number of groups might lead to a more accurate prediction of soot movement; however, the computational cost also increases. To make the model practical, the strategies to group soot particles were considered with a compromise between computational efficiency and performance accuracy. Three strategies were developed and their performance was investigated by simulating soot movement in an artificial chamber. These tests showed that using one single representative soot size for all soot particles is not sufficient to describe the soot movement. The strategies to divide soot particles into several groups (Method 2 and Method 3 in section 4.3.3) produced better predictions of soot concentration. Method 3 divided the soot particles into three groups for a variety of combustible materials. The

computational cost of the extra governing equations for these groups is considered acceptable (see Section 5.5 and Section 9.5).

This achievement addressed research Objective 1(a) and 1(b).

10.1.1.2 Validation experiments

The efficiency of the MPS model to simulate soot transport was demonstrated by simulating several experiments: two large-scale cable fire experiments conducted in a long corridor (Chapter 5) and one soot transport in a large building with a high ceiling (Chapter 6). The achievement satisfies research objective 1(c) concerned with validating the new soot transport model.

Two cable fires in a long corridor

Two large-scale cable fire experiments conducted in a U-shaped long corridor (44.6 m) were simulated using the MPS model and the Conventional Model (see Chapter 5). L-shaped cable trays were mounted in the Inlet corridor and released intensive soot during the experiments. In Test I, the cable was a PVC cable and, in Test II, the cable was a polyethylene cable. The predictions of both models were compared with the measured data and video recordings (see section 5.3). Both models were able to reasonably reproduce the soot distributions in the upper layers. However, the two models predicted significantly different levels of soot in the lower layer. The Conventional Model failed to reproduce the obscuration phenomenon of the light source on the floor near the exit door in both tests. However, the MPS model under-predicted the obscuration time of the light source only by 5.7% (0.6 minutes) in Test I and 2.7% (0.5 minutes) in Test II. The observed obscuration times and reappearing times of the marking at 0.5 m above the floor at position 15 (far away from the fire source) were also compared with the predicted times. The Conventional Model over-predicted the obscuration time by 81% (7.6 minutes) in Test I and by 27.6% (4.2 minutes) in Test II respectively, and failed to predict the reappearing time in the two tests. On the other hand, the MPS model over-predicted the obscuration time by 20 % (2 minutes) in Test I and by 12% (1.7 minutes) in Test II. Moreover, the MPS model also successfully predicted the marking remained invisible in Test I and only under-predicted the reappearing time of the marking by 8.9% (2.5 min) in Test II. Thus, the MPS model greatly improved the precision of the prediction for the soot movement in the lower layer compared with the Conventional Model. This achievement addresses research objective 1(c).

The deficiency of using temperature to estimate soot levels was highlighted by comparing the visibilities at position 15 predicted from the temperature approach with the experimental observation (see Section 5.4).. The performance of the soot particle group division strategies was also investigated by comparing the soot concentration predicted from two different group divisions (see Section 5.5). This showed that the use of three groups for grouping soot particles was adequate to describe the effect of soot particle size on the transportation in the cable fires. Lastly, the computational cost of the model was discussed. The MPS model took approximately 9% longer than the Conventional Model in the simulations of the corridor fires – a modest increase in computational time for the improved accuracy. This achievement addresses research objective 1(b).

Large building with a high ceiling

The soot movement in a test within a large warehouse with a width of 171×90 m and a height of 7.25 m was simulated using the MPS model and the Conventional Model (see Chapter 6). A soot generator SG3000 was used in the test to produce soot and three repeat experiments were performed during the normal operation of the facility. Due to the experiments not being fully controlled, the predicted soot obscuration tendency rather than the exact soot obscuration was compared with the measurement and observation.

The predicted soot obscuration profiles in the vertical cut plane at several time points from both models were compared with each other (see Chapter 6.4).. The Conventional Model did not predict the downward movement of the soot layer while the MPS model predicted the soot descent phenomenon that was observed during the tests. Also, the obscuration tendencies measured by three lasers and two detectors were compared with the predictions from the two models. The MPS model produced reasonable predictions of the obscuration tendency at all of the positions. However, the Conventional Model significantly under-predicted the obscuration at the positions of the two detectors and two of the three lasers. This achievement further addresses research objective 1(c).

10.1.2 Development of a soot generation model and validation experiments

As the chemical mechanism responsible for soot generation has not yet been unambiguously identified, the semi-empirical approach with acceptable computational cost and a small set of empirical parameters remains the most practical way to model soot generation in fire simulations. One shortcoming of this approach is that the semi-empirical models are usually designed for a specific fuel and extension of this type of model beyond the operating conditions for which it was developed may lead to unreliable predictions. Another issue that needs to be considered is to close the soot generation term in turbulent flames without resulting in high computational costs. The soot chemical reaction rates are highly nonlinear functions of scalars (temperature, species concentration, etc.) and the fluctuations of these scalars are usually non-negligible in fires. The current approaches to close the soot source term may significantly increase the computational cost to an unacceptable level for the applications in fire safety engineering application.

10.1.2.1 Beta soot generation model

In this study, a global and computationally-efficient soot model called Beta soot generation model (BSG model) was developed (see Chapter 7). The model considers the soot evolution simply as two processes of soot formation and oxidation. This simplification of soot processes reduces the number of conservation equations related to modelling on these processes to just one for soot mass fraction.

As the values of temperature, species concentrations and so on all depend strongly on the mixture fraction in an adiabatic condition, the soot generation rate was modelled as a function of mixture fraction in non-premixed flames and in a similar formation to the probability density function of the beta distribution. To include the effects on soot generation caused by the difference of temperature/oxygen mass fraction between the adiabatic and non-adiabatic conditions, extra functions were added to model the soot generation rate in non-adiabatic conditions (see Section 7.3.2-7.3.3).

The soot generation rate was generalized to a wide range of fuels by employing the fuel's laminar smoke point height (L_{sp}), which is a fuel-specific measurable constant. L_{sp} of a fuel is inversely proportional to its soot propensity, and this was represented by the parameter of the fuel's peak soot formation rate in the model. Other parameters in the model were

calculated from fuel properties such as the stoichiometric value of mixture fraction (see Section 7.3.4).

The soot source term was closed in turbulence with a statistical approach that made use of a prescribed probability density function (beta PDF was used). The PDF-weighted average of soot generation rate was calculated with a relatively low cost by utilizing the characteristic of a beta function (see Section 7.3.6)..

The achievement satisfies research Objective 2(a) and 2(b).

10.1.2.2 Validation experiments

The newly developed model was validated with two turbulent non-premixed flames (see Chapter 8). The diffuser burner with an exit diameter D= 7.1 cm was fuelled by methane or ethylene in uniform velocities. The burning occurred in quiescent ambient air in an open environment and the averages of soot volume fractions at four elevations were measured.

The simulations were carried out by using a mesh with a minimum size of $4\times3.5\times5$ mm^3. First, the predicted fields of temperature, mixture fraction and soot volume fraction on the central cut plane of the two flames were investigated (see Section 8.4). It was found that the predicted distributions of soot volume fraction in both fires qualitatively match with the possible distribution indicated by the values of temperature and mixture fraction according to the mechanisms of soot generation. Second, the predicted soot volume fraction at four elevations of H=1D, 2D, 3D, and 4D were compared with the measurements. The results showed that the predicted soot volume fractions were in reasonably good agreement with the measurements at the four elevations. The achievement satisfies research objective 2(c).

The computational cost was investigated by comparing the simulation time of the BSG model with that of the Conventional soot generation model, which treated soot yield as a constant rate (see Section 8.5). The BSG model took 5.5% longer (3 minutes) than the Conventional Model in the two simulations — an acceptable increase in the computational cost. This achievement further addresses research objective 2(c).

10.1.3 Integration of the soot generation and transport model and its validation

10.1.3.1 Integration of the soot generation and transport model

The Beta soot generation model (BSG) and Multi-Particle-Size model (MPS) were integrated into one single soot model (BSG+MPS model) (see Section 9.2). The soot source term was modelled by the soot BSG model using one fuel-specific constant — laminar smoke point height. The MPS model divided the soot particles into several groups according to the uneven soot mass size distribution. For each group, a conservation equation of the soot mass fraction of the particles in the group was used to describe the soot transport. . This achievement satisfies research Objective 3(a).

10.1.3.2 Validation experiment

The performance of the soot BSG+MPS model was examined by simulating a large-scale corridor fire which had been simulated by the constant yield (CY) +MPS model (see Section 9.4). First, the predicted upper light extinctions at two positions (near and far away from the fire source) derived from the three models were compared with the measurements. It showed that the light extinctions derived from the BSG+MPS model were in good agreement with the measurements while the CY+MPS model substantially under-predicted the light extinctions. Second, the soot mass flow rates through a cut plane at the end of the Inlet Corridor predicted by the BSG+MPS model and CY+MPS model were compared with video recordings of the test. The BSG+MPS model reproduced the phenomenon of a dramatic increase in soot generation rate occurring between 15 min to 16.5 min while the CY+MPS model failed to predict it. Third, the predicted time of visibility for the light on the floor near the exit door was compared with the video recording. The BSG+MPS model improved the predicted reappearance time of the light by 8.9% (2.5 minutes) compared with that of the CY+MPS model.

According to the video recording and measured light extinctions, the soot yield valauein the initial stage (before 15 min) might be smaller than the mean yield value, which was measured in a small well-ventilated fire, but the yield valuein the later stage (15 min to 21 min) was much greater than the mean yield rate. Thus the constant soot yield might not adequately describe the varying soot generation rate in fires.

The achievement satisfies research objective 3(b).

10.2 Future work

10.2.1 Improve the soot transport model

The Multi-Particle-Size (MPS) model mainly addresses the aspects that influence soot movement, without taking account of the interaction between soot and flow. As soot behaviours differ from flow behaviours, the friction force between gas-phase flow and soot not only affect the transportation of soot, but also the movement of the gas-phase flow. When the mass fraction of soot increases, the effect might increase and become quite an important factor to affect flow movement. Although the average soot yield values are much less than 0.1 kg/kg for most combustible materials under small-scale well-ventilation conditions [Butler & Mulholland, 2004; Mulholland, 2002], the average yield rates vary with fuels and combustion conditions, and can be much higher than 0.1kg/kg for some fuels. Wade *et al*. [2007] indicated that the average soot yield value in the pre-flashover stage may be 0.2 kg/kg and in the post-flashover stage may be 0.4 kg/kg for the flaming combustion of pure polyurethane foam. The average soot yield valuefor polystyrene under a well-ventilated flaming combustion was estimated to be 0.303 kg/kg [Robbins & Wade, 2008]. If a large proportion of fuels is transformed into soot in an enclosure fire, the interaction between the soot phase and gas phase should be considered for modelling the soot/gas movement.

In this study, the soot mass size distribution of a combustible material is critical to determine the representative sizes of soot particle groups and their corresponding soot mass fractions. This information is available for only a small number of combustible materials. As there are enormous different combustible materials widely used in the building industry, efforts are required to collect the soot mass size distributions of these materials.

10.2.2 Improve the soot generation model

To simplify the calculation of the model, the difference in temperature/oxygen mass fraction between adiabatic and no-adiabatic combustion conditions was modelled in a way that was not sensitive to the fluctuation of mixture fraction. This simplification might not be correct if the fluctuation of mixture fraction is significant. Also, some parameters used in the model were derived from other soot generation models without the support of any experimental data, such as the peak soot oxidation rate, mixture fraction limits for soot formation/oxidation in an adiabatic condition. Further research in this respect is needed.

As soot generation is very sensitive to the enthalpy gain/loss, a more accurate enthalpy defect/excess model is required to improve the prediction of the current soot generation model. In chapter 8, the poor prediction of the temperature field in the low elevation of the fire plume reduced the accuracy of the prediction of soot generation. An extended conserved scalar combustion model [Brookes & Moss, 1999; Yao. 2011a] might be a solution for obtaining a more accurate enthalpy field.

10.2.3 Further validation of the BSG+MPS model

The BSG+MPS model has been validated by a few experiments in this study. Research shows that the soot generation and transport in fire varies with the fuel types and combustion conditions [Tewarson, 2002; Mulholland, 2002; Shahad & Mohammed, 2000; Bento, *et al.*, 2006]. The value range of the average soot yield is usually between 0.001kg/kg to 0.17 kg/kg for most flaming combustions [Bankston, *et al.*, 1981], and can reach to 0.4 kg/kg in flaming combustion of pure polyurethane foam [Wade *et al.*, 2007]. For a certain fuel, the combustion conditions, such as pressure and dilution, can also affect soot generation and transport (see Section 3.2.3 and Section 3.4.1).

Therefore, further validations are required to demonstrate applicability of the BSG+MPS model over a wide range of different type of fuels and combustion conditions. There are two aspects of the further validations, one is to test the model for different types of fuels and a number of specific fuels in each type, and the other one is to test the model in a variety of different combustion configurations.

10.2.4 Other aspects of the soot model

In a real fire, a large fraction of soot produced by combustion can be deposited on walls, ceilings and floors. Its neglect can be a notable source of error in soot simulations.

Soot deposition is a very complex phenomenon in fire. The mechanisms related with soot particle motion also influence soot deposition rate, and the primary mechanisms include gravitational, diffusive and thermophoretic forces. A gravitational force acts upon soot particles by depositing soot to horizontal surfaces. Owing to the influence of gravity on large particles, horizontal floors are likely to experience higher rates of particle deposition than

vertical walls or horizontal ceilings. A diffusive force transports soot particles over a concentration gradient and thermophoretic forces transport soot particles over a temperature gradient. In a laminar diffusion reacting flow, the soot particles move via the concentration or temperature gradient. In turbulent diffusion flames, interactions between particles and air turbulence frequently determine particle deposition rates. Besides the forces and mechanisms discussed above, the physical surrounding roughness is also likely to control particle deposition rates. A large number of investigations demonstrate that micro/macro surface roughness enhances soot particle deposition relative to the case of a smooth surface.

The soot deposition approach applied in this study is an empirical model, which is not sufficient to reliably predict soot deposition in practice. A more accurate soot deposition model is necessary in simulations to the burning of heavy ‘sooting’ fuels.

Appendix A.

The Beta soot generation model is a semi-empirical model that contains several empirical parameters. The calculation formulas for these parameters have been discussed in detail in chapter 7. In this appendix, the value ranges of the four parameters ($a_{sf,}\, b_{sf}$, $a_{so,}\, b_{so}$) and the mixture fraction where soot formation ends and the mixture fraction where soot oxidation starts in adiabatic conditions will be discussed.

The value range of parameters $a_{sf,}\, b_{sf}$

The Beta generation model uses Equation (7.5) to describe the soot formation rate against mixture fraction. In Equation (7.5), there are two parameters ($a_{sf,}\, b_{sf}$) which are calculated from mixture fraction limits $\xi_{sf,L}$, and $\xi_{sf,P}$ by Equation (7.9)-(7.11). The values of the two parameters determine the trend of soot formation rate. It is essential to investigate the value range of these parameters.

The lower mixture fraction $\xi_{sf,L}$ is the position where soot formation starts to dominate soot evolution in adiabatic conditions. The Beta model sets the value of $\xi_{sf,L}$ to be the stoichiometric mixture fraction ξ_{st}:

$$\xi_{sf,L} = \xi_{st} \tag{A. 1}$$

Mixture fraction limit $\xi_{sf,P}$ represents the position where the soot formation rate reaches its peak and it is calculated from the stoichiometric mixture fraction ξ_{st} as:

$$\xi_{sf,P} = \psi_{sf,P}\xi_{st} \tag{A. 2}$$

where $\psi_{sf,P}$ is assumed to be a fuel-independent constant and must be greater than 1 ($\psi_{sf,P}$ >1). The Beta model sets it to be $\psi_{sf,P} = 1.9$.

Before discussing the value range of the two parameters $a_{sf,}\, b_{sf}$, the value of denominator C_{sf} in the Equation (7.9) and (7.10) is discussed. C_{sf} is defined by Equation (7.11) and contains two inputs $\xi_{sf,L}$ and $\xi_{sf,P}$. Substituting Equation (A.1) and (A.2) into Equation (7.11), we get:

$$C_{sf} = \psi_{sf,P}\xi_{st}\ln(\frac{1}{\psi_{sf,P}}) + (1-\psi_{sf,P}\xi_{st})\ln\left(1+\frac{(\psi_{sf,P}-1)\xi_{st}}{1-\psi_{sf,P}\xi_{st}}\right) \quad \text{(A. 3)}$$

As $0 < \frac{(\psi_{sf,P}-1)\xi_{st}}{1-\psi_{sf,P}\xi_{st}} < 1$, the term $\ln\left(1+\frac{(\psi_{sf,P}-1)\xi_{st}}{1-\psi_{sf,P}\xi_{st}}\right)$ in the right hand side of Equation (A.3) can be expanded by the Taylor series as:

$$\ln\left(1+\frac{(\psi_{sf,P}-1)\xi_{st}}{1-\psi_{sf,P}\xi_{st}}\right) = \sum_{k=1}^{\infty}\frac{(-1)^{k-1}}{k}\left(\frac{(\psi_{sf,P}-1)\xi_{st}}{1-\psi_{sf,P}\xi_{st}}\right)^{k} \quad \text{(A. 4)}$$

Therefore,

$$\frac{(\psi_{sf,P}-1)\xi_{st}}{1-\psi_{sf,P}\xi_{st}} - \frac{1}{2}\left(\frac{(\psi_{sf,P}-1)\xi_{st}}{1-\psi_{sf,P}\xi_{st}}\right)^{2} < \ln\left(1+\frac{(\psi_{sf,P}-1)\xi_{st}}{1-\psi_{sf,P}\xi_{st}}\right) < \frac{(\psi_{sf,P}-1)\xi_{st}}{1-\psi_{sf,P}\xi_{st}} \quad \text{(A. 5)}$$

As $(1-\psi_{sf,P}\xi_{st}) > 0$, Equation (A.3) can be deduced as follows by using Equation (A.5)

$$\psi_{sf,P}\xi_{st}\ln(\frac{1}{\psi_{sf,P}}) + (\psi_{sf,P}-1)\xi_{st} - \frac{1}{2}\frac{(\psi_{sf,P}-1)^2{\xi_{st}}^2}{(1-\psi_{sf,P}\xi_{st})} < C_{sf} < \psi_{sf,P}\xi_{st}\ln(\frac{1}{\psi_{sf,P}}) + (\psi_{sf,P}-1)\xi_{st} \quad \text{(A. 6)}$$

Equation (7.9) calculates the parameter a_{sf} as:

$$a_{sf} = \frac{\psi_{sf,P}\xi_{st}\ln\sigma}{C_{sf}} \quad \text{(A. 7)}$$

Substituting C_{sf} by Equation (A.6), we get:

$$\frac{\ln\sigma}{\ln(\frac{1}{\psi_{sf,P}}) + \frac{\psi_{sf,P}-1}{\psi_{sf,P}} - \frac{1}{2}\frac{(\psi_{sf,P}-1)^2\xi_{st}}{\psi_{sf,P}(1-\psi_{sf,P}\xi_{st})}} < a_{sf} < \frac{\ln\sigma}{\ln(\frac{1}{\psi_{sf,P}}) + \frac{\psi_{sf,P}-1}{\psi_{sf,P}}} \quad \text{(A. 8)}$$

Thus:

$$\frac{\ln\sigma}{\ln(\frac{1}{\psi_{sf,P}}) + \frac{\psi_{sf,P}-1}{\psi_{sf,P}} - \frac{1}{2}\frac{(\psi_{sf,P}-1)^2}{\psi_{sf,P}}} < a_{sf} < \frac{\ln\sigma}{\ln(\frac{1}{\psi_{sf,P}}) + \frac{\psi_{sf,P}-1}{\psi_{sf,P}}} \quad \text{(A. 9)}$$

The term $\ln(\frac{1}{\psi_{sf,P}})$ can be written as:

$$\ln(\frac{1}{\psi_{sf,P}}) = \ln(1-\frac{\psi_{sf,P}-1}{\psi_{sf,P}}) \quad \text{(A. 10)}$$

As $0 < \frac{\psi_{sf,P} - 1}{\psi_{sf,P}} < 1$, the above term can be expanded as:

$$\ln(\frac{1}{\psi_{sf,P}}) = \ln(1 - \frac{\psi_{sf,P} - 1}{\psi_{sf,P}}) = \sum_{k=1}^{\infty} \frac{-1}{k} \left(\frac{\psi_{sf,P} - 1}{\psi_{sf,P}} \right)^k \quad \text{(A. 11)}$$

Therefore,

$$\ln(\frac{1}{\psi_{sf,P}}) < -\frac{\psi_{sf,P} - 1}{\psi_{sf,P}} \quad \text{(A. 12)}$$

According to the Equation (A.12) and (A.9), the parameter a_{sf} must be positive when $\psi_{sf,P} > 1 \text{and} \sigma < 1$.

Using $\psi_{sf,P}$ =1.9 and $\sigma = 0.01$, the value range of parameter a_{sf} is:

$$12.0769 < a_{sf} < 27.3841 \quad \text{(A. 13)}$$

According to the Equation (7.10), the parameter b_{sf} can be calculated as:

$$b_{sf} = \frac{(1 - \xi_{sf,P})}{\xi_{sf,P}} a_{sf} \quad \text{(A. 14)}$$

Therefore,

$$12.0769 \frac{(1 - \xi_{sf,P})}{\xi_{sf,P}} < b_{sf} < 27.3841 \frac{(1 - \xi_{sf,P})}{\xi_{sf,P}} \quad \text{(A. 15)}$$

As $\frac{(1 - \xi_{sf,P})}{\xi_{sf,P}}$ is much greater than 1, the parameter b_{sf} should be much greater than 12.

The value range of parameters $a_{so,}\, b_{so}$

Equation (7.21) contains two parameters ($a_{so,}\, b_{so}$) which are calculated from mixture fraction limits $\xi_{so,H}$, $\xi_{so,P}$ by Equation (7.24)-(7.26). The values of the two parameters determine the trend of soot surface oxidation rate. The value ranges of the two parameters are discussed in a similar way as the above section.

The mixture fraction $\xi_{so,H}$ is the position where soot oxidation nearly ends in adiabatic conditions. The Beat model sets

$$\xi_{so,H} = \xi_{st} \quad \text{(A. 16)}$$

Mixture fraction limit $\xi_{so,P}$ represents the position where soot oxidation surface rate reaches its peak and it is calculated from the stoichiometric mixture fraction ξ_{st} as:

$$\xi_{so,P} = \psi_{so,P}\xi_{st} \tag{A. 17}$$

where $\psi_{so,P}$ is assumed to be a fuel-independent constant and must be less than 1 ($\psi_{so,P}$ <1). The Beta model sets it to be $\psi_{so,P} = 0.85$.

Substituting Equation (A.16) and (A.17) in Equation (7.26), we get:

$$C_{so} = \psi_{so,P}\xi_{st}\ln(\frac{1}{\psi_{so,P}}) + (1-\psi_{so,P}\xi_{st})\ln\left(1-\frac{(1-\psi_{so,P})\xi_{st}}{1-\psi_{so,P}\xi_{st}}\right) \tag{A. 18}$$

Because

$$-2\frac{(1-\psi_{so,P})\xi_{st}}{1-\psi_{so,P}\xi_{st}} < \ln\left(1-\frac{(1-\psi_{so,P})\xi_{st}}{1-\psi_{so,P}\xi_{st}}\right) < -\frac{(1-\psi_{so,P})\xi_{st}}{1-\psi_{so,P}\xi_{st}} \tag{A. 19}$$

Equation (A.18) could be deduced to:

$$\psi_{so,P}\xi_{st}\ln(\frac{1}{\psi_{so,P}}) - 2(1-\psi_{so,P})\xi_{st} < C_{so} < \psi_{so,P}\xi_{st}\ln(\frac{1}{\psi_{so,P}}) - (1-\psi_{so,P})\xi_{st} \tag{A. 20}$$

Equation (7.24) calculates the parameter a_{so} as:

$$a_{so} = \frac{\psi_{so,P}\xi_{st}\ln\sigma}{C_{so}} \tag{A. 21}$$

Substituting C_{so} by Equation (A.20) to the above equation, we get:

$$\frac{\ln\sigma}{\ln(\frac{1}{\psi_{so,P}}) - 2\frac{1-\psi_{so,P}}{\psi_{so,P}}} < a_{so} < \frac{\ln\sigma}{\ln(\frac{1}{\psi_{so,P}}) - \frac{1-\psi_{so,P}}{\psi_{so,P}}} \tag{A. 22}$$

Similar solution as Equation (A.12), we have:

$$\ln(\frac{1}{\psi_{so,P}}) < \frac{1-\psi_{so,P}}{\psi_{so,P}} \tag{A. 23}$$

Therefore, according to the Equation (A.22) and (A.23), a_{so} is a positive constant when $0 < \psi_{so,P} < 1 \text{and} \sigma < 1$.

Using $\psi_{so,P}$ =0.85 and $\sigma = 0.01$, the value range of parameter a_{so} is:

$$24.1840 < a_{so} < 330.0805 \tag{A. 24}$$

According to the Equation (7.25), the parameter b_{so} could be calculated as:

$$b_{so} = \frac{(1-\xi_{so,P})}{\xi_{so,P}} a_{so} \tag{A. 25}$$

Therefore,

$$24.1840\frac{(1-\xi_{so,P})}{\xi_{so,P}} < b_{so} < 330.0805\frac{(1-\xi_{so,P})}{\xi_{so,P}} \tag{A. 26}$$

As $\frac{(1-\xi_{so,P})}{\xi_{so,P}}$ is much greater than 1, the parameter b_{so} should be much greater than 24.

The value of mixture fraction where the formation rate ends

$\xi_{sf,H}$ is the position where soot formation is assumed to end and is calculated as $\xi_{sf,H} = \psi_{sf,H}\xi_{st}$ in some models [Lautenbergers, 2005; Lautenbergers, 2002; Yao, *et al*., 2011a]. The value of $\psi_{sf,H}$ varies from 2.15 to 3.0 for different fuels in these models. As $\psi_{sf,H}$ tends to vary with fuel, it is not used in the Beta soot generation model.

The Beta soot generation model assumes that the soot formation rate increases from around zero at a mixture fraction of $\xi_{sf,L}$ to a peak rate at mixture fraction $\xi_{sf,P}$, then it falls back to around zero at some point. According to the work of Lautenbergers [2005; 2002] and of Yao, *et al*.[2011a], the point was close to $2.15\xi_{st}$ or $3.0\xi_{st}$. In this section, the point where the soot formation ends in adiabatic conditions will be discussed.

According to the characteristic of the Beta distribution function, the mean, mode and skewness of the soot formation rate function (Equation (7.5)) in adiabatic conditions are:

$$mean = \frac{a_{sf}+1}{a_{sf}+b_{sf}+2} \tag{A. 27}$$

$$\mathrm{mod}\, e = \frac{a_{sf}}{a_{sf}+b_{sf}} = \xi_{sf,P} \tag{A. 28}$$

$$skewness = \frac{2(b_{sf}-a_{sf})\sqrt{a_{sf}+b_{sf}+3}}{(a_{sf}+b_{sf}+4)\sqrt{(a_{sf}+1)(b_{sf}+1)}} \tag{A. 29}$$

As the previous discussion shows the parameters a_{sf}, b_{sf} both are positive and $a_{sf} < b_{sf}$, skewness is greater than 0 according to Equation (A.29). Therefore, the function (7.5) is positive skewness.

Equation (A.27)-(A.28) shows that

$$mean - \mathrm{mod}\, e = \frac{b_{sf} - a_{sf}}{(a_{sf} + b_{sf})(a_{sf} + b_{sf} + 2)} < \frac{1}{a_{sf} + b_{sf} + 2} \qquad \text{(A. 30)}$$

Because parameters $b_{sf} >> a_{sf}$ > 12, the difference between the mean and the mode is very small. Therefore, the skewness is very small too. As a result, the Beta formation rate function (Equation (7.5)) should be approximately symmetrical at $\xi = \xi_{sf,P}$, which is the mode point of the function. The mixture fraction $\xi_{sf,L}$ and $2.8\xi_{st}$ ($2.8\xi_{st} = 2\xi_{sf,P} - \xi_{sf,L}$) are symmetrical against point $\xi_{sf,P}$. As the formation rate $f_{sf}'''(\xi_{sf,L})$ is very small compared with its peak $f_{sf}'''(\xi_{sf,P})$, the formation rate $f_{sf}'''(2.8\xi_{st})$ should also be very small compared with $f_{sf}'''(\xi_{sf,P})$. It means soot formation rate nearly ends at mixture fraction $2.8\xi_{st}$, which is between $2.15\xi_{st}$ and $3.0\xi_{st}$ as suggested by Lautenbergers and Yao, *et al*.. Thus the mixture fraction $2.8\xi_{st}$ is a reasonable value for the mixture fraction where the formation rate falls to near zero.

The value of mixture fraction where the oxidation starts

The Beta soot generation model assumes that the soot oxidation rate increases from around zero at a mixture fraction of $\xi_{so,L}$ to a peak rate at mixture fraction $\xi_{so,P}$, then it falls back to around zero at $\xi_{so,H}$. The mixture fraction $\xi_{so,L}$ is the position where soot oxidation starts. It is calculated as $\xi_{so,L} = \psi_{so,L}\xi_{st}$ ($\psi_{so,L} = 0.56$) in the model developed by Lautenbergers [2005; 2002] or just set to be zero in the model developed by Yao, *et al*. [2011a]. the Beta soot generation model doesn't use $\xi_{so,L}$ to model soot oxidation surface rate. In this section, the mixture fraction where soot oxidation starts in adiabatic conditions will be discussed in a way similar to the last section.

The previous discussion shows that the parameters $b_{so} >> a_{so}$ > 24, so the soot oxidation rate Function (7.21) is positive skewed and the skewness is very small. Therefore, the Beta soot oxidation rate should be approximately symmetrical at $\xi = \xi_{so,P}$, which is the mode of the

Function (7.21). In the Beta generation model, $\xi_{so,H} = \xi_{st}$ and $\xi_{so,P} = 0.85\xi_{st}$, therefore, the soot oxidation rate $f''_{so}(0.7\xi_{st})$ is close to $f''_{so}(\xi_{so,H})$, which is very small compared with the peak soot oxidation rate. As a results, the soot oxidation rate at $0.7\xi_{st}$ is close to zero too. Therefore, the soot oxidation in the adiabatic condition is assumed to start at about $\xi = 0.7\xi_{st}$, which is slightly higher than the parameter used in the model of Lautenbergers [2005].

REFERENCES

Anon. (1997, May). Fire death trends:An International Perspective. Federal Emergency Management Agency, United States Fire Administration, National Fire Data Centre.

APTEC. (2013). APTEC Report-The jilin Baoyuanfeng Poultry Processing Plant Fire. APTEC technology Consulting.

Ashe, B., McAneney, K. J., & Pitman, A. J. (2009). Total cost of fire in Australia. Journal of Risk Research, 12(2), 121-136.

Axelbalim, R. L. (1988). Dilution and temperature effects of inert addition on soot formation in counterflow diffusion flames. Combustion science and technology, 61(3), 51-73.

Axelbaum, R. L., & Law, C. K. (1991, December). Soot formation and inert addition in diffusion flames. I Symposium (International) on Combustion (Vol. 23, ss. 1517-1523). Elsevier.

Babrauskas, V. (2003). Ignition handbook. Fire Science Publ.

Balthasar, M. P. (2002). Implementation and validation of a new soot model and application to aeroengine combustors. Journal of engineering for gas turbines and power, 124(1), 66-74.

Bankston, C. P., Zinn, B. T., Browner, R. F., and Powell, E. A. (1981). Aspects of the Mechanism of Smoke Generation by Building Materials. Combustion and Flame, 41, 273-292.

Beji, T., Zhang, J. P., & Delichatsios, M. (2008). Determination of soot formation rate from laminar smoke point measurements. Combustion Science and Technology, 180(5), 927-940.

Beltrame, A., Porshnev, P., Merchan-Merchan, W., Saveliev, A., Fridman, A., Kennedy, L. A., & Charon, O. (2001). Soot and NO formation in methane–oxygen enriched diffusion flames. Combustion and flame, 124(1), 295-310.

Benson, T. (2004). Fire Kills 283 At Supermarket In Paraguay. International NEw York Time.

Bento, D. S., Thomson, K. A., & Gülder, Ö. L. (2006). Soot formation and temperature field structure in laminar propane–air diffusion flames at elevated pressures. Combustion and flame, 145(4), 765-778.

Bilger, R. W. (1976). Turbulent jet diffusion flames. Progress in Energy and Combustion Science, 1(2), 87-109.

Bilger, R. W. (1990). On reduced mechanisms for methane- air combustion in nonpremixed flames. Combustion and Flame, 80(2), 135-149.

Blomqvist, J. (2003). *Smoke detection in buildings with high ceilings.* Sweden: SP Swedish National Testing and Research Institute.

Breden, L.H. and Meisters, M. (1976). The Effect of Sample Orientation in the Smoke Density Chamber. *Fire and Flammability, 7*, 234.

Briggs, W. L., & McCormick, S. F. (2000). *A multigrid tutoria.* Siam.

Brookes S. J., Moss J. B. (1999). Predictions of soot and thermal radiation properties in confined trubulent jet diffusion flames. *Combustion and Flame, 116*, 486–503.

Brownh, A. J., & Heywood, J. B. (1988). A fundamentally-based stochastic mixing model method for predicting NO and soot emissions from direct injection diesel engines. *Combustion science and technology, 58*(1-3), 195-207.

Butler, K. M., & Mulholland, G. W. (2004). Generation and transport of smoke components. *Fire Technology, 40*(2), 149-176.

Calcote, H. F., & Manos, D. M. (1983). Effect of molecular structure on incipient soot formation. *Combustion and Flame, 49*(1), 289-304.

Chen, F., & Lai, A. C. (2004). An Eulerian model for particle deposition under electrostatic and turbulent conditions. *Journal of aerosol science, 35*(1), 47-62.

Chen, F., Yu, S., & Lai, A. C. (2006). Modeling particle distribution and deposition in indoor environments with a new drift–flux model. *Atmospheric Environment, 40*(2), 357-367.

Chen, Z., Wen, J., Xu, B., & Dembele, S. (2014). Extension of the eddy dissipation concept and smoke point soot model to the LES frame for fire simulations. *Fire Safety Journal, 64*, 12-26.

Chien, W. P., & Seader, J. D. (1975). Prediction of specific optical density for smoke obscuration in an NBS smoke density chamber. *Fire Technology, 11*(3), 206-218.

Chowdhury N, Rowe I and Sayer G. (2013). *Fire statistics,Great Britain, 2011 to 2012.* Department for Communities and Local Government.

Coelho, P. J., & Carvalho, M. G. (1997). A conservative formulation of the discrete transfer method. *Journal of Heat Transfer, 119*(1), 118-128.

Crocker, J. C. (1997). Crocker, J. C. (1997). Measurement of the hydrodynamic correctBrownian motion of two colloidal spheres. *Crocker, J. C. (1997). Measurement of the hydrodynamic corrections toJournal of Chemical Physics, 106*(6), 2837-2840.

Cumber, P. S. (1995). Improvements to the discrete transfer method of calculating radiative heat transfer. *International Journal of Heat and Mass Transfer, 38*(12), 2251-2258.

Dederichs, A. S. (2004). *Flamelet modelling of soot formation in diffusion flames (Doctoral dissertation).* Lund University.

Delichatsios, M. A. (1994). A phenomenological model for smoke-point and soot formation in laminar flames. *Combustion science and technology, 100*(1-6), 283-298.

DiNenno, P., Beyler, C. L., Custer, R. L. P., Walton, W. D., and Watts, J. M., Jr., Editors. (1988). *SFPE handbook of fire protection engineering.* Boston: National Fire Protection Association Quincy, MA.

Dobbins, R. A., Mulholland, G. W., & Bryner, N. P. (1994). Comparison of a fractal smoke optics model with light extinction measurements. *Atmospheric Environment, 28*(5), 889-897.

Du, J., & Axelbaum, R. L. (1995). The effect of flame structure on soot-particle inception in diffusion flames. *Combustion and Flame, 100*(3), 367-375.

Durst, F., Miloievic, D., & Schönung, B. (1984). Eulerian and Lagrangian predictions of particulate two-phase flows: a numerical study. *Applied Mathematical Modelling, 8*(2), 101-115.

Edelman, R. B., & Harsha, P. T. (1977). Current status of laminar and turbulent gas dynamics in combustors. In *Combustion Institute, Spring Technical Meeting, Cleveland, Ohio, Mar. 28-30* (Vol. 1, p. 224).

Evans, D. D., & Stroup, D. W. (1986). Methods to calculate the response time of heat and smoke detectors installed below large unobstructed ceilings. *Fire Technology, 22*(1), 54-65.

Ewer, J., Galea, E. R., Patel, M. K., Taylor, S., Knight, B., & Petridis, M. (1999). SMARTFIRE: an intelligent CFD based fire model. *ournal of Fire Protection Engineering, 10*(1), 13-27.

Ewer, J., Jia, F., Grandison, A., Galea, E. R., & Patel, M. (2008). *SMARTFIRE V4. 1 user guide and technical manual smartfire tutorials.* Fire Safety Engineering Group.

Fairchild, P. W., Smith, G. P., & Crosley, D. R. (1983). Collisional quenching of A 2Σ+ OH at elevated temperatures. *The Journal of chemical physics, 79*(4), 1795-1807.

Fairweather, M., Jones, W. P., Ledin, H. S., & Lindstedt, R. P. (1992). Predictions of soot formation in turbulent, non-premixed propane flames. I *Symposium (International) on Combustion* (Vol. 24, ss. 1067-1074). Elsevier.

Fenimore, C. P., & Jones, G. W. (1967). Oxidation of soot by hydroxyl radicals. *The Journal of Physical Chemistry, 71*(3), 593-597.

Ferraris, S. A., & Wen, J. X. (2008). LES of the sandia flame D using laminar flamelet decomposition for conditional source-term estimation. *Flow, turbulence and combustion, 81*(4), 609-639.

Fiveland, W. A. (1991). The selection of discrete ordinate quadrature sets for anisotropic scattering. *Fundamentals of radiation heat transfer, 160*, 89-96.

Fletcher, D. F., Kent, J. H., Apte, V. B., & Green, A. R. (1994). Numerical simulations of smoke movement from a pool fire in a ventilated tunnel. *Fire Safety Journal, 23*(3), 305-325.

Floyd, J. , Overholt, K., & Ezekoye, O. (2014). Soot Deposition and Gravitational Settling Modeling and the Impact of Particle Size and Agglomeration. *Fire Safety Science, 11*, 174.

Fredrik Ahlström, A., & Ingemar Odenbrand, C. U. (1989). Combustion characteristics of soot deposits from diesel engines. *Carbon, 27*(3), 475-483.

Frenklach, M., & Wang, H. (1991, December). Detailed modeling of soot particle nucleation and growth. In *Symposium (International) on Combustion* (Vol. 23, pp. 1559-1566). Elsevier.

Frenklach, M., & Wang, H. (1994). Detailed mechanism and modeling of soot particle formation. I *Soot formation in combustion* (ss. 165-192). Berlin Heidelberg: Springer.

Frenklach, M., Clary, D. W., Gardiner Jr, W. C., & Stein, S. E. (1985). Detailed kinetic modeling of soot formation in shock-tube pyrolysis of acetylene. I *Symposium (International) on Combustion* (Vol. 2, ss. 887-901). Elsevier.

Friedlander, S. K. (2000). *Smoke, dust, and haze* (Vol. 198). New York: Oxford University Press.

Galea, E. R., & Ierotheou, C. S. (1992). Fire-field modelling on parallel computers. *Fire safety journal*, *19*(4), 251-266.

Galea, E. R., Wang, Z., Veeraswamy, A., Jia, F., Lawrence, P. J., & Ewer, J. (2008, September). Coupled fire/evacuation analysis of the Station Nightclub fire. I *Proc of 9th IAFSS Symp* (ss. 465-476).

Gao, Y., & Chow, W. K. (2005). A BRIEF REVIEW ON COMBUSTION MODELING. *International Journal on Architectural Science*, *6*(2), 38-69.

Glassman, I. (1979). *Phenomenological models of soot processes in combustion systems.* PRINCETON UNIV NJ DEPT OF MECHANICAL AND AEROSPACE ENGINEERING.

Glassman, I., & Yaccarino, P. (1981, December). The temperature effect in sooting diffusion flames. I *Symposium (International) on Combustion* (Vol. 18, ss. 1175--1183). Elsevier.

Gomez, A., Littman, M. G., & Glassman, I. (1987). Comparative study of soot formation on the centerline of axisymmetric laminar diffusion flames: fuel and temperature effects. *Combustion and Flame*, *70*(2), 225-241.

Gomez, A., Sidebotham, G., & Glassman, I. (1984). Sooting behavior in temperature-controlled laminar diffusion flames. *Combustion and flame*, *58*(1), 45-57.

Gonzales, D. (2002). *Lima Street Vendors Caught Between Police and Poverty.* Liam: The New York Times.

Gouesbet, G., & Berlemont, A. (1998). Eulerian and Lagrangian approaches for predicting the behaviour of discrete particles in turbulent flows. *Progress in Energy and Combustion Science*, *25*(2), 133-159.

Graham, S. C. (1981). The modelling of the growth of soot particles during the pyrolysis and partial oxidation of aromatic hydrocarbons. *Proceedings of the Royal Society of London. A. Mathematical and Physical Sciences*, *377*(1769), 119-145.

Gross, D., Loftus, J. J., & Robertson, A. F. (1967). Method for measuring smoke from burning materials. I *Symposium on Fire Test Methods—Restraint and Smoke, ASTM STP* (Vol. 422, s. 166).

Grosshandler, W. L., Bryner, N., Madrzykowski, D., & Kuntz, K. (2005). *Report of the technical investigation of the station nightclub fire.* Gaithersburg: National Institute of Standards and Technology Gaithersburg,, MD.

Gülder, Ö. L., Snelling, D. R., & Sawchuk, R. A. . (1996). Influence of Hydrogen Addition to Fuel on Temperature Field and Soot Formation in Diffusion Flames. *Symposium (International) on Combustion*, *26*, ss. 2351-2357.

Hall, J. R. (2014). *The total cost of fire in the United States.* National Fire Protection Association.

Hamins, A. (1993). Soot. I I. Puri (Red.), *Environmental Implications of Combustion Processes* (ss. 71--95).

Harris, S. J., & Weiner, A. M. (1983). Surface growth of soot particles in premixed ethylene/air flames. *Combustion Science and Technology, 31*(3-4), 155-167.

Hasemi, Y. (2008). Surface Flame Spread. I J. D. Philip, *The SFPE Handbook of Fire Protection Engineering* (4. utg., Vol. 2, ss. 278-290). Natl Fire Protection Assn.

He, M., Jiang, Y., & Perez, C. (2004). *Use FDS to Assess Effectiveness of Air Sampling Smoke Detection in Large Open Spaces.* Vision Fire & Security.

He, Y. (1997). On experimental data reduction for zone model validation. *Journal of Fire Sciences, 15*(2), 144-161.

He, Y., Fernando, A., & Luo, M. (1998). Determination of interface height from measured parameter profile in enclosure fire experiment. *Fire Safety Journal, 31*(1), 19-38.

Hertzberg, T., & Blomqvist, P. (2003). Particles from fires—a screening of common materials found in buildings. *Fire and materials, 27*(6), 295-314.

Heskestad, G. (1997). Flame Heights of Fuel Arrays with Combustion in Depth. *Fire Safety Science--Proc*, 427-438 .

Hinds, W. C. (1982). *Aerosol technology: properties, behavior, and measurement of airborne particles.* New York: Wiley.

Hinze, J. (1975). *Turbulence.* New York: McGraw-Hill Book Company.

Hiroyasu, H., Kadota, T., & Arai, M. (1983a). Development and use of a spray combustion modeling to predict diesel engine efficiency and pollutant emissions: Part 1 combustion modeling. *Bulletin of JSME, 26*(214), 569-575.

Hiroyasu, H., Kadota, T., & Arai, M. (1983b). Development and use of a spray combustion modeling to predict diesel engine efficiency and pollutant emissions: Part 2 computational procedure and parametric study. *Bulletin of JSME, 26*(214), 576-583.

Hjohlman, M., Försth, M., & Axelsson, J. (2009). *Design fire for a train compartment.* SP Technical Research Institute of Sweden.

Holgate, P. (1989). The lognormal characteristic function. *Communications in Statistics-Theory and Methods, 18*(12), 4539-4548.

Holman, J. P. (2002). *Heat transfer.* New York, USA: McGrawHill.

Holmberg, S., & Chen, Q. (2003). Air flow and particle control with different ventilation systems in a classroom. *Indoor air, 13*(2), 200-204.

Hu, X. F., Wang, Z., Jia, F., Galea, E. R., & Patel, M. K. (2011). Simulating smoke transport in large scale enclosure fires using a multi-particle-size model. *Fire Safety Science, 10*, 445-458.

Hu, X., Wang, Z., Jia, F., & Galea, E. R. (2010). Simulating a train car fire using a flame spread model. *In Proceedings of the 12th International Fire Science & Engineering Conference, Interflam 2010,. 2*, ss. 1725-173. University of Nottingham.

Hu, X., Wang, Z., Jia, F., & Galea, E. R. (2012). Numerical investigation of fires in small rail car compartments. *Journal of Fire Protection Engineering, 22*(4), 245-270.

Hunt, R. A. (1953). Relation of smoke point to molecular structure. *Industrial & Engineering Chemistry, 45*(3), 602-606.

Husted, B. P. (2004). *Optical smoke units and smoke potential of different products.* DIFT report.

Hwang, J. Y., & Chung, S. H. (2001). Growth of soot particles in counterflow diffusion flames of ethylene. Combustion and flame, 125(1),. *125*(1), 752-762.

Ierotheou, C. S., & Galea, E. R. (1992). A fire field model implemented in a parallel computing environment. *International journal for numerical methods in fluids, 14*(2), 175-187.

Imtiaz S. (2012). *Fires engulf Pakistan factories killing 314 workers.* REUTERS.

Isaksson, S., Persson, B., & Tuovinen, H. (1999). Simulation of smoke detection in a room with a perforated suspended ceiling. *Proceeding of the 8th international Fire Science & Engineering Conference, Interflam, 1*, ss. 441-452.

Jia, F., Galea, E. R., & Patel, M. K. (1999). The numerical simulation of the noncharring pyrolysis process and fire development within a compartment. *Applied Mathematical Modelling, 23*(8), 587-607.

Jia, F., Patel, M. K., Galea, E. R., Grandison, A., & Ewer, J. (2006a). CFD fire simulation of the Swissair flight 111 in-flight fire-Part 1: Prediction of the pre-fire air flow within the cockpit and surrounding areas. *Aeronautical Journal, 110*(1103), 41-52.

Jia, F., Patel, M. K., Galea, E. R., Grandison, A., & Ewer, J. (2006b). CFD fire simulation of the Swissair flight 111 in-flight fire-part II: fire spread analysis. *Aeronautical Journal, 110*, 303-314.

Jiang, X., & Lai, C. H. (2009). *Numerical techniques for direct and large-eddy simulations.* CRC Press.

Jin, T. (1978). Visibility through Fire Smoke. *Journal of Fire and Flammability, 9*, 135-157.

Joo, H. I., & Gülder, Ö. L. (2009). Soot formation and temperature field structure in co-flow laminar methane–air diffusion flames at pressures from 10 to 60atm. *Proceedings of the Combustion Institute, 32*(1), 769-775.

K Lai, A. C., & Nazaroff, W. W. (2000). Modeling indoor particle deposition from turbulent flow onto smooth surfaces. *Journal of aerosol science, 31*(4), 463-476.

Kennedy, I. M. (1997). Models of soot formation and oxidation. *Progress in Energy and Combustion Science, 23*, ss. 95-132.

Kennedy, I. M., Kollmann, W., & Chen, J. Y. (1990). A model for soot formation in a laminar diffusion flame. *Combustion and Flame, 81*(1), 73-85.

Kennedy, I. M., KOLLMANN, W., & Chen, J. Y. (1991). Predictions of soot in laminar diffusion flames. *AIAA journal, 29*(9), 1452-1457.

Kent, J. H., & Honnery, D. R. (1990). A soot formation rate map for a laminar ethylene diffusion flame. Combustion and Flame. *Combustion and Flame, 79*(3), 287-298.

Kent, J. H., & Wagner, H. G. (1985). Temperature and fuel effects in sooting diffusion flames. *In Symposium (International) on Combustion. 20*, ss. 1007-1015. Elsevier.

Khan, I. M, Greeves, S., Probert, D. M. (1971). *Prediction of soot and nitric oxide concentrations in diesel engine exhaust, in: Air pollution control in transport engines.* London: Institute of Mechanical Engineers.

Kittelson, D., Watts, W., & Johnson, J. . (2002). *Diesel Aerosol Sampling Methodology–CRC E-43.* Coordinating Research Council.

Kouremenos, D. A., Rakopoulos, C. D., & Kotsiopoulos, P. (1990). Comparative performance and emission studies for vaporized diesel fuel and gasoline as supplements in swirl-chamber diesel engines. *Energy, 15*(2), 1153-1160.

Kumfer, B. M., Skeen, S. A., Chen, R., & Axelbaum, R. L. (2006). Measurement and analysis of soot inception limits of oxygen-enriched coflow flames. *Combustion and flame, 147*(3), 233-242.

Kwon, K.J. & Mullen, J. (2014). *Fire at South Korean hospital for elderly kills 21.* CNN.

Lall, A. A., and Zachariah, M.R. (537-568). Combustion Generated Fine Carbonaceous Particles,, Scientific Publishing. I H. Bockhorn, *Combustion generated fine carbonaceous particles.*. KIT Scientific Publishing.

Launder, B. E., & Spalding, D. B. (1974). The numerical computation of turbulent flows. *Computer methods in applied mechanics and engineering, 3*(2), 269-289.

Lautenberger, C. W. (2002). *CFD simulation of soot formation and flame radiation.* WORCESTER POLYTECHNIC INSTITUTE.

Lautenberger, C. W., de Ris, J. L., Dembsey, N. A., Barnett, J. R., & Baum, H. R. (2005). A simplified model for soot formation and oxidation in CFD simulation of non-premixed hydrocarbon flames. *Fire Safety Journal, 40*(2), 141-176.

Lee, K. B., Thring, M. W., & Beer, J. M. (1962). On the rate of combustion of soot in a laminar soot flame. *Combustion and Flame, 6*, 137-145.

Leung, K. M., Lindstedt, R. P., & Jones, W. P. (1991). A simplified reaction mechanism for soot formation in nonpremixed flames. *Combustion and flame, 87*(3), 289-305.

Lindstedt, P. R. (1994). Simplified soot nucleation and surface growth steps for non-premixed flames. I *Soot Formation in Combustion* (ss. 417-441). Berlin Heidelberg: Springer .

Liu, F., Guo, H., Smallwood, G. J., Gülder, Ö. L., & Matovic, M. D. (2002). A robust and accurate algorithm of the β-pdf integration and its application to turbulent methane–air diffusion combustion in a gas turbine combustor simulator. *International journal of thermal sciences, 41*(8), 763-772.

Lockwood, F. C., & Shah, N. G. (1981, December). A new radiation solution method for incorporation in general combustion prediction procedures. *Symposium (international) on combustion. 18*, ss. 1405-1414. Elsevier.

Magnussen, B. F. (2005, June). The eddy dissipation concept a bridge between science and technology. I *ECCOMAS thematic conference on computational combustion* (ss. 21--24).

Magnussen, B. F., & Hjertager, B. H. (1977). On mathematical modeling of turbulent combustion with special emphasis on soot formation and combustion. *In Symposium (International) on Combustion. 16*, ss. 719-729. Elsevier.

Magnussen, B. F., & Hjertager, B. W. (1981). On the structure of turbulence and a generalized eddy dissipation concept for chemical reaction in turbulent flow. *In 19th AIAA Aerospace Meeting.* St. Louis, USA.

Magnussen, B. F., Hjertager, B. H., Olsen, J. G., & Bhaduri, D. (1979). Effects of turbulent structure and local concentrations on soot formation and combustion in C2 H2 diffusion flames. I *Symposium (International) on Combustion* (Vol. 17, ss. 1383-1393). Elsevier.

Mahalingam, A. (2007). *Modelling the generation of toxic combustion products and its transport in enclosure fires(Doctoral dissertation).* University of Greenwich.

Mahalingam, A., Jia, F., Patel, M., & Galea, E. R. (2007). Modelling generation and transport of toxic combustion products in enclosure fires using bench-scale test data. *Interflam* , (ss. 1631-1636).

Malalasekera, W., Versteeg, H. K., Henson, J. C., & Jones, J. C. (2002). Calculation of radiative heat transfer in combustion systems. *Clean Air, 3*(1), 113-143.

Mansurov, Z. A. (2005). Soot formation in combustion processes (review). *Combustion, Explosion and Shock Waves, 41*(6), 727-744.

Manual, F. (u.d.). *Version 6.2. 16, 2005, Fluent.*

Markatos, N. C., Malin, M. R., & Cox, G. (1982). Mathematical modelling of buoyancy-induced smoke flow in enclosures. *Journal of Heat and Mass Transfer, 25*, 63-75.

Markatou, P. W. (1993). A computational study of sooting limits in laminar premixed flames of ethane, and acetylene. *Combustion and flame, 93*(4), 467-482.

Mauss, F., Trilken, B., Breitbach, H., & Peters, N. . (1994). Soot formation in partially premixed diffusion flames at atmospheric pressure. I *Soot formation in combustion* (ss. 325-349). Berlin Heidelberg: Springer.

Maxey, M. R. (1987). The gravitational settling of aerosol particles in homogeneous turbulence and random flow fields. *Journal of Fluid Mechanics, 174*, 441-465.

McGrattan, K. B., Hostikka, S., Floyd, J. E., Baum, H. R., Rehm, R. G., Mell, W., & McDermott, R. (2004). Fire dynamics simulator (version 5), technical reference guide. *NIST special publication, 1018*, 5.

McLaughlin, J. B. (1993). The lift on a small sphere in wall-bounded linear shear flows. *Journal of Fluid Mechanics, 246*, 249-265.

Modest, M. F. (2013). *Radiative heat transfer.* Academic press.

Moin, P. (2002). Advances in large eddy simulation methodology for complex flows. *International Journal of Heat and Fluid Flow, 23*, 710-720.

Moin, P., & Mahesh, K. (1998). Direct numerical simulation: a tool in turbulence research. *Annual Review of Fluid Mechanics, 30*(1), 539-578.

Moss, J. B., Stewart, C. D., & Young, K. J. (1995). Modeling soot formation and burnout in a high temperature laminar diffusion flame burning under oxygen-enriched conditions. *Combustion and flame, 101*(4), 491-500.

Mulholland, G. W. (1986). Global soot growth model. *Fire safety science*, 709-718.

Mulholland, G. W. (2002). Smoke Production and Properties. I P. Dinenno, *The SFPE Handbook of Fire Protection Engineering* (3. utg., ss. 2-258).

Mulholland, G. W., Lee, T. G., & Baum, H. R. (1977). The coagulation of aerosols with broad initial size distributions. *Journal of Colloid and Interface Science, 62*(3), 406-420.

Murakami, S., ato, S.K. and Suyama, Y. (1989). Numerical study on diffusion field as affected by arrangement of supply and exhaust openings in conventional flow-type clean room. ASHRAE Transactions 95(2). *ASHRAE Transactions, 95*(2).

Murakami, S., Kato, S., Nagano, S., & Tanaka, Y. (1992). Diffusion characteristics of airborne particles with gravitational settling in a convection-dominant indoor flow field. *Ashrae Transactions, 98*(1), 82-97.

Nagle, J., & Strickland-Constable, R. F. (1962). Oxidation of Carbon between 1000-2000 C. *In Proceedings of the fifth carbon conference, 1*, ss. 154-164. New York: Pergamon.

Neoh, K. G., Howard, J. B., & Sarofim, A. F. (1981). Soot oxidation in flames. I *Particulate Carbon* (ss. 261--282). Springer.

Novozhilov, V. (2001). Computational fluid dynamics modeling of compartment fires. *Progress in Energy and Combustion science, 27*(6), 611-666.

Olson, D. B., Pickens, J. C., & Gill, R. J. (1985). The effects of molecular structure on soot formation II. *Combustion and flame, 62*(1), 43-60.

Pal, I., & Ghosh, T. (2014). Fire Incident At AMRI Hospital, Kolkata (India): A Real Time Assessment For Urban Fire. *Journal Of Business Management & Social Sciences Research, 3*(1), 9-13.

Patankar, S. (1980). *Numerical heat transfer and fluid flow.* CRC Press.

Peacock, R. D., & Babrauskas, V. (1991). Analysis of large-scale fire test data. *Fire Safety Journal, 17*(5), 387-414.

Persson, H. (2006). *Labyrinth Project Full Scale Tests in a Corridor Arrangement.* Sweden: SP Swedish National Testing and Research Institute Report BRs 6119.

Pletcher, R. H., Tannehill, J. C., & Anderson, D. (2012). *Computational fluid mechanics and heat transfer.* CRC Press.

Pope, S. B. (1985). PDF methods for turbulent reactive flows. *Progress in Energy and Combustion Science, 11*(2), 119-192.

Puri, R., Santoro, R. J., & Smyth, K. C. (1994). The oxidation of soot and carbon monoxide in hydrocarbon diffusion flames. *Combustion and Flame, 97*(2), 125-144.

Quintiere, J. G. (1998). *Principles of fire behavior.* Cengage Learning.

Quintiere, J. G. (2006). *Fundamentals of fire phenomena.* England: John Wiley & Sons.

Rhodes, J., Smith, C., & Stec, A. A. (2011). Characterisation of soot particulates from fire retarded and nanocomposite materials, and their toxicological impact. *Polymer Degradation and Stability, 96*(3), 277-284.

Rizk, N. K., & Mongia, H. C. (1990). Three-dimensional combustor performance validation with high-densityfuels. *Journal of Propulsion and Power, 6*(5), 660-667.

Rizk, N. K., & Mongia, H. C. (1991). Three-dimensional analysis of gas turbine combustors. *Journal of Propulsion and Power, 7*(3), 445-451.

Robbins, A. P., & Wade, C. A. (2008). *Soot yield values for modelling purposes: residential occupancies.* BRANZ.

Rodi, W. (1993). *Turbulence models and their application in hydraulics.* CRC Press.

Roditcheva, O. V., & Bai, X. S. (2001). Pressure effect on soot formation in turbulent diffusion flames. *Chemosphere, 42*(5), 811-821.

Rubini, P. A., Zhang, Q., & Moss, J. B. (2007). Simulation of visibility in smoke laden environments. *InterFlam 2007, 11th International Conference on Fire Science and Engineering.* London, UK: University of Hull.

Saffman, P. (1965). The lift on a small sphere in a slow shear flow. *Journal of fluid mechanics, 22*(02), 385-400.

Saffman, P. (1968). The lift on a small sphere in a slow shear flow - Corrigendum. *Journal of Fluid Mechanics, 31*(03), 624.

Said, R., Garo, A., & Borghi, R. (1997). Soot formation modeling for turbulent flames. *Combustion and Flame, 108*(1), 71-86.

Samson, R. J., Mulholland, G. W., & Gentry, J. W. . (1987). Structural analysis of soot agglomerates. *Langmuir, 3*, 272--281.

Santoro, R. J., Puri, R., Moser, M., Léonard, S., & Smyth, K. C. (1994). *Fundamental mechanisms for CO and soot formation.* National Institute of Standards and Technology.

Schaenman, P. (1991). Estimated impact of the center for fire research program on the costs of fire. *Fire technology, 27*(4), 346-349.

Schlichting, H., & Gersten, K. (2000). *Boundary-layer theory.* Springer.

Seader, J. D., & Einhorn, I. N. (1977). Some physical, chemical, toxicological, and physiological aspects of fire smokes. I *Symposium (International) on Combustion* (Vol. 16, ss. 1423-1445). Elsevier.

Shahad, H. A., & Mohammed, Y. K. (2000). Investigation of soot formation and temperature field in laminar diffusion flames of LPG–air mixture. *Energy conversion and management, 41*(17), 1897-1916.

Siegel, R., & Howell, J. R. (1992). Thermal radiation heat transfer. *NASA STI/Recon Technical Report A, 93*, 17522.

Sippola, M. R., & Nazaroff, W. W. (2002). *Particle deposition from turbulent flow: Review of published research and its applicability to ventilation ducts in commercial buildings.*

Skeers, J. (2006). *Bangladesh: 54 workers killed in textile factory fire.* the International Committee of the Fourth International (ICFI).

Smyth, K. C. (2010, May). *Diffusion flame measurements.* Hentet fra http://www.bfrl.nist.gov

Spalding, D. B. (1971). *Mixing and chemical reaction in steady confined turbulent flames* (Vol. 13). Elsevier.

Spalding, D. B. (1979). *Combustion and Mass Transfer.* New York: Pergamon Press, Oxford.

Strick, J. (2014). *Development of Safety Measures for Nightclubs.* Department of fire safety engineering, Lund University, Sweden.

Surovikin, V. F. (1976). Analytical description of the processes of nucleus-formation and growth of carbon black in the thermal decomposition of aromatic hydrocarbons in the gas phase. *Khimiya Tverdogo Topliva, 10*(1), 111–122.

Syed, K. J., Stewart, C. D., & Moss, J. B. (1991). Modelling soot formation and thermal radiation in buoyant turbulent diffusion flames. I *Symposium (International) on Combustion* (Vol. 23, ss. 1533-1541). Elsevier.

Takahashi, F., & Glassman, I. (1984). Sooting correlations for premixed flames. *Combustion Science and Technology, 37*(1), 1-19.

Talbot, B. L., Cheng, R. K., Schefer, R. W., & Willis, D. R. (1980). Thermophoresis of particles in a heated boundary layer. *Journal of fluid mechanics, 101*(04), 737-758.

Tanzawa, T., & Gardiner Jr, W. C. (1980). Reaction mechanism of the homogeneous thermal decomposition of acetylene. *The Journal of Physical Chemistry, 84*(3), 236-239.

Tesner, P. A., Smegiriova, T. D., & Knorre, V. G. (1971). Kinetics of dispersed carbon formation. *Combustion and Flame, 17*(2), 253-260.

Tewarson, A. (1988). *Smoke point height and fire properties of materials.* National Institute of Standards and Technology.

Tewarson, A. (2002). Generation of heat and chemical compounds in fires. I *SFPE handbook of fire protection engineering* (3. utg., ss. 83-161).

Tewarson, A., Jiang, F. H., & Morikawa, T. (1993). Ventilation-controlled combustion of polymers. *Combustion and flame, 95*(1), 151-169.

Thermo, K. (2014). *Generator set range SG-3000 & SG-4000 series.* Ingersoll-Rand Company Limited. Hentet fra http://www.americanstandardair.com

Thomas Mckinnon, J., & Howard, J. B. (1992, December). The roles of PAH and acetylene in soot nucleation and growth. I *Symposium (International) on Combustion* (Vol. 24, ss. 965-971). Elsevier.

Thomson, K. A., Gülder, Ö. L., Weckman, E. J., Fraser, R. A., Smallwood, G. J., & Snelling, D. R. (2005). Soot concentration and temperature measurements in co-annular, nonpremixed CH4/air laminar flames at pressures up to 4 MPa. *Combustion and Flame, 140*(3), 222-232.

Venyavsky, S. (2007). 62 dead in Russian nursing home fire. *thestar*.

Versteeg, H. K., & Malalasekera, W. (2007). *An introduction to computational fluid dynamics: the finite volume method.* Pearson Education.

Vetterling, W. T., Flannery, B. P., Press, W. H., & Teukolski, S. A. (1989). *Numerical Recipes in Fortran-The art of scientific computing.* University Press.

Veynante, D., & Vervisch, L. (2002). Turbulent combustion modeling. *Progress in energy and combustion science, 28*(3), 193-266.

Wade C., Beever P., Fleischmann C., Lester J., Lloydd D., Moule A., Saunders N., and Thorby P. (2007). Developing Fire Performance Criteria for New Zealand's Performance Based Building Code. *Presented at the Fire Safety Engineering International Seminar.* Paris.

Walton, W. D. (1985). ASET-B: A room fire program for personal computers. *Fire Technology, 21,* 293-309.

Walton, W. D., Baum, H. R., Notarianni, K. A., Lawson, J. R., Tang, H. C., Keydel, K. R., ... & Tennyson, E. J. (1992). *In-situ burning of oil spills: Mesoscale experiments.* National Institute of Standards and Technology.

Wang, H., & Frenklach, M. (1997). A detailed kinetic modeling study of aromatics formation in laminar premixed acetylene and ethylene flames. *Combustion and flame, 110*(1), 173-221.

Wang, Q., Squires, K. D., Chen, M., & McLaughlin, J. B. (1997). On the role of the lift force in turbulence simulations of particle deposition. *International Journal of Multiphase Flow, 23*(4), 749-763.

Wang, Z., Galea, E. R., & Jia, F. . (2007, October). A computational study of the characteristics of aircraft post-crash fires. *In Proc Int Aircraft Fire & Cabin Safety Conf.*

Wang, Z., Jia, F., & Galea, E. R. (2012). Fire and evacuation simulation of the fatal 1985 Manchester airport B737 fire. *Proceedings of the 5th International Symposium* (ss. 159-170). Cambridge: Interscience Communications Ltd.

Wang, Z., Jia, F., Galea, E. R., & Patel, M. K. (2011). Predicting toxic gas concentrations at locations remote from the fire source. *Fire and Materials, 35*(7), 505-526.

Wang, Z., Jia, F., Galea, E. R., Patel, M. K., & Ewer, J. (2001). Simulating one of the CIB W14 round robin test cases using the SMARTFIRE fire field model. *Fire Safety Journal, 36*, 661-677.

Warnatz, J., Maas, U., & Dibble, R. W. (2006). *Combustion: physical and chemical fundamentals, modeling and simulation, experiments, pollutant formation.* Springer.

Wen, J. X., Heidari, A., Ferraris, S., & Tam, V. H. Y. (2011). Numerical simulation of propane detonation in medium and large scale geometries. *Journal of Loss Prevention in the Process Industries, 24*(2), 187-193.

Wesseling, P. (1995). *Introduction To Multigrid Methods.* INSTITUTE FOR COMPUTER APPLICATIONS IN SCIENCE AND ENGINEERING HAMPTON VA.

Wey, C., Powell, E. A., & Jagoda, J. I. (1984). The Effect of Temperature on the Sooting Behavior of Laminar Diffusion Flames. *Combustion Science and Technology, 41*(3-4), 173-190.

Wilcox, D. A. (1994). Simulation of transition with a two-equation turbulence model. *AIAA journal, 32*(2), 247-255.

Wilcox, D. C. (1988). Reassessment of the scale-determining equation for advanced turbulence models. *AIAA journal, 26*(11), 1299-1310.

Wilcox, D. C. (2004). *Turbulence modeling for CFD* (2. utg.). La Canada: CA: DCW industries.

Williams, F. A. (2000). Progress in knowledge of flamelet structure and extinction. *Progress in Energy and Combustion Science, 26*(4), 657-682.

Wilmot, T. (1986). National fire costs-a wasteful past but a better future. *In Proceedings of First International Symposium on Fire Safety Science, 1*, pp. 1009-1018.

Xin, Y., & Gore, J. P. . (2005). Two-dimensional soot distributions in buoyant turbulent fires. *Proceedings of the Combustion Institute, 30*(1), 719-726.

Xin, Y., Gore, J. P., McGrattan, K. B., Rehm, R. G., & Baum, H. R. (2005). Fire dynamics simulation of a turbulent buoyant flame using a mixture-fraction-based combustion model. *Combustion and Flame, 141*(4), 329-335.

Xu, F., El-Leathy, A. M., Kim, C. H., & Faeth, G. M. (2003). Soot surface oxidation in hydrocarbon/air diffusion flames at atmospheric pressure. *Combustion and flame, 132*(1), 43-57.

Yakhot, V., Orszag, S. A., Thangam, S., Gatski, T. B., & Speziale, C. G. (1992). Development of turbulence models for shear flows by a double expansion technique. *Physics of Fluids A: Fluid Dynamics, 4*(7), 1989-1993.

Yao, W. (2010). *soot modelling in laminar and turbulent combustion(Doctoral dissertation).* University of Ulster.

Yao, W., Delichatsios, M., Beji, T., & Zhang, J. (2011b). A simple approach of laminar soot modeling calibrated by nonsmoking, incipient-smoking and smoking ethylene diffusion flames. *In Proceedings of the European Combustion Meeting, 18*, ss. 1-6.

Yao, W., Zhang, J., Nadjai, A., Beji, T., & Delichatsios, M. A. (2011a). A global soot model developed for fires: Validation in laminar flames and application in turbulent pool fires. *Fire Safety Journal, 46*(7), 371-387.

Zhang, J. (1998, October). *particle technology –study notes (Motion of particles through fluids, chapter 2). upon tyne.* . Hentet fra STUDY NOTES for CPE 124 Particle Technology: hppt://lorien.ncl.ac.uk/ming/particle/cep124p2.html

Zhang, J., & Huang, Y. (2014). The research of prison fire risk assessment. *Journal of Chemical & Pharmaceutical Research, 6*(7).

Zhang, Z., & Chen, Q. (2006). Experimental measurements and numerical simulations of particle transport and distribution in ventilated rooms. *Atmospheric environment, 40*(18), 3396-3408.

Zhao, B., Yang, C., Yang, X., & Liu, S. (2008). Particle dispersion and deposition in ventilated rooms: testing and evaluation of different Eulerian and Lagrangian models. *Building and Environment, 43*(4), 388-397.

Zhao, B., Zhang, Y., Li, X., Yang, X., & Huang, D. (2004). Comparison of indoor aerosol particle concentration and deposition in different ventilated rooms by numerical method. *Building and Environment, 39*(1), 1-8.

Zhu, X. L., & Gore, J. P. (2005). Radiation effects on combustion and pollutant emissions of high-pressure opposed flow methane/air diffusion flames. *Combustion and flame, 141*(1), 118-130.